



Alma Mater Studiorum – Università di Bologna

Dottorato di Ricerca in Geofisica
XXIV ciclo

*Integrating new and traditional approaches
for the estimate of slip-rates of active faults:
examples from the Mw 6.3, 2009 L'Aquila
earthquake area, Central Italy*

Settore Concorsuale di afferenza: 04/A4/Geo10 – GEOFISICA DELLA TERRA SOLIDA

Presentata da: Riccardo Civico

Coordinatore Dottorato

Relatore

Prof. Michele Dragoni

Dott. Paolo Marco De Martini

Esame finale anno 2012

To Giulia

Abstract

This thesis developed a multidisciplinary and multi-scale investigation strategy based on the integration of traditional and innovative approaches aimed at improving the normal faults seismogenic identification and characterization, focusing mainly on slip-rate estimate as a measure of the fault activity.

The L'Aquila Mw 6.3 April 6, 2009 earthquake causative fault was used as a test site for the application, testing, and refinement of traditional and/or innovative approaches, with the aim to 1) evaluate their strength or limitations 2) develop a reference approach useful for extending the investigation to other active faults in the area and 3) translate the results of the methodological approaches into new inputs to local seismic hazard.

The April 6, 2009 L'Aquila earthquake occurred on a so far poorly known tectonic structure, considered having a limited seismic potential, the Paganica - San Demetrio fault system (PSDFS), and thus has highlighted the need for a detailed knowledge in terms of location, geometry, and characterization of the active faults that are the potential sources for future earthquakes.

To fill the gap of knowledge enhanced by the occurrence of the 2009 L'Aquila earthquake, we developed a multidisciplinary and multiscale-based strategy consisting of paleoseismological investigations, detailed geomorphological and geological field studies, as well as shallow geophysical imaging and an innovative methodology that uses, as an alternative paleoseismological tool, core sampling and laboratory analyses but also *in situ* measurements of physical properties.

The integration of geomorphology, geology as well as shallow geophysics, was essential to produce a new detailed geomorphological and geological map of the PSDFS and to define its tectonic style, arrangement, kinematics, extent, geometry and internal complexities.

Our investigations highlighted that the PSDFS is a 19 km-long tectonic structure characterized by a complex structural setting at the surface and that is arranged in two main sectors: the Paganica sector to the NW and the San Demetrio sector to SE. The Paganica sector is characterized by a narrow deformation zone, with a relatively small (but deep) Quaternary basin affected by few fault splays. The San Demetrio sector is characterized by a strain distribution at the surface that is accommodated by several tectonic structures, with the system opening into a set of parallel, km-spaced fault traces that exhume and dissect the Quaternary basin.

The integration of all the fault displacement data and age constraints (radiocarbon dating, optically stimulated luminescence (OSL) and tephrochronology) resulting from paleoseismological, geomorphological, geophysical and geological investigations played a primary role in the estimate of the slip-rate of the PSDFS. Slip-rates were estimated for different time intervals in the Quaternary, from Early Pleistocene (1.8 Ma) to Late Holocene (last 5 ka), yielding values ranging between

0.09 and 0.58 mm/yr and providing an average Quaternary slip-rate representative for the PSDFS of 0.27 - 0.48 mm/yr.

We contributed also to the understanding of the PSDFS seismic behavior and of the local seismic hazard by estimating the max expected magnitude for this fault on the basis of its length (ca. 20 km) and slip per event (up to 0.8 m), and identifying the two most active fault splays at present. Our multidisciplinary results converge toward the possibility of the occurrence of past surface faulting earthquakes characterized by a moment magnitude between 6.3 and 6.8, notably larger than the 2009 event, but compatible with the M range observed in historical earthquakes in the area. The slip-rate distribution over time and space and the tectonic style of the PSDFS suggested the occurrence of strain migration through time in the southern sector, from the easternmost basin-bounding fault splay toward the southwestern splays. This topic has a significant implication in terms of surface faulting hazard in the area, because it can contribute defining the fault splays that have a higher potential to slip during future earthquakes along the PSDFS.

By a methodological point of view, the multidisciplinary and multiscale-based investigation strategy emphasizes the advantages of the joint application of different approaches and methodologies for active faults identification and characterization. Our work suggests that each approach alone may provide sufficient information but only the application of a multidisciplinary strategy is effective in providing robust results and in defining a proper framework of active faults.

TABLE OF CONTENTS

Abstract	i
Table of contents	iii
Acknowledgments	vii
1. Introduction	1
2. Active faults in geology	5
2.1. Faults: basic concepts	5
2.1.1. Faults and stress	5
2.1.2. Fault growing	7
2.2. Active faults	8
2.2.1. Definition	8
2.2.2. Faults and slip accumulation models	9
2.2.3. Faults and strain release models	10
2.2.4. Faults geometry and regional stress field	11
2.2.5. Geologic evidence of active normal faults	14
2.2.6. Landforms associated with active normal faults	14
2.3. Examples from the Basin and Range Province and from the Walker Lane, Nevada, USA	18
2.4. Slip-rate	23
3. The Mw 6.3 April 6, 2009 L'Aquila earthquake	25
3.1. Seismic sequence and causative fault	25
3.1.1. The seismic sequence	26
3.1.2. The earthquake causative fault	29
3.2. Earthquake effects on the environment	30
3.2.1. Coseismic deformation	30
3.2.2. Coseismic surface effects and ground ruptures	35
3.3. Summary	40
3.4. Open questions raised by the 2009 earthquake	42
3.5. Other examples of surface faulting earthquakes and coseismic deformation	42
3.5.1. The 2010 (Mw 7.2) El Major – Cucapah earthquake	42
3.5.2. The 1915 Pleasant Valley (Ms 7.7), 1954 Fairview Peak (Ms 7.2) and Dixie Valley (Ms 6.8) earthquakes and their surface ruptures	46
4. Brief seismotectonic overview of the Central Apennines	51

5. Paleoseismological approach	55
5.1. Introduction	55
5.2. Paleoseismology – method	56
5.2.1. Trenching	58
5.2.2. Coring	60
5.2.3. Chronological constraints	61
5.2.3.1. Radiocarbon dating	61
5.2.3.2. Archeological evaluation of pottery shards	64
5.3. Paleoseismological trenching along the PSDFS	64
5.3.1. Aqueduct site	65
5.3.2. Zaccagnini site	67
5.3.3. Mo’Tretteca site	69
5.3.4. 250K site	71
5.4. Main results	73
6. Tectonic geomorphological and geological approach	75
6.1. Introduction	75
6.2. Tectonic geomorphological approach	76
6.2.1. LiDAR	77
6.2.2. Large-scale view of the Middle Aterno basin	80
6.2.3. Landforms	80
6.2.4. Across-strike topographic profiles	85
6.2.5. Main results of the tectonic geomorphological approach	88
6.3. Geological approach	93
6.3.1. Geological mapping	93
6.3.2. Quaternary deposits	94
6.3.3. Chronological constraints	99
6.3.3.1. Optically Stimulated Luminescence (OSL)	100
6.3.3.2. Tephrochronology	102
6.3.4. Geological cross sections	104
7. Geophysical approach	107
7.1. Introduction	107
7.2. High-resolution petrophysical correlations	107
7.2.1. Introduction	107
7.2.2. Mo’Tretteca site	108
7.2.3. Fossa site	115
7.3. Electrical resistivity tomography	118
7.3.1. Method	118
7.3.2. Results	121
7.3.3. San Vittorino site	121
7.3.4. Villa Sant’Angelo site	123
7.3.5. L’Annunziata site	124
7.3.6. San Gregorio site	126
7.3.7. Pie’ i colle site	128
7.3.8. Campo di Contra site	129
7.4. High-resolution seismic tomography	130
7.4.1. Method	130
7.4.2. Results	132

8. Discussion	135
8.1. Tectonic style of the PSDFS	135
8.2. PSDFS length	136
8.3. Partitioning of deformation along the PSDFS	138
8.4. Slip-rate of the PSDFS	140
8.5. Slip-rates through time and space	146
8.6. Strain migration	147
8.7. Contribution to seismic hazard	149
9. Conclusions	153
References	157
Appendix A - Geomorphological map of the PSDFS	
Appendix B - Geological map of the PSDFS	
Appendix C - Geological cross sections of the PSDFS	
Appendix D1-2-3-4 - Topographic profiles across the PSDFS	
Appendix E - Along-strike plot of the morphological throws	
Appendix F - Evolution in time and space of the extension-rates of the PSDFS	
Appendix G - <i>Emergeo Working Group (2010), Evidence for surface rupture associated with the Mw 6.3 L'Aquila earthquake sequence of April 2009 (central Italy), Terra Nova, 22, 1, 43-51, doi: 10.1111/j.1365-3121.2009.00915.x.</i>	
Appendix H - <i>Cinti, F.R., Pantosti, D., De Martini, P.M., Pucci, S., Civico, R., Pierdominici, S., Cucci, L., Brunori, C.A., Pinzi, S., Patera, A. (2011), Evidence for surface faulting events along the Paganica Fault prior to the April 6, 2009 L'Aquila earthquake (Central Italy). J. Geophys. Res., 116, B07308, doi:10.1029/2010JB007988.</i>	
Appendix I - <i>Improta, L., Villani, F., Bruno, P.P., Castiello, A., De Rosa, D., Varriale, F., Punzo, M., Brunori, C.A., Civico, R., Pierdominici, S., Berlusconi, A., Giacomuzzi, G. (2011), High-resolution controlled-source seismic tomography across the Middle Aterno basin in the epicentral area of the 2009, Mw 6.3, L'Aquila earthquake (central Apennines, Italy). In press on the Italian Journal of Geosciences.</i>	
Appendix L - <i>Brunori, C.A., Civico, R., Cinti, F.R., Ventura, G. (2011), Characterization of active fault scarps from LiDAR data: a case study from Central Apennines (Italy). Submitted to the International Journal of Geographic Information.</i>	

Acknowledgements

First and foremost I offer my sincerest gratitude to my supervisor, Paolo Marco De Martini, who has supported me throughout my thesis with his patience and knowledge. Without his encouragement and effort this thesis would not have been completed or written. One simply could not wish for a better and friendlier supervisor.

I would like to express my deep and sincere gratitude to Daniela Pantosti. Her wide knowledge and her logical way of thinking have been of great value for me. Her understanding and encouraging have provided a good basis for the present thesis.

I'm also grateful to Stefano Pucci for guiding me through part of this thesis and for transferring me his experience, enthusiasm and for sharing a lot of fieldwork.

I'm much obliged to Marina Iorio, for her valuable instructions and suggestions throughout this thesis and for giving me the opportunity to collaborate with the IAMC-CNR.

Special thank goes to Steven G. Wesnousky, for the stimulating discussions and for being supportive during my time at the Center for Neotectonic Studies, University of Nevada, Reno.

During this work I have collaborated with many researchers for whom I have great regard, and I wish to extend my warmest thanks to all those who have helped me with my work at the Istituto Nazionale di Geofisica e Vulcanologia: Francesca Romana Cinti, Carlo Alberto Brunori, Antonio Patera, Alessandra Smedile, Paola Del Carlo, Andrea Cavallo, Luigi Improta, Guido Ventura, Roberto Basili, Stefania Pinzi, Luigi Cucci.....a complete list is impossible!

I'm greatly indebted to the Istituto Nazionale di Geofisica e Vulcanologia for the financial and logistical support.

I'm also grateful to other PhD students who shared study and laughter in Rome: special thanks to "i ragazzi del Pollajo": Michele, Leda, Irene, Luigi, Debora, Cosmiana, Mariagrazia, Matteo and the others.

I owe my loving thanks to Simona. Without her encouragement and understanding it would have been impossible for me to finish this work.

Finally, I am forever grateful to my mom and to my family, for supporting me through my never-ending education.

1 Introduction

Italy is one of the areas with the highest seismic hazard in the Mediterranean region. The Italian seismic history is characterized by a 2,000 yr-long history of small-to-large magnitude earthquakes occurred through the centuries that often have left a strong imprint on the country's heritage, economy, but also landscape.

One of these events was the Mw 6.3 April 6, 2009 L'Aquila earthquake, that struck a densely populated area in the central Apennines causing more than 300 casualties and leaving more than 60,000 homeless.

This earthquake was the strongest in Italy since the Mw 6.9 1980, Irpinia event and it was the first that struck so close to a densely populated Italian town (L'Aquila; ca 70,000 inhabitants) since the Mw 7.1 1908, Messina earthquake.

The L'Aquila Mw 6.3 April 6, 2009 earthquake struck a sector of the central Apennines that is characterized by the presence of several active faults accommodating prevalent NE-SW oriented extension. Some of these faults activated during historical times producing earthquakes with M up to 7; this magnitude seems to represent the Max magnitude expected for the area also on the basis of tectonic, geologic, and geomorphic observations from nearby faults.

The present knowledge on the active faults in this area derives from decades of studies in geomorphology and Quaternary geology as well as from some paleoseismological investigations. The April 6, 2009 L'Aquila earthquake is probably the best seismologically, geodetically and geologically documented earthquake so far in Italy. The large amount of experimental data acquired during the whole L'Aquila sequence concurred to image the fault that slipped during the event. This fault was reported in some of the pre-earthquake active fault compilations although, it was poorly known and because of this, considered with a limited seismic potential.

Besides underlining the fragility of our residential, historical, and monumental patrimony, the 2009 L'Aquila earthquake has highlighted the need for a detailed knowledge in terms of location, geometry, and characterization of the active faults that are the potential sources for future earthquakes. This is because, a systematically developed knowledge of the location and of the seismogenic behavior of the active faults in a region, is an innovative and relevant contribution to seismic hazard. More specifically it is a contribution to the development of earthquake recurrence and segmentation models as input for time-dependent probabilistic SHA, to the modeling of ground-motion scenarios and to the definition of fault hierarchy, evolution, migration for surface faulting hazard estimates.

To fill the gap of knowledge enhanced by the occurrence of the 2009 L'Aquila earthquake, this thesis was thought to contribute to a better knowledge of the earthquake source fault with the idea of developing a reference approach useful for extending the investigation to other active faults in the area. Actually, the focus of

this thesis was established a few months before the occurrence of this earthquake and was mostly centered on a methodological analysis and the application of different traditional and innovative approaches for the estimate of active fault slip-rates. This core of the thesis was not changed, but it was readdressed on one specific fault: the 2009 L'Aquila earthquake fault. Practically, the estimate of the slip-rate of the fault by using different approaches remains the leading subject of the thesis but, this methodological part has now an immediate practical application in the improvement of the understanding of L'Aquila 2009 earthquake fault.

Thus, the thesis has developed following a twofold path: on the one side, the application, testing, and improvement of traditional or innovative approaches for slip rate estimates, on the other side, the study of the L'Aquila earthquake fault by applying what learned methodologically to provide new inputs to local seismic hazard. Slip-rate and Max expected magnitude are the critical parameters to input in seismic hazard calculations. Slip rate is a measure of the activity of a fault as it represents the amount of strain it accommodated during a given period of time. Max magnitude is strictly related to the size of the slipping fault that is given by length and amount of coseismic slip. A further needed contribution for seismic hazard, that was strongly highlighted for the first time in Italy by the 2009 earthquake, was the definition of the surface faulting hazard (e.g. the Tempera aqueduct pipe broke because crossed by surface faulting). This awareness stimulated a substantial refinement of the fault mapping, including also the minor and blind active fault traces with the aim to define those that have a higher potential to slip during future earthquakes.

During the three years of doctorate we developed a multidisciplinary and scale-based strategy consisting of paleoseismological investigations, detailed geomorphological and geological field studies, as well as shallow geophysical imaging, and an innovative methodology that uses, as an alternative paleoseismological tool, core sampling and laboratory analyses but also *in situ* measurements of physical properties. The different approaches were integrated to provide the best slip-rate estimate for the 2009 earthquake fault, to map the fault component at the surface and to define the fault segment boundaries.

In particular we performed a three steps approach:

- 1) paleoseismological, including a trenching and coring campaign with the excavation of 4 trenches and the realization of 2 boreholes;
- 2) geomorphological and geological, integrating field survey and dating of Quaternary layers by means of Optically Stimulated Luminescence (OSL), radiocarbon dating and tephrochronology together with LiDAR-derived high resolution DEM and air-photo analysis;
- 3) geophysical, including high resolution petrophysical correlations, electrical resistivity tomography (ERT) and shallow seismic profiling.

The present thesis is composed of nine chapters. Apart for this introduction (namely chapter 1) a brief outline of each of the following chapters is given below.

Chapter 2 summarizes the basic concepts on faulting, and then focuses on describing some main parameters constraining the geometries of active normal faults as well as geological and geomorphological elements characterizing them. A brief description of slip-rate significance is provided too.

Chapter 3 gives a brief overview of the Mw 6.3 April 6, 2009 L'Aquila earthquake and its seismic sequence and then focuses on the coseismically induced effects on the environment, with special attention to the displacement field as imaged by DInSAR and GPS and to the surface ruptures detected during the geologic field survey performed in the epicentral area. A brief discussion on the questions raised by the occurrence of this earthquake is presented too.

Chapter 4 summarizes the main seismotectonic characteristics of the central Apennines, focusing in particular on the present-day deformation.

Chapter 5 presents the paleoseismological approach to the characterization of active faults and illustrates the main results of a paleoseismological campaign carried out across the northwestern portion of the L'Aquila 2009 earthquake fault with the main goal to reconstruct its recent seismic history and to estimate the short-term slip-rate (up to ~30 ka).

Chapter 6 introduces the basic methodologies of the geomorphological and geological investigations in active areas with particular attention to the identification, and characterization of the long-term expression of faults through the study and dating of continental deposits and landforms affected by different fault splays. The results of the detailed survey carried out in the Middle Aterno valley over an area of ~140 km² supported by extensive thematic mapping is presented too. The main goal of this chapter was to provide new insights on the Quaternary deformational history of the fault and to obtain a long-term slip-rate estimate (~2 Ma).

Chapter 7 illustrates the main results always in terms of offset measurement, fault location, and slip rates estimates of a multidisciplinary and multiscale-based geophysical investigation approaches; these includes an innovative methodology based on measurements of physical properties, 2D-electrical resistivity tomography (ERT), and high-resolution seismic tomography. For each of the methodology applied we have discussed both the benefits and limitations

Chapter 8 integrates and discusses the main results and implications of this thesis and presents some perspectives about its possible contribution to seismic hazard assessment.

The Conclusions chapter (namely 9), shortly summarizes the different phases of the development of this thesis, the results from each of the approaches employed and discuss their integration in the key of the seismic hazard of the area.

2 Active faults in geology

The most common class of active faults found in Central Italy are normal faults, in good agreement with the present-day regional stress conditions showing that the Apenninic belt is undergoing extension (Montone et al., 1999, 2004; Mariucci et al., 2010). Because extensional tectonics prevails in the study area, in this chapter, after a brief description of some basic concepts on faulting, we will focus on the description of geological and geomorphological evidence of active normal faults and of their evolution.

2.1 Faults: basic concepts

2.1.1 Faults and stress

Faulting occurs in response to imposed stresses and is fundamentally a brittle mechanism for achieving shear displacement along discrete fracture surfaces, under conditions of low temperatures and confining pressures.

The displacement observed along a fault can be achieved in several ways:

- by a single fault surface;
- by a “fault zone”, composed of numerous sub-parallel and interconnecting closely spaced fault surfaces;
- by a shear zone, where shear displacement is achieved by a wide zone of distributed simple shear that accommodates movement of one side of the shear zone relative to the other. Shear zones are common at deep crustal level, where temperatures and confining pressures are greater.

Anderson (1905, 1951) developed the modern mechanical concepts of the origin of faults and highlighted their role in tectonics. He recognized that principal stress orientation could vary among geological provinces within the upper crust of the Earth and postulated a fundamental relationship between fault types and the orientation of the causative stress tensor relative to the Earth's surface.

Considering the boundary between the Earth surface and the atmosphere a no-shear plane and the Earth as a perfect sphere, Anderson pointed out that one principal axis of crustal stress tensors will, at any point, be close to vertical (perpendicular to the Earth's surface) and the other two axes close to horizontal (figure 2.1).

The type of faulting depends upon the principal stress directions in combination with the Coulomb criterion of failure. According to the theory of Anderson, if principal stress direction near or at the Earth's surface is vertical, and if the angle of internal friction for most rocks is about 30°, only three basic fault types should be able to form. In particular, normal, strike-slip, and thrust faults occur depending on whether σ_1 , σ_2 or σ_3 respectively, is vertical.

Even if this theory is conceptually useful, it is an approximation and it does not explain the occurrence of some faults, such as low-angle normal faults (with dips of

$\leq 30^\circ$), flat thrust faults, or faults that develop in previously fractured, anisotropic rock.

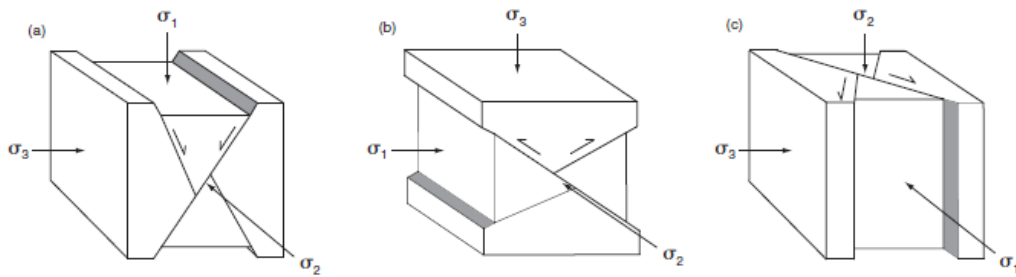


Figure 2.1 - Schematic representation of the three classes of faults determined by the orientation of the principal stresses: (a) normal fault; (b) thrust fault; (c) strike-slip fault (after Angelier, 1994). σ_1 , σ_2 or σ_3 are the three principal stress directions.

We can also identify main classes of faults with respect to the absolute direction, sense and magnitude of movement. These three components constitute the slip, which represent the actual displacement. On this basis we can recognize (figure 2.2):

- Strike-slip faults, accommodating horizontal slip between adjacent blocks;
- Dip-slip faults, characterized by translation directly up or down the dip of the fault surface. Movement on a dip-slip fault is described with respect to the relative movement of hanging wall and footwall.

Moreover, in the broad field of dip-slip faults, we can distinguish normal-slip faults, reverse-slip faults (including thrust) and low-angle normal faults. A normal-slip fault, in particular, is one in which the hanging wall moves down with respect to the footwall.

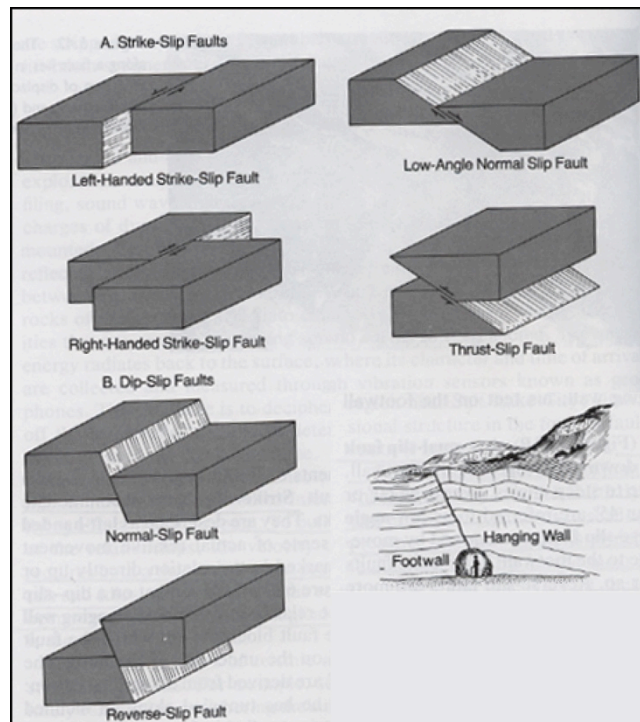


Figure 2.2 - Faulted blocks showing the characteristic displacement for the different classes of faults (modified after Davis and Reynolds, 1996).

Fault systems can range in length and displacement from small breaks with millimetric offset to regional crustal structures extending hundreds to more than 1000 km and accommodating up to hundreds of km offset.

2.1.2 Fault growing

How do faults grow from an initial rupture to a mature geological fault?

Cartwright et al. (1995) suggested two models for fault growth from an initial rupture to a mature geological fault (figure 2.3): 1) radial propagation and 2) segment linkage:

- During fault growth by radial propagation, an individual fault simply lengthens over time and accumulates displacement according to a well-defined linear relationship. Displacement increases steadily as the fault grows (figure 2.3a).
- Alternatively, small individual fault segments (t1) can gradually link up to create one large fault. In this case the total length of the fault suddenly increases, whereas the total displacement does not substantially change (t2). Over time, the composite fault may smooth out the slip deficit near the former segment boundaries (t3), re-adjusting the shape of the displacement profile following the idealized bow-shaped displacement gradient (figure 2.3b).

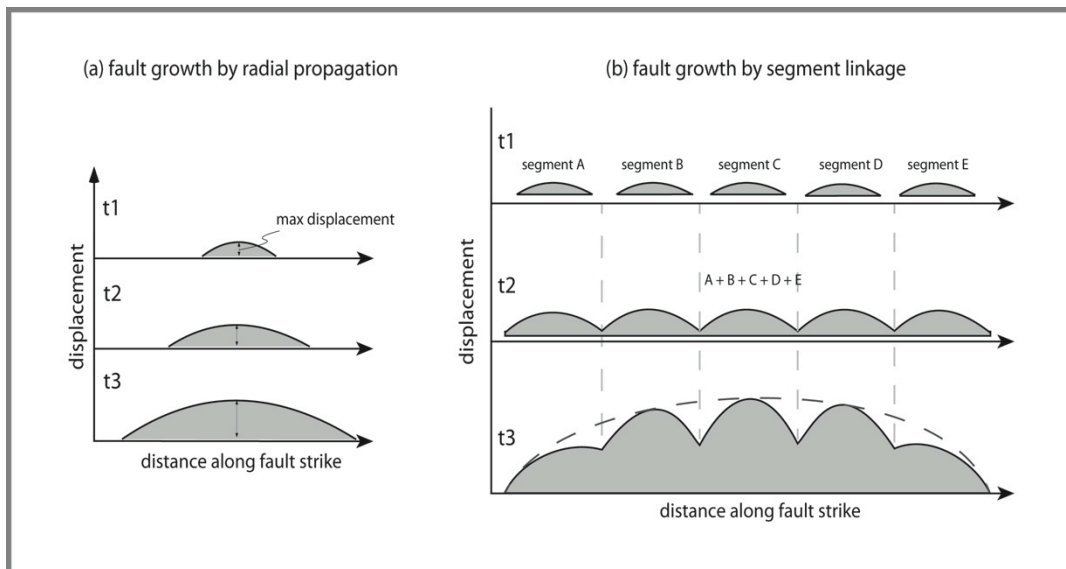


Figure 2.3 – (a) Growth of an idealized individual extensional fault (redrawn after Cartwright et al., 1995), and (b) of an idealized extensional fault array.

2.2 Active faults

2.2.1 Definition

The activity of a fault is generally defined by the way it cumulates displacement over time; we can think about an active fault as one that cumulated some displacement in the recent past and is considered likely to move again in the near future.

There is not a fixed rule about what time scale should be used to address the activity of a fault:

- According to Slemmons & De Polo (1986), to define a fault as active, we must identify two key elements: 1) the potential or probability of future displacements in the present tectonic regime; 2) the timing of the most recent displacements (historical, Holocene (11.7 ka), Quaternary (2.6 Ma) or “in the present seismotectonics regime”);
- Boschi et al. (1996) proposed a "Consensus Statement" in which "An active fault of interest for Seismic Hazard Assessment is a structure that has an established record of activity in the Late Pleistocene (i.e. in the past 125 ka) and a demonstrable or inferable capability of generating major earthquakes.";
- The State of California, in the 2007 Alquist-Priolo Earthquake Fault Zoning Act define an active fault as one which has “had surface displacement within Holocene time (11.7 ka)”;
- In the Basin and Range Province, the WSSPC - Western States Seismic Policy Council (2011) defines three classes of active faults: 1) Holocene fault – a fault whose movement in the past 11,700 calibrated years B.P. (Cohen and Gibbard, 2010) has been large enough to break the ground surface; 2) Late Quaternary fault – a fault whose movement in the past 130,000 years has

been large enough to break the ground surface; 3) Quaternary fault – a fault whose movement in the past 2,600,000 (Cohen and Gibbard, 2010) years has been large enough to break the ground surface;

- The International Atomic Energy Agency (IAEA) guidelines (2010) make a distinction between active structures in different tectonic settings by proposing to consider an Upper Pleistocene-Holocene time frame in interplate regions and a Pliocene-Quaternary time frame in intraplate regions.

2.2.2 Faults and slip accumulation models

In order to classify fault behavior, not in function of time, Schwartz and Coppersmith (1984) proposed three models of displacement associated with individual earthquakes (figure 2.4):

Several different scenarios have been proposed to accommodate a given regional strain field: in the variable slip model (a), both the amount of slip at a given point and the length of rupture may vary between successive earthquakes, producing variability in earthquake size and a uniform slip-rate along the length of the fault. In the uniform slip model (b) there is a constant displacement per event at any point, a constant slip-rate all along the fault and a constant magnitude of large earthquakes, with more frequent moderate sized events. If the fault ruptures producing earthquakes with about the same magnitude, then the fault is said to generate characteristic earthquake (c). In this latter case the displacement per event is the same at any point, while the slip-rate is variable along the length of the fault.

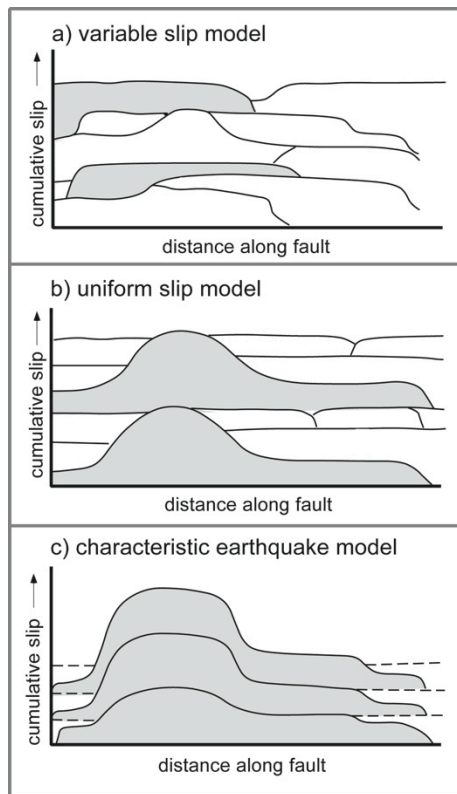


Figure 2.4 - Diagrammatic representation of three hypothetical models of slip accumulation. (redrawn after Schwartz and Coppersmith (1984).

2.2.3 Faults and strain release models

Reid (1910) proposed a theory for the earthquake cycle known as “elastic rebound theory”. According to him, elastic strain accumulates for a long period on a locked fault (interseismic phase), until strain reaches a critical value (elastic limit) and the frictional resistance is overcome. An earthquake occurs when a sudden displacement of the two sides of the fault takes place to reach a position of minimum strain (coseismic phase). A third phase of the seismic cycle correspond to a period of minutes to years after an earthquake when the crust and fault both “adjust” to the modified state of crustal stress caused by the occurrence of the earthquake (postseismic phase).

Fault activity over time has been described in the literature by four main strain release models (figure 2.5).

In the “perfectly periodic” (a) model (Reid, 1910), the elastic strain energy accumulated across completely locked faults is periodically released during earthquakes of fairly uniform slip and recurrence interval. On the other and, some researchers highlighted that the time until the next earthquake and the size of earthquakes on a particular fault are not perfectly periodic and proposed two models: “time-predictable” model and the “slip-predictable” model (Shimazaki and Nakata, 1980). According to the “time-predictable” model (b), earthquakes always occur when a critical stress threshold is attained. In this model, the time of the next

earthquake can be predicted based on the slip-rate of the fault and on the size of the previous event. Alternatively, the “slip-predictable” model (c) suggests that, for any given event, all the strain energy accumulated since the last earthquake is released. This model, based on the slip-rate of the fault and on the time since the last earthquake, is able to predict the size, but not the time, of the next seismic event. All the three models assume a constant rate of far-field displacement and strain accumulation. Some faults may be characterized, at different time scales, by temporal grouping of slip events releasing the strain energy (Wallace, 1987). This latter behavior (d) is characterized by a great increase in the slip-rate for a relatively short period, separated by long quiescence intervals.

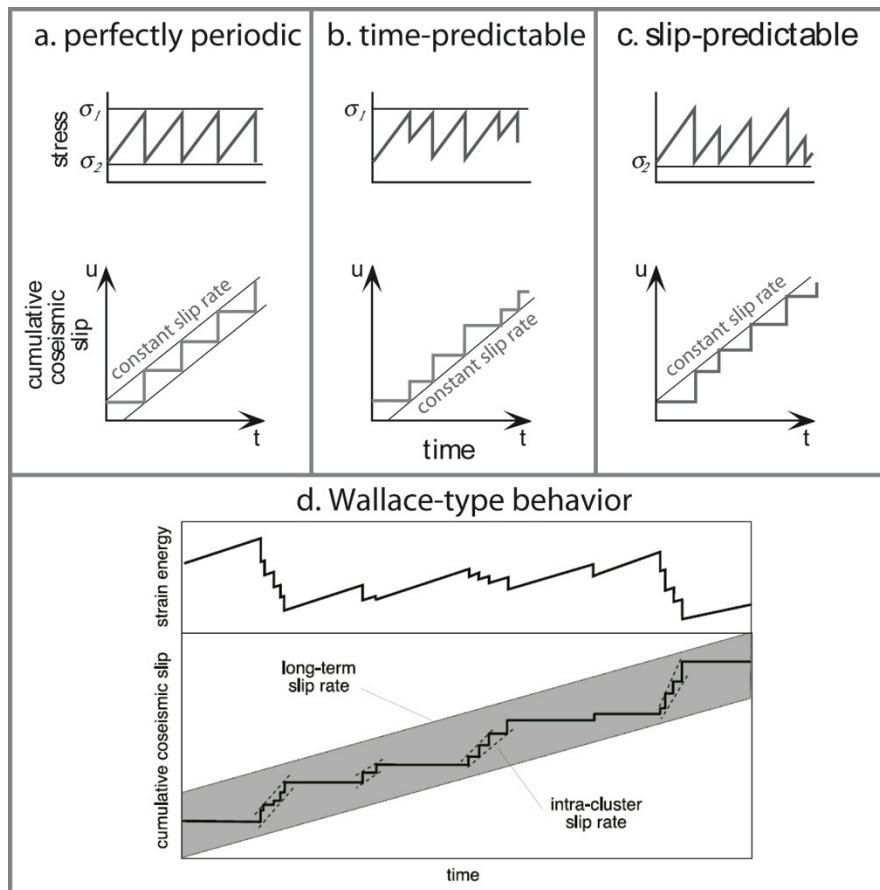


Figure 2.5 - Strain release models for earthquakes (a - c redrawn after Scholz [1990], d after Friedrich et al., 2003)

2.2.4 Faults geometry and regional stress field

We have seen in the previous section that normal faulting accommodates extension and vertical shortening, and can occur in settings where the maximum compressive stress (σ_1) is vertical and there is a deviatoric tensile stress in a horizontal orientation.

Normal faults are the dominant fault class along mid-oceanic spreading centers and in rifted continental margins, as well in continental sedimentary basins and in passive margins and they represent a way in which individual rock layers, or the lithosphere itself, can lengthen and stretch in brittle or semibrittle fashion.

A great variety of normal faulting styles have been seen, or inferred, from geological outcrops or indirect geophysical surveys, including steep planar faults, strongly curved listric (concave-up) faults that become virtually flat within the upper crust, and very low-angle faults dipping at less than 20° .

For the purposes of this thesis, we will mainly focus on active normal faulting in continental regions undergoing extension today, trying to obtain different sources of information.

Regions of active continental extension experiencing present-day normal faulting include the western U.S.A., Greece, western Turkey, Italy, the Gulf of Suez, Tibet, Yunnan, Mongolia, the Lake Baykal region, parts of China and East Africa. Seismological and surface observations of seismogenic normal faults in all the above mentioned regions provide information on the three-dimensional geometry of the present-day extensional deformation.

If we look at earthquake focal depths the most important observation is that earthquakes are usually confined in the upper 10-20 km of the crust (Jackson and White, 1989).

The thickness of this seismogenic layer appears to influence the length scale of the deformation in the crust, in particular with respect to the lateral continuity of normal faults and width of the extensional basins (graben) that form in extensional provinces.

Continental normal fault systems are commonly segmented, and the maximum segment length appear to be influenced by the seismogenic thickness (T_s), being typically ~20-25 km-long with $T_s \sim 15$ km and increasing to ~60-100 km with the $T_s \sim 30-35$ km (Jackson and White, 1989; Wallace, 1989; Jackson and Blenkinsop, 1997;).

Control on maximum width of tilted-blocks or half-graben is supported by observations showing that maximum half-graben widths are typically ~10-25 km where T_s is 15 km but can be much wider (up to 60 km) in those parts of East Africa where $T_s \sim 30-35$ km (Jackson and Blenkinsop, 1993).

Observations coming from continental normal faulting earthquakes in a variety of location worldwide show a characteristic pattern of dips at depth that are typically confined to a range of about $30-65^\circ$, whether determined from body-wave focal mechanism, waveform modeling or centroid moment tensor (CMT) analyses (figure 2.6).

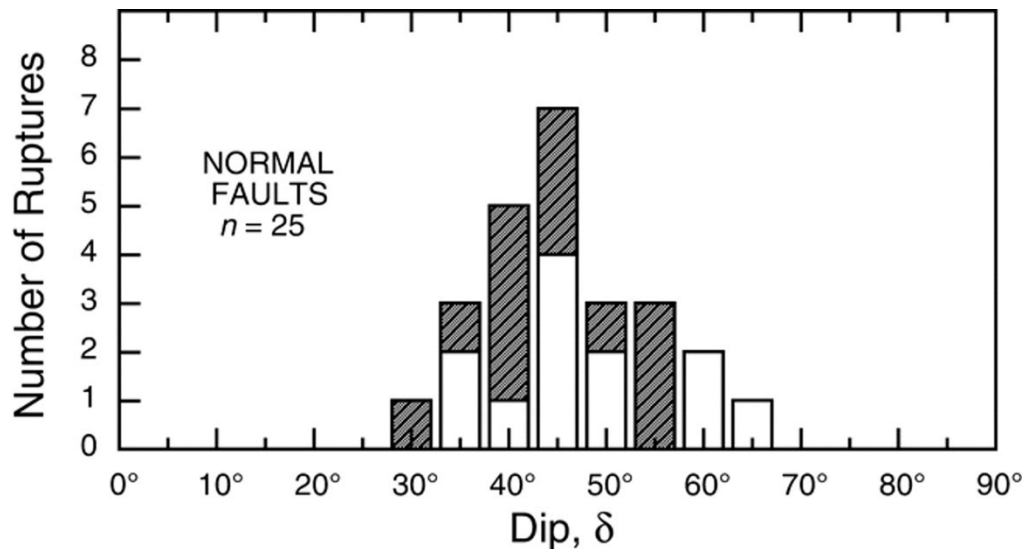


Figure 2.6 – dip distribution for continental normal faulting earthquakes with $M > 5.5$, from compilation of Jackson and White (1989) (no pattern) and Collettini and Sibson (2001) (after Collettini and Sibson (2001)).

A schematic cross section of a region where normal faults are the dominant fault class emphasizes the presence of a set of different structures (figure 2.7).

The upper or overlying block along the master fault plane is called the hanging wall; the block below is called the footwall.

Other structures may develop mainly within the hangingwall block:

- synthetic faults (dipping in the same direction with similar sense of throw);
- antithetic faults (dipping in the opposite direction with an opposite sense of throw);
- horst, that are uplifted, unrotated blocks bounded on either sides by outward-dipping normal faults;
- graben, relatively down-dropped, unrotated block, bounded on either side by inward-dipping normal faults.

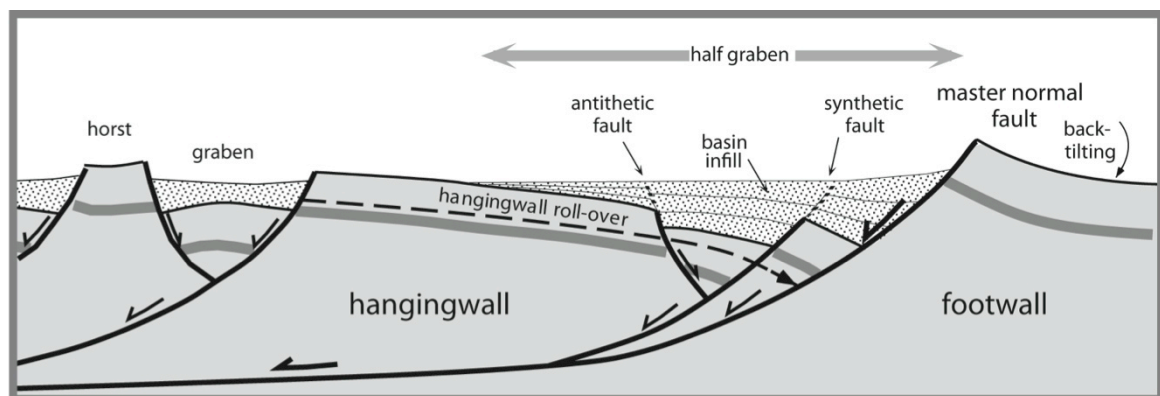


Figure 2.7 - idealized schematic cross section of a region undergoing extension (modified after Burbank and Anderson, 2001).

2.2.5 Geologic evidence of active normal faults

One of the most simple but convincing evidence of fault activity is the cross-cutting or non-cross-cutting relationship with geologic deposits of known age. The age of the offset unit and the amount of the offset can be used to calculate the fault slip-rate and thus to estimate the fault activity.

A wide variety of types of geologic deposits are commonly used in evaluating fault activity, most commonly alluvial and volcanic deposits. Chronological constraints can be obtained by means of a variety of relative and absolute dating methods; some of them will be discussed more in detail in chapter 6.

The structural aspects of geologic units adjacent to faults may also provide information about activity of a fault. Adjacent units may be brecciated and shattered, have open fissures, be tilted or warped.

2.2.6 Landforms associated with active normal faults

Some of the most remarkable topography on land and beneath the oceans is associated with crustal extension and normal faulting. Classic examples are the rift valleys, typically observable along the axes of oceanic ridges and at smaller scale on continents (i.e. the East African Rift system) and the Basin and Range Province, within the western United States.

Landscape development is the results of the interplay between tectonic processes (faulting and folding) that tend to build topography and erosional/depositional processes at the surface that act to restore the equilibrium. The basic concept is that any ongoing change in style, rate, and location of tectonic processes is able to produce, under favorable conditions, detectable changes in the landscape, creating disequilibrium in the geologic and geomorphic processes.

Earthquakes, for example, have the capability to produce instantaneous permanent deformations of the ground surface that reflect the movements occurred as a result of deep-seated processes. Landform development can thus be closely related to the active deformation taking place in the Earth's crust.

For the purposes of this thesis we will focus on those landform features produced by repeated movements along continental active normal faults as results of repeated seismic events.

Active normal faulting produces mainly vertical deformations and tends to build a typical tectonically rising and subsiding landscape characterized by key features that include the following:

- fault scarps;
- triangular facets: roughly planar surfaces with broad bases and upward-pointing apexes that occur between valley that drain the mountain ranges;
- linear and steep mountain fronts;
- fault-bounded basins.

At the time scale of a single earthquake, the most obvious manifestation of active deformation at the surface are coseismic fault scarps, tectonic landforms generally coincident with a fault plane and produced almost instantaneously when an earthquake rupture propagates up to the surface. Scarp formed by normal faulting earthquakes are generally located along preexisting faults at the contact between bedrock and colluvial or alluvial deposits or can occur as fresh, steeply inclined scarps within unconsolidated sediments (figures 2.8 – 2.9). Normal fault scarps resulting from a single increment of displacement along a fault can range in height from few centimeters to more than 10 meters.

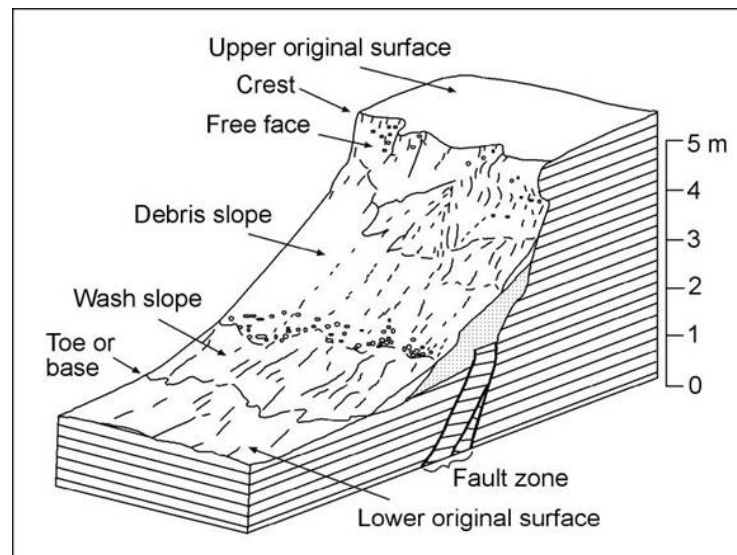


Figure 2.8 - Basic slope elements that may be present on a piedmont fault scarp (after Wallace, 1977).



Figure 2.9 - Coseismic fault scarp of the 1915 Pleasant Valley (M_s 7.7) earthquake

A more detailed description of the geomorphic characteristics of young fault scarps can be found in Wallace, 1977.

Repeated displacements along the same fault can concur to form a compound fault scarp (Slemmons, 1957), also called composite (Stewart and Hancock, 1990) or multiple-event fault scarps, as the one visible in figure 2.10.



Figure 2.10 - Compound fault scarp – Humboldt range, Nevada, USA

At a mature stage, when deformation has been cumulated for several seismic cycles, normal faulting generates a characteristic basin and range topography, common in regions of presently active extension like large parts of Nevada, Utah, Greece, western Turkey and Italy.

In these regions the most evident landforms are mountain fronts that represent zones of topographic transition between uplifted mountains and plains. A typical normal fault mountain front is characterized by an assemblage of landforms that includes the escarpment, the streams that dissect it and the adjacent piedmont landforms (figure 2.11).



Figure 2.11 - Stillwater range, Dixie Valley, Nevada

The cumulative displacements on a range-bounding normal fault create disequilibrium and a base-level fall that causes deep valleys (e.g. wine glasses valleys) to be carved in the relatively uplifted footwall block and favors the sedimentation of alluvial-fan deposits in the subsided hangingwall (figure 2.12 - modified after Keller and Pinter, 2002).

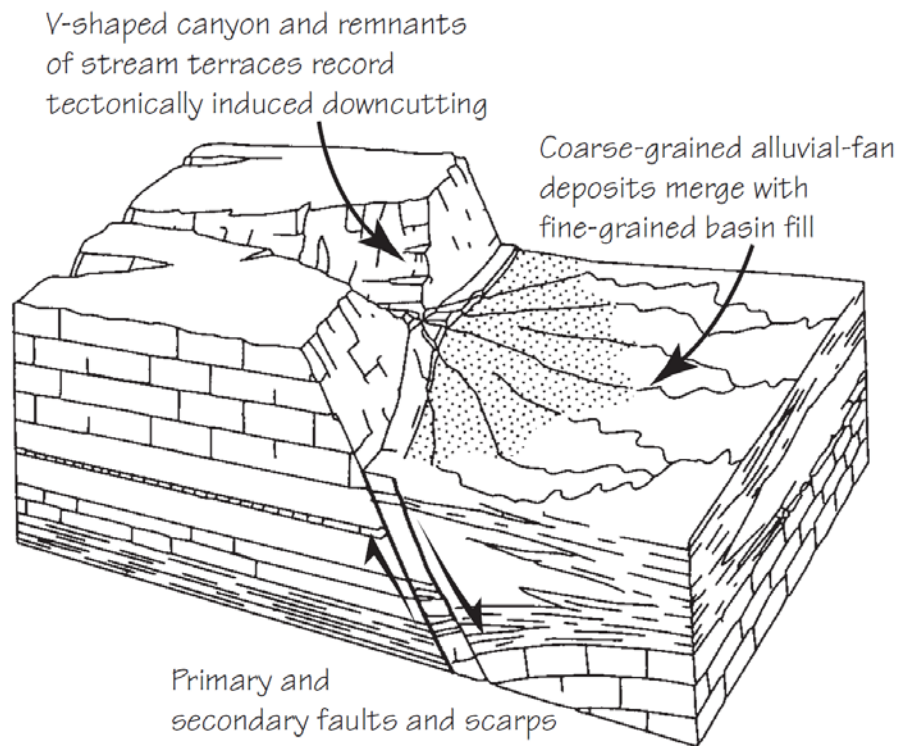


Figure 2.12 - idealized diagram showing the topographic expression of an active normal fault system (after Keller and Pinter, 2002).

An ideal sequential development of a single fault-generated mountain escarpment is well depicted in figure 2.13 and may be useful to visualize some of the concepts showed before. Initial faulting creates a linear scarp (A) that later on tends to migrate away from the base of the rising range (B). At stage C, tectonically induced valleys are notched into the rising block; the occurrence of earthquakes along the same structure maintains a steep, straight mountain front (D). After cessation of uplift, or with more competitive erosional processes, the mountain front becomes sinuous and the relief starts to degrade, lowering the ridgecrests (E).

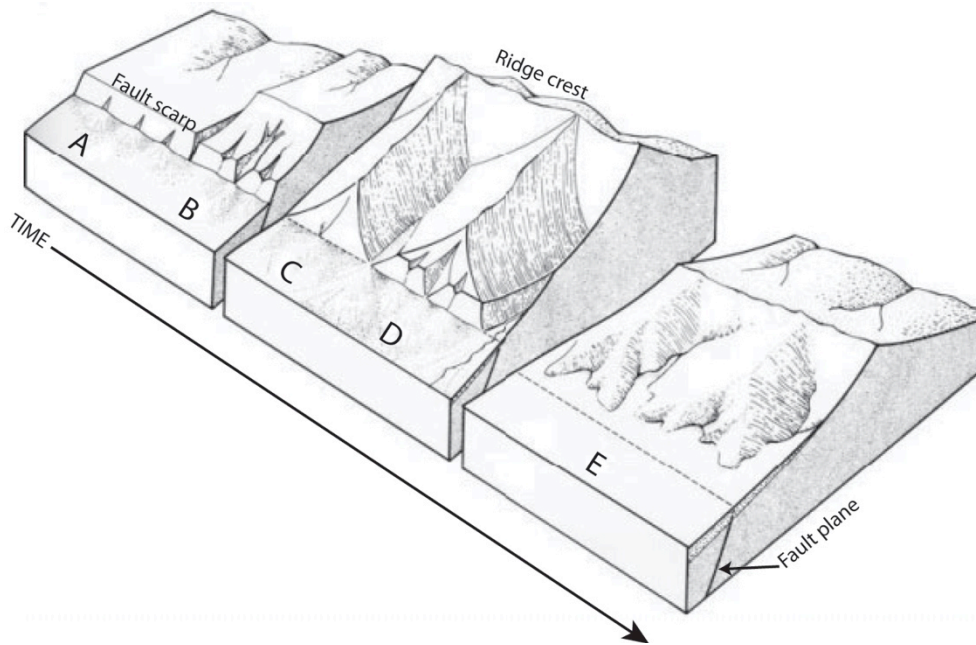


Figure 2.13 - block diagram showing the sequential development of a single fault-generated mountain escarpment (modified after Wallace, 1977)

2.3 Examples from the Basin and Range Province and from the Walker Lane, Nevada, USA

During the time I spent at the Center for Neotectonic Studies of the University of Nevada, Reno, I had the opportunity to visit some of the best morphological expressions of active normal faults in the western U.S.A., in particular the Humboldt Range and the Wassuk Range, located in the Basin and Range Province and the Walker Lane, respectively.

The Humboldt range is a uplifted block with important normal faults on both E-W sides (horst) composed primarily of Permo-Triassic metasedimentary and intrusive rocks (Silberling and Wallace, 1967; Wallace et al., 1969), with peaks rising to elevations of ~ 2900 m a.s.l. close to the adjacent basins laying at ~ 1300 m a.s.l..

Figure 2.14 is a large-scale view of the Humboldt Range, where the morphological expression of Quaternary displacement is greater along the western flank, with a set of range-front normal faults and series of echelon scarps along piedmont faults.

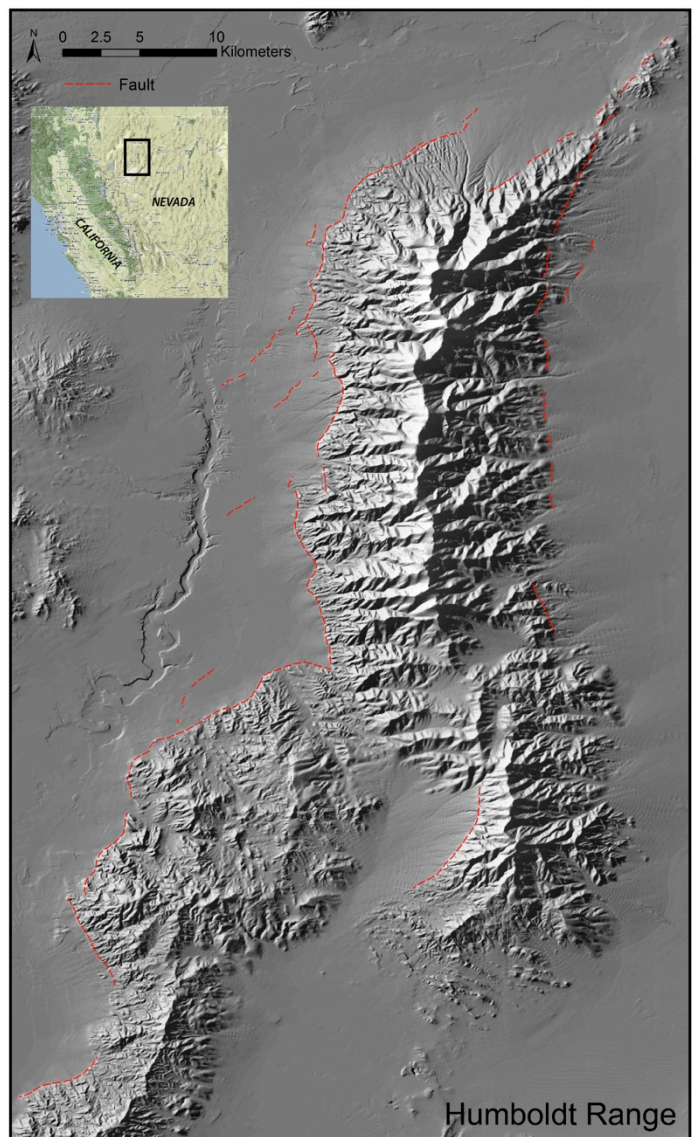


Figure 2.14 – Shaded relief view of the Humboldt Range

Youthful and repeated movement along the range-bounding faults is expressed by offset of highstand shoreline features (figure 2.15) of pluvial Lake Lahontan (about 13 ka - Adams & Wesnousky, 1999) and by the truncation and progressively increasing offset of older alluvial fan surfaces (figure 2.16).

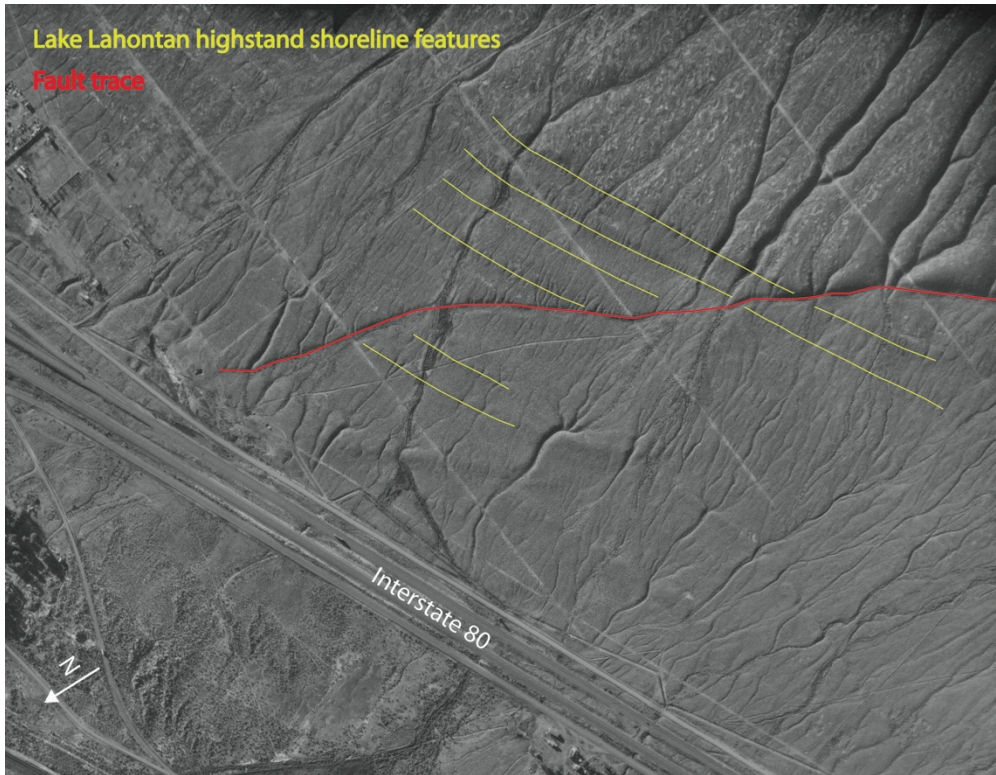


Figure 2.15 - Fault scarp truncating the highstand shoreline features of pluvial Lake Lahontan along the northern end of the fault – Humboldt Range, Nevada, USA

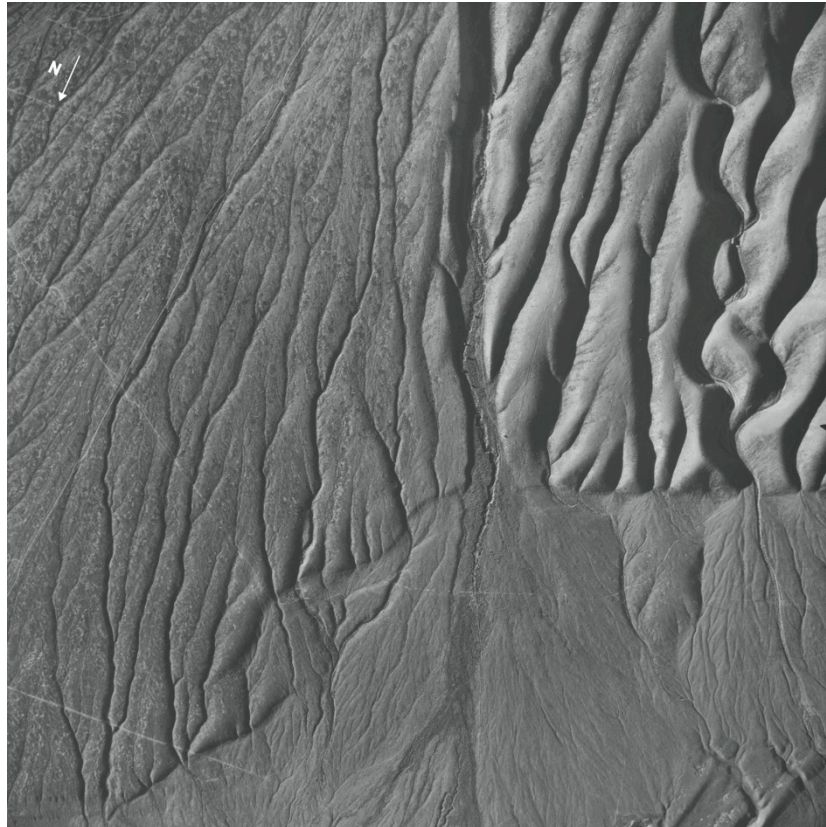


Figure 2.16 - Aerial view of alluvial fan surfaces showing progressively increasing offset; the older alluvial surface (on the right) is characterized by greater uplift and dissection – Humboldt Range, Nevada, USA

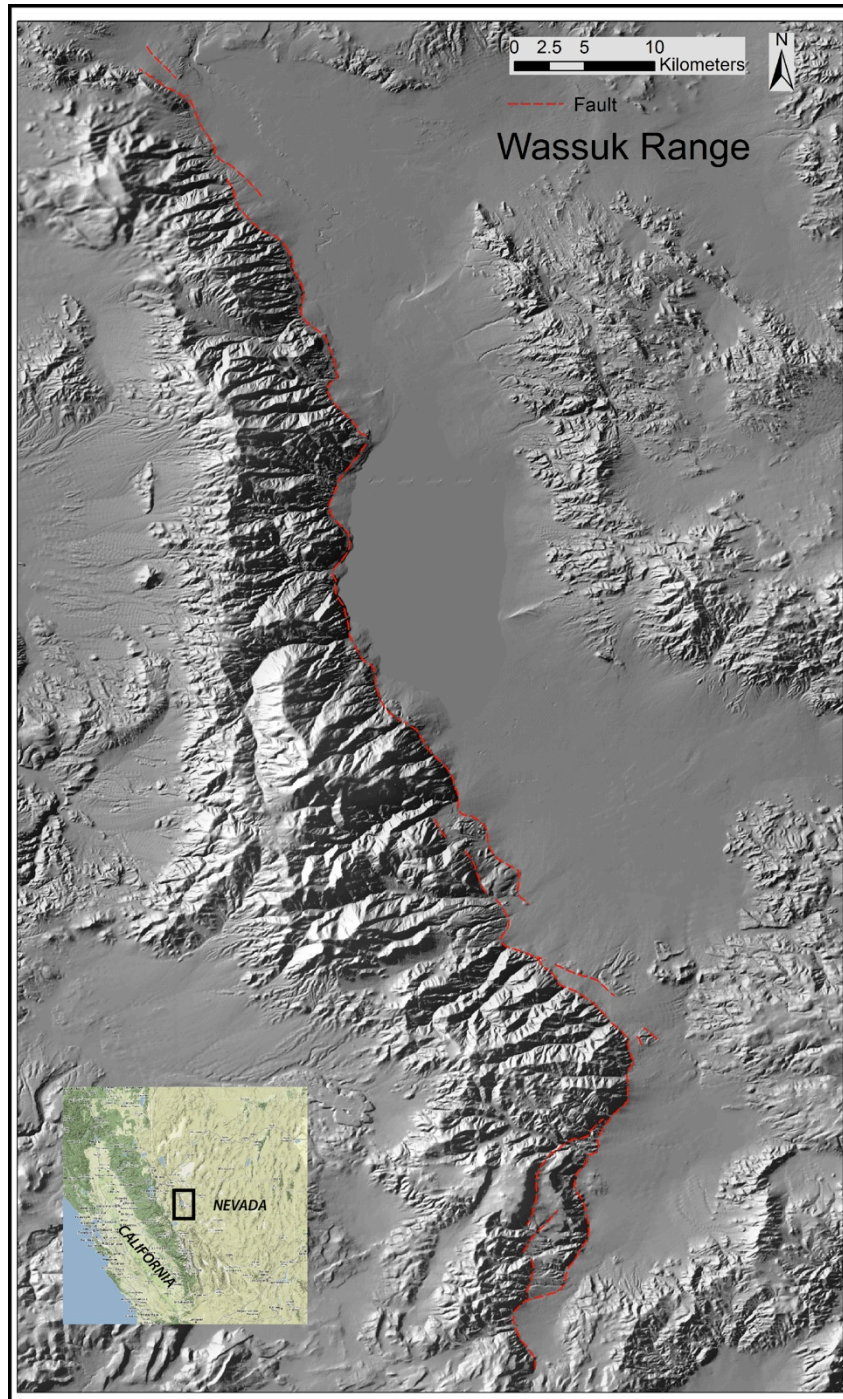


Figure 2.17 – Shaded relief view of the Wassuk Range

Moreover, the Wassuk Range is an east-tilted actively uplifting mountain block composed predominantly of granite with lesser amounts of granodiorite and metavolcanics located near the western margin of the Great Basin. The range strikes northwesterly about 90 kilometers and reaches elevations of more than 3000 m; the adjacent basin being partially filled by the Walker lake.

The overall morphology is dominated by the steep east flank, bounded by a high-angle normal fault with an abrupt sinuous trace and triangular facets, reflecting active normal faulting (figure 2.17 and 2.18).



Figure 2.18 - steep mountain front along a portion of the east flank of the Wassuk Range, Nevada, USA

Chronological constraints of the Quaternary activity of this fault come from Late Pleistocene shorelines related to the highstand of pluvial Lake Lahontan (about 13 ka - Adams & Wesnousky, 1999), preserved along the mountain front. Holocene fault scarps are present along the entire rangefront and at the mouths of active drainages commonly reach 4 to 6 m height, (figure 2.19). Longer-term Quaternary offset is visible in 20 m to 40 m high scarps truncating older alluvial fan surfaces along the northern sector of the range (Wesnousky, 2005).



Figure 2.19 - Quaternary fault scarp in alluvial fan deposits along the northern portion of the Wassuk Range, Nevada, USA

2.4 Slip-rate

The main subject of this thesis is the slip-rate and the different methodologies that can concur to estimate it.

Fault slip-rate is essentially a space/time problem, which in geology translates into a displacement/age problem.

More in detail, the slip-rate represents the amount of strain that accumulates and then is released across a fault in a given time period and is defined as the ratio of slip (displacement) to the time interval over which that slip occurred.

A key fact about slip-rate to keep in mind is that it does not represent constant motion along a fault, even though the motions of tectonic plates are constant. Instead, the slip-rate represents an average of the total slip along a fault over a certain period of time.

Slip-rate is one of the fundamental descriptors of fault activity and represents a key in understanding the relative "importance" of faults in an area, as well as tectonic activity and earthquake recurrence in a region.

As a consequence, slip-rates are critical input data for assessing the seismic hazard assessment (SHA) of active fault zones. For this reason a great amount of efforts is spent trying to estimate slip-rates and discriminate between seismically active and inactive faults.

There are several ways to estimate the slip-rate of an active fault. In any case, we need a data set containing fault displacement and precise age control on deformed deposits spanning a significant portion of a fault's life.

These data are often difficult to find, mainly because their preservation requires a delicate balance to be maintained between sedimentation, erosion, regional tectonic uplift and fault displacement through sufficiently long periods of time.

In order to obtain these data, we can use both direct and indirect approaches.

Direct approaches are those mainly related to geological disciplines, such as geology, geomorphology and tectonic, while indirect approaches are commonly related to geophysical disciplines, such as seismology, geodesy and subsurface geophysics.

Depending on the type of the available information, fault slip-rates can be estimated at different spatial and temporal scales. It is possible to estimate fault slip-rates over spans of millions of years (several seismic cycles of large-magnitude earthquakes on a fault) to hundreds of years (a single seismic cycle, or a part of a cycle).

Moreover, it is possible to estimate fault slip-rates taking into account the deformation recorded by an entire range front, or using the cumulative displacement on a surface (an alluvial fan surface, i.e.) as well as analyzing a single-event displacement.

A common and direct way to estimate the slip-rate of a fault is to find a geological or morphological feature, the age of which can be determined, that has been offset by the fault being studied. A faulted paleosurface, which may contain deposits suitable to be dated, is an excellent example. Dividing the offset showed by the two portions of the paleosurface by the estimated time since the paleosurface was first created (before it was cut by the fault), it is possible to estimate a slip-rate for the fault.

It is important to note that geological slip-rate estimates are minimum estimates, because the feature used to define fault offset formed some unknown time prior to fault initiation.

3 The Mw 6.3 April 6, 2009 L'Aquila earthquake

The Mw 6.3 April 6, 2009 L'Aquila earthquake, with its long aftershock sequence, probably produced the largest amount of experimental data ever recorded in Italy for a single earthquake. These include seismological, geodetic, subsurface exploration and geological data.

For the purposes of this thesis, after a brief overview of the seismic sequence and of the main event, we will focus on coseismically induced deformations on the environment, with special attention to the displacement field as imaged by DInSAR and GPS and to the surface effects and ruptures detected during the geologic field survey.

3.1 Seismic sequence and causative fault

On April 6, 2009 (01:32 UTC – 03:32 Italian time), a strong earthquake (Mw 6.3) struck a densely populated area in the Apennines portion of the Abruzzi region and was felt in a wide area of central Italy (figure 3.1). More than 300 people were killed and more than 60,000 were left homeless. Although seismic hazard maps considered this area as one with the highest earthquake probability, this disaster highlighted the fragility of our historical towns and the need for a better understanding of the Italian active faults and of their seismic potential. Data recorded by permanent and temporary stations of the National Seismic Network (RSNC) managed by the Istituto Nazionale di Geofisica e Vulcanologia (INGV), by the national and local geodetic network, remote sensing and geologic data, all allowed to define the space-time evolution of the entire seismic sequence and to obtain important information on the location and geometry of the fault system responsible for the event.

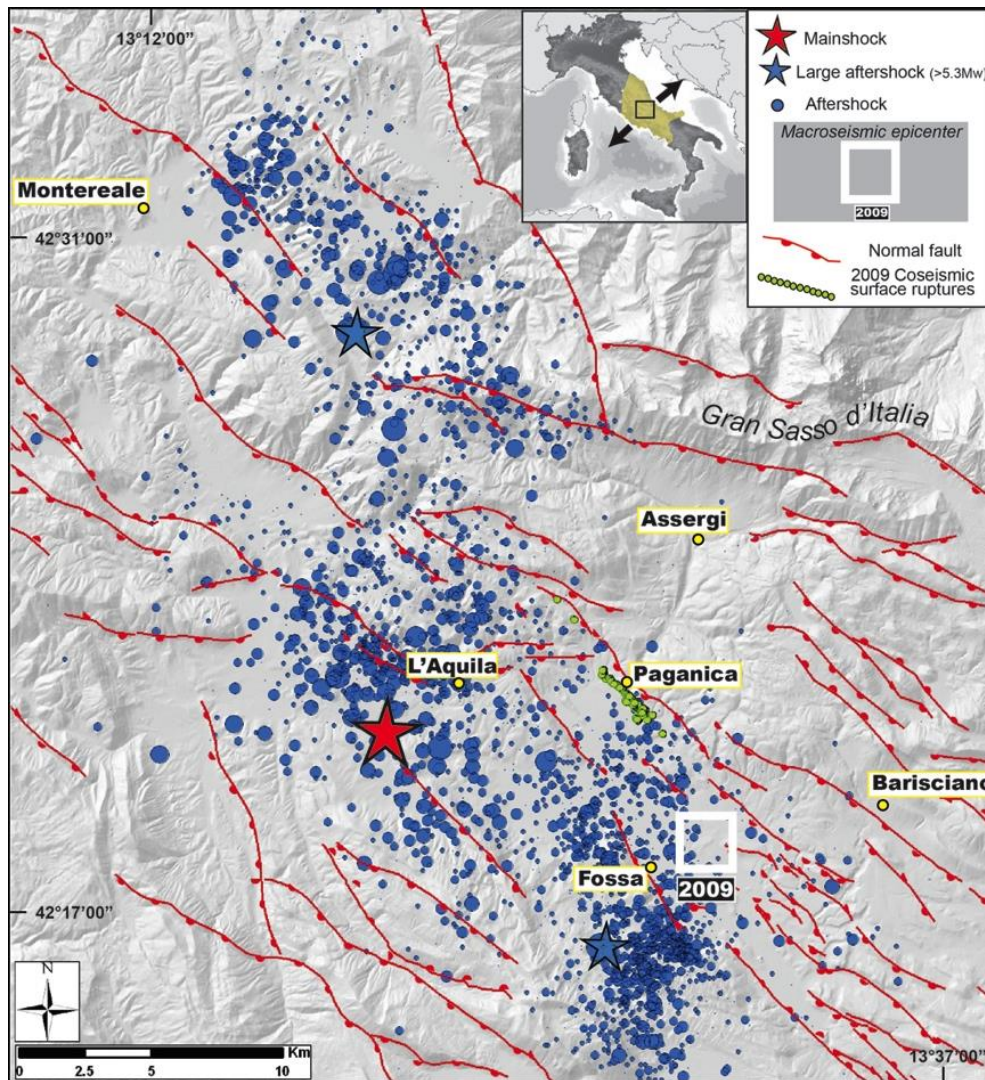


Figure 3.1 - The 2009 L'Aquila seismic sequence as recorded by the INGV Italian National Seismic Network (Chiarabba et al., 2009). Focal mechanism of the main shock and of the two largest aftershocks (Pondrelli et al., 2010) are shown (modified after Cinti et al., 2011). The macroseismic epicenter location (from damage and felt reports) of the 2009 event was computed using the Code Boxer 4.0 (Gasperini et al., 2010). The white box is the projection to the surface of the ~ 18 km-long fault modeled by Cirella et al., (2009). The white line is the expected emergence of the fault at surface. The inset in the upper right shows the direction of extension across the central Apennines (black arrows) and the regional felt area for the 6 April mainshock (colored area).

3.1.1 The Seismic sequence

The Mw 6.3 April 6, 2009 mainshock was preceded by a long seismic activity characterized by a sequence of foreshocks clustering around the main shock nucleation area. This foreshock sequence started in October 2008 and culminated with a Mw 4.4 event on March 30, 2009 and a Mw 4.2 earthquake a few hours before the mainshock. The main shock is located just beneath the town of L'Aquila and nucleated in the upper crust at a depth of ~9.5 km.

Following the April 6 mainshock, a total area of more than 1000 km² was interested by a sequence of aftershocks, occurring both to the northeast and to the southeast

with respect to the mainshock epicenter (figure 3.1). The 2009 L'Aquila seismic sequence activated a normal fault system reaching a total length of about 50 km in the NW-trending direction. Most of the events show hypocentral depths ranging from ~15 km to ~2 km, within the typical seismogenic thickness of central Apennines. Moreover, the southern seismicity cluster was characterized by the deepest hypocentral depths, with earthquakes deeper than 20 km.

A total of seven $M_W \geq 5$ and numerous $M_W \geq 4$ aftershocks occurred during the weeks after the mainshock, with more than 30,000 seismic events recorded during the whole sequence.

The plot in figure 3.2 shows the cumulative energy released during the 2009 L'Aquila seismic sequence (from January to July 2009). It is noticeable that the relative contribution in terms of energy related to the whole foreshock sequence is comparable to the energy released by the M_W 4.4 event of March 30, while it is clear that most of the energy released in the whole seismic sequence is related to the M_W 6.3 April 6, 2009 mainshock. Taking into account this information, we can expect that most of the coseismic deformation at depth and at the surface is related to the April 6 mainshock.

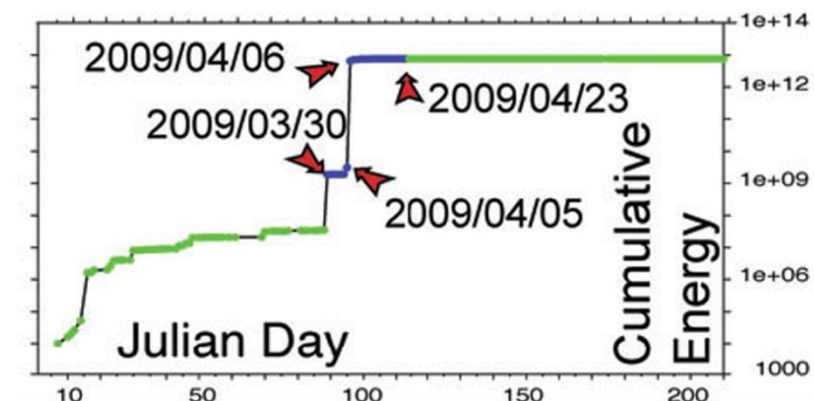


Figure 3.2 – Cumulative seismic energy release (joule) from January to July 2009 (after Pondrelli et al., 2010).

Looking at the focal mechanisms of the larger earthquakes, we can see that the entire seismic sequence is dominated by NE-SW oriented extension, in good agreement with geodesy and regional tectonics (figure 3.3), with only few events showing a strike-slip component (Pondrelli et al., 2010).

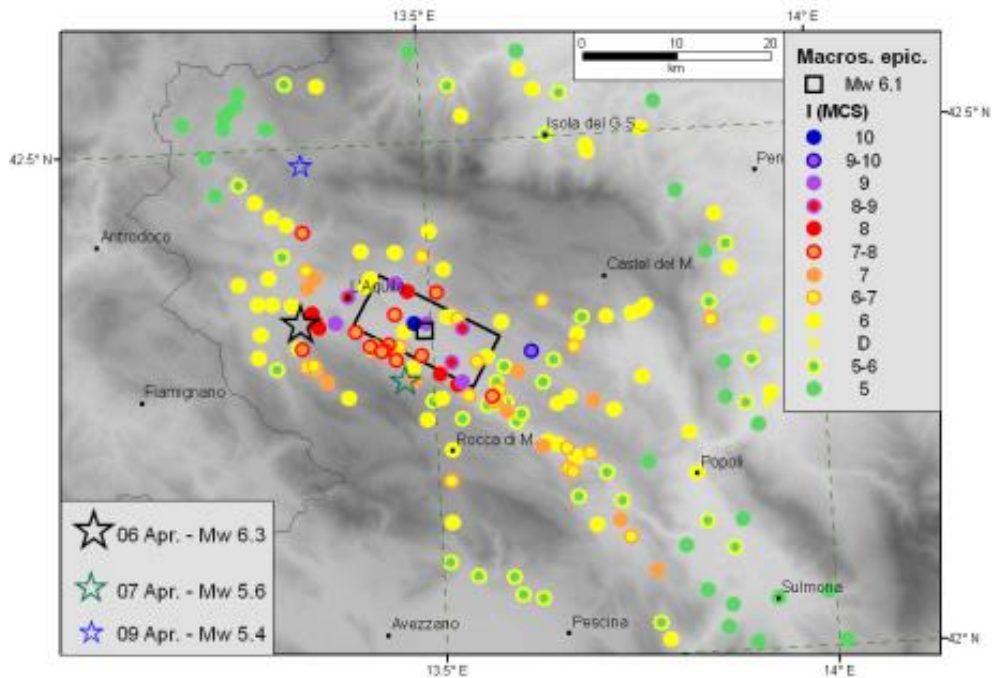


Figure 3.4 – Map showing the results of the macroseismic survey. The black rectangle indicates the macroseismic box based on the distribution of macroseismic intensities. (after Galli and Camassi, 2009).

3.1.2 The earthquake causative fault

The large amount of data acquired during the sequence was used to constrain the location and the geometry of the fault system responsible for the 2009 L'Aquila mainshock. In particular the aftershocks distribution (figure 3.5), together with DInSAR analysis, body waves seismology, strong motion records and GPS observations and surface faulting all concurred to image the geometry of the fault responsible for the 6 April main shock.

Source modeling resulting from the inversion of geodetic and seismological data revealed a heterogeneous slip distribution on the fault plane (Anzidei et al., 2009; Atzori et al., 2009; Cheloni et al., 2010; Cirella et al., 2009; Pino & Di Luccio, 2009; Trasatti et al., 2011). The rupture pattern was characterized by two main slip patches: the largest slip concentration at depth was located southeastward from the hypocenter and showed a maximum slip of ~ 1.1 m; a second smaller patch was observed above the hypocenter and was characterized by a maximum slip of ~ 0.7 m. The rupture history is characterized by directivity effects, with an up-dip initial rupture propagation followed by a second rupture propagating along fault strike to the south-east (Cirella et al., 2009; Pino & Di Luccio, 2009). Slip on the fault plane was predominantly normal dip-slip (Chiarabba et al., 2009; Pondrelli et al., 2010), with a minor right-lateral component (Cirella et al., 2009; Walters et al., 2009).

All the modeling efforts (Anzidei et al., 2009; Atzori et al., 2009; Cheloni et al., 2010; Chiarabba et al., 2009; Cirella et al., 2009; Pino & Di Luccio, 2009; Trasatti et al., 2011; Walters et al., 2009) converge toward a causative fault characterized by:

- a NW-SE orientation;
- 15-18 km of length;
- 42°- 55° dip to the SW.

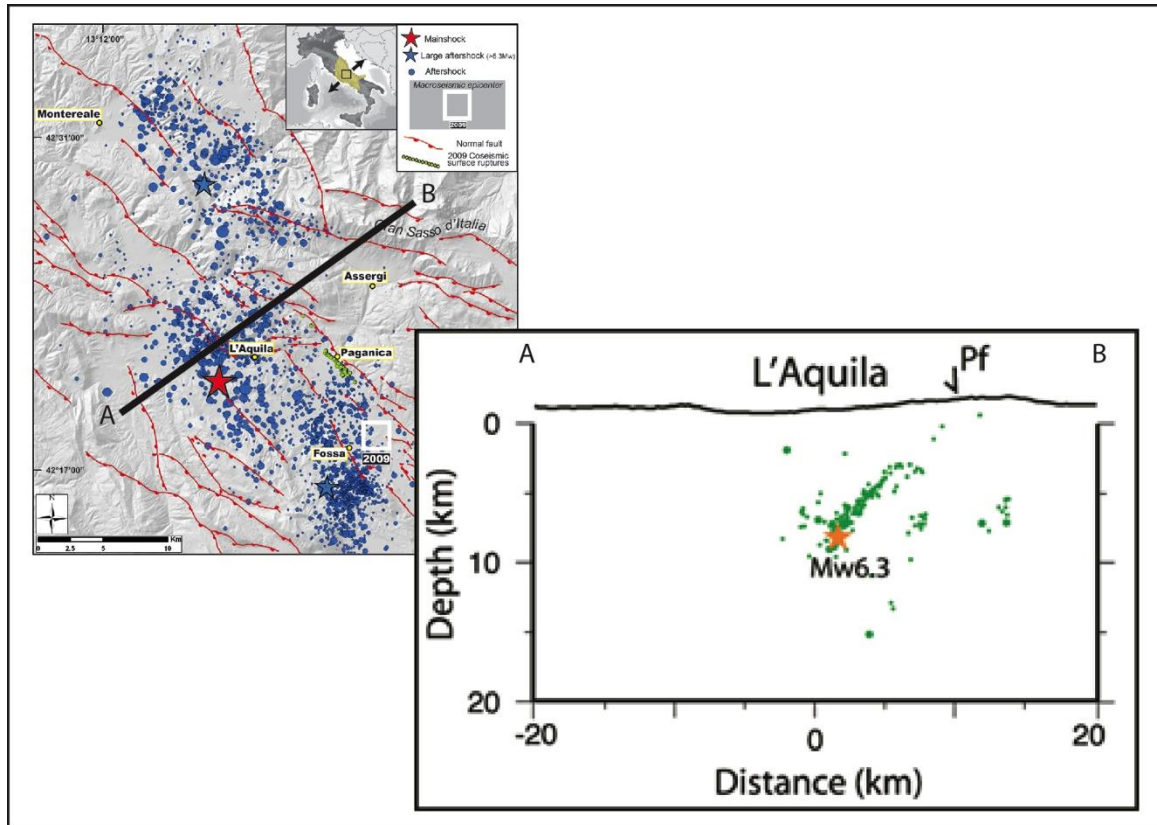


Figure 3.5 – Vertical section across the 2009 L'Aquila earthquake causative fault with aftershocks showing fault geometry.

3.2 Earthquake effects on the environment

The Mw 6.3 April 6, 2009 L'Aquila earthquake was associated with an extensive and complex set of surface coseismic deformations, involving an area of hundreds of km².

In the following section the whole coseismic deformation pattern will be illustrated, starting from the “big picture” revealed by DInSAR and GPS analysis and then describing the most relevant surface ruptures recognized during the field survey.

3.2.1 Coseismic deformation

An important amount of information on the coseismic deformation related to the April 6, 2009 earthquake came from satellite data (DInSAR and GPS, mainly).

Differential SAR Interferometry (DInSAR) is a microwave remote sensing technique that uses the phase difference (interferogram) between two temporally separated Synthetic Aperture Radar (SAR) images of an investigated area to detect elevation

changes in the radar line of sight (LOS) over large areas. DInSAR is an effective technique in measuring ground deformations and provides spatially dense deformation fields with great accuracy (1 cm or less) (Gabriel et al., 1989).

After the 2009 L'Aquila earthquake several authors applied this technique to the L'Aquila area, with the aim to image the coseismic ground deformation at a large scale.

The deformation induced by the earthquake as seen by DInSAR is almost vertical and is detectable over an area of about 500 km² extending SE from the mainshock epicenter. The concentric color fringe pattern visible in the three interferograms, (figure 3.6) define the displacement field which is evident as subsiding areas (~65%) in the hangingwall of the Paganica fault and as uplifted areas (~35%) in the footwall block.

The maximum displacement (lowering) occurred between L'Aquila town and Fossa village, with values ranging from 16 to 28 cm for COSMO ascending and ENVISAT ascending and descending, respectively while the maximum footwall uplift not exceeded 10 cm (Atzori et al., 2009; Walkers et al., 2009; Papanikolaou et al., 2010; Trasatti et al., 2011).

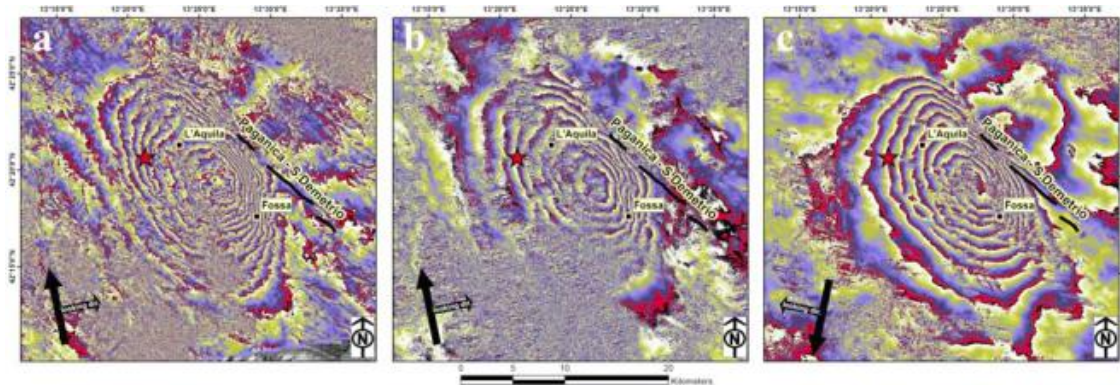


Figure 3.6 - Differential interferograms from: (a) COSMO-SkyMed ascending, (b) Envisat ascending, (c) Envisat descending (with looking directions). The main event of the April 6, 2009 (red star) and the 2009 L'Aquila earthquake causative fault are also shown (after Atzori et al., 2009).

The spatial variability of ground deformation is highlighted by a set of cross sections drawn both perpendicular and parallel to the activated fault plane (figure 3.7 - Papanikolaou et al., 2010). The abovementioned profiles revealed an asymmetric deformation pattern, with the maximum subsidence recorded near the hangingwall center (Profiles A03 and B03 in figures 3.8c and 3.9c, respectively).

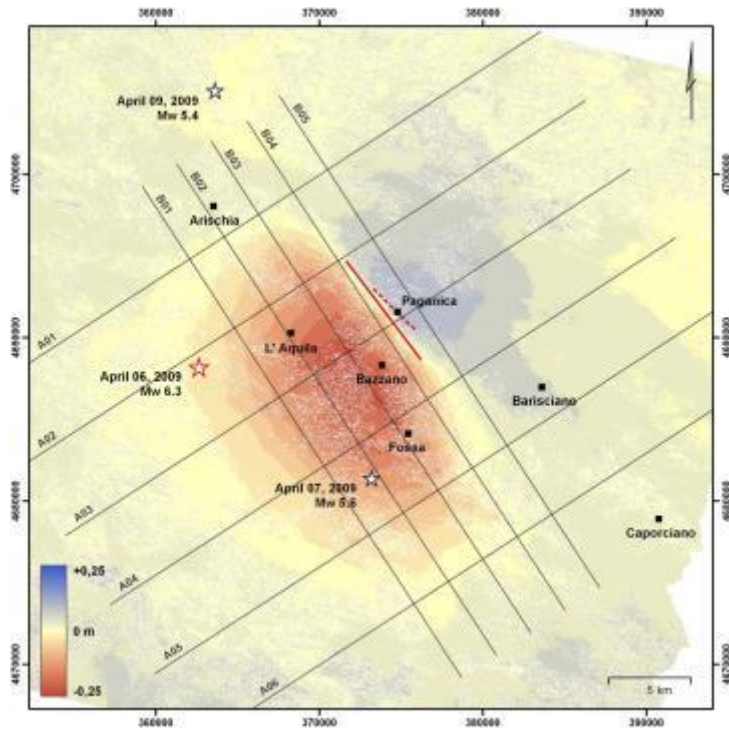


Figure 3.7 – Displacement field of the 6 and 7 April 2009 earthquakes and location of the cross-sections showing differences in the deformation field (after Papanikolaou et al., 2010).

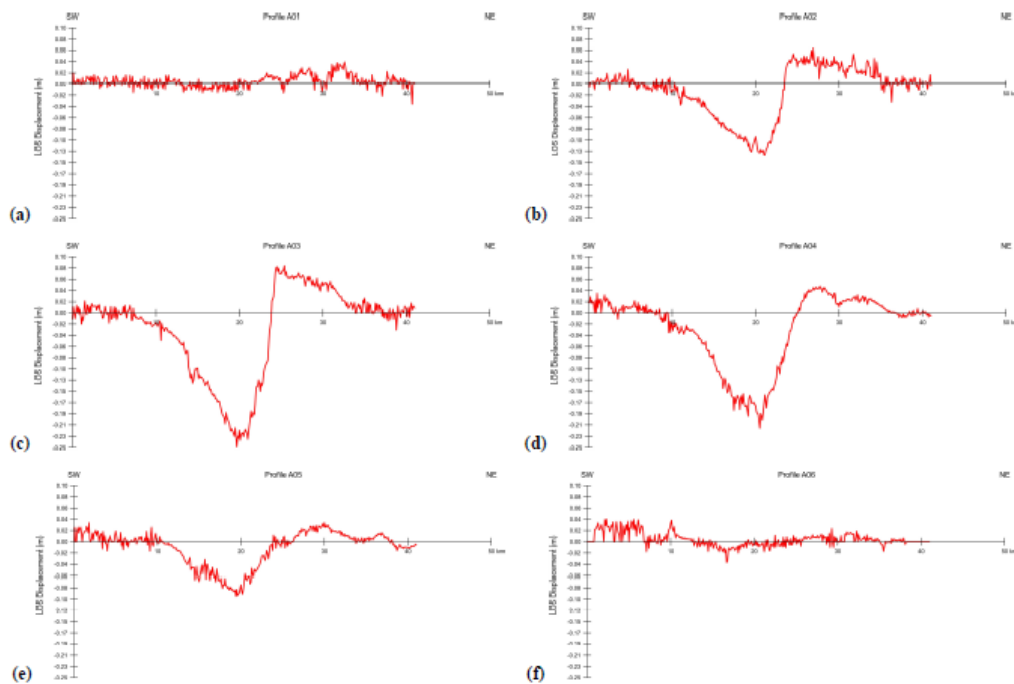


Figure 3.8 - Profiles perpendicular to the activated fault plane (after Papanikolaou et al., 2010).

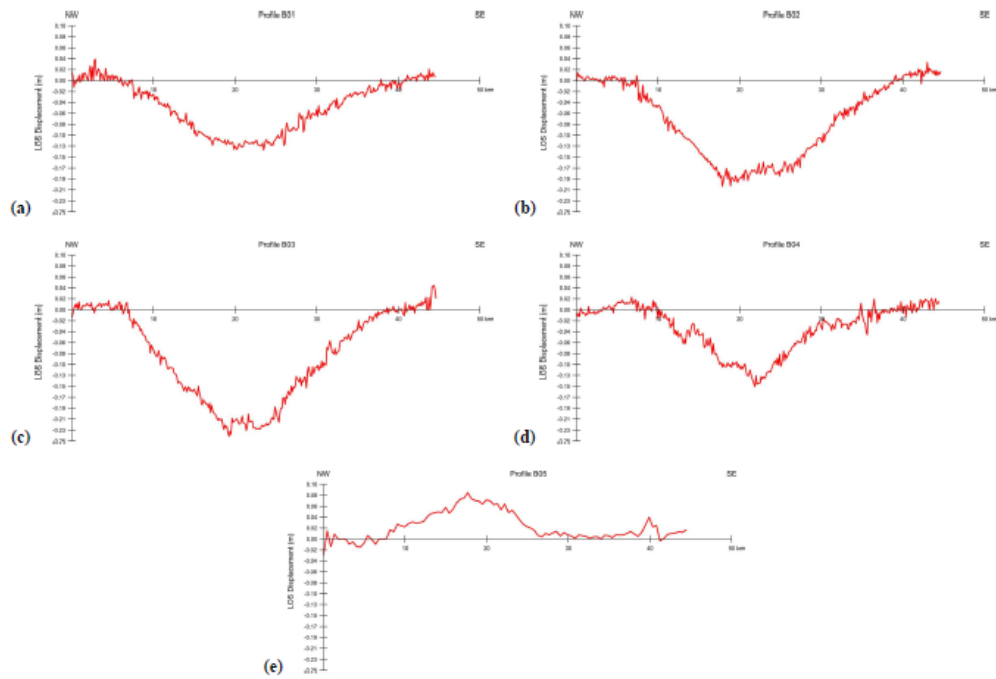


Figure 3.9 – Profiles parallel to the activated fault plane (after Papanikolaou et al., 2010).

Furthermore, interesting information was derived from continuous and survey-style GPS stations located in the epicentral area of the mainshock.

The Global Positioning System (GPS) is a geodetic space technique effective in defining the relative positions of observation sites located on the Earth's surface with centimetric precision and without the limitation of the terrestrial techniques, such as the mutual visibility between the observation sites. This technique allows to study tectonic processes both on regional and local scale and to estimate the ongoing crustal deformation within a region.

Analysis based on continuous and survey-style GPS stations that measured directly the coseismic displacement, allowed researchers estimating the deformation due to the L'Aquila earthquake (Anzidei et al., 2009; Cheloni et al., 2010) and highlighted significant horizontal and vertical permanent deformations in the epicentral area, within a radius of ~ 60 km from the mainshock (figure 3.10).

GPS sites showed clear evidence for coseismic offset, with maximum horizontal and vertical coseismic displacements of ~ 10 and ~ -15 cm, respectively, observed in the hangingwall of the Paganica fault, while the displacement related to the footwall motion was ~ 7 cm.

Due to the daily sampling of the GPS time-series, Cheloni et al., 2010 provided also an estimate of the afterslip occurred during the first day, that reach values between 1.0 and ~ 5 cm (figure 3.11).

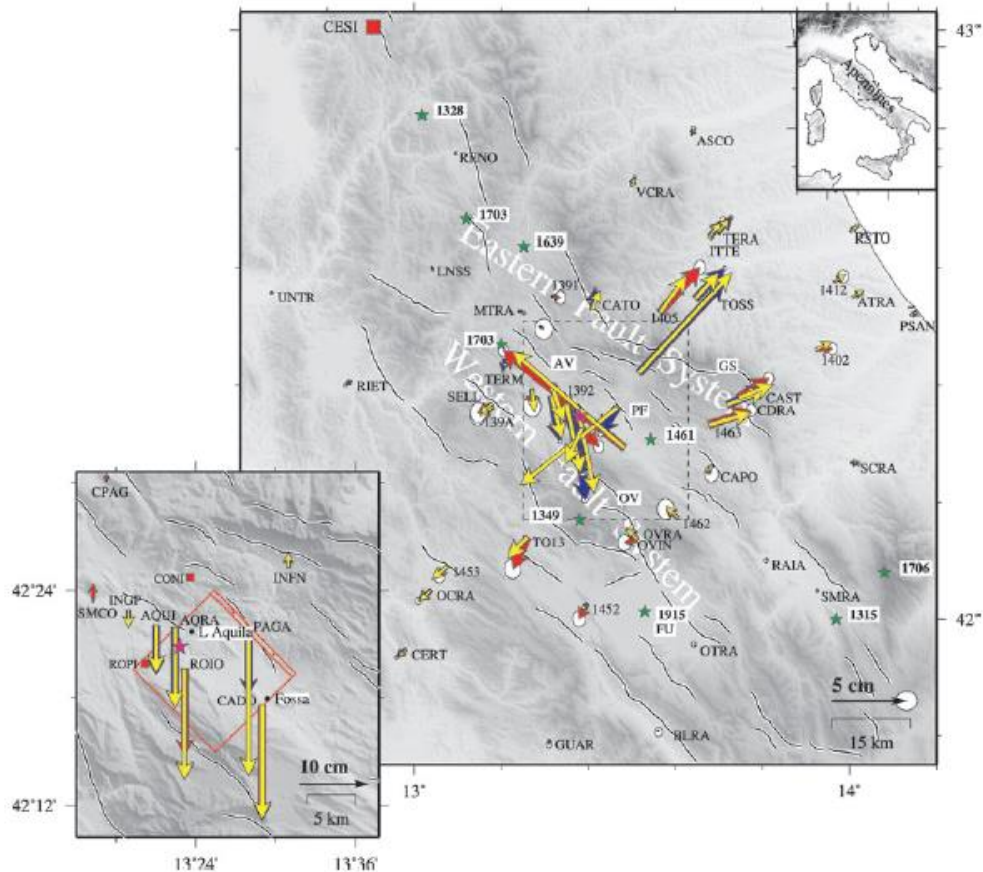


Figure 3.10 - GPS coseismic displacements of the 2009 April 6th Mw 6.3 L'Aquila earthquake (pink star, epicentre; blue vectors, continuous GPS; red, survey-style GPS; yellow, uniform slip dislocation model; error ellipses at 95 per cent C.I.; green stars, $I_{max} > X$ historic earthquakes labeled with A.D. epoch). Black lines are active faults from Galli et al. (2008), Boncio et al. (2004) and Roberts & Michetti (2004). The red square indicates the position of the station CESI. The inset shows observed (blue) and calculated (yellow) vertical displacements. (after Cheloni et al., 2010)

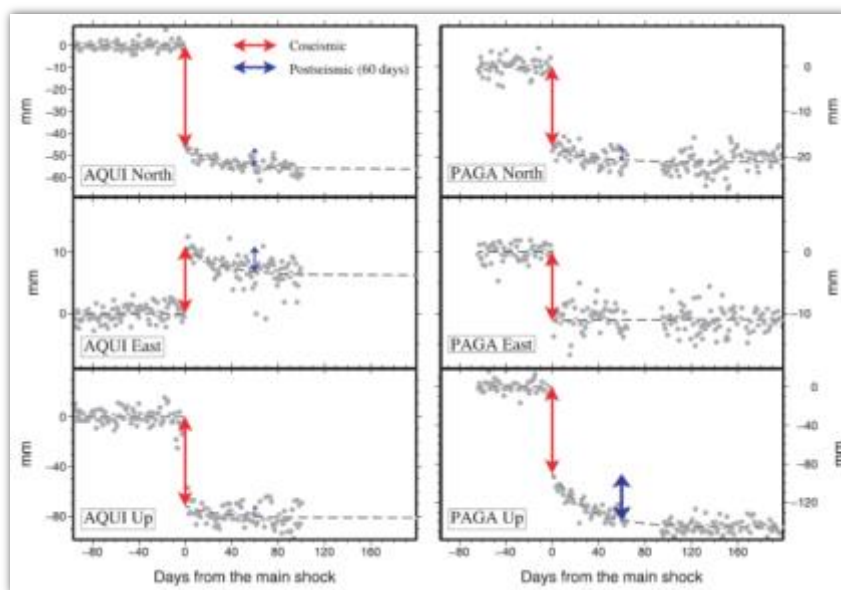


Figure 3.11 - Time-series of PAGA and AQUI sites. The dashed line is the best-fitting exponential function. Arrows correspond to estimated coseismic offsets (red) and post-seismic cumulated displacements (blue) (after Cheloni et al., 2010).

3.2.2 Coseismic surface effects and ground ruptures

Immediately after the April 6 2009 mainshock and in the following weeks, a field geological survey was performed in the epicentral area by several geologists, among them the EMERGEIO Working Group (INGV prompt geological survey team), in order to identify and to characterize the coseismic surface effects. During my work at the INGV, I had the opportunity to join the geological survey team and to gather observations and data regarding type, style and magnitude of the coseismic surface deformations. The data collected (about 400 sites) during the post-earthquake field campaigns evidenced a widespread and diversified set of geological surface effects (figure 3.12).

Most of the deformation at the surface was expressed as tectonic ruptures with or without throw, showing similar, if not identical strikes. These coseismic features were mostly observed on Quaternary deposits along pre-existing scarps, paralleling the Paganica fault. Other discontinuous, short, open cracks occurred along both pre-existing fault traces or on the plain and these effects may be interpreted as related mainly to triggered slip or seismic shaking. Rock falls, landslides, liquefactions, soil compactations and mobilization of loose deposits were among the other secondary surface effects observed in the epicentral area and likely related to seismic shaking and/or gravitational phenomena.

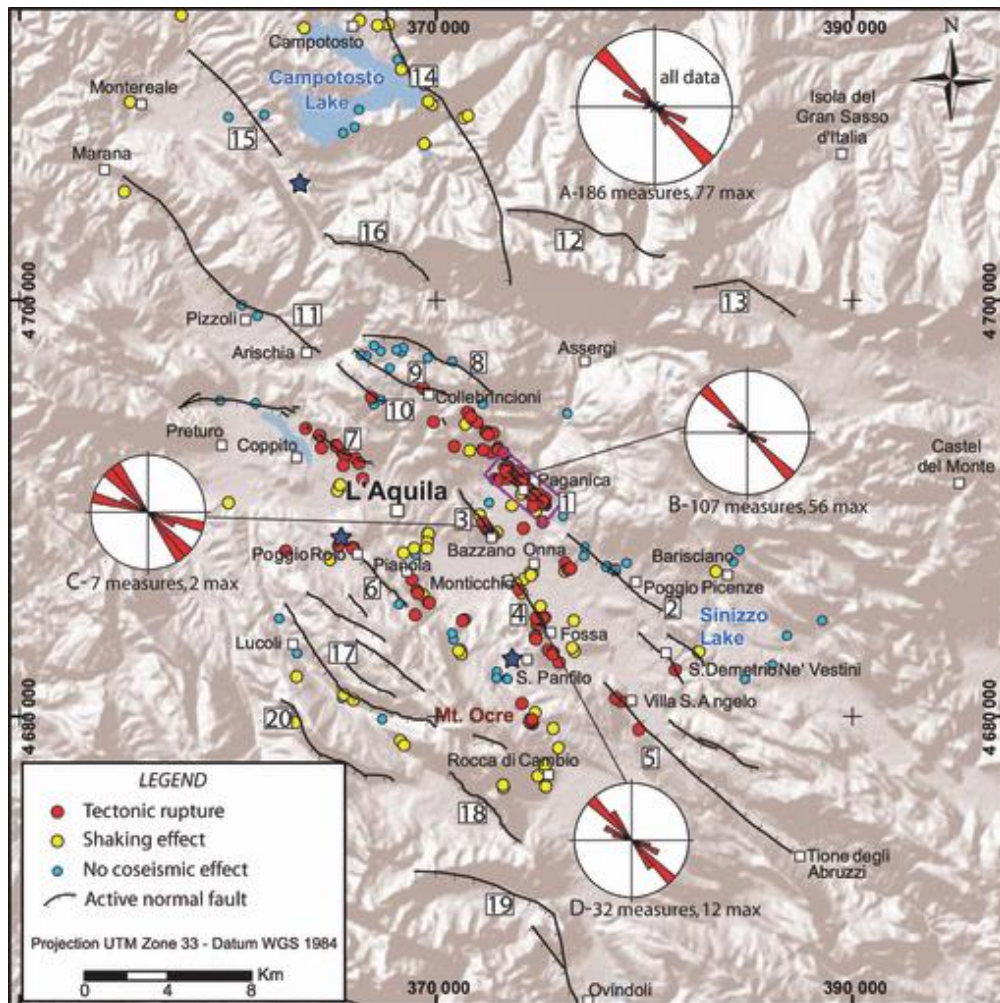


Figure 3.12- Map of the investigated sites for the survey of coseismic geological effects. Colors indicate sites with different types of observations: tectonic ruptures and shaking effects. The purple box includes the Paganica ruptures, which are interpreted to be primary surface faulting. We also show the sites along faults where no ruptures or other effects were observed. Stars indicate the three main events. Rose diagrams of the tectonic surface ruptures: (A) total data; (B) Paganica fault; (C) Mt. Bazzano fault and (D) Monticchio-Fossa fault. We do not report rose diagrams when the data are less than five measurements (after Emergeo Working Group, 2010).

The observed coseismic ground effects in the epicentral area were arranged in a typical pattern for a $M \sim 6$ earthquake, as described by the idealized schematic block-diagram of figure 3.13 (Dramis & Blumetti, 2005).

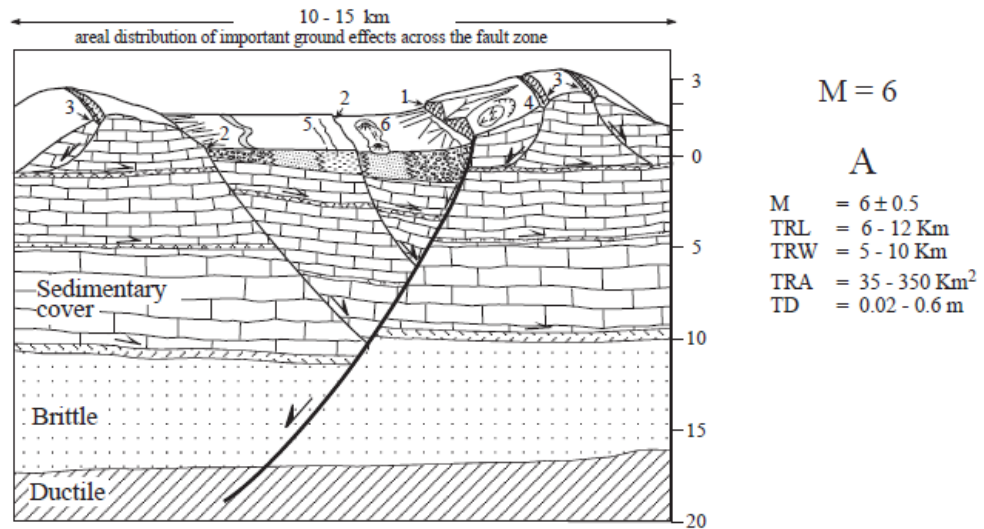


Figure 3.13 – Schematic block-diagram of a Quaternary intramontane basin associated with a $\cong M 6$ earthquake. Typical seismo-tectonic and seismo-gravitational landforms related to the repetition of coseismic effects along the same seismogenic structure. 1) primary surface ruptures; 2) secondary and sympathetic surface ruptures; 3) deep-seated gravitational deformation; 4) landslide; 5) ground failure; 6) liquefaction. (after Dramis and Blumetti, 2005).

Among all the surveyed coseismic effects, the most prominent tectonic ruptures were observed in the eastern side of the Middle Aterno valley, along a portion of the escarpment bounding the Paganica village. Here the surface ruptures can be observed with a clear expression for a continuous extent of ~ 3 km in coincidence with the long-term morphological expression of the fault and are usually confined within ~ 30 m from the fault scarp (figure 3.14).

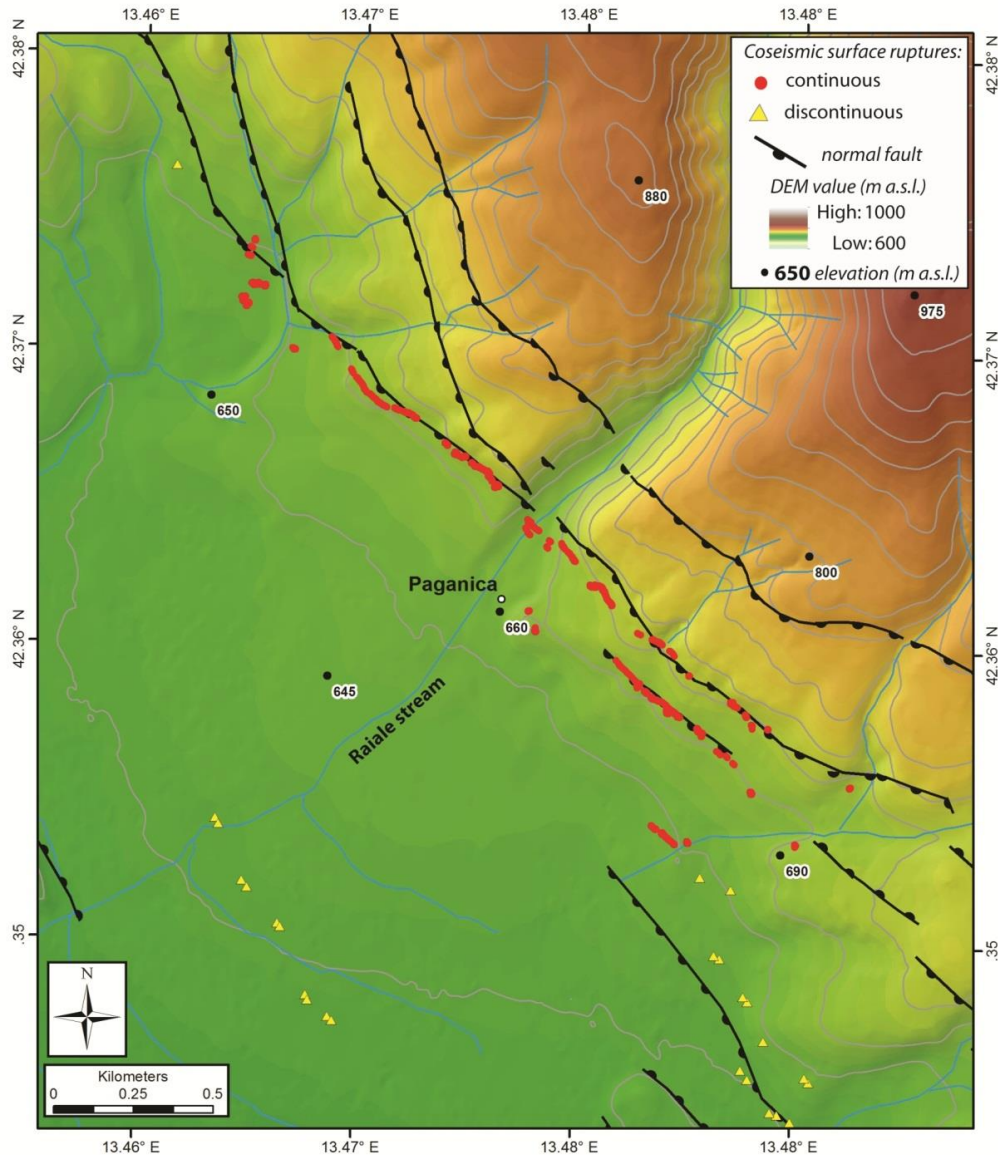


Figure 3.14 - Detail of the area of the 3 km long continuous surface ruptures along the escarpment bounding the Paganica village. Topographic color ramp derived from a 5 m resolution DEM. Contour lines interval is 25 m (modified after Cinti et al., 2011).

The main characteristics of the surface ruptures are:

- mostly open cracks (maximum opening ~10 cm) – figure 3.16;
- vertical dislocations or flexural scarps with a maximum vertical throw of 15 cm (southwest-side down) – figure 3.15;
- the alignment of the ruptures shows a clear spatial continuity and persistent orientation of N130° - N140°;
- commonly organized in en-echelon arrangement;
- occur regardless of slope angle, the type of deposits crossed or the type of manmade feature, and thus independently from gravitational effects.



Figure 3.15 - Surface rupture with a maximum throw of 15 cm.



Figure 3.16 - Surface rupture with a maximum opening of 10 cm and a negligible throw.

Despite maximum vertical throws not exceeding 15 cm, the location, continuity and the consistency of the surface ruptures along the Paganica fault were not observed along any other structure within the epicentral area.

Both to the north and to the south of this ~ 3 km continuous section, the surface ruptures fade out and discontinuous open fissures occurred along similar trends. Depending on whether or not these discontinuous fissures are interpreted as evidence of coseismic slip on the causative fault at depth, different interpretation report the length of the April 6, 2009 primary surface faulting between 3 and 19 km (Falcucci et al., 2009; Boncio et al., 2010; Emergeo Working Group, 2010; Galli et al., 2010, Vittori et al., 2011).

3.3 Summary

Summarizing, both DInSAR and GPS dataset analysis revealed the amount and spatial extent of the coseismic deformation field and allowed to model the source parameters and the slip distribution on the fault plane (Atzori et al., 2009; Cirella et al., 2009; Cheloni et al., 2010; Walters et al., 2009, Papanikoalou, 2010).

The location of the 3 km-long surface faulting zone observed during the field campaign coincides with the zone of maximum coseismic slip at depth imaged through the joint inversion of GPS and strong motion data (Cirella et al., 2009).

Moreover, the aftershocks distribution, the focal plane solutions, the geometry and kinematics of the 2009 surface ruptures along the escarpment bounding the Paganica village, together with the whole coseismic displacement field, all are consistent with the long-term trace of the previously identified NW-SE, SW-dipping Paganica fault.

This tectonic structure was reported in some of the pre-earthquake works, but only roughly traced, with length ranging between 9 and 15 km (Bagnaia et al., 1992; Vezzani and Ghisetti, 1998; Boncio et al., 2004; Geological Map of Italy, scale 1:50.000, sheet 359, L'Aquila, APAT, 2006) and was poorly characterized.

Moreover, the coseismically uplifted areas coincide with the footwall block of the Paganica fault, while the subsiding areas with the basin in the active hangingwall (figure 3.17).

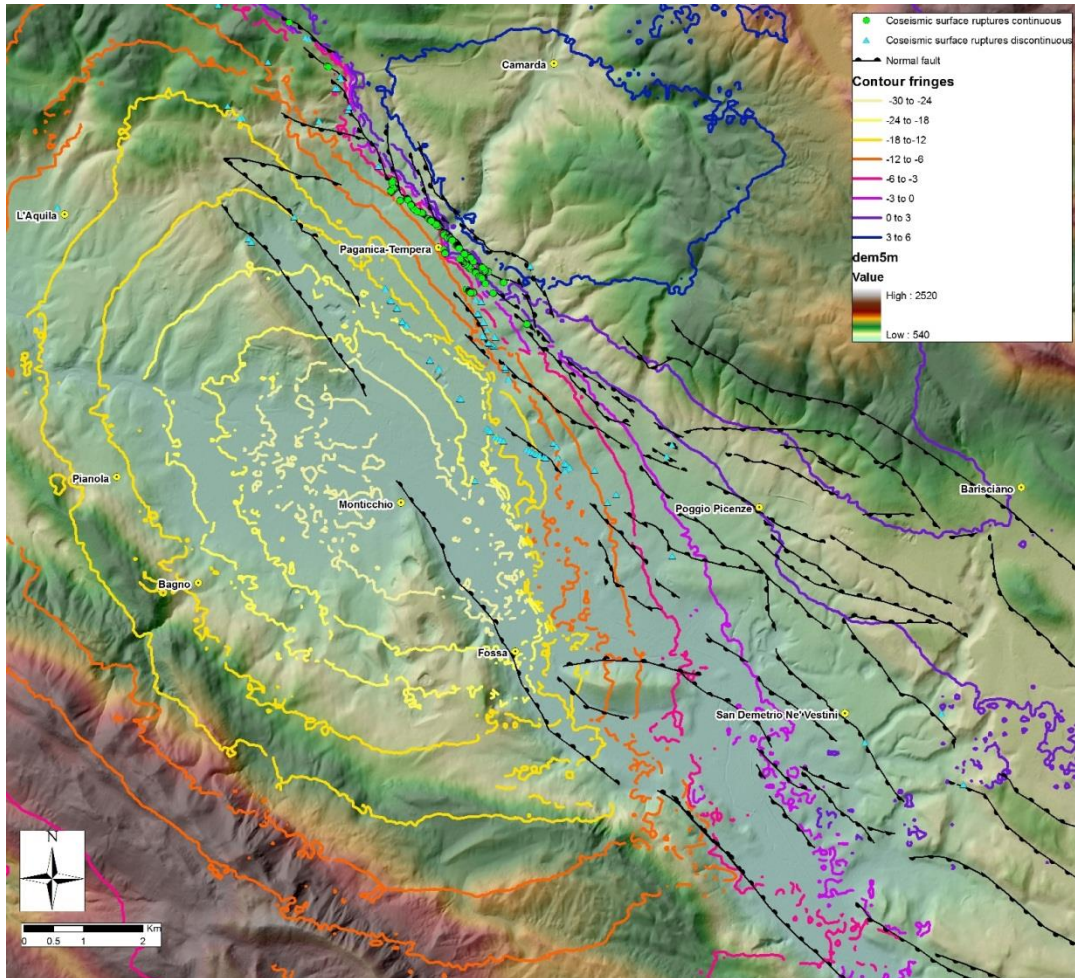


Figure 3.17 - The coloured contour fringes define the displacement field from the ENVISAT differential Interferogram. The maximum lowering is ca. 0.28 m N of Monticchio. Green dots represent continuous coseismic surface ruptures, light blue triangles are discontinuous open fissures.

Taking into account all these observations, there is evidence that the Mw 6.3 April 6, 2009 earthquake occurred on the Paganica fault.

In the following, we will discuss the whole Paganica – San Demetrio fault system (PSDFS hereinafter), including the Paganica fault and all the tectonic structures affecting the eastern side of the Middle Aterno valley.

A detailed description of the field geological survey and of the observations of the surface geological effects in the epicentral area is available in the attached Terra Nova article *“Evidence for surface rupture associated with the Mw 6.3 L’Aquila earthquake sequence of April 2009 (Central Italy)”* which I co-authored (Appendix G).

3.4 Open questions raised by the 2009 earthquake

The occurrence of the 2009 L'Aquila earthquake has highlighted the need for a detailed knowledge in terms of location, geometry, and characterization of the active faults that are the potential sources for future earthquakes.

The comparison between the length of the coseismic surface ruptures with observed throws (3km) and the length of the long-term expression of the PSDFS as defined by geology and geomorphology by previous works (9 to 15 km) highlighted that the 2009 L'Aquila earthquake coseismic surface ruptures clearly reactivated only a 3 km-long portion of the whole PSDFS.

A second point was that the centimetric coseismic throw (max 0.15 m near Paganica) that occurred in 2009, can hardly contribute to the growth of the fault escarpment, which is in places up to tens of meters high. In fact, in order to compete with erosional and depositional processes, coseismic surface displacements substantially larger than those observed in 2009 are needed.

The limited consistency between the observed coseismic ruptures and the long-term morphologic expression of the PSDFS, both in terms of location and size, raised some questions about the maximum expected magnitude on the fault

Given the abovementioned open questions, a better understanding of the seismic potential of the PSDFS was needed in order to provide new insights on its Quaternary deformational history and thus to contribute to seismic hazard assessment for the area struck by the 2009 L'Aquila.

3.5 Other examples of surface faulting earthquakes and coseismic deformation

During my work at the INGV, I had the opportunity to survey other surface faulting earthquakes, with different magnitude and prevalent extensional kinematic (normal dip-slip and mixed strike-slip and normal dip-slip). In this section I will present a summary on the surface deformations related to the 2010 Mw 7.2 El Mayor-Cucapah (Mexico) and to the 1915 Pleasant Valley (Ms 7.7), 1954 Fairview Peak (Ms 7.2) and Dixie Valley (Ms 6.8) earthquakes.

3.5.1 The 2010 (Mw 7.2) El Mayor-Cucapah earthquake

The 2010 Mw 7.2 El Mayor-Cucapah earthquake occurred within the Mexican Pacific margin in northern Baja California (BC), a region of high seismicity straddling the complex Pacific–North America plate boundary (figure 3.18). The principal plate boundary in northern Baja California consists of a series of northwest-trending strike-slip (transform) faults that are separated by pull-apart basins accommodating NW-SE oriented extension. At the latitude of the 4 April 2010 earthquake, the Pacific plate moves northwestward with respect to the North America plate at about 45 mm per year.

This earthquake produced a ~120 km-long discontinuous surface rupture extending from the northern tip of the Gulf of California northwestward to nearly the Mexico-USA border. The surface rupture pattern was complex, with breaks along multiple fault strands (figure 3.20, 3.21, 3.22), including minor re-activation of the fault scarps associated with the 1892 Laguna Salada earthquake and several other older seismic events.

Few months after the earthquake, I surveyed the northern half of the rupture that extends ~20 km along the Laguna Salada and Pescadores faults and then it jumps in a left step-over to the Borrego fault.

The southern part of the rupture consists of a zone of distributed fracturing and liquefaction that cuts across the Colorado River delta.

Displacements due to the earthquake involved both normal and strike-slip motion, with horizontal displacements generally larger. The maximum measured displacement occurred along the Borrego fault in Borrego Valley (figure 3.19) and was about 3.1 m of strike slip and another 2 m of east-down dip slip on a nearly vertical fault, yielding an oblique slip of nearly 4 m.

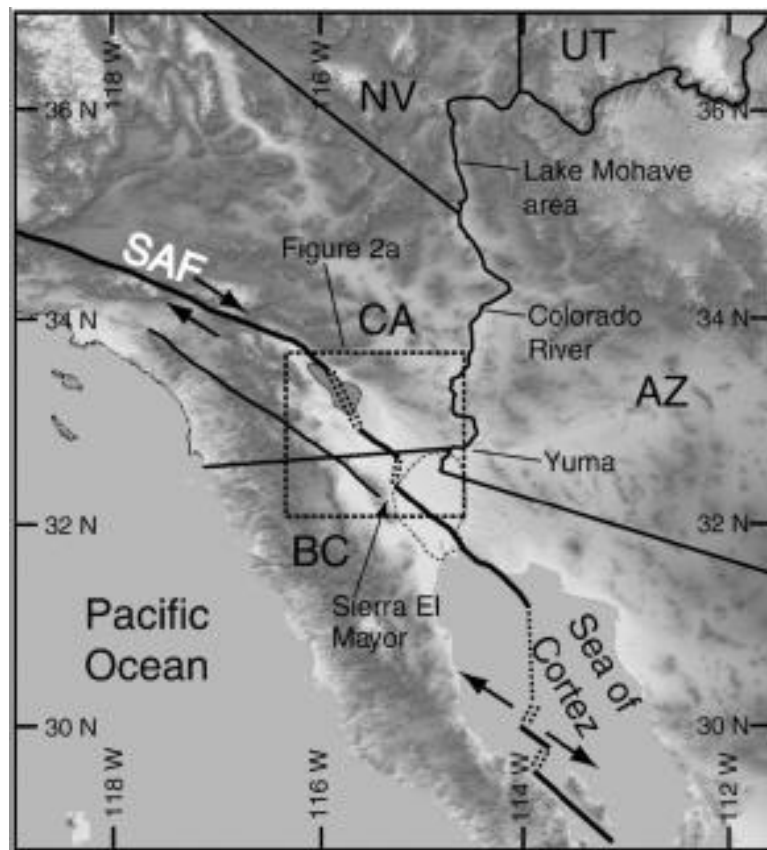


Figure 3.18 - Regional map of topography and main faults of the San Andreas fault system in the southwestern United States and northwestern Mexico. ABF—Agua Blanca fault; CDD—Canada David detachment; CPF—Cerro Prieto fault; E—Ensenada; ECSZ—eastern California shear zone; EF—Elsinore fault; IF—Imperial fault; LA—Los Angeles; LSF—Laguna Salada fault; SAF—San Andreas fault; SD—San Diego; SJFZ—San Jacinto fault zone; SSPMF—Sierra San Pedro Martir fault; T—Tijuana; WSDF—West Salton detachment fault; Y—Yuma. (after Dorsey et al., 2011).



Figure 3.19 - Map of the rupture in Borrego Valley, and along the Laguna Salada range front. Selected displacements shown are representative.

After http://www.geerassociation.org/GEER_Post%20EQ%20Reports/Baja%20California_2010/Baja10_Ch03.html



Figure 3.20 - Borrego fault, ground ruptures with mainly dip-slip displacement confined in a narrow zone at the base of the long-term mountain front - Sierra Cucapah, Baja California, México.



Figure 3.21 – Coseismic fault scarps at the base of the range forming a zone of distributed deformation.



Figure 3.22 - Coseismic fault scarps emerging on the slope in a zone of distributed deformation.



Figure 3.23 – Coseismic fault scarp crossing the alluvial plain.

3.5.2 The 1915 Pleasant Valley (Ms 7.7), 1954 Fairview Peak (Ms 7.2) and Dixie Valley (Ms 6.8) earthquakes and their surface ruptures

During the months I spent at the Center for Neotectonic Studies of the University of Nevada, Reno, I had the opportunity to survey the surface ruptures related to the 1915 Pleasant Valley (Ms 7.7), 1954 Fairview Peak (Ms 7.2) and Dixie Valley (Ms 6.8) earthquakes.

Those events occurred in the Central Nevada Seismic Belt (CNSB), a ~300 km-long NE-SW oriented zone of strike-slip, oblique-slip and dip-slip historical surface faulting earthquakes that extend northward through eastern California and central Nevada (figure 3.24).

In particular, the 1915 Pleasant Valley earthquake (Ms 7.7) was the largest event of the historical sequence, and it produced predominantly normal faulting with vertical displacements up to 4 m while only in few locations it was observed some dextral offset.

The Ms 7.2 Fairview Peak earthquake occurred on 16 December 1954 in central Nevada and was followed ~ 4 minutes later by the nearby Ms 6.8 Dixie Valley earthquake. The focal mechanism of the Fairview Peak event shows right-oblique motion on an east-dipping fault, while a best fit for the Dixie Valley event shows a pure dip-slip motion on an eastward-dipping plane (Doser, 1986). Normal-right-oblique surface ruptures related to the 1954 Fairview Peak and Dixie Valley earthquakes were distributed among six different faults that together define a complex zone extending northward for about 100 km and over 15 km wide.

More in detail, the Fairview event produced a 32 km-long surface rupture with right-oblique slip and a maximum of 3.8 m of vertical separation and 2.9 m of lateral offset.

The 1954 Dixie Valley created ~ 50 km of fault scarps which dipped 50° to 70° to the east. The sense of slip was normal, with a maximum vertical offset observed of 2.8 m (Caskey et al., 1996).

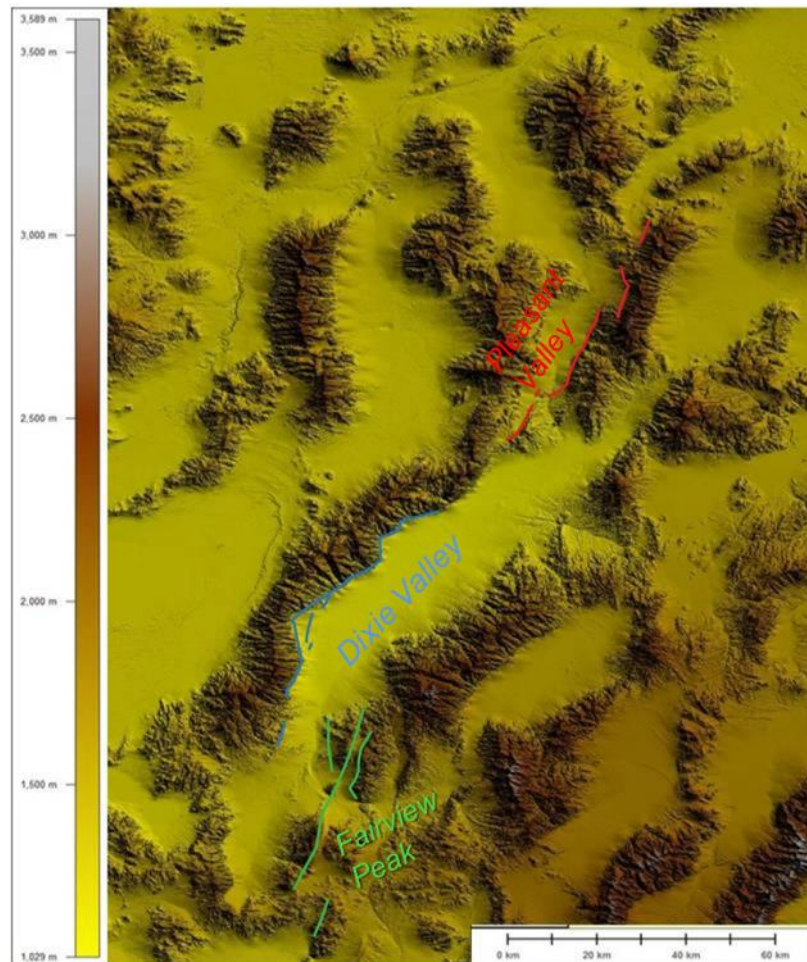


Figure 3.24 - Location of some of the historic earthquakes occurred in the Central Nevada Seismic Belt (CNSB).



Figure 3.25 – Coseismic fault scarp (white strip) at the base of the range – Pleasant Valley, Nevada (1915 Ms 7.7 Pleasant Valley earthquake).

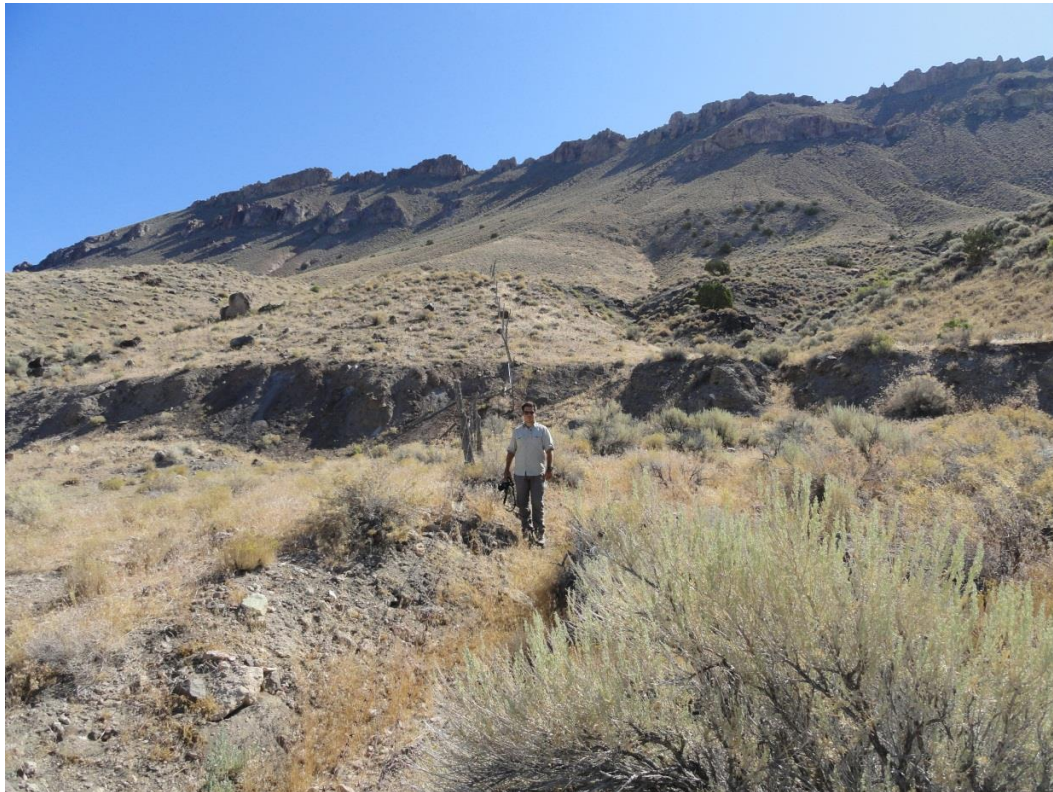


Figure 3.26 - Coseismic fault scarp at the base of the range (1915 Ms 7.7 Pleasant Valley earthquake).



Figure 3.27 - Willow canyon – coseismic graben with almost null vertical separation (1954 Ms 6.8 Dixie Valley earthquake).

Summarizing, the observations of the surface ruptures associated with the abovementioned earthquakes allowed to make some general considerations highlight some differences and to make some comparison with respect to what we saw in the L'Aquila 2009 earthquake.

Despite the differences in the energy released and in the prevalent kinematics, the 2009 L'Aquila, 2010 Baja California and some of the historical CNSB earthquakes are characterized by a similar style of deformation, with different scale structures arranged in well-defined and recurrent geometries.

A lesson learned is that coseismic deformations in earthquakes with a pure or large normal dip-slip sense of motion generally occur in a relatively narrow zone at the base of the morphological range (figures 3.20, 3.21, 3.25, 3.26), even if sometimes is possible to follow the ground breakages up in the slopes or within the valley floor (figures 3.22 and 3.23).

In some other cases the ground ruptures branch out in multiple overlapping strands that tend to distribute the coseismic displacement in a wider zone of deformation.

It has been observed that the deformation due to several seismic cycles, as a general rule, tends to occur along the same fault zone for a significant period of time.

Consequently, this behavior results in the creation of typical assemblages of landforms for active normal faults, characterized by cumulative fault scarps and mountain fronts that record progressively longer period of time and progressively larger displacements.

Accordingly to this concept, coseismic ground ruptures (their location, continuity and consistency) may guide our investigation for short and long-term slip-rate estimates.

4 Brief seismotectonic overview of the Central Apennines

The central Apennines are part of a northeast-verging imbricate fold-and-thrust mountain belt formed during Neogene-Quaternary times as a result of the subduction of Tethyan ocean crust and the collision between African continental fragments and the Eurasian plate (Dewey et al., 1973; Mazzoli and Helman, 1994).

The Central Apennines are bordered to the east by a foredeep, filled up by Pliocene-Pleistocene deposits (Casnedi et al., 1981; Consiglio Nazionale delle Ricerche, 1992) and to the west by the Tyrrhenian back arc basin (Kastens et al., 1988) developed at least since middle Miocene. The orogenesis affected Triassic to Miocene sedimentary sequences belonging to different basin and platform paleogeographic domains of the Adria Mesozoic paleomargin (e.g., Ben Avraham et al., 1990; Ciarapica and Passeri, 2002; Lentini et al., 2002; Patacca and Scandone, 2007).

During the formation of the belt the external compressional front progressively migrated toward east and north-east as a consequence of the geodynamic and kinematic processes that were the objects of different interpretations in the literature (e.g. Lavecchia, 1988; Patacca et al., 1990).

The progressive migration of the compressional deformation toward the Adriatic foreland is clearly documented by the development and evolution of a series of eastward progressively younger foredeep basins and by the occurrence of several piggyback basins, which developed on top of the advancing allochthonous units (Patacca and Scandone, 2001). During the Quaternary, the flexural subsidence, the compressional deformation and the eastward retreat of the subduction hinge all decreased dramatically (Patacca et al., 1992; Cinque et al., 1993) and the Apennines became dominated by crustal extension and by significant regional uplift. This new stress regime led to a crustal thinning that favored the arising of magmas during the Pleistocene and the formation of volcanic districts along the Tyrrhenian margin of the chain (Cosentino and Parotto, 1986; Cavinato et al., 1994).

The extensional regime is contemporary to the chain regional uplift (D'Agostino et al., 2001; Salustri Galli et al., 2002; Centamore and Nisio, 2003; Galadini et al., 2003a; Pizzi, 2003) and is responsible for the activity of the normal and normal-oblique faulting during most of the Quaternary.

The Apennines extensional belt consists of active and seismogenic, mainly NW-SE and NNW-SSE striking normal and normal-oblique faults, paralleling the physiographic and structural axis of the chain and offsetting the fold-and-thrust belt inherited by the compressive deformation.

The important vertical displacements related to the activity of these faults have controlled the development of several intermontane tectonic depressions, such as L'Aquila, Sulmona and Fucino basins, partially filled with sequences of continental deposits of Plio-Quaternary age up to hundreds of metres-thick (Cavinato & De Celles, 1999).

The onset of the continental deposition occurred during Pliocene, thus indicating the emersion of the Central Apennine belt since this period (e.g. Bosi et al., 2003, Galadini et al., 2003b).

The Quaternary normal faults activity was not stationary; in fact stratigraphic data suggest an eastward migration (Galadini and Messina, 2004;). As a result of this migration, some of the normal faults located in the western part of the Apennines are not active nowadays (on the basis of lack of recent dislocation at the surface and of the scarce seismicity, both historical and instrumental). Conversely, persistent activity at least since the Lower Pleistocene is shown by several faults located in the eastern sectors.

At present the Central Apennines are characterized by active extension.

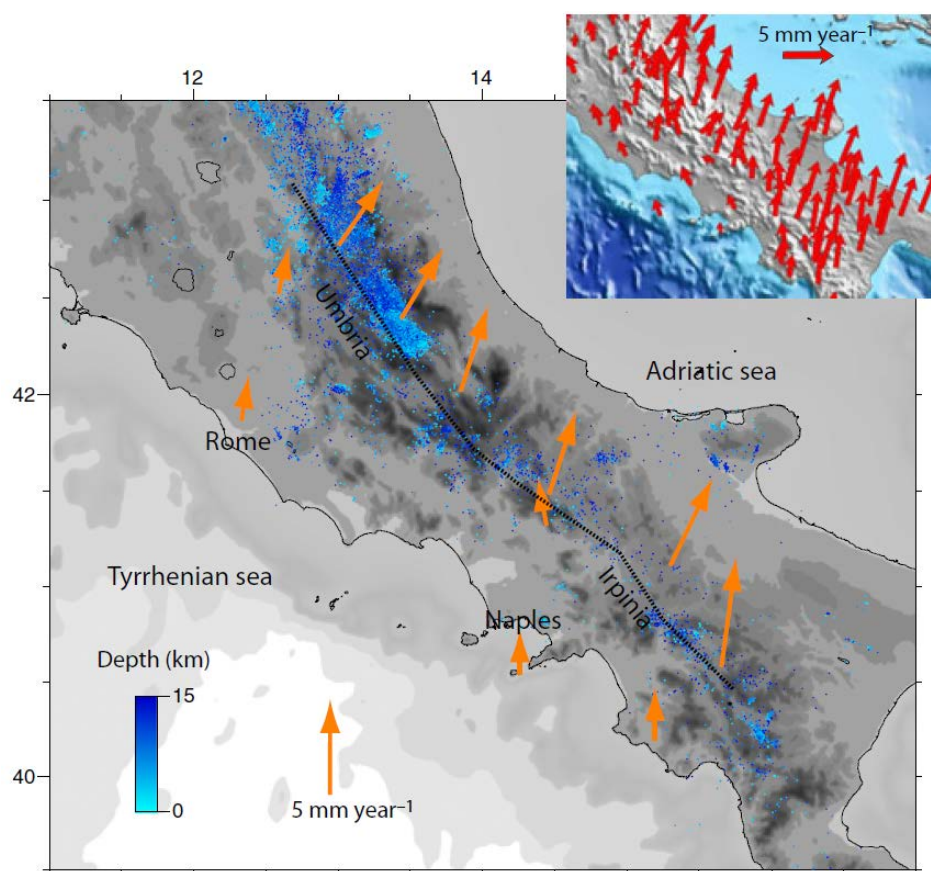


Figure 4.1 - Seismicity map of the central-southern Apennines for 2003–2009. Hypocenters are from relocation using the criteria of the CSI 1.1 catalogue (<http://csi.rm.ingv.it/>) with data from Centro Nazionale Terremoti of INGV. Arrows are a selection of GPS site velocities with respect to a fixed Eurasia (Avallone et al., 2010). The dashed line is the narrow zone where the extension is concentrated. The inset in the upper part of the figure shows the GPS velocity field relative to Eurasia (http://www.gm.ingv.it/images/stories/LabGIS/Mappe_G8/GPSItaly2_1500*2143.jpg).

Active extension follows the main topographic ridge and is concentrated in 40-60 km wide belt where, in general, historical and instrumental seismicity, as well as active faults, are located (figure 4.1, 4.2 and 4.3).

The current rate of extension, estimated in 2–3 mm/year (Hunstad et al., 2003, D’Agostino et al., 2011), together with stress indicators (fault slip data, borehole breakout measurements and focal mechanisms of earthquakes) point out a well-defined nearly NE-oriented active extension (e.g. Calamita & Pizzi 1994; Lavecchia et al. 1994; Montone et al. 1999; Montone et al. 2004; Pondrelli et al. 2010).

Looking more closely at our study area, the Abruzzi region of the Central Apennines is characterized by the presence of several active faults accommodating the prevalent NE-SW oriented extension. The present knowledge on the active faults in this area derives from decades of studies in geomorphology and Quaternary geology as well as from some paleoseismological investigations. The active tectonic structures are made of segments, usually dipping towards W and SW, with length ranging between 5 and 20 km. Shorter segments are organized in fault systems made by 3-to-5 minor faults. The length of the fault systems rarely exceeds 33 km (i.e. the cases of the Fucino fault and the Assergi - Campo Imperatore fault system). Some of these faults during historical times were responsible for earthquakes with M up to 7; notably this magnitude seems to represent the Max magnitude expected for the area also on the basis of tectonic, geologic, and geomorphic observations from nearby faults.

The slip-rates estimated in this area on nearby faults (figure 4.2) range from 0.4 to 1.2 mm/yr, with intermediate values preferred, i.e. 0.6-0.8 mm/yr (Galadini and Galli, 2000; Galli et al., 2008 and references therein).

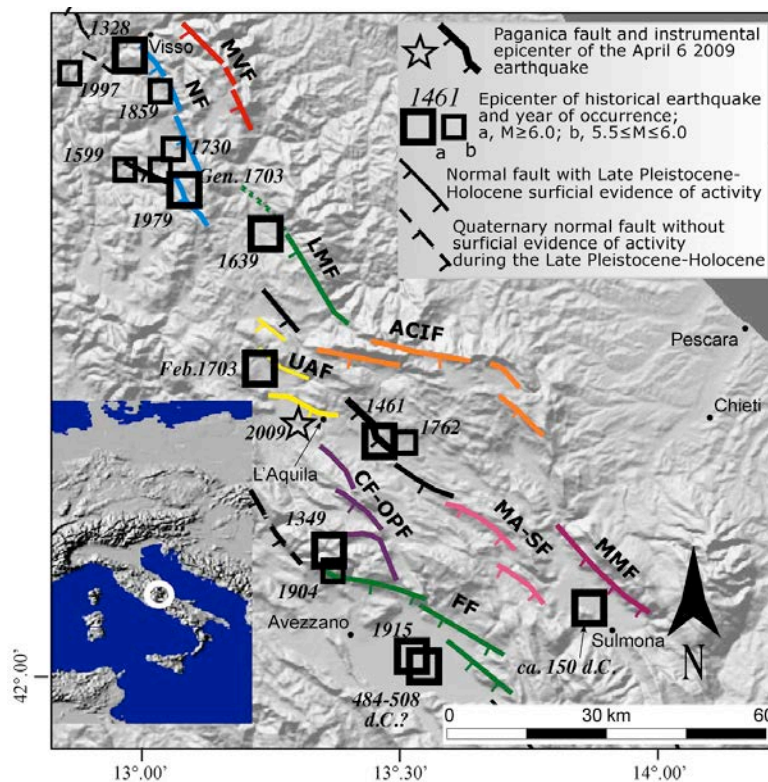


Figure 4.2 - Seismotectonic framework of the central Apennines (after Galadini et al., 2009). MVF - Mt. Vettore fault; NF – Norcia fault system; LMF - Laga Mts. fault; UAF - Upper Aterno fault system; ACIF – Assergi-Campo Imperatore fault system; CF-OPF - Campo Felice-Ovindoli-Pezza fault system; MA-SF - Middle Aterno-Subequana valley fault system; MMF - Mt. Morrone fault; FF - Fucino fault.

The Italian historical records report that the Abruzzi region has been repeatedly hit by large magnitude, destructive earthquakes (figure 4.2). The available catalogs report the 1349, 1703, and 1915 events (all having $M \geq 6.5$ and $I > 10$ MCS) as the strongest earthquakes in this area (CPTI Working Group, 2004) and occurring within 35 km from the 2009 epicenter.

The historical earthquakes closest to the L'Aquila area (figure 4.3) have $M < 6.5$ and are the 1791 Maw 5.4, 1762 Maw 5.9 and the 1461 Maw 6.4 events (Maw=average weighted Magnitude derived from macroseismic intensities (CPTI Working group, 2004)).

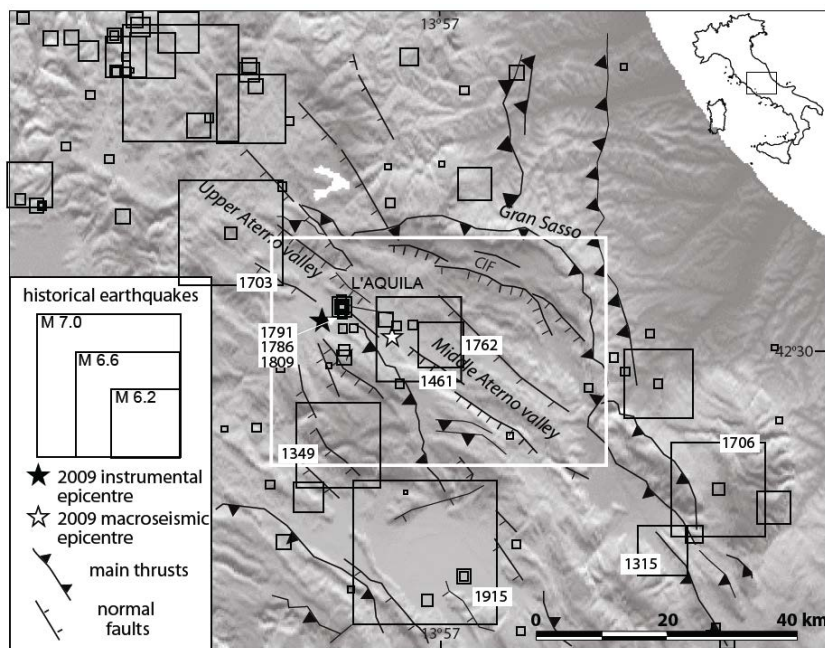


Figure 4.3 - Historical seismicity (squares) from the *Catologo Parametrico dei Terremoti Italiani* (CPTI Working Group 2004). A simplified tectonic framework of the Central Apennines is also shown. (after Tertulliani et al., 2009).

The analysis of the instrumental seismicity in the area show low levels of seismicity during the past 20 years (Chiarabba et al., 2005). In fact, during the latter period the area has only been affected by minor seismic episodes (in 1992, 1994 and 1996), while the background seismicity is sparsely distributed (Bagh et al., 2007; Chiaraluce et al., 2009). Minor sequences are located close to the L'Aquila area, with a maximum magnitude $M_L = 4.0$ (De Luca et al., 2000; Pace et al., 2002; Boncio et al., 2004; and Ciaccio et al., 2009).

The historical record and the instrumental seismicity in the 2009 epicentral area seems to describe only moderate-size seismicity, with earthquakes less energetic than in the surrounding region. However, this difference may be only apparent, since from paleoseismological studies we learn that the average recurrence time for $M > 6.5$ earthquakes in the region is on the order of one or more millennia (Michetti et al., 1996; Pantosti et al., 1996; Galadini & Galli 1999; D'Addezio et al., 2001; Galli et al., 2002; Moro et al., 2002; Galadini et al., 2003; Salvi et al., 2003).

5 Paleoseismological approach

5.1 Introduction

Immediately after the field geological survey to collect the evidence of the 2009 L'Aquila earthquake geological coseismic effects, we organized a paleoseismological campaign to be carried out across the northwestern portion of the Paganica - San Demetrio fault system (PSDFS hereinafter). The main goal of this campaign was to reconstruct the recent paleoseismological history of the PSDFS and to estimate the short-term (~ 30 ka) slip-rate.

As already discussed in Chapter 4, the long-term morphological expression of a fault is the result of repeated displacements along the same tectonic structure.

Active normal faulting produces mainly vertical deformations that, when cumulated for several seismic cycles along the same fault, can concur to form compound fault scarps (Slemmons, 1957), also called composite (Stewart and Hancock, 1990) or multiple-event fault scarps.

Taking into account this concept, and considering all the logistic limitations due to the density of buildings and activities in the area, we selected the best trench sites along the fault system section that consistently ruptured the surface in 2009 where we could expect the preservation of the evidence of repeated surface faulting events. We studied in detail four paleoseismological trenches/cuts by analyzing stratigraphy and structures and developing a reference chronological framework based on radiocarbon dating and archeological evaluation of pottery fragments found within the deposits involved in the deformation.

All the studied trenches were located at the base of the main fault escarpment bounding the Paganica village (figure 5.1), along the portion of the SW-dipping PSDFS where the most significant 3 km-long continuous surface ruptures occurred and that were considered to be direct evidence for fault displacement at depth (Falcucci et al., 2009; Boncio et al., 2010; Emergeo Working Group, 2010).

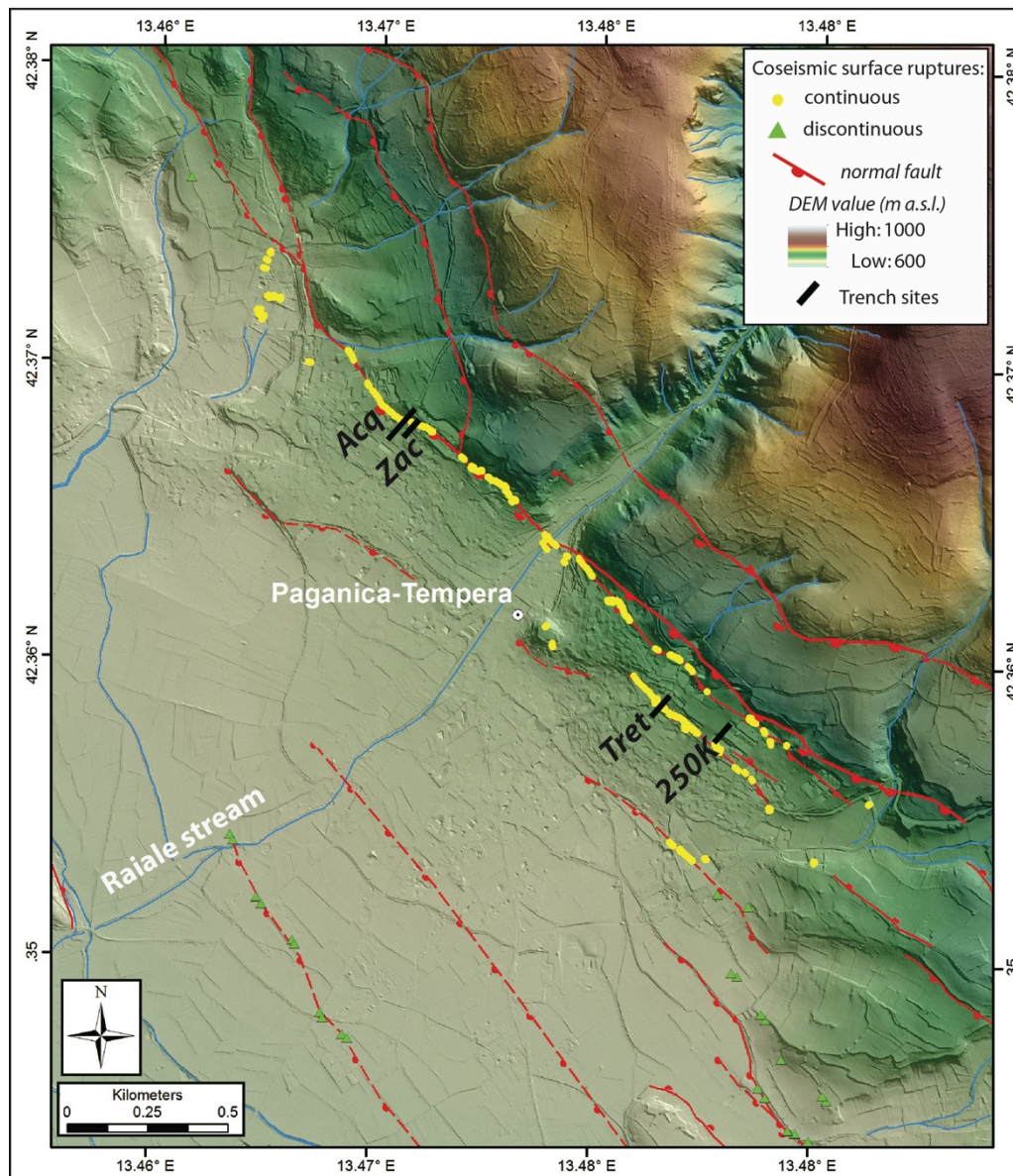


Figure 5.1 - Detail of the area of the 3 km long continuous surface ruptures along the escarpment bounding the Paganica village and location of trench sites. Acq= Aqueduct site; Zac= Zaccagnini site; Tret= Mo'Tretteca site; 250K= 250K site. Topographic color ramp is derived from a 1 m resolution LiDAR DEM.

The excavations were realized in a densely populated area that made difficult the selection of the trench sites. Two trenches were newly excavated (Zaccagnini and Mo'Tretteca sites), whereas other two sites took advantage of artificial cuts (250K and Aqueduct site).

We also drilled two cores at Aqueduct and Mo'Tretteca sites in order to check the stratigraphy and to measure the vertical offset of correlative deposits deeper than the trench walls exposure.

5.2 Paleoseismology - method

Paleoseismology is the study of the earthquakes of the past through the recognition of their geological and geomorphic signatures. Paleoseismology allow the definition

of the location (link of the earthquake with its causative fault) timing and size of earthquakes of the past both historical and pre-historical.

Paleoseismological investigations permit to study the distribution of individual paleoearthquakes in space and over time. The main goal is to extend the instrumental and historical seismicity record over periods of thousands or tens of thousands of years. This allows a better understanding of fault seismic behavior and thus contribute to the upgrade of the related seismic hazard.

The main assumption at the base of the paleoseismological approach is that moderate (moment magnitude, $M_w > 5.5$) or greater earthquakes are able to produce detectable permanent deformations of the ground surface that may be directly related to the fault movement at depth.

These deformations may appear clearly on the Earth surface at the intersection of the fault plane with the ground surface where fault scarps occur (see Chapter 2), but also within an area of tens to hundreds km^2 around the seismogenic structure where both horizontal and vertical deformations take place.

Paleoseismological investigations are also based on the fact that the permanent coseismic deformations of the ground surface are able to produce a disequilibrium, both at local and regional scale in the erosional and depositional processes that were acting at the surface at the time the earthquake. This disequilibrium is mainly due to the coseismic formation of relatively uplifted and subsided areas, of dammed or offset drainages etc. This results in the generation of new erosional features and related depositional processes that take place in the attempt to restore the pre-earthquake equilibrium. These earthquake triggered features represent the geological records of the occurrence of past earthquakes.

The possibility that these records can survive through time is strictly dependent on the geomorphic and geologic setting of the area where the earthquake occurred (topography and lithology) as well as on the climatic conditions.

Under favorable conditions, the geological records of earthquakes of the past can be preserved by burial by younger deposits, allowing the paleoseismologist to recognize the cumulative deformation due to repeated earthquakes along a fault and/or the evidence for the occurrence of individual paleoearthquakes.

Paleoseismological studies take advantage of different investigations methods and techniques, performed both at regional and local scale:

- interpretation of aerial and satellite imagery and digital elevation models (DEMs) in order to detect indicators of paleoseismic events (e.g. uplifted marine shorelines, linear range fronts, offset drainages, etc.);
- study of near-fault geomorphology (fault-scarps, streams, fans, alluvial terraces, etc.);
- realization of exploratory trenches across and/or parallel to the investigated faults;
- analysis of the landscape features and deposits associated with ground shaking (liquefactions, turbidites, landslides, etc.);
- study of tsunami-related deposits.

The results of those types of investigations can furnish useful information to estimate some of the principal parameters describing a seismogenic fault:

- fault geometry, length and prevalent kinematics;
- fault displacement and its variability along strike;
- time elapsed since the last event;
- average recurrence time and related variations;
- slip-rates.

5.2.1 Trenching

Even if there are no standard techniques to perform paleoseismological investigations because they depends a lot on the type of structure, problematic and environment, trenching of a fault scarp is probably the most common and effective method for investigating an active fault with surface deformation.

This methodology consists in the preparation of an artificial exposure (trench wall) crossing the investigated fault to recognize the evidence of repeated fault displacements as recorded in the trenched stratigraphic sequence. As already mentioned above, the geological records do not have the same likelihood to be preserved through time at every site along a fault. A careful trench site selection, thus, represent a crucial step in paleoseismology.

The trench site should be selected taking into account two main factors:

- the location of the fault should be known with a certainty of a few meters;
- the geomorphological setting of the site should favor the preservation of the geological records of paleoearthquakes (little or null erosion and moderate deposition);
- presence of soft and recent datable sediments across the fault.

A paleoseismological trench is usually dug in the ground using a backhoe (figure 5.2) or, less commonly, by hand excavation. Trenches are excavated depending on the type of fault to be studied. Dip-slip faults trenches are generally opened perpendicularly with respect to the fault because deformation can be seen in a 2D across-fault view. Conversely, strike-slip faults require a double set of trenches (parallel and perpendicular to the fault) because deformation is best seen in 3D.

The dimensions of a trench are dependent on the width of the fault zone to be investigated. In general, a trench is 20 to 40-m long, 3 to 4-m deep and 1 to 4-m wide. Size depends strongly on the safety of the workers involved, so it can be increased if shoring and other tools increasing wall stability are adopted.

In any case the trench should be extended enough in order to include all the possible deformation zones.



Figure 5.2 - Example of a paleoseismological trench dug with a backhoe.

After a preparatory phase (cleaning and gridding), a log of the trench wall is realized by hand-drawing and/or photomosaicking the stratigraphy and its relationships with the tectonic structures, highlighting the possible geological records of individual surface-deforming earthquakes of the past. In unlucky cases it is possible to recognize only the evidence of cumulated deformation due to repeated paleoearthquakes.

The stratigraphic level that was the ground surface at the time the earthquake occurred is generally known as the event horizon.

Some features that are widely accepted as evidence for paleoearthquakes include:

- colluvial wedges, wedge shaped deposits that accumulate at the base of a scarp following the sudden and sharp elevation change of the ground surface caused by dip-slip earthquakes, or because of lateral juxtaposition of topography. A Colluvial wedge represents a post-earthquake deposit and the event horizon will be located at its base (figure 5.3a);
- upward fault terminations, an abrupt upward termination of faults against an unconformity (the event horizon) at several locations in the trench (figure 5.3b);
- tilted or folded strata overlaid by less deformed strata, forming an angular unconformity that represents an event horizon;
- increasing amount of deformation with increasing age of sediments (figure 5.3c). When a stratigraphic unit shows a greater amount of displacement with respect to the overlaying sequence, the boundary between the sequences can be interpreted as an event horizon. This can be particularly clear when there is a vertical component of slip;
- identification of fissure infills (figure 5.3d);
- identification of liquefaction features within the stratigraphy.

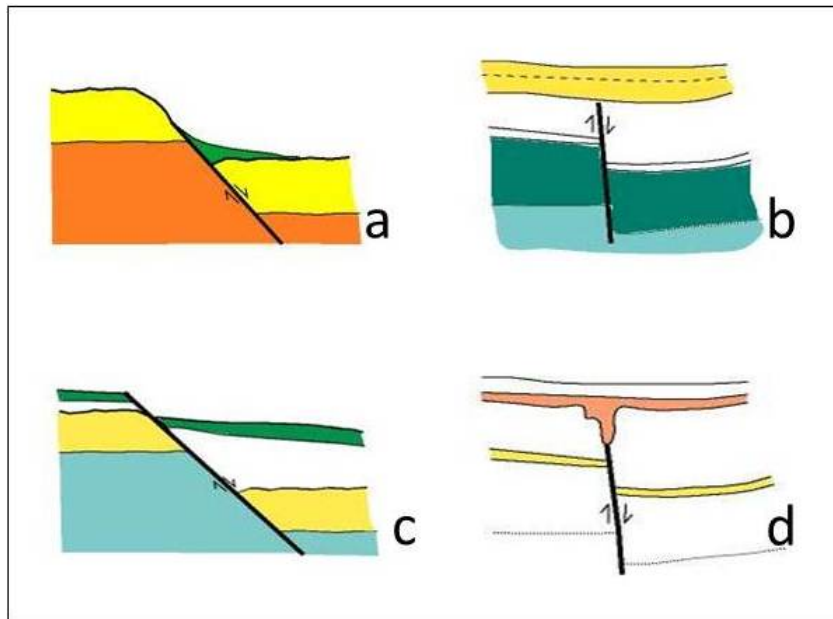


Figure 5.3 - Some features widely accepted as evidence for paleoearthquakes. a) colluvial wedge (green wedge-shaped deposit); b) upward fault termination; c) increasing amount of deformation with increasing age of sediments; d) fissure infill. Figure courtesy of D.Pantosti.

5.2.2 Coring

Shallow cores (1 to 10 m in depth) represent another useful tool to investigate and characterize fault zones.

Drilling cores can be considered as a preliminary method to investigate recent faulting in unconsolidated continental deposits and to extend the paleoseismic record beyond the limits of trenching (Mattson et al., 2003) or can provide a viable alternative when trenching is impractical (Improta et al., 2010).

In order to extend the depth of investigation and reach older sediments involved in the deformation, during the paleoseismological campaign in L'Aquila, two cores were extracted from boreholes drilled by a vibrocoring system (gasoline-powered percussion hammer) at Aqueduct and Mo'Tretteca sites.

The equipment used in this work is a percussion drilling set for heterogeneous soils with gasoline-powered percussion hammer (Atlas COPCO COBRA TT1).

The drilling set contains, among other accessories, the following main equipment:

- gasoline-driven percussion hammer (figure 5.4);
- percussion gouges (figure 5.4) in various diameters (from 40 to 100 mm) and lengths (50, 100 and 200 mm);
- core sampler equipped with a PVC sampling tube;
- mechanical extraction system.



Figure 5.4 – gasoline-powered percussion hammer (to the left) and percussion gouges with extensions rods (to the right).

This drilling set can be used to take reasonably undisturbed samples from depth to about 10 meters, without the use of drilling liquid. The design of the percussion gouges allows easy emptying and cleaning operations. Moreover, the PVC sampling tube with the undisturbed sample can be sealed for transport and further analyses in a laboratory.

The characteristics of the abovementioned drilling tool enable an easy transportation of the entire set to the desired investigation area, even in unfavorable logistic conditions. The main limitations are generally related to the type of materials to be drilled: gouges will not penetrate soft rock, large stones or sound concrete.

5.2.3 Chronological constraints

A critical step of the paleoseismological investigations is to obtain temporal constraints for the coseismic displacement of the past. Dating of the identified paleoearthquakes is crucial to estimate the average slip-rate of the fault and to evaluate the average recurrence time between earthquakes on the same fault segment.

Once the layer that represents the event horizon (the ground surface at the time of the paleoearthquake) is set in the stratigraphy, it is possible date the paleoearthquake by using the maximum and minimum ages from sediments deposited shortly before the earthquake and shortly after the event, respectively.

During our paleoseismological investigations, we developed a chronological framework based on 27 samples collected for radiocarbon dating as well as on archeological evaluation of pottery shards found within late Holocene deposits.

5.2.3.1 Radiocarbon dating

Radiocarbon dating is probably the most common method for dating in paleoseismology. Quaternary continental deposits may contain charcoal fragments, shells, bones, organic layers and soils that may be suitable for ^{14}C dating.

Radiocarbon dating has been one of the first radiometric techniques to be developed (the first radiocarbon measurements were published in 1949) and perhaps the most widely used. This is an isotopic method based on the radioactive decay of the naturally occurring ^{14}C isotope of carbon. The other two isotopes, ^{12}C and ^{13}C are both stable, while ^{14}C is unstable and undergoes β -decay to a stable form of ^{14}N . Atoms of ^{14}C are constantly produced by the interaction of cosmic rays and nitrogen. The atoms produced in this process are then combined with oxygen to form a particular form of $^{14}\text{CO}_2$. This is the way the ^{14}C becomes part of the earth's global carbon cycle and is assimilated by plants through the photosynthesis and by animals through the ingestion of plant tissues. When plants and animals die, they stop exchanging carbon with the biosphere and their ^{14}C content then starts to decrease at a rate determined by the law of radioactive decay.

Radiocarbon dating is essentially a method designed to measure residual radioactivity. By knowing how much ^{14}C is left in a sample, the age of the death of the organism can be known. The half-life of a ^{14}C atom is $5,730 \pm 40$ years, and under normal circumstances, the limit of measurement of ^{14}C activity is eight half-lives. This translates into an upper age limit of around 45,000 years.

This method can be applied to a wide range of materials that contain carbon originally fixed from atmospheric CO_2 , including wood, macrofossils, shells, bones, charcoals, soils and paleosols, peat and pedogenic carbonate.

Physical and chemical pretreatments are done on these materials to remove possible contaminants before they are analyzed for their radiocarbon content.

Two approaches are generally in use for measuring the residual ^{14}C activity in samples relative to modern standards. 1) Beta counting, measures the ^{14}C activity of the sample by decay counting the beta particles emitted by a given sample. Beta particles are products of radiocarbon decay; 2) accelerator mass spectrometry (AMS), which employs a particle accelerator to count the relative number of ^{14}C atoms in a sample, as opposed to the decay products.

The calculation of radiocarbon ages of samples assumes that the specific activity of the ^{14}C in the atmospheric CO_2 has been constant through time. However, early in the history of radiocarbon dating it was recognized that atmospheric ^{14}C was not constant. After measurements are done, it is thus important to calibrate ^{14}C -dating results in order to convert raw radiocarbon ages (usually reported in years Before Present –BP, where “present” means 1950 by convention) to calendar years. This can be done using a calibration dataset constructed by measuring the radiocarbon age of tree rings of known age or other independently dated samples. The radiocarbon ages used in this work were corrected according to Calib Rev 6.0 (Stuiver, Reimer and Reimer, 2005; Reimer et al., 2004) and reported as AD/BC for Holocene ages and as BP for Pleistocene ages (table 5.1).

In order to compare the results and assure reliable ages, our radiocarbon samples (both charcoals and bulk) were sent to two different specialized laboratories (Beta Analytcs. Inc – Florida, USA and Poznan Radiocarbon Laboratory – Poland).

Site	Unit	Sample, Lab Code ^a	Type	Conventional Age BP ^b	Calibrated Age ^c	Probability Distribution
ACQ	90	ACQ-B3, Beta-273363	bulk	31370 ± 260	36490–35150 BP	1.000
ACQ	93	ACQ-B4, Beta-273364	bulk	24600 ± 150	30050–28920 BP	1.000
ACQ	82	ACQ-B5, Beta-273365	bulk	7500 ± 50	6440–6250 BC	1.000
ACQ	93	ACQ-B7, Beta-273366	bulk	25560 ± 160	30850–30170 BP	0.934
					30010–29730 BP	0.066
ZAC	80	ZAC-B2, Poz-33712	bulk	14810 ± 90	18510–18230 BP	0.365
					18150–17680 BP	0.635
ZAC	50	ZAC-B4, Poz-33711	bulk	4440 ± 40	3330–3210 BC	0.341
					3190–3160 BC	0.069
					3130–2930 BC	0.589
ZAC	38	ZAC-B5, Poz-33710	bulk	1410 ± 35	580–670 AD	1.000
ZAC	35	ZAC-C1, Beta-273371	charcoal	1400 ± 40	570–680 AD	1.000
TRET	60	TRET-B50, Poz-33714	bulk	1330 ± 30	650–720 AD	0.814
					740–770 AD	0.186
TRET	80	TRET-C805, Poz-33716	charcoal	755 ± 35	1220–1290 AD	1.000
TRET	81	TRET-C300, Poz-33720	charcoal	1205 ± 30	690–700 AD	0.005
					710–750 AD	0.091
					770–890 AD	0.904
TRET	81	TRET-C1, Beta-266355	bulk	1330 ± 40	650–770 AD	1.000
TRET	80	TRET-C31, Poz-33719	charcoal	1025 ± 30	900–920 AD	0.029
					970–1040 AD	0.945
					1100–1120 AD	0.023
					1140–1150 AD	0.004
TRET	80	TRET-C4, Poz-33718	charcoal	1035 ± 30	900–920 AD	0.056
					950–960 AD	0.009
					960–1040 AD	0.935
TRET	90	TRET-C2, Poz-33721	charcoal	2020 ± 35	150–140 BC 110	0.020
					BC–60 AD	0.980
TRET	90	TRET-C11, Poz-33722	charcoal	1130 ± 30	780–790 AD	0.008
					810–840 AD	0.054
					860–990 AD	0.939
TRET	210	TRET-B10, Poz-33715	bulk	2460 ± 35	760–680 BC	0.265
					670–410 BC	0.735
TRET	200	TRET-C30, Beta-266356	charcoal	2510 ± 40	790–510 BC	0.987
					440–420 BC	0.013
TRET	90	TRET-B20, Beta-273368	bulk	1070 ± 40	890–1020 AD	1.000
TRET	302	TRET-S1a, Beta-273370	bulk	22210 ± 130	27570–27210 BP	0.104
					27110–26170 BP	0.896
250K	62	250K-B1, Poz-32265	bulk	2605 ± 30	820–760 BC	0.985
					680–670 BC	0.015
250K	70	250K-B2, Poz-32266	bulk	6010 ± 40	5000–4800 BC	1.000
250K	60	250K-B3, Poz-32267	bulk	2535 ± 35	800–720 BC	0.360
					690–540 BC	0.640
250K	90	250K-B30, Beta-273359	bulk	23500 ± 140	28610–27920 BP	1.000
250K	80	250K-B50, Beta-273360	bulk	15520 ± 70	18870–18580 BP	1.000
250K	65	250K-B70, Beta-273361	bulk	4200 ± 40	2900–2830 BC	0.286
					2820–2660 BC	0.702
					2650–2640 BC	0.012
250K	50	250K-C101, Beta-273362	charcoal	20 ± 40	1690–1730 AD	0.216
					1810–1920 AD	0.717
					1950–1955 ^d AD	0.067

Table 5.1 – Measured and calibrated ages of the ¹⁴C samples collected (after Cinti et al., 2011)

^aLab. code: Beta, Beta Analytics Inc. (Florida); Poz, Poznan Radiocarbon Laboratory, Poland. ^bMeasured radiocarbon age corrected for isotopic fractionation, calculated using the delta ¹³C. It is not calendar calibrated. ^cAge dendrochronologically corrected for the ¹²C/¹⁴C changes in the atmosphere according to Calib Rev 6.0.0 and rounded to the nearest decade. Holocene ages are given as AD/BC, and Pleistocene ages as BP. 2σ range. ^dDenotes influence of nuclear testing ¹⁴C.

5.2.3.2 Archeological evaluation of pottery shards

Human settlements and economic ascent in the area since ~ 1000 AD (the town of L'Aquila was founded in 1229 AD) facilitated the presence of archeological remains within the very recent deposits of this portion of the Middle Aterno basin.

The reference chronological framework obtained by means of radiocarbon dating was thus also integrated with age estimates from archeological evaluation of pottery shards (figure 5.5) found within the stratigraphy of the trenches. A summary of the evaluation of pottery fragments is provided in Table 5.2.

Sample	Unit	Age Interval ^a
250K-P4	61	XI-XIII century
TRET-PY	50	XIV-XV century
TRET-P3	50	XIII-XIV century
TRET-P2	90	XI-XIII century
TRET-P10	90	XI-XIII century
TRET-P200	90	XI-XIII century
ACQ-P2	10	XII-XIII century
ACQ-P1	81	<XII-XIII century

Table 5.2 - Evaluation of Pottery Fragments. ^aExpert evaluation of archeologists: Enrico Cirelli and Hermann Borghesi.



Figure 5.5 – pottery fragments found within the stratigraphy of Mo'Tretteca trench.

5.3 Paleoseismological trenching along the PSDFS

As already mentioned above, we studied in detail four paleoseismological trenches along the northwestern portion of the PSDFS. The trench sites selection was guided primarily by the field observations of the 2009 coseismic ruptures and by the geomorphological long-term expression of the PSDFS, and represented the best compromise between specific geologic targets and logistic/environmental difficulties.

All the investigated sites (Aqueduct, Zaccagnini, Mo'Tretteca and 250K) are located at the base of the main escarpment bounding the Paganica village and share a similar stratigraphic setting.

In particular, the lowermost deposits common to all trench walls are represented by middle Pleistocene alluvial fan and alluvial deposits, made of calcium carbonate gravels generally clast-supported in a fine-grained sandy matrix (numbered as unit 100 at all sites).

The top of this deposit is abruptly truncated by an erosional surface on which developed brown to dark brown paleosols that predate the Last Glacial Maximum (LGM, ~22-19 ka - Yokoyama et al., 2000). Slope deposits overlie the paleosols and are truncated by a second erosional surface associated with the LGM. This surface is overlain by a series of Holocene fine to coarse-grained alluvial and slope-derived deposits.

For the purposes of this thesis we will describe the results of our paleoseismological investigations focusing on those data that allowed us to estimate a slip-rate for the Late Pleistocene and Late Holocene.

5.3.1 Aqueduct site

This excavation is the result of the rupture of the Gran Sasso water pipeline due to the 2009 coseismic surface faulting along the PSDFS. The ejected over-pressurized water (25 atm, Cinti et al, 2011) deeply scoured the ground and opened an 80 m-long and up to 4 m-deep trench. We then deepened (1 to 2 m) and rectified the NW wall in order to better analyze the stratigraphic sequence.

This excavation provided an exceptional exposure of sediments and fault structures across the ~20 m-high compound scarp of the PSDFS, and allowed us to characterize the main fault zones and to estimate the short-term (~30 ka) slip-rate by correlating units across the fault zones.

More in detail, the northeastern (upper) portion of the excavation (from meters 36 to 78.5, figure 5.6) exposed a sequence of calcareous conglomerates with whitish, fine-grained silty/sandy matrix and interbedded layers of brown clayey silt. These deposits are affected by several high-angle (50°-70°), mostly SW-dipping normal faults. At m 35-36 a fault (F in Figure 5.6B) marks the separation between the upper portion of the excavation and younger sequence of alluvial, colluvial and slope wash deposits (meters 0 to 36).

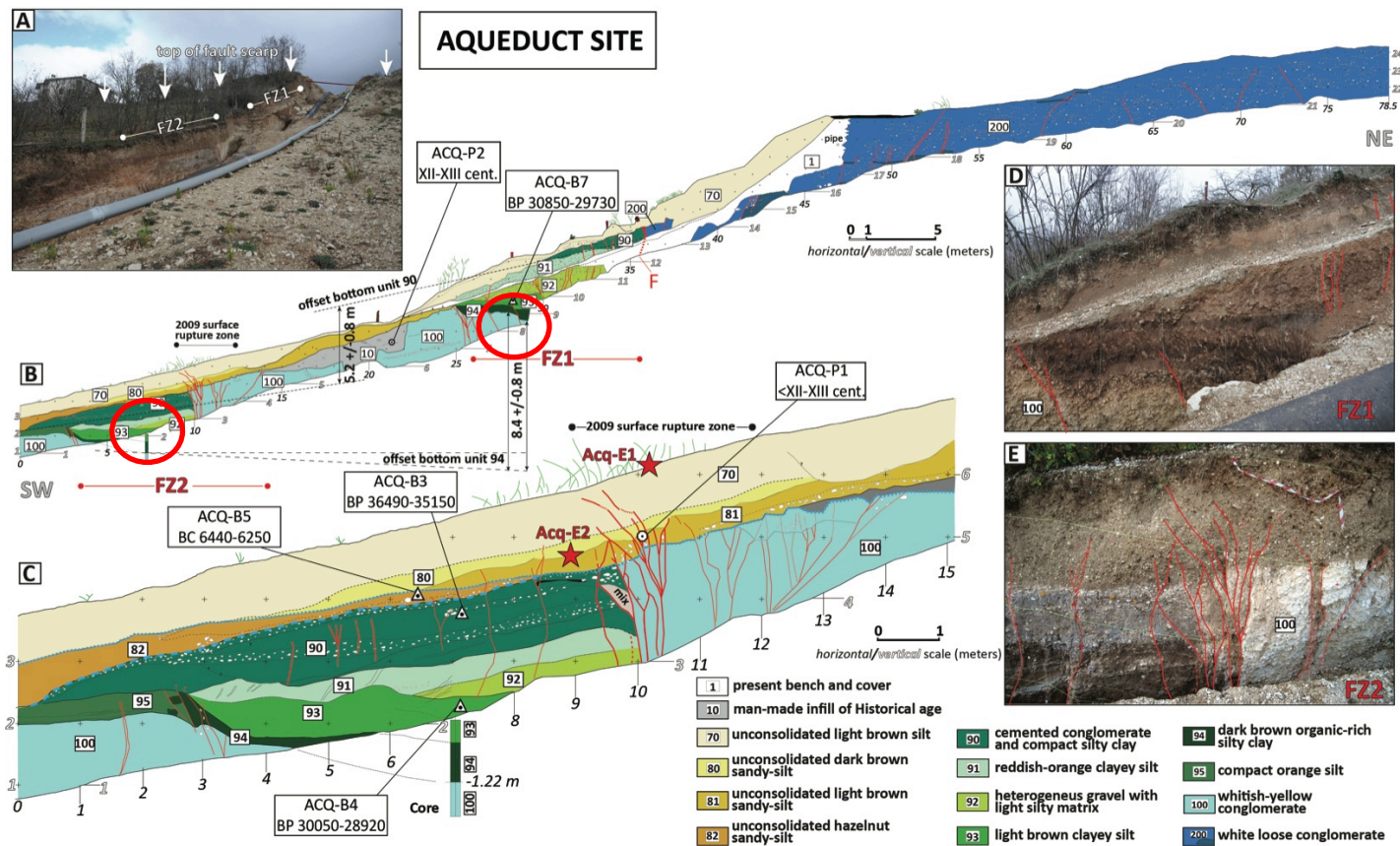


Figure 5.6 - Acq site. (a) View of the excavation along the water pipeline where it crosses the ~20 m high cumulative scarp. (b) Simplified log of the NW wall from a 1:20 scale survey. Triangles indicate dated radiocarbon samples (Table 5.1); circles indicate evaluated pottery shards (Table 5.2). Dashed gray lines show correlations of units for long-term vertical slip rate evaluation. Dashed and dotted blue thick lines mark erosional contacts associated with the LGM and with probable medieval quarrying, respectively. (c) Enlargement of fault zone FZ2. Symbols are the same as in Figure 5.6B; red stars indicate location of event horizons (ground surfaces at the time of surface faulting earthquakes). (d) View of the graben associated with fault zone FZ1 approximately between m 25 and 33. (e) View of the active fault traces of fault zone FZ2 approximately between m 8 and 12. In this zone the 2009 ruptures produced diffuse deformation accompanied both by cracking and warping. After Cinti et al., 2011.

Two main fault zones characterize this portion of the exposure: fault zone 1 (FZ1) at m 25-36 and fault zone 2 (FZ2) at m 3-13 (figure 5.6). The two fault zones share a similar graben-like structure formed by closely spaced, high-angle, SW and NE dipping normal faults and show clear evidence of repeated paleoearthquakes. Both fault zones involve also the same depositional sequence. In order to completely expose this sequence within the graben of FZ2, we drilled a borehole at meter 7 which confirmed that unit 100 is capped by the same units (93-94) that fills the base of the FZ1 graben.

This correlation is also supported by radiocarbon ages of $\sim 30 \pm 1$ ka from unit 93 in both fault zones (ACQ-B4 and ACQ-B7 in table 1).

The evidence for similar deposits with the same age (red solid circles in figure 5.6) allowed us to measure the vertical separation between the same units and to estimate a vertical slip-rate.

We can use the apparent offset at the base of unit 94 (which is the oldest unit preserved into the graben structures) across FZ2, between borehole at meter 7 and the FZ1 graben, to roughly estimate a total throw of 8.4 ± 0.8 m. Dividing the measured total throw by the ages of unit 93 (calibrated age of 30850-28920 BP, ACQ-B4, ACQ-B7, table 5.1), we obtain a vertical slip-rate of 0.25-0.32 mm/yr since 30 ka (Late Pleistocene).

Moreover, at this site we found evidences for 1 paleoearthquake, that is event Acq-E2, showing a throw of 0.35-0.4 m. Using the age and throw of the penultimate event at Aqueduct site (Acq-E2), we can estimate a slip-rate for a younger time interval at this site. In fact, dividing the measured cumulated offset of unit 81 (0.35 – 0.4 m) by the age constraints derived from a pottery found within the same unit (ACQ-P1, XII–XIII century, table 5.2), we can estimate a Late Holocene slip-rate of 0.41-0.53 mm/yr.

5.3.2 Zaccagnini site

The Zaccagnini trench is located ~ 30 m SE of the Aqueduct site (figure 5.1); at this location the 2009 coseismic surface ruptures consist of a SW facing free face with a throw of about 0.10 ± 0.05 m, locally accompanied by ground warping. The overall geomorphic situation is the same as at the Aqueduct site, with the 2009 ruptures running along the base of the main scarp. The trench was NE-SW oriented and about 12 m-long.

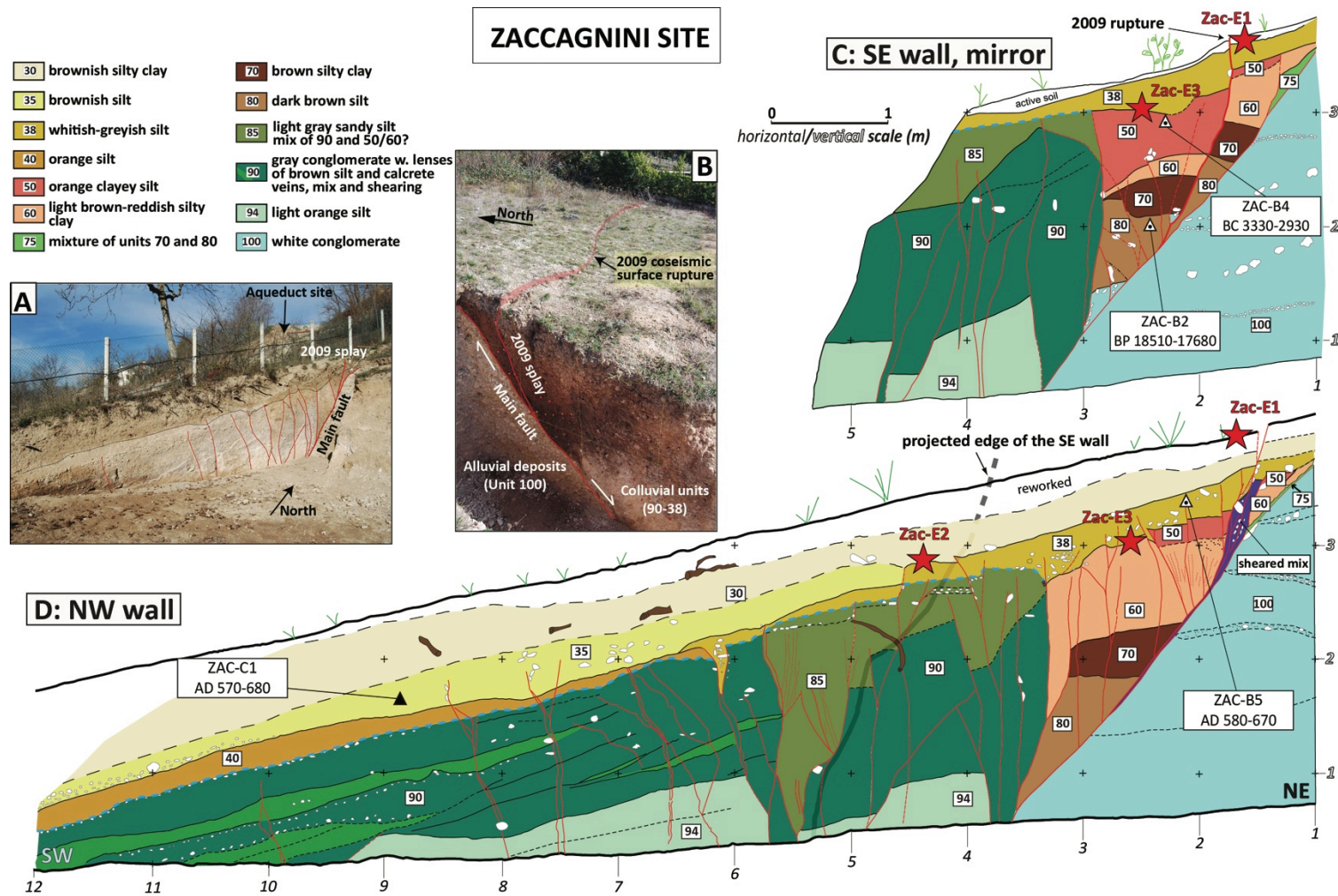


Figure 5.7 - Zaccagnini site. (a) View of the NW trench wall. (b) View of the shorter SE trench wall. (c) Simplified log of the SE wall from a 1:20 scale survey. Triangles indicate dated radiocarbon samples (Table 5.1), red stars indicate location of event horizons, dashed thick blue line marks the erosional contact associated with the LGM. (d) Simplified log of the NW wall, symbols are the same as in figure 5.6c. After Cinti et al., 2011.

This excavation exposed a prominent N130° striking and 50°– 55° SW dipping main normal fault and a 4 m wide zone of subvertical hanging wall faults, which includes the 2009 ruptures, with a very similar geometry with respect to that of FZ2 at the Aqueduct site.

Based on their sedimentological and stratigraphical characteristics, some of the deposits exposed at Zaccagnini site can be correlated with those exposed at the nearby Aqueduct site.

The Zaccagnini site provided evidence for at least two paleoearthquakes: event Zac-E2 with a throw of 0.10-0.15 m and event Zac-E3 with a throw of 0.25-0.30 m.

Using the age (BC 3330 670 AD, with the younger part of the interval preferred) and the cumulated throw of these events (0.45-0.55 m), we can estimate a Late Holocene slip-rate at this site of 0.09 – 0.43 mm/yr, with the higher slip-rate value preferred.

5.3.3 Mo'Tretteca site

The Mo'Tretteca trench was dug across a secondary splay of the 2009 coseismic ruptures occurred along a ~ 5 m-high, southwest facing minor scarp of the PSDFS. Here the 2009 coseismic rupture displayed up to 0.1-0.15 m of vertical displacement, a few cm of warping and up to 0.05 m of opening. The trench was NE-SW oriented, about 20 m-long and up to 3 m-deep, and was cut across an abandoned alluvial fan surface.

In coincidence of the 2009 surface rupture, the trench wall exposed a single, 2 m wide, V-shaped fault zone composed of a main fault plane and several synthetic splays (figure 5.8).

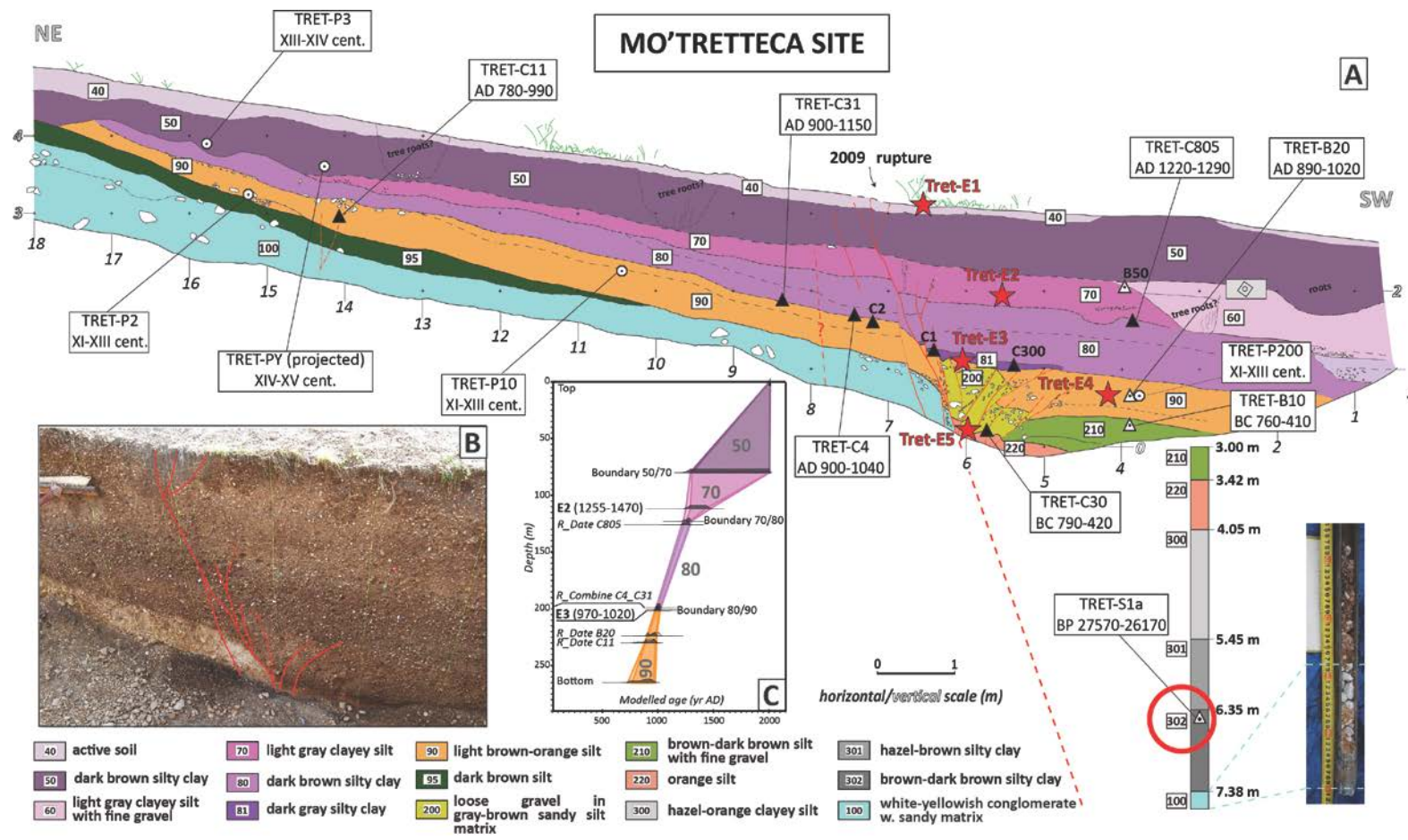


Figure 5.8 – Tret site. (a) Simplified log of the SE wall from a 1:20 scale survey. Triangles indicate dated radiocarbon samples (Table 5.1), circles indicate evaluated pottery shards location (Table 2), red stars indicate location of event horizons. (b) Photo of the fault zone approximately between m 4 and 8. (c) Age-depth model obtained for units 90 to 50 using a P sequence from OxCal v4.1.5 [Bronk Ramsey, 2008, 2009]. The best estimate of the age ranges of events Tret-E2 and Tret-E3 are derived from this model. After Cinti et al., 2011.

The sedimentary sequence exposed in this trench is composed of partially cemented whitish alluvial gravel within a yellow sandy matrix (unit 100) buried under a silty to silty clay colluvial sequence deposited during the past 3 millennia (see details in Cinti et al., 2011).

With the aim of finding deposits correlative with the oldest ones exposed on the footwall (units 95 and 100), we cored the hanging wall to a depth of 7.6 m. The core intercepted the gravel of unit 100 between m -7.38 and -7.60 (although we cannot preclude that this material may be reworked and that the in situ unit 100 is a little deeper).

Taking into account the dip of unit 100 from the trench wall and assuming limited erosion of the footwall, we can estimate a minimum throw of about 4.7 ± 0.1 m.

A late Pleistocene vertical slip-rate of 0.16-0.18 mm/yr can be estimate for this splay of the PSDFS dividing the measured throw by the age constraints derived from a bulk sample collected in the core one meter above unit 100 (red solid circle in figure 5.8, calibrated age of 27570-26180 BP, TRET-S1a, Table 5.1).

At Mo'Tretteca site we found evidences for 4 paleoearthquakes, characterized by different throw per event: event Tret-E2, with a throw of 0.15-0.20 m; event Tret-E3, with a throw of 0.10-0.20 m; event Tret-E4, with a throw of 0.30-0.45 m and event Tret-E5, with a throw of 0.35 m.

We can use the age and throw of the recognized individual events to estimate the following Late Holocene slip-rates at this site. If we consider the cumulated throw of individual events at this site (1 - 1.35 m) and divide it by the age of the deposits (calibrated age of BC790 - 410, TRET-C30 and TRET-B10, table 5.1), we obtain a Late Holocene slip-rate of 0.36-0.56 mm/yr.

5.3.4 250K site

At this site we took advantage of a NE-SW cut in a building yard located in between the two 2009 coseismic rupture splays (figure 5.1). This artificial excavation was logged in detail because it contained faulted late Pleistocene and Holocene deposits. The stratigraphic sequence is composed by a set of colluvial deposits overlying the white middle Pleistocene alluvial gravel found also at the other sites (unit 100). Two main normal fault zones displace the entire sequence (figure 5.9).

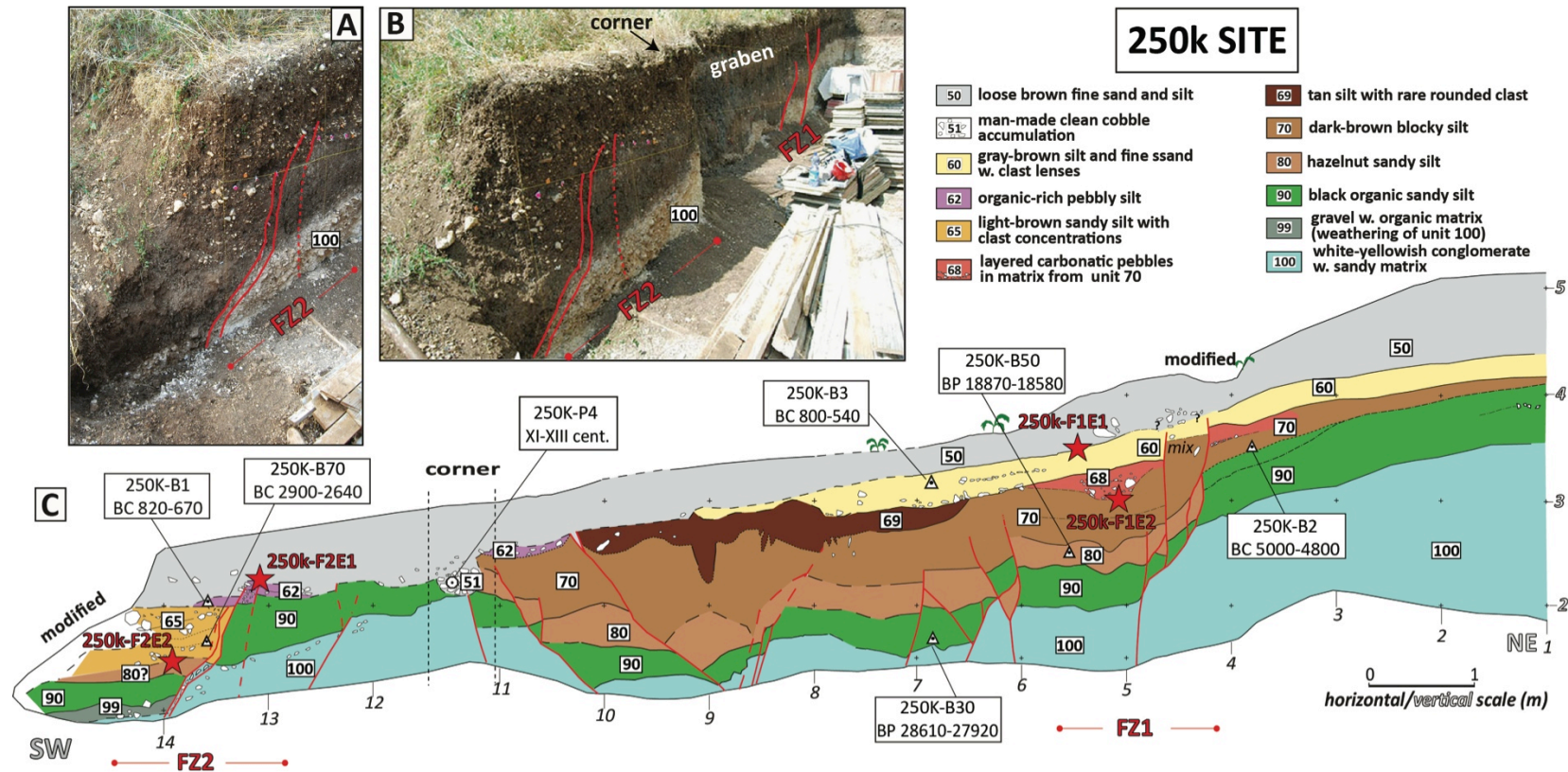


Figure 5.9 – The 250k site. (a) View of fault zone FZ2 on the NW wall of the excavation juxtaposing the colluvial wedge unit 65 (on the right) with unit 90. (b) View of the NW wall of the excavation. The two fault zones FZ1 and FZ2 and part of the FZ1 graben are visible; the wall is not rectilinear but forms a corner between m 12 and 11. (c) Simplified log of the NW wall from a 1:20 scale survey. Triangles indicate dated radiocarbon samples (Table 5.1), circles indicate evaluated pottery shards location (Table 2), red stars indicate location of event horizons. Notice that because of the corner in the wall between m 11 and 12, the distance between these two reference lines exceeds 1 m. After Cinti et al., 2011.

Fault zone 1 (FZ1) is composed of a set of subvertical fault splays that merge in a single plane within unit 100. This fault zone is faced by a ~ 6 m wide graben structure formed by a set of synthetic and antithetic fault splays, showing a similar deformational style compared to the Aqueduct site. Fault zone 2 (FZ2,) is exposed at the SW edge of the wall and appears composed by a set of subvertical, normal, down to the SW, fault splays. Unfortunately, the record on the hanging wall side of this fault zone has been partially removed and thus it was not possible to clearly observe the relationship between this tectonic structure and the 2009 coseismic rupture mapped ~15 m southwest.

Projecting the top of unit 100 across FZ1 and FZ2, and assuming minor/null erosion in the footwall, the net vertical offset is up to 2 m. Using the measured throw and dividing it by the age of the overlaying unit (calibrated age of 28610 - 27920 BP, 250K-B30, table 5.1), we can estimate a Late Pleistocene slip-rate of 0.07 mm/yr. However, because this site does not cross the entire zone of deformation, this value should be considered as a minimum.

Moreover, we are also able to estimate a Late Holocene slip-rate at this site. Given the cumulated deformation (1.2 -1.3 m) due to the occurrence of the recognized paleoearthquakes at this exposure and the available age constraints (between calibrated ages of 5000 BC, 250K-B2, and 540 BC, 250K-B3, table 5.1), we may estimate a Late Holocene slip-rate of 0.17 – 0.52 mm/yr for this site.

At this site we found evidences for 2 paleoearthquakes, characterized by different throw per event: event 250K--F1/F2 E1, with a throw of 0.40-0.50 m and event 250K--F1/F2 E2, with a throw of 0.80 m.

5.4 Main results

On the basis of the paleoseismological investigations, including trench analysis and coring, we reconstructed the recent paleoseismological history of the northwestern portion of the PSDFS and obtained Late Holocene and Late Pleistocene vertical slip-rates. The main results of this study in term of slip-rate evaluation are summarized in table 5.3.

Site	Time interval	Vertical slip-rate
Aqueduct	Late Holocene (last 5 ka)	0.41 - 0.53 mm/yr
Zaccagnini	Late Holocene (last 5 ka)	0.09 - 0.43 mm/yr
Mo'Tretteca	Late Holocene (last 5 ka)	0.36 - 0.56 mm/yr
250 K	Late Holocene (last 5 ka)	0.17 - 0.52 mm/yr
Aqueduct	Late Pleistocene (30 ka)	0.25 - 0.32 mm/yr
Mo'Tretteca	Late Pleistocene (30 ka)	0.16 - 0.18 mm/yr

Table 5.3 - Late Holocene and Late Pleistocene vertical slip-rates estimated by means of paleoseismological investigations.

Moreover, we derived average vertical slip-rate values from the two time intervals by averaging the minimum and maximum values from table 5.3.

The results are listed as follows:

- the average Late Holocene vertical slip-rate is of 0.26 - 0.51 mm/yr.
- the average Late Pleistocene vertical slip-rate is of 0.21 - 0.25 mm/yr.

The vertical slip-rates estimated at different sites are well comparable, but taking into account the presence of other parallel fault splays (figure 5.1), they should be considered as minimum values.

The other paleoseismological results, including the description of the evidences for the occurrence of distinct paleoearthquakes, the timing and correlation of the events, along with the implications for fault segmentation, recurrence and seismic hazard, are described in detail in the attached article "Evidence for surface faulting events along the Paganica fault prior to the 6 April 2009 L'Aquila earthquake (central Italy)", published on Journal of Geophysical Research in 2011, which I co-authored.

6 Tectonic geomorphological and geological approach

6.1 Introduction

In this chapter we present the extensive 1:10.000 scale geomorphological and geological investigations, supported by field survey and by aerial photo and digital topography analyses, carried out in the Middle Aterno valley over an area of ~140 km². We focused on the identification, and characterization of the long-term expression of Paganica-San Demetrio Fault System (hereinafter PSDFS), through the study of continental deposits and landforms affected by cumulative offset. The main goal is to provide new insights on the Quaternary deformational history of the PSDFS and to obtain long-term (up to ~2 Ma) slip-rate estimates.

Through the field survey, a total number of ca. 500 observations points of data collection were georeferenced (figure 1) using a hand-held Global Positioning System (GPS) device. Most of the collected observations points are located along the eastern flank of the Middle Aterno valley, where most of the deformation is concentrated.

All the collected field survey data were organized in a Geographical Information System (GIS) environment to analyze spatial relationships as well as to model spatial processes.

The software used is ArcGIS® Desktop, an integrated suite of software and data used to view and manage information in three dimensions with specialized tools as 3D Analyst and Spatial Analyst.

The GIS environment was particularly useful in analyzing all the data and in managing the high-resolution topographic dataset, as well as in integrating the topographic data and raster imagery with geomorphologic and geologic mapping.

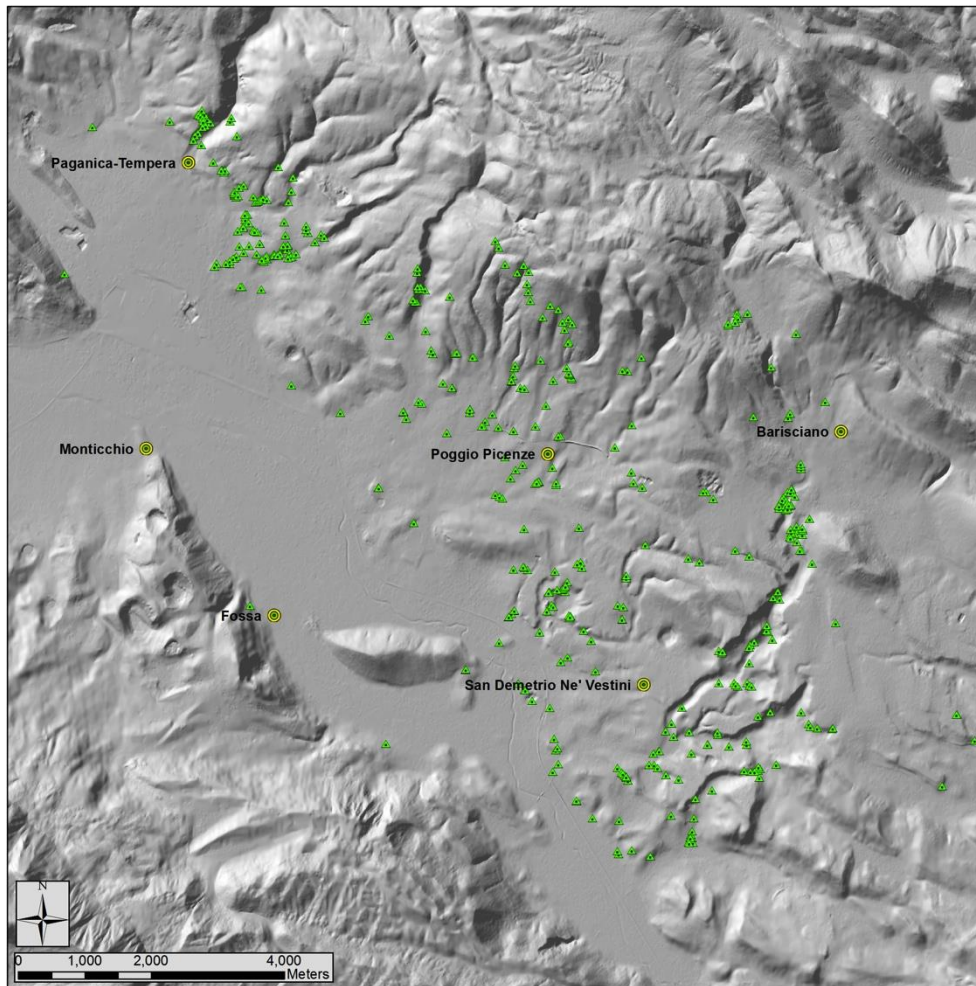


Figure 6.1 - Observation points collected along the Paganica-San Demetrio fault system

6.2 Tectonic geomorphological approach

Tectonic geomorphology is based on the study of landforms and landscapes developed in subaerial conditions that are deformed by tectonics and record a measurable tectonic signal (i.e. geomorphic markers; Burbank and Anderson, 2001). This allows to recognize and understand deformational processes over a wide and relatively recent range of spatial and temporal scales, according to the morphogenic epoch duration (i.e. from Plio-Pleistocene to Holocene in the study area). In particular, tectonic geomorphology analysis is a useful tool to estimate geometrical and behavioral parameters of active faults, such as their crucial rate of slip and its distribution along the fault strike.

In order to estimate the amount of deformation related to tectonic processes, it is typically necessary to have an identifiable and measurable feature of the landscape that has been tectonically displaced. The best geomorphic markers are usually readily recognizable landforms, surfaces or linear trends characterized by: 1) an hypothetical undeformed geometry; 2) a determinable age; 3) a high preservation potential with respect to the time scale of the process being investigated.

Therefore active tectonic studies must begin with a detailed analysis of the recent landscape. In fact, the first step in this study was to undertake a detailed geomorphological analysis aimed at identifying, among other features and other tectonic-related landforms, individual fault scarps that cross displaced geomorphic markers that can be used as piercing points for the measure of the offset amount . The main assumption to use measured displacements in the estimate of slip-rates is that slip occurs repeatedly on a fault, cumulates through time and produce scarps or displacements in the landscape which are thus representative of the amount of deformation occurred since their formation. In the case of normal faulting, for example, fault scarp may reach heights of hundreds of meters.

In this work, landscape analysis and mapping were performed at a 1:10.000 scale using LiDAR-derived Digital Elevation Model (DEM) and its standard derivatives (hillshade, slope, aspect, etc.), by observations and interpretation made on 1:33,000 scale aerial photographs (Gruppo Aereo Italiano – GAI, 1954/1955) and other raster imagery, as well as by fieldwork.

Among all the landforms identified and reported on the map, particular attention was devoted to those morphological features that contribute to the identification of tectonic lineaments, such as scarps, base of scarps, slope changes, paleosurfaces, saddles and ridges, as well as to the morphological features related to the drainage system (terrace risers, piracies, wind gaps, paleovalleys, strong incisions, drainage diversions, etc.).

6.2.1 LiDAR

An airborne LiDAR (Light Detection And Ranging, also known as Airborne Laser Swath Mapping or ALSM) survey was performed few days after the April 6, 2009 L'Aquila mainshock by the Civil Protection of Friuli Venezia Giulia (Italy). We took advantage of the availability of this high-resolution topographic data for the area hit by the 2009 earthquake to generate a high-resolution digital elevation model.

Airborne LiDAR is a recent technology that allows rapid and low-cost measurement of topography over large areas using an active sensory system (laser light) to determine distances. When mounted on a moving platform like an aircraft, this device can rapidly measure distances between the sensor on the airborne and points on the ground surface, collecting densely spaced and highly accurate elevation data. The LiDAR measures and collects multiple returns of a laser beam aimed at the ground and is able to discriminate between the first return, usually from the top of the forest canopy, and the last return, from the bare earth surface. Moreover, by isolating the last returns, LiDAR is capable of revealing the ground surface even in highly vegetated areas.

High-resolution digital topographic data products such as LiDAR-derived digital elevation models (DEMs), allows studying, both qualitatively and quantitatively, some of the processes responsible for landscape development, including tectonic, fluvial, hillslope, biological and anthropogenic.

Earth-science applications of LiDAR survey include coastal change studies (Sallenger et al., 1999), landslide analysis (Dietrich et al., 2001; Glenn et al., 2006;), volcanic deformation monitoring (Hasegawa et al., 2007), identification and mapping of fault traces and recently active breaks (Haugerud et al., 2003; Sherrod et al., 2004; Cunningham et al., 2006; Kondo et al., 2008; Arrowsmith & Zielke, 2009), slip-rate estimate from offset geomorphic features (Frankel et al., 2007; Amos et al., 2011), definition of fault geometry and kinematics (Begg & Mouslopoulou, 2010). Only a limited number of works took advantage of high-resolution LiDAR-derived topography data focusing on detailed fault scarp morphologic analyses (De Long et al., 2010; Hilley et al., 2010) and on the investigation of the spatial distribution of slope and aspect on active fault scarps (Brunori et al., 2011 submitted – see also Appendix L).

The LiDAR survey in the area struck by the 2009 L’Aquila earthquake was performed using the Optech ALTM 3100 EA Airborne Laser Terrain Mapper System. The main technical parameters related to the LiDAR acquisition are listed in table 6.1.

System	Optech ALTM 3100 EA
Operating altitude	80 – 3500 m
Vertical accuracy	10 cm < 1000 m (1 sigma) 15 cm < 2000 m (1 sigma) 20 cm < 3000 m (1 sigma)
Horizontal accuracy	1/5500 x flying altitude (1 sigma)
Range resolution	1 cm
Scan angle	Variable from 0 to $\pm 25^\circ$
Swath width	Variable from 0 m to 0.93 x altitude
Angular resolution	0.01°
Scan frequency	Variable, maximum 70 Hz
Laser wavelength	1064 nm
Laser repetition rate	Variable from 33 to 100 kHz
Beam divergence	Variable: 0.2 mrad (1/e) or 0.8 mrad (1/e)
“Eye safe” altitude limit	80 m @ 0.8 mrad 400 m @ 0.2 mrad
Intensity	Measurement of intensity of each pulse received
Collected data	Simultaneous measurement in range of first and last pulse for each pulse emitted
Laser classification	Class IV laser products (FDA CFR 21)
GPS receiver	Internal Novatel Millennium DL
Power requirements	28 VDC @35 A peak
Operating temperature	15-35 °C
Humidity	0-95 % non-condensing

Table 6.1 - summary of the LiDAR acquisition parameters

The entire mass of points produced by LiDAR was acquired as a point cloud (x_i, y_i, z_i , where x and y are the horizontal coordinate axes, z is the vertical, and i is the index of the point). Vertical and horizontal errors associated with the LiDAR acquisition are less than 0.2 and 0.5 meters, respectively.

Subsequently, the original LiDAR point cloud was processed in order to obtain a regular 1 by 1 m DEM and several derivative digital maps (hillshade, slope, aspect, etc.), suitable for geomorphologic and geologic analyses. Among these maps, hillshade is a hypothetical shaded relief with customizable illumination source angle and shadows derived from a surface raster (i.e., LiDAR DEM).

Moreover, the high-resolution topographic data stored in the LiDAR-derived DEM may be digitally manipulated to enhance and reveal subtle topographic features, something not possible with most aerial photographs, satellite imagery, or lower-resolution digital elevation data.

Figure 6.2 compares the resolution of traditional photogrammetry-generated (5 m resolution - figure 6.2a) and LiDAR-generated hill-shades (figure 6.2b) of the San Demetrio nè Vestini region (SE of the study area). Both the figures highlight how the very high-resolution (1m) LiDAR-derived representation of the ground surface can be a very effective tool in visualizing the landscape with unprecedented detail.

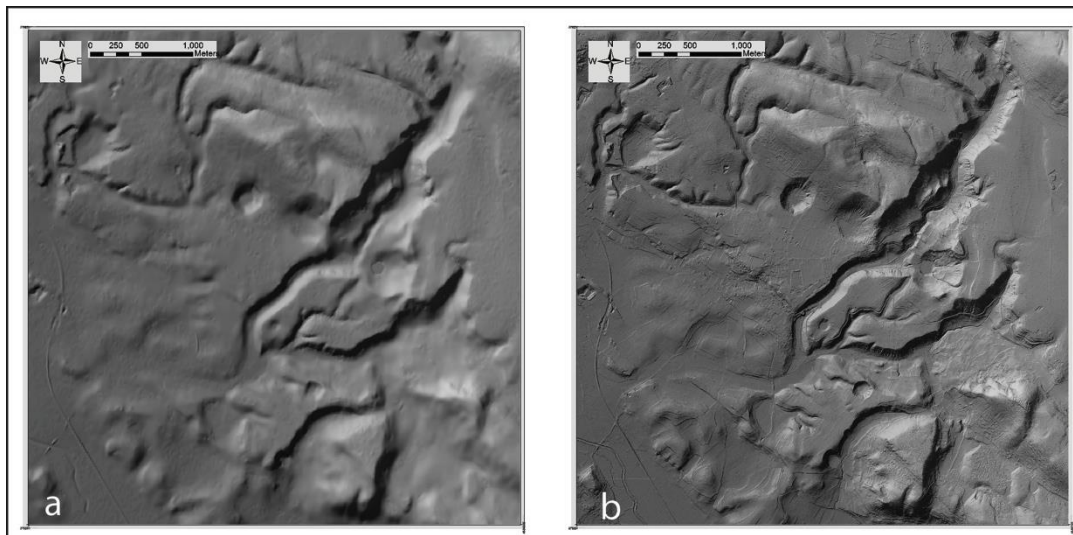


Figure 6.2 - Comparison between 5m resolution (a) and 1-m resolution (b) hillshades

More in detail, in figure 6.2 we note how the LiDAR-derived hillshade has the potential to substantially increase the confidence to locate and trace the faults through an enhanced visualization and consequent mapping of the morphological features that may be related to faulting activity. In figure 6.3 the LiDAR-derived hillshade of the area close to the San Gregorio village (south of the Paganica village) allows to display, among other, some subtle landforms like small fault-related scarps and enhanced drainage incisions (entrenchment that testifies the uplifted fault hangingwall).

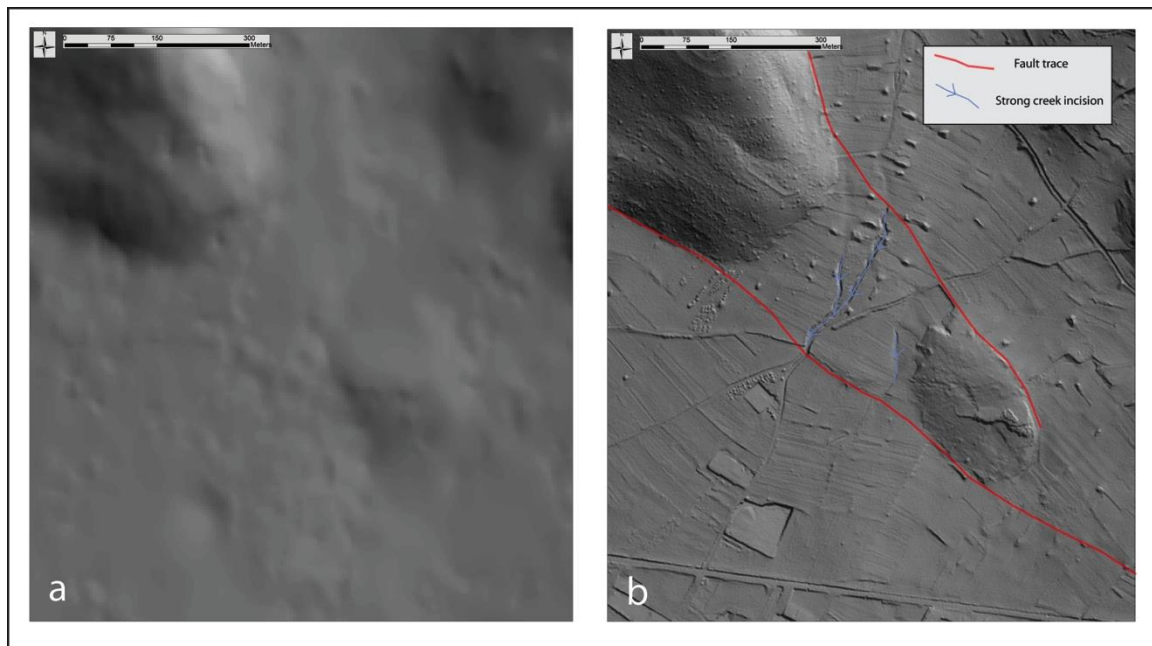


Figure 6.3 - Comparison between 5m resolution (a) and 1-m resolution (b) hillshades

6.2.2 Large-scale view of the Middle Aterno basin

The Middle Aterno basin is a 17 x 2 to 7 km intermountain depression located in the axial zone of central Apennines. The basin floor lies at about 600 - 550 m a.s.l., whereas the eastern and western ranges reaches elevations of 1400 m and 1200m, respectively.

The eastern flank of the basin appears strongly controlled by the activity of the PSDFS that produce a staircase-like landscape, with paleosurfaces separated by scarps (mostly in the southern portion).

The western flank of the Middle Aterno basin shows a completely different morphologic expression with respect to the eastern one, with steep slopes controlled by the activity of the antithetic Monticchio - Fossa fault system.

6.2.3 Landforms

All the morphological elements identified and mapped by means of geomorphologic analysis can be grouped into three main categories: 1) planar, 2) linear and 3) punctual landforms.

1) The recognized planar landforms are predominantly represented by paleosurfaces. We should mention that erosional and/or depositional processes act continuously to modify geomorphic markers like paleosurfaces, so what we observe in the present-day landscape are only fragments of a formerly continuous landscape. Several patches of remnant land surfaces were identified and mapped within the eastern flank of the Middle Aterno valley from LiDAR topography and aerial optical images interpretation. Most of the paleosurfaces are located in the southeastern

portion of the basin (figure 6.4), lying at different elevations with respect to the basin floor and ranging in size from $\sim 0,002$ to $\sim 0,62$ km². These include both erosional surfaces carved on the local bedrock and alluvial depositional surfaces, displaying different architecture and amount of preservation depending on their age and elevation. These landscape features are particularly important because they provide useful piercing points to measure tectonic displacement, provided a good knowledge of their original shape.



Figure 6.4 – Paleosurfaces (light shaded polygons) in the southeastern sector of the Middle Aterno river valley.

2) The intersection of the fault planes with the surface presents a morphologic expression, called “tectonic lineament”, characterized by the alignment of linear features of the landforms. Most of these linear features of the landforms are scarps. As already mentioned in Chapter 2, normal faulting produces mainly vertical deformations. Repeated movements cumulated for several seismic cycles along active normal faults can concur to form compound or multiple-event scarps that separate an uplifting footwall block from a subsiding hangingwall block, building a typical tectonically rising landscape bounded by basin-like areas.

Among all the linear features identified and reported on the map, particular attention was devoted to landforms such abrupt change in the slope dip angle, inner and outer edge of paleosurfaces, hinge line of saddles and ridges. We took in consideration the fact that these morphological features can be produced by both tectonic and erosive/depositional processes, so the tectonic origin of the identified lineaments was inferred using at least one of the following criteria: a) the linear feature is independent and far from the influence of the of the erosive/depositional

players (e.g. fluvial or lacustrine dynamics); b) the linear feature is not of anthropic genesis; c) the lineament is represented by a scarp that trends parallel or sub-parallel to other known faults; d) the lineament is a lateral continuation of a clearly identifiable fault-trace.

Different fault scarp sets are mapped with different strokes on the basis of their morphological expression, taking into account in particular the continuity of the trace, the preservation of the fault scarp and its height. Active normal faults characterized by large escarpments are reported on the map with a red bold continuous line, other active normal faults are mapped with a solid red line while both inferred and buried normal fault traces are mapped using a red dashed line.

Together with tectonic scarps, most of the linear features recognizable in the landscape are related to fluvial processes. The drainage system is very sensitive to any little change on its longitudinal profile induced by both local or regional scale tectonics (i.e. fault-related dislocations and regional uplift/subsidence, respectively). On this light, it is possible to recognize linear landforms as the response to such perturbations in fluvial system and to assess recent near-fault activity. With this aim, near-fault river valleys characterized by a V-shaped cross-section and strong incisions are mapped since they are witnesses of footwall uplift. Other linear features include fluvial terrace risers that bound fluvial terraces. Terrace risers are typically due to the downcutting of the channel on alluvial and fluvial deposits as well as in bedrock, in response to base level lowering (mainly due to either changes in climate and/or to local or regional tectonic uplift). Following this idea, we also highlighted other landscape features like average drainage directions.

3) In this area we also identified some punctual geomorphic features, such as peaks and sinkholes. Peaks highlighted the presence of double crests along the slope, morphological features commonly associated with normal faulting. Sinkholes are also present in our study area, and are interestingly aligned along main escarpments. Being usually related to significant fluid circulation, an alignment of several sinkholes may suggest a tectonic origin for the escarpment (fault).

The main results of landform analysis and mapping are illustrated in the geomorphological map of figure 6.5 (see also Appendix A).

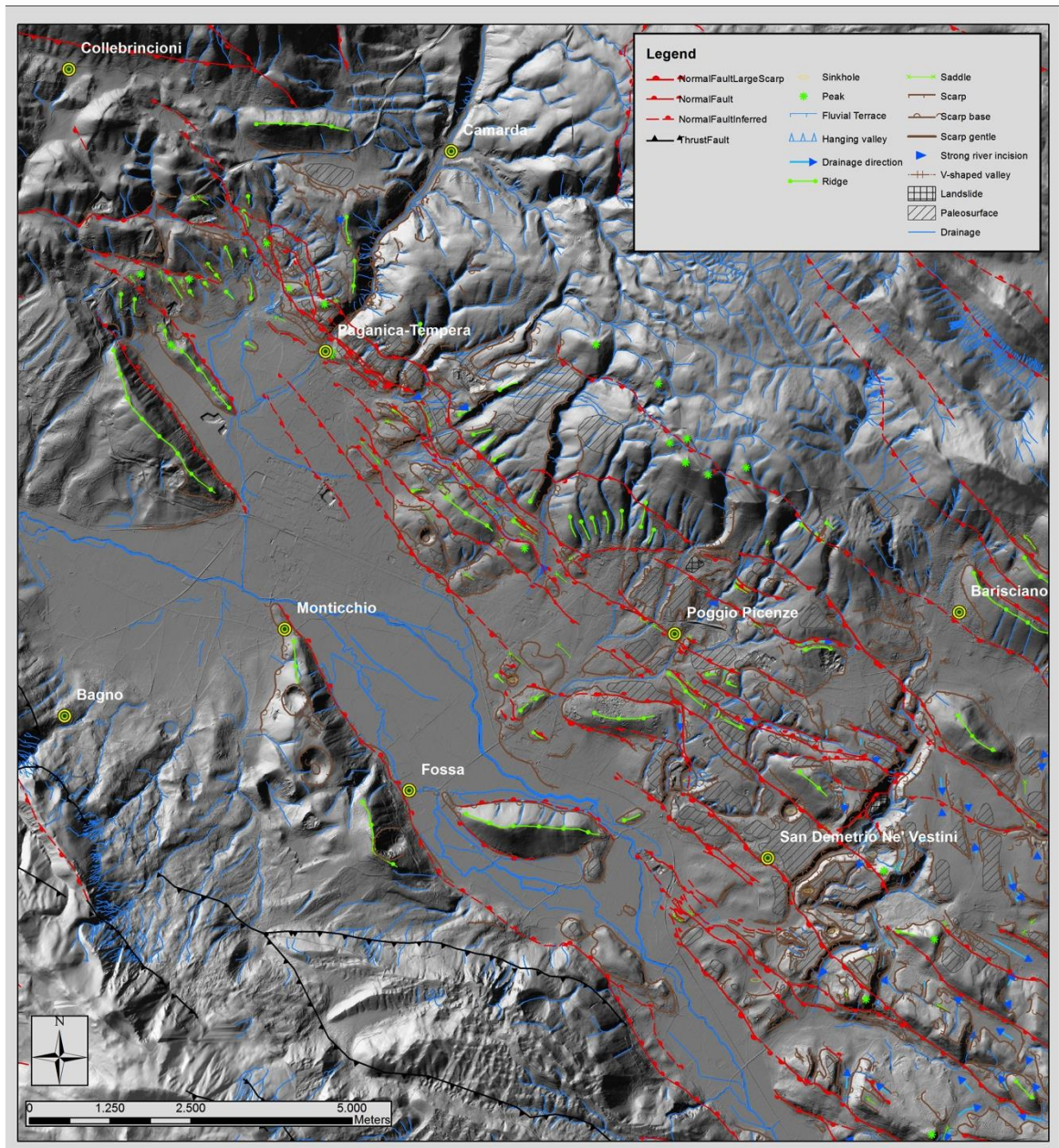


Figure 6.5 - Geomorphological map of the PSDFS (see also Appendix A)

Geomorphological analysis was crucial to identify and map several tectonic structures in the study area, as well as to characterize their predominant dip-slip (or better normal-slip) behavior.

At the surface, the structural setting of the PSDFS is quite complex being characterized by the presence of several normal parallel fault splays (i.e. overlapping strands with similar trends) frequently arranged in a quasi-fractal sequence of horsts and grabens of variable size.

Looking at the surface pattern of faulting of the PSDFS, we can distinguish two main different structural arrangements: along the northern portion of the PSDFS, between Collebrincioni and Paganica villages, the deformation is localized on few closely spaced splays, in a ~ 1 km-wide band.

In the southeastern sector, the structural arrangement become more complex, the deformation appears to be accommodated by several tectonic structures with the PSDFS opening into a set of parallel, km-spaced fault traces.

In order to reduce the complexity of the PSDFS at the surface and to identify the main tectonic elements, we combined all the individual fault traces into splay taking into account, among other criteria, the relative location (in map view) of fault traces with respect to neighboring faults. Fault traces (both synthetic and antithetic) that are aligned or approximately aligned to a main fault trace were, for example, assumed to be part of the same fault splay and consequently named (figure 6.6).

As a rule, we decided to name all the fault splays using different prefixes to differentiate between the two sectors (e.g. P1 stands for splay number 1 in the Paganica sector, S6 for splay number 6 in the San Demetrio sector).

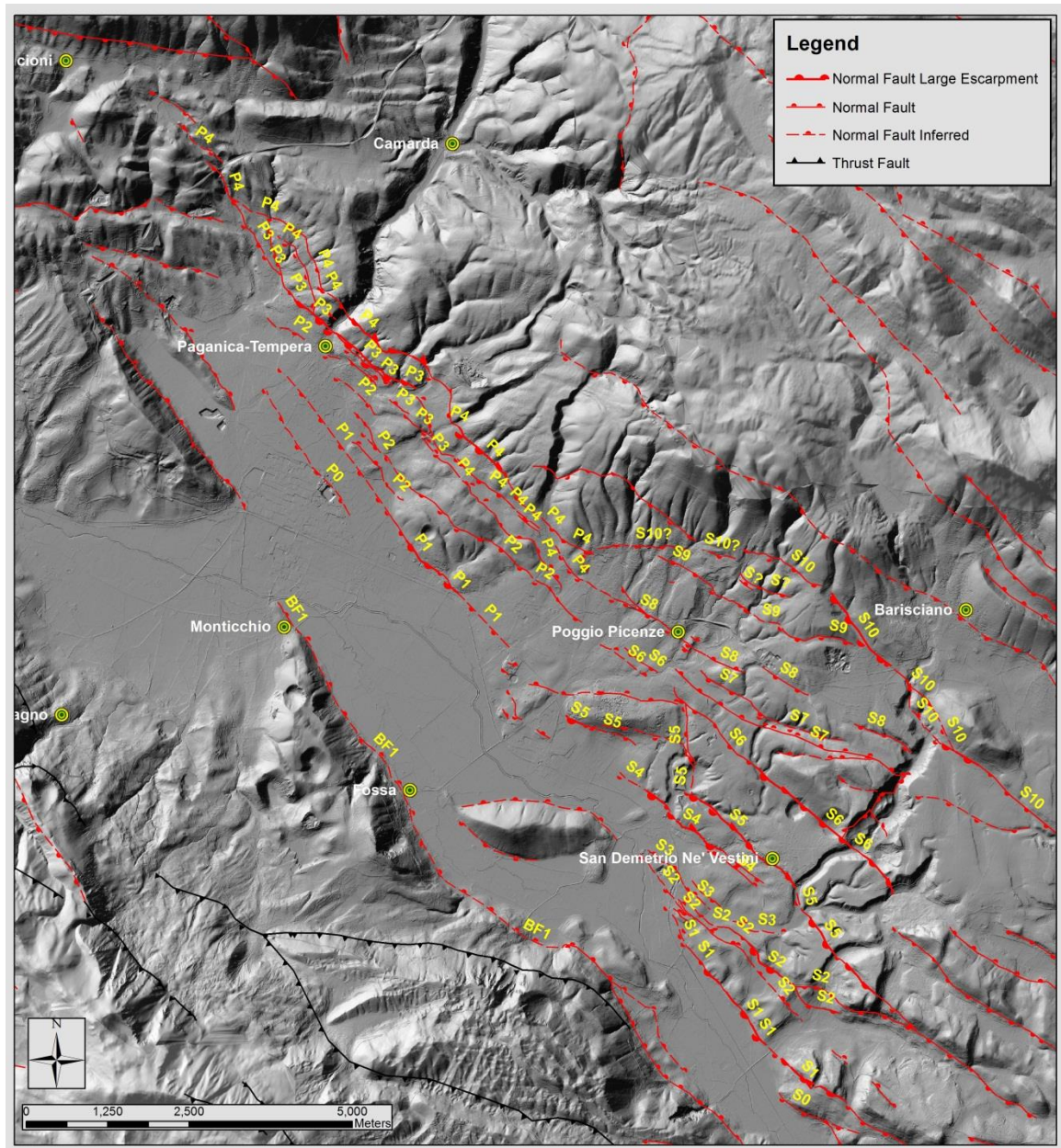


Figure 6.6 - Structural setting of the PSDFS at the surface. The fault splays are named using different prefixes to differentiate between the Paganica and San Demetrio sectors (e.g. P1 stands for splay number 1 in the Paganica sector, S6 for splay number 6 in the San Demetrio sector).

6.2.4 Cross-strike topographic profiles

In order to calculate morphological throws associated with previously recognized fault splays and to define a first-order hierarchy among the numerous fault splays affecting the eastern flank of the Middle Aterno valley, once a reference frame for the surface pattern of faulting was created, a series of 30 topographic profiles across the PSDFS were extracted from the high-resolution (1m) LiDAR-derived DEM.

The 30 topographic profiles were referenced to a baseline (red bold solid line in figure 6.7) that averages the strike of the fault splays identified along the PSDFS and is located on the fault system footwall. The average spacing between each profile is

~650 m, with minimum and maximum profile lengths of 5200 m and 9500 m, respectively.

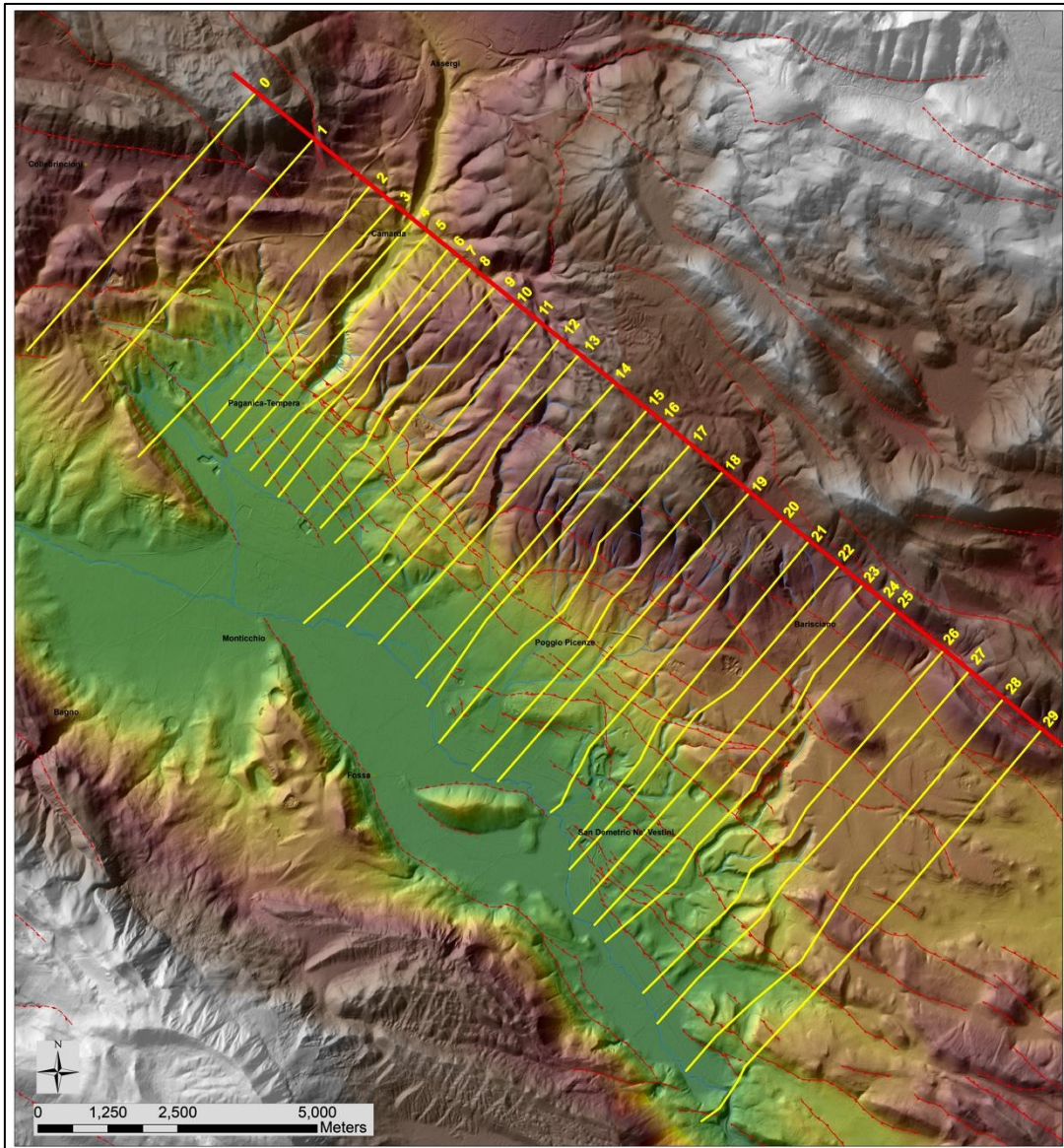


Figure 6.7 - Traces of the 30 topographic profiles across the PSDFS

The trace of each topographic profile was drawn in order to describe and to measure those displaced geomorphic markers previously identified by geomorphological mapping.

Each topographic cross section shows the position of the fault splays and the morphological throws associated with their cumulated activity through time (figure 6.8). Particular attention was devoted to the analysis of paleosurfaces, both erosional and depositional, used as piercing points to measure fault throws. Moreover, when two different inclinations of the original surfaces can be reasonably assumed, we measured both morphological throw values, using in our calculations a single average value with its uncertainty.

Total morphological throw values for each profile were also measured considering the difference between the maximum elevation at the footwall of the PSDFS (in correspondence of the starting line of each profile) and the elevation of the Middle Aterno basin floor at the hangingwall.

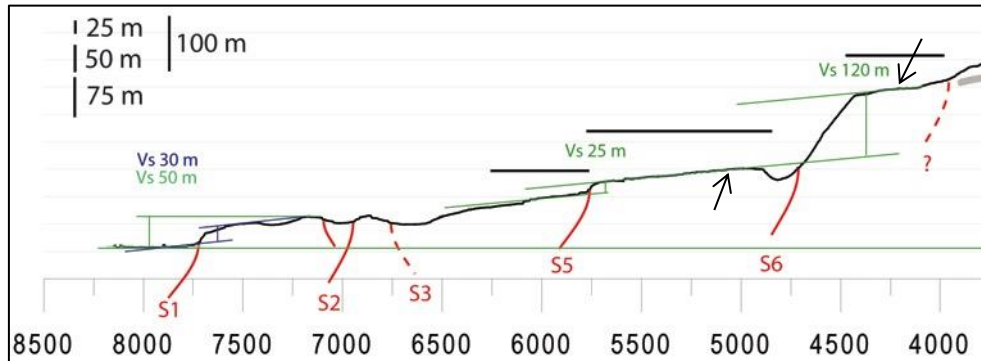


Figure 6.8 - Examples of measurements made on topographic profiles. Vertical exaggeration associated to the topographic profiles is 3x. The measured morphological throws are represented by the vertical component of the separation between an upper and a lower original reference surface (black arrows). The methodological uncertainty associated to each offset measurement is about 10 meters.

We should always be aware of the fact that a fault scarp (but also lake shorelines and terrace risers), once is formed, immediately begins to degrade, changing its morphology through time. Erosional processes tend to dismantle the footwall, while in the hangingwall depositional processes are dominant.

These topographic profiles are also useful in describing the morphology of the slopes bounding the eastern flank of the Middle Aterno valley. In fact, this flank of the basin appears to be strongly controlled by the activity of the PSDFS. To analyze more in detail its overall morphology 3 topographic profiles are selected among the 29, from the northwestern, central and southeastern sector of the fault, respectively (figures 6.9, 6.10 and 6.11).

Looking at the shape of the selected topographic cross sections, we can appreciate how the northwestern sector (figure 6.9 and profiles 3-14 in Appendix D1-D2) is characterized by steep slopes and by the presence of few fault splays (<7) accommodating the long-term deformation located mainly at the base of the range front. In the central section (figure 6.10 and profile 15-21 in Appendix D2-D3) the range bounding the eastern flank of the Middle Aterno valley reach its maximum elevation. This sector of the PSDFS is characterized by the presence of relatively few fault splays (< 7).

The southeastern sector of the Middle Aterno valley (figure 6.11 and profile 22-29 in Appendix D3-D4) shows a completely different morphology. The long-term expression of the slopes appears strongly controlled by the activity of numerous fault splays (> 7) that tend to dissect the original surfaces producing a staircase topographic profile, characterized by the presence of erosional and depositional paleosurfaces separated by fault scarps.

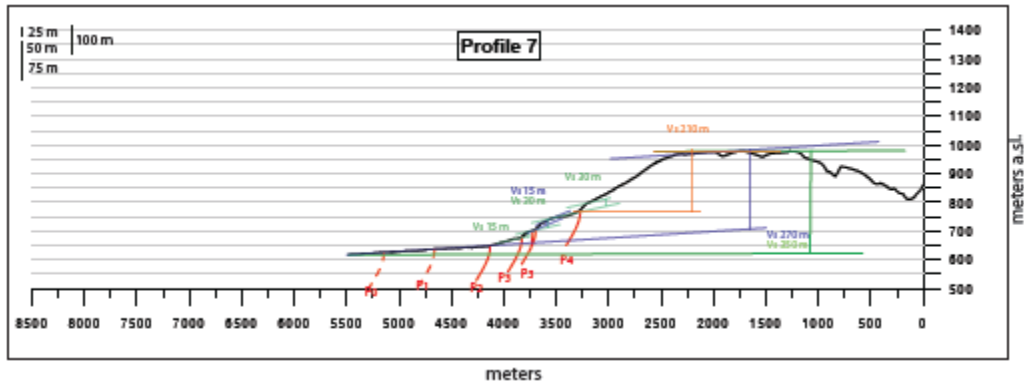


Figure 6.9 – Topographic profile across the northwestern sector of the PSDFS

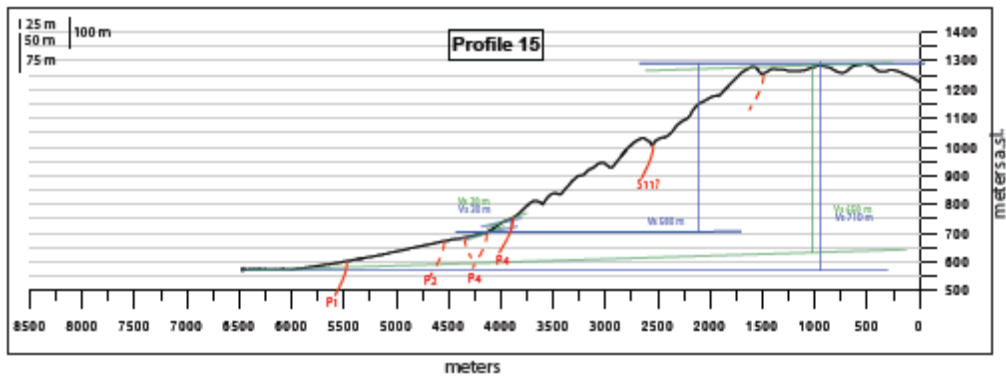


Figure 6.10 – Topographic profile across the central sector of the PSDFS

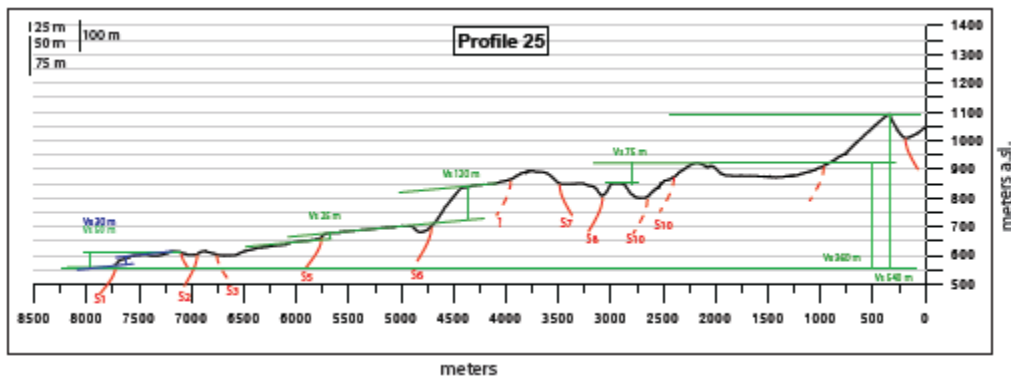


Figure 6.11 - Topographic profile across the southeastern sector of the PSDFS

6.2.5 Main results of the tectonic geomorphological approach

We analyzed the cumulated displacement distribution by plotting on the baseline the morphological throw values measured from the 30 topographic profiles (with the exception of those small fault splays showing a null or non-measurable offset). The resulting figure 6.12 shows the total morphological throws reported with a black solid line. Differently, morphological throws for each fault splay are presented in different colors and with different symbols to distinguish between throw values calculated from offset reference surfaces (i.e. piercing points) carved in bedrock or in unconsolidated deposits or a combination of the abovementioned.

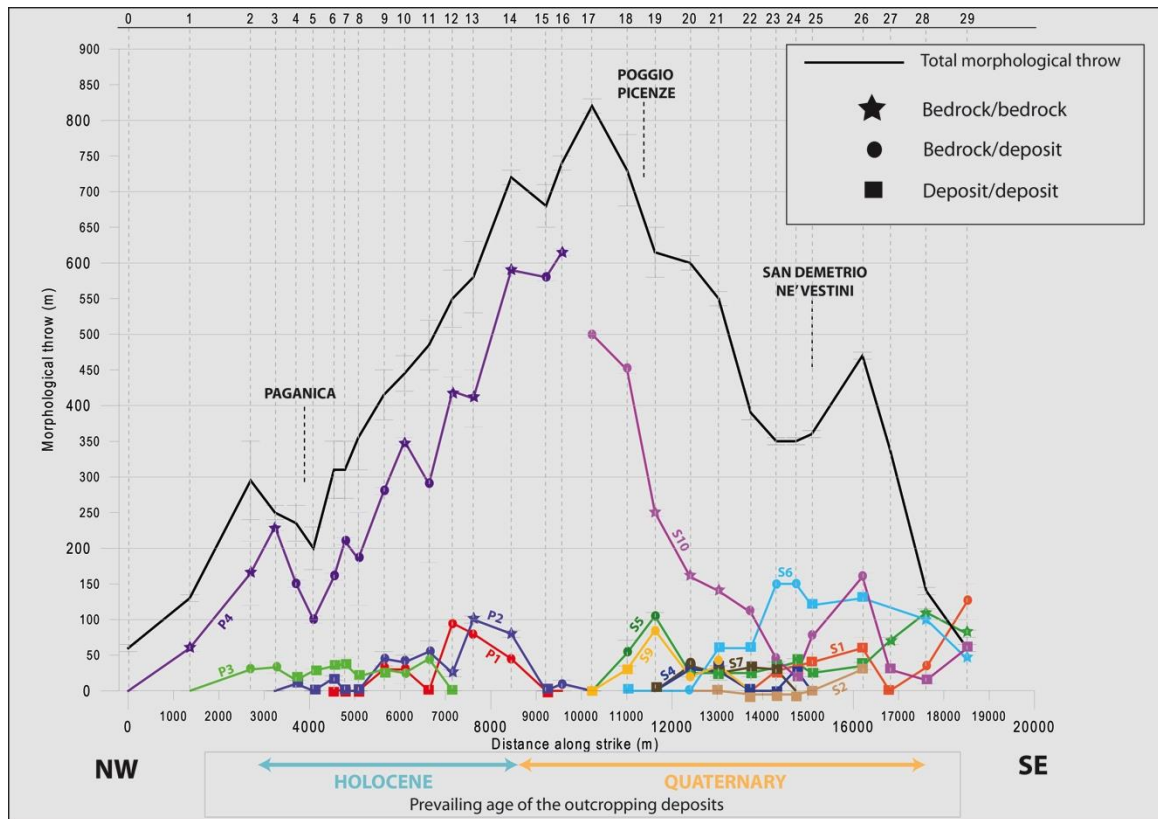


Figure 6.12 – Along-strike plot of the morphological throws measured from the topographic profiles across the PSDFS. Morphological throws for each fault splay are presented in different colors and with different symbols to distinguish between throw values calculated from offset reference surfaces (i.e. piercing points) carved in bedrock (star) or in unconsolidated deposits (square) or a combination of the abovementioned (point); see also Appendix E.

The preservation, continuity and height of the tectonic escarpments, as well as the morphological throws, concurred to define a first-order hierarchy among all the tectonic structures recognized in the area.

A summary of some statistical properties associated with the PSDFS is displayed in figure 6.13. Individual fault splays display an average strike of 140° and an average length of 4500 m. Measurable average vertical offsets range from 5 m to 280 m, while maximum vertical displacements range from 30 m to 615 m.

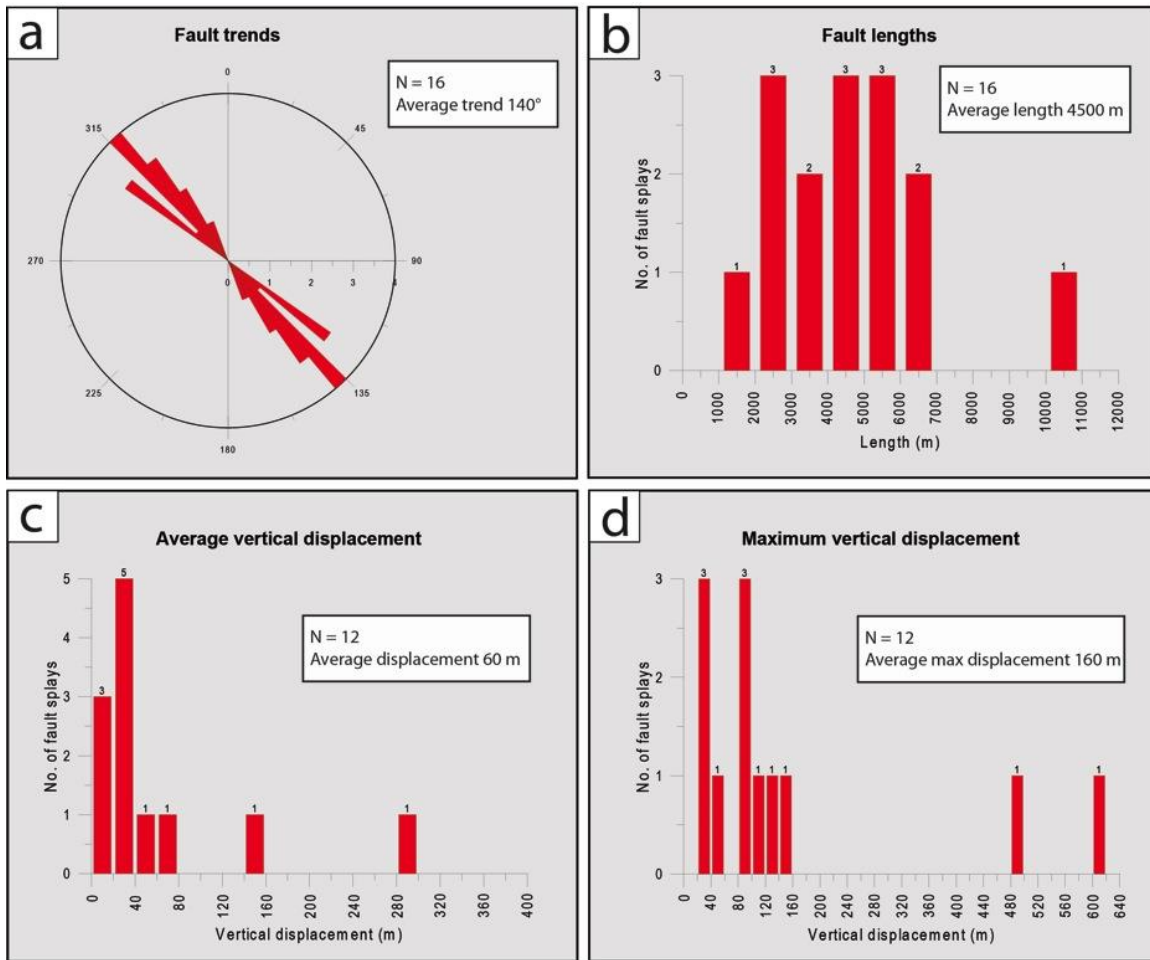


Figure 6.13 - Some statistical properties associated with the major fault splays of the PSDFS. a) Rose diagram illustrating the distribution of trends of the faults within the PSDFS; b) Histogram showing the lengths of fault splays; c) Histogram of the average vertical displacements; d) Histogram of the maximum fault displacements.

Looking at figure 6.12, we note that the total morphological throw graph (black solid line) approximates a symmetric bell-shaped curve, reproducing a throw profile comparable to that of an isolated individual extensional fault (see Chapter 2).

The maximum value of morphological throw reaches as much as 820 meters, and the overall length for long-term expression of the PSDFS as shown from the topographic profiles analysis approximates 19 km, thus in good agreement with the length of the seismogenic fault that ruptured during the April 6 earthquake, as defined by coseismic seismologic and geodetic observations (from 15 to 18 km - see Chapter 3). Figure 6.14 is another plot of all the morphological throw values measured from the abovementioned 30 topographic profiles: the orange dotted curve represents the aggregation of individual fault splays, built summing up the relative contribution of each fault, while the green and the blue solid lines represent the sum of all the other fault splays with exception of P4 and S10, respectively. In order to highlight the relative contribution of the splays displacing Quaternary sediments (without considering throw values measured from the bedrock) we also reported two

different colored areas for the Paganica sector (in green) and the San Demetrio sector (in blue).

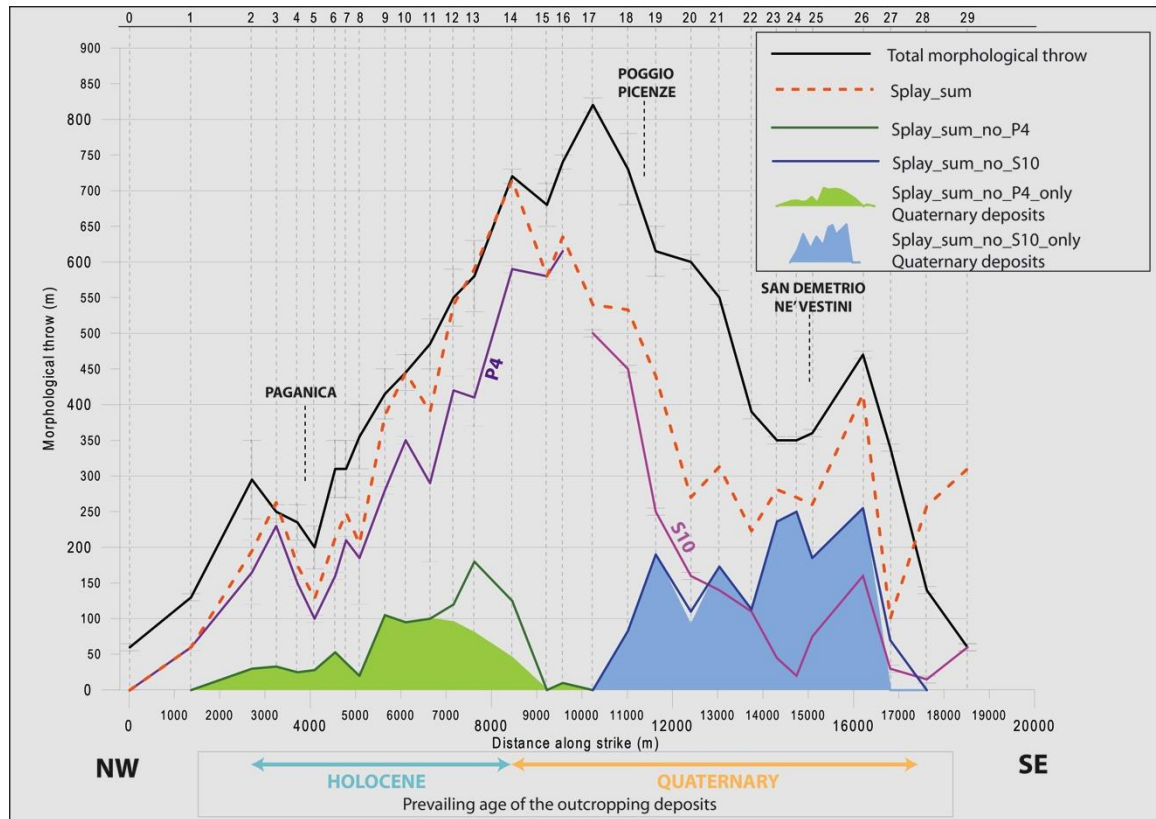


Figure 6.14 - Along-strike plot of all the morphological throw values measured from the topographic profiles. The orange dotted curve represents the sum of the relative contribution of each fault, while the green and the blue solid lines represent the sum of all the fault splays with exception of P4 and S10, respectively. Green and blue areas show the relative contribution of the splays displacing Quaternary sediments in the Paganica and San Demetrio sector, respectively.

A first-order consideration is that two different behaviors are visible from the morphological throw plot of figure 6.14: from profile 0 to profile 14 the orange curve mimics both shape and magnitude (81%) of the long-term deformation measured as total morphological throw. Differently, moving from profile 15 to the end of the PSDFS, the sum of the contributions of all individual fault strands take account of only 68% of the total morphological throw.

The mismatch between total morphological throw (black solid line) and the sum of all tectonic contributions (orange dotted curve) could be tentatively explained by:

- a systematic bias introduced by the morphological throw measurements, affecting mainly the San Demetrio sector where the deformation appears to be accommodated by several tectonic structures;
- the evidence of syntectonic deposition of some of the Quaternary sediments, that could result in a possible underestimation of the morphological throw values;
- the presence of an inherited paleotopography.

More in detail, we can note that most of the deformation in the area appears to be accommodated by the two most external fault splays (P4 and S10 – figure 6.14 and 6.15) affecting mainly the bedrock. These tectonic structures bound the Middle Aterno basin and contribute for 68% (P4 - northwestern sector) and 34% (S10 - southeastern sector), respectively, to the total morphological throw.

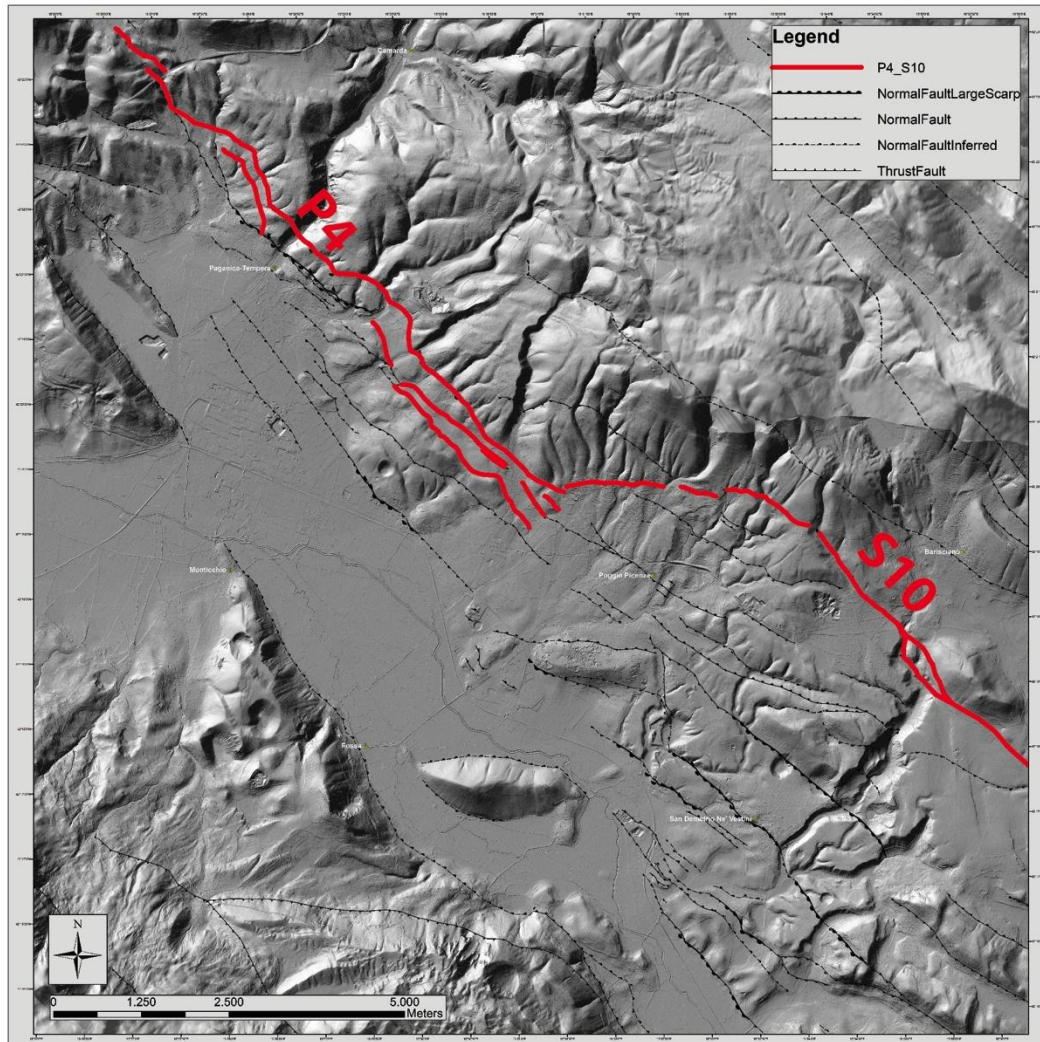


Figure 6.15 – Fault splays P4 and S10

Moreover, the amount of deformation related to the other tectonic structures affecting the Quaternary deposits (green and blue areas in figure 6.14) appears to be variable between the two sectors.

The Quaternary fault splays in the Paganica area account for an average ~ 15% of the total deformation, with a maximum value of ~ 25%, while in the San Demetrio sector the amount of deformation reaches values of ~ 40% (average) and ~ 70% (maximum). It is interesting to note that the relative contribution of the Quaternary tectonic structures tends to become predominant in the San Demetrio sector (in particular starting from profile 23), in correspondence of the decrease in throw values measured for splay S10 (figure 6.14).

In summary the morphological approach was useful to define the fault system structure, extent, geometry and boundaries. The most important limitation using this approach is that the morphological-derived throws do not allow age estimations and thus, we are missing information to calculate slip-rates.

6.3 Geological approach

As already highlighted chronological constraints are needed to translate displacement measurements into slip-rates. The following paragraph presents the geological investigations carried out in the area of the Middle Aterno valley with the aim of integrating the morphologic analysis with geological information and chronological constraints on displaced features and deposits.

The geological approach consisted in mapping and dating the deposits outcropping in the Middle Aterno valley.

6.3.1 Geological mapping

Geological mapping was carried out at a 1:10.000 scale and comprised several fieldwork campaigns performed during the whole 3 years-long PhD period. The survey started from the verification of previously published maps (Geological Map of Italy, scale 1:50.000, sheet 359, L'Aquila, APAT, 2006; Bertini and Bosi, 1993;) and benefited also of new public data collected for seismic microzonation after the 2009 L'Aquila earthquake (Italian Civil Protection Department), and was therefore integrated with new, essential field survey data.

Particular attention was devoted to the detailed differentiation of the continental deposits outcropping in the area, with the aim of obtaining chronological constraints useful for the long-term (~ 2 Ma) slip-rate estimate of the PSDFS.

In most of the cases, the Plio-Quaternary deposits subdivision and the relative ages already proposed by Bertini and Bosi (1993) were adopted also in our mapping. Accordingly to this subdivision, our ages refer to the pre-2009 global chronostratigraphical scale, with the base of the Pleistocene epoch set at ~1.8 Ma BP.

The stratigraphic sequence of the pre-Plio-Quaternary bedrock in the study area was mapped following the subdivision already proposed by the Geological Map of Italy, scale 1:50.000, sheet 359, L'Aquila (APAT, 2006).

The Middle Aterno valley is characterized by the presence of an extensive cover of lacustrine and alluvial Quaternary deposits accumulated upon a mainly Meso-Cenozoic bedrock.

The substratum is characterized by three different stratigraphic sequences of marine origin characterized by the presence of several units belonging to the transitional domain between the Lazio-Abruzzi carbonate shelf platform and the

Umbria-Marche pelagic basin, as well as by sin-orogenic turbidite deposits pertaining to the Miocene foredeep:

- A. Monte Ocre - Valle Aterno - Monte Camarda: Lazio-Abruzzi carbonate platform and edge sequences; flysch sequences of the Lazio-Abruzzi domain;
- B. Monte Cappellone – Paganica: basin and slope sequences of the Gran Sasso and Conca Subequana;
- C. Monte Pettino: basin and slope sequence.

6.3.2 Quaternary deposits

The Pliocene? – Quaternary Middle Aterno Basin infill is prevalently composed by terrigenous sediments. These deposits overlying the bedrock sequence were investigated in the past by several authors (Bosi and Bertini, 1970; Bertini and Bosi, 1993; D’Agostino et al., 1997).

It is worth noting that the continental sedimentary units found in the Middle Aterno basin can be correlated to other continental deposits found in other of the intermountain basins of central Apennines. A stratigraphic framework of the Plio-Quaternary continental deposits in the Latium-Abruzzi Apennines is available in Bosi et al. (2003).

Detailed geological field surveys allowed us to recognize, in several outcrops, 16 main Plio-Pleistocene to Holocene continental sedimentary units outcropping in the Middle Aterno basin; these are generally separated by unconformities and/or juxtaposed by the several fault splays detectable in the area.

The main sedimentary units are listed below:

- “Valle Valiano” - Pliocene? - Early Pleistocene: this unit comprises the oldest deposits detectable in the area. It consists of slope-derived breccias with eotheropic alluvial fan deposits, made of angular to rounded carbonate pebbles and cobbles. The basal portion of the unit comprises boulders up to some m³ within a whitish silty-sandy matrix. This unit can be mainly found at the north-eastern flank of the continental basin.
- “Fonte Vedice” unit - Early Pleistocene: slope-derived cemented limestone breccias with a typical orange-pink matrix. D’Agostino et al., 1997 defined a reverse magnetic polarity for this unit, which suggests an age older than ~781 ka. This unit unconformably covers the top of the Valle Valiano unit.
- “Valverde” unit - Early Pleistocene: is composed of few tens of meters of well layered limestone rounded gravels, occasionally well cemented; in the upper part the calcium carbonate gravels are interfingering with sand and sandy-silt layers. This unit represents an alluvial fan body entrenched in the Valle Valiano unit and could be partially interfingering with the San Nicandro unit deposited at the edge of the lacustrine basin.



Figure 6.16 - Valverde Unit

- “San Nicandro”- Early Pleistocene: The unit is predominantly made of whitish, well layered carbonate silts occasionally containing rounded gravel layers. These deposits are related to a lacustrine environment with few gravelly channels and landslides, located in particular close to the basin edge. This formation predominantly crops out in the southeastern portion of the investigated area and reaches a maximum thickness of more than 100 meters. Paleomagnetic analyses revealed a reverse magnetic polarity (Speranza, personal communication, 2011), thus suggesting for this unit an age older than the Bruhnes-Matuyama limit (~781 ka). This unit generally appears to overlap the “Valle Valiano” unit.



Figure 6.17 – San Nicandro Unit

- “Vall’Orsa” unit - Early Pleistocene: this unit is made of gravels and conglomerates, locally within a whitish silty lacustrine matrix and locally is characterized by a typical foreset-bedding attitude of the strata, possibly related to a deltaic complex progradating into the lacustrine basin. Generally covers but occasionally interfingers the “San Nicandro” lacustrine silts.



Figure 6.18 - Vall'Orsa unit

- “Valle dell’Inferno” unit - Middle Pleistocene: it is usually a well-layered calcium carbonate conglomerate and gravel with subordinated silty-sandy lenses. The total thickness of the unit is variable from a few meters in the southeastern sector to tens of meters in the western sector. The top depositional surface related to this unit is preserved at several locations. This unit unconformably lays on the Vall’Orsa unit.



Figure 6.19 - Valle dell'Inferno unit

- “San Mauro” unit – Middle Pleistocene: this unit can be subdivided into two main sub-units composed by alluvial fan and fluvial related deposits, respectively. Silts rich in volcanic minerals or component, sands and rounded calcium carbonate gravels are common. Age constraints were derived from the abundance of tephra layers, which are completely missing in the underlying deposits, and from one optically stimulated luminescence (OSL) sample. The resulting ages define a time interval for the deposition of the alluvial fan and fluvial deposits of 561 ± 2 ka - 172 ± 12 ka (see OSL sample SEF 2 – and Table 6.1 in this chapter).



Figure 6.20 – San Mauro unit (a – alluvial fan related deposits; b – fluvial related deposits)

- Late Pleistocene - Holocene alluvial fan unit: fan-shaped heterometric deposits composed by unconsolidated or poorly cemented well-stratified limestone gravels and sands. These deposits appear to be deeply entrenched in the older basin infill deposits and produced a set of telescopic alluvial fans, particularly clear in the SE part of the basin. Age constraints for this unit are derived from one Optically Stimulated Luminescence sample, that gave an age of ~ 27 ka and from ^{14}C dating, resulting in ages of ~ 30 ka (see OSL sample GREG FAN in the table 6.3 and sample ACQ-B4, ACQ-B7 in Chapter 5 - table 5.1).



Figure 6.21 - Late Pleistocene- Holocene alluvial fan unit

All these units are unconformably covered by slope debris and fluvial, alluvial, eluvial, colluvial and alluvial fan deposits.

The geological mapping is synthesized in the geological map of figure 6.22.

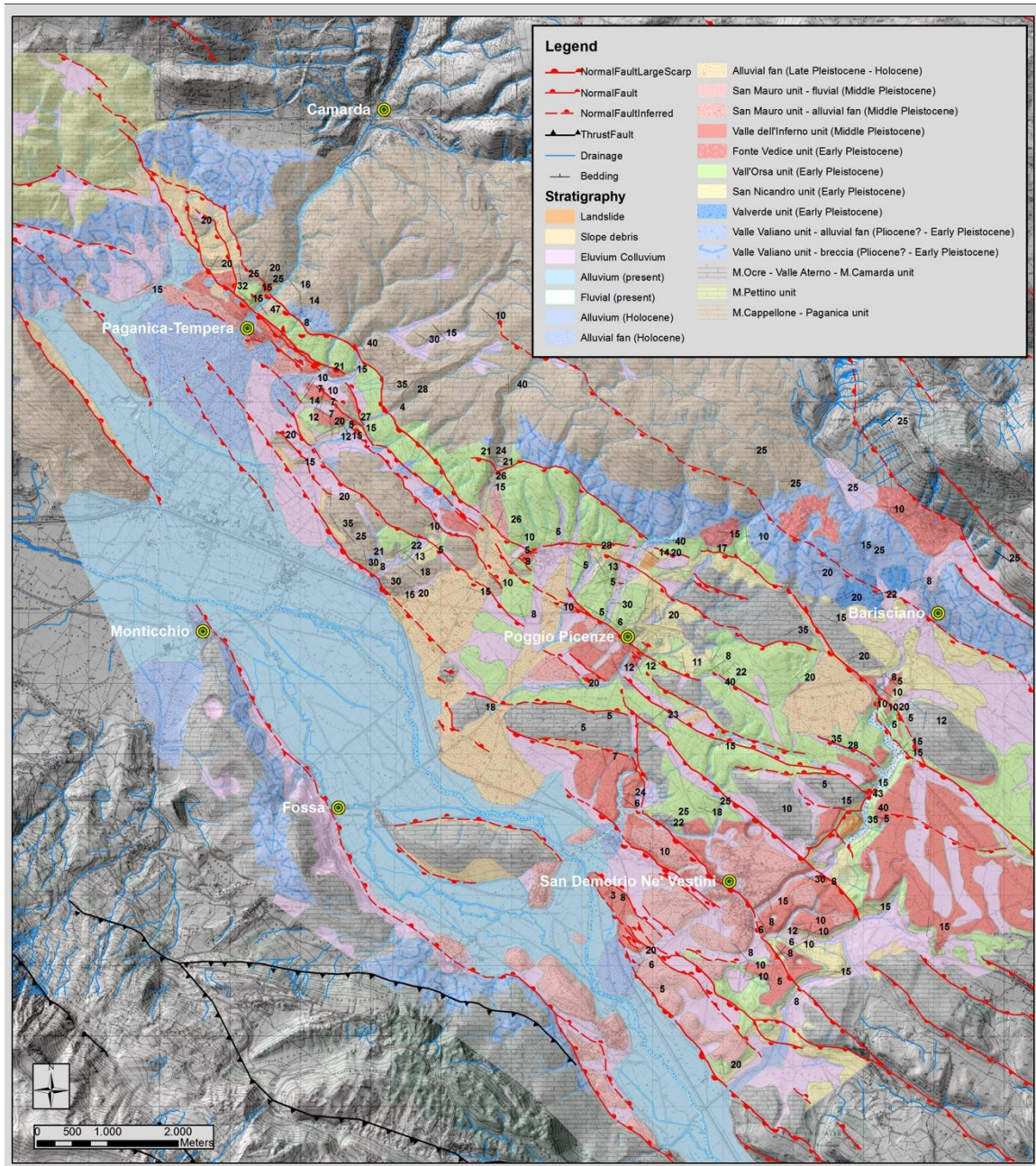


Figure 6.22 - Geological map of the PSDFS (see also Appendix B).

The detailed geological investigations undertaken in the area of the Middle Aterno valley and in particular along the PSDFS allowed us to highlight the presence of several continental deposits characterized by different facies suggesting a complex history in the development of the Middle Aterno basin.

This depositional evolution from the clastic deposits at the edge of a fault-controlled basin to a low-energy deposition at the depocenter, followed by a clastic phase

characterized by a sequence of entrenched alluvial bodies, suggests a progressive closure of the basin, possibly related to an exhumation of the Quaternary deposits that could testify a local tectonic uplift.

6.3.3 Chronological constraints

In order to determine the rate at which a fault slips or a surface is deforming, a critical issue is to provide a chronological constrain for the observed displacements/offsets. To acquire such information, we needed to date the displaced geomorphic markers wherever recognized.

A great variety of Quaternary dating methods are available. A useful classification is based on the type of age provided: numerical-age, calibrated-ages, relative-ages and correlated-ages methods. Numerical-age dating methods are those able to provide an absolute numerical age (in years), producing quantitative estimates of ages and uncertainty on an absolute time scale. Common examples are represented by radiogenic methods like luminescence dating or by isotopic methods like radiocarbon dating. Correlated-age dating methods are those that are not related to time-dependent processes. To obtain an age estimate, a geologic unit is supposed to be coeval to another geologic unit, which has been independently dated by means of a variety of properties. A common example is represented by tephrochronology.

It is often difficult to obtain chronological constraints on continental deposits mainly due to the scarcity of guide fossil remains with respect to the marine environment and to the limited applicability of direct dating methods providing numerical ages. This is because not all the deposits are suitable for dating due to the lack in their composition of the necessary minerals or organic matter (e.g. Quartz for OSL and charcoal for ^{14}C) and due to limitation in the time range of applicability of the dating method itself. Most of the chronological constraints in literature were based on stratigraphic and paleontological correlations. Very limited direct dating existed. To overcome this paucity, we focused on the refinement of previously published chronological data through the collection and analysis of new samples within the continental deposits in the area of the Middle Aterno valley.

In this work we dated displaced Quaternary landforms and deposits using predominantly numerical-age and correlated-age dating methods, in particular radiocarbon dating, optically stimulated luminescence (OSL) and tephrochronology. We developed a chronological framework based on 27 samples collected for radiocarbon dating (already presented in Chapter 5 - Paleoseismological investigations), 4 samples for OSL dating and 27 samples for tephrochronology (figure 6.22), as well as on archeological evaluation of pottery shards found within late Holocene deposits (already presented in Chapter 5 - Paleoseismological investigations). In the following the background of OSL dating and tephrochronology is presented.

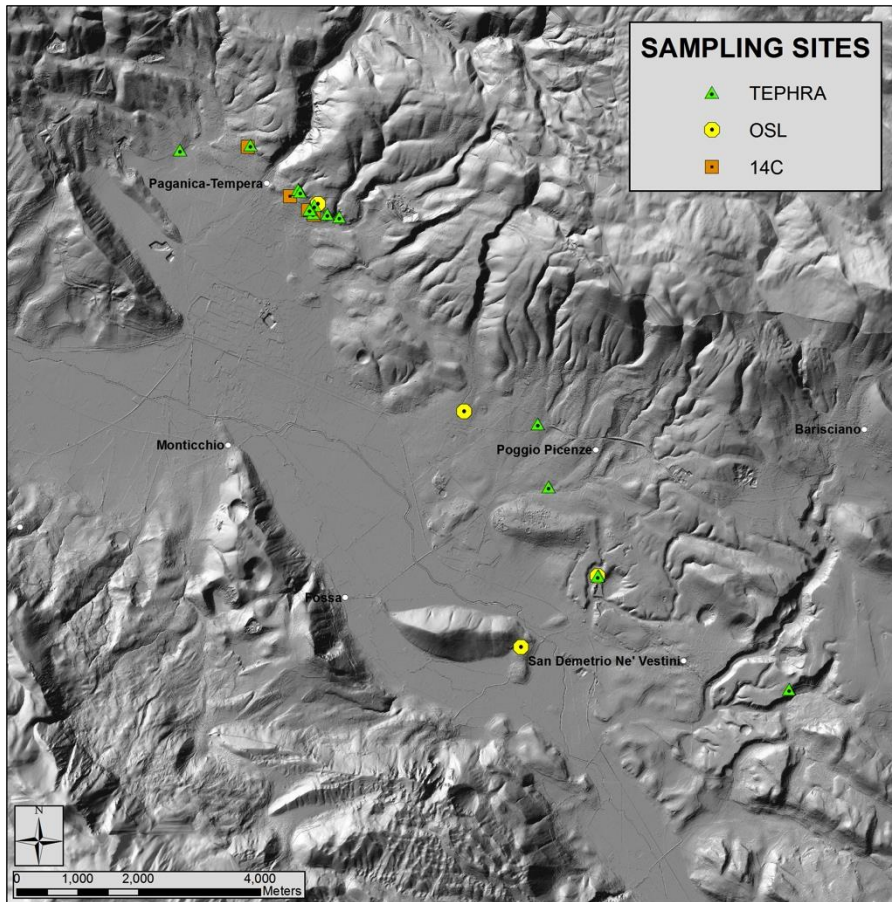


Figure 6.23 - location of the ^{14}C , OSL and tephra samples collected along the PSDFS

6.3.3.1 Optically stimulated luminescence (OSL)

In this work we took advantages from optically stimulated luminescence (OSL), a valuable Quaternary dating method that can be applied in a variety of continental stratigraphic settings (eolian, fluvial, alluvial and colluvial, among others). This method is able to provide ages for the deposition of sediments using the most common minerals on the Earth face, quartz and feldspar, covering a time range spanning from a few years up to ~300 – 500 ka (Murray and Olley, 2002; Duller, 2004; Wintle, 2008). The advantage of luminescence dating over other dating methods is its ability to give a constraint for the time a sediment was buried by other deposits, measuring the time elapsed since the last exposure to light or heat of its quartz and feldspar mineral grains.

OSL dating method is based on the fact that sediments are exposed to ionizing radiation emitted by materials containing naturally occurring radioactive isotopes, such as ^{238}U , ^{232}Th or ^{40}K , as well as, in the near surface, by cosmic rays. This radiation emits α , β and γ particles at a rate dependent on the amount of radioactive elements in the sediments. The emitted particles remain trapped in mineral lattice defects and chemical impurities until electronic traps are saturated, becoming subsequently a source for luminescence signals. This signal generally increases with time, reflecting a longer exposure time to environmental radiation. If irradiation

continues, then electron traps will fill until a further dose of radiation will not result in more luminescence being measured; this condition is referred to as “saturation”. When exposed to sunlight, the electrons are released and the inherited luminescence signal is reduced (bleached) to a low definable level. This level, called the residual level, is the point from which, after burial, the luminescence signal starts again to accumulate.

An important assumption in using OSL is that daylight exposure was sufficient to completely remove any pre-existing luminescence signal. OSL dating takes advantages from the fact that the inherited time-dependent luminescence signal can be released in the laboratory in response to some external stimulus, such as by visible light exposure. OSL measures the release of electrons from the light-sensitive mineral traps, the radiation level necessary to reproduce the stimulated signal (equivalent dose) and the environmental radioactivity of the sediment (dose rate). By dividing the equivalent dose by the dose rate it is possible to define an age for the time the sediment was buried by other deposits.

The selection and sampling of sediments represent a crucial step in OSL dating. By a practical point of view, in order to insure samples integrity, sediments were collected in the field at about 1 m below the surface, in order to insure samples integrity, by hammering into the suitable deposits an aluminum pipe (5 cm in diameter and 25 cm long), keeping the sample in the dark using end caps (figure 6.24). In order to allow dose rate and mineralogic and granulometric analyses, additional ca. 100 g of the same material were collected.



Figure 6.24 - example of sampled sediments for OSL dating and sampling technique

The 4 samples collected in the area were then sent to the Luminescence Dating Research Laboratory of the Department of Earth and Environmental Sciences, University of Illinois at Chicago (USA) and to the University of Catania (Italy).

The main results of OSL dating are shown in table 6.2.

Site	Sample	Optical age
San Gregorio fan	GREG FAN 2	27030 ± 1845
Fossa Prinesca	SEF 2	171610 ± 12170
Sant'Eusanio Forconese	CAT 1	Still under analysis
Paganica	PAG 2	>28340 (saturated)

Table 6.2 – Main results from OSL dating.

6.3.3.2 Tephrochronology

Tephrochronology is a correlated-age dating method that uses distinct physical or chemical characteristic of the sampled material to allow the identification of volcanic products belonging to a well-defined eruption.

Tephra is the term used to describe all pyroclastic materials erupted from a volcanic vent and transported at least in part through the air or by volcanic gases (Thorarinsson, in Westgate and Gold, 1974). Volcanic eruptions are usually relatively short-lived events, and products like tephra have the possibility to be injected into the atmosphere and be transported for large distances.

Tephra layers offer precise correlation and dating of various geological archives in both terrestrial and marine environments since they represent virtually instantaneous events, isochrones, are rapidly deposited and often have a widespread distribution. Moreover, one of the key factors in using tephra as a stratigraphic age marker and correlation tool is distinguishing between primary tephra and reworked tephra.

Tephra layers possess essential physical and chemical characteristics by which they can be distinguished one from another regardless of the location at which they are found. Three main components can be found in a tephra which are useful for a proper identification: lithic fragments, volcanic glass and mineral crystals. Tephra layers may be in some cases dated directly using primary minerals (such as zircon, K-feldspar, biotite, quartz) or glass from within the tephra layer, or indirectly on enclosing or encapsulated material: in this case the resulting chronological constraints will be greatly improved.

Field work allowed us to find a variety of tephra layers in the area of the Middle Aterno valley, and after appropriate field examinations, we collected 27 tephra samples, mainly from depositional and erosional paleosurfaces (figure 6. 25).



Figure 6.25 - Example of tephra layers found in the study area (red arrows).

To assure a proper identification of the collected tephra layers we performed petrographic examinations and electron probe microanalysis (EPMA) at the INGV laboratories (thanks to Dr. Paola Del Carlo and Dr. Andrea Cavallo) (figure 6.26). Geochemistry was used to confirm correlation of the tephra layers to a source volcano and/or eruption event, while morphology and geochemistry were used to discriminate between primary or reworked tephra.

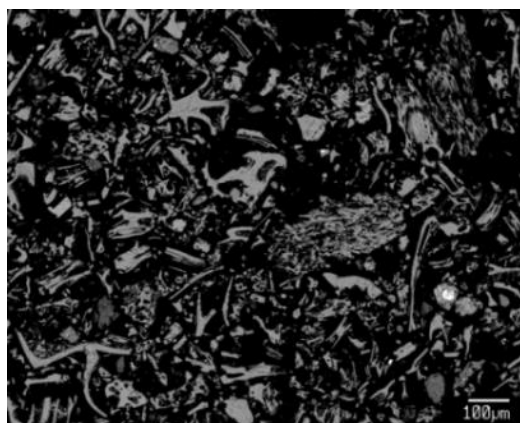


Figure 6.26 - Electron microprobe image of one of the tephra samples analyzed at the INGV laboratory.

Some of the analyzed samples were very weathered such that the tephra component were unrecognizable. The preserved samples showed physical and chemical characteristics that fit with those related to the main activity of some peri-Tyrrhenian volcanoes of the Roman Comagmatic Province (Colli Albani, Sabatini, Cimino, Vulturno and Vico). More in detail, we found evidences for the presence of discrete tephra layers and cryptotephra belonging to the activity of two of the nearest eruptive centers, the Colli Albani and Sabatini volcanic complexes. The reported activity for these volcanoes covers a time span ranging from 561 ± 2 ka to 365 ± 4 ka (Karner et al., 2001; Marra et al., 2009), thus suggesting a Middle Pleistocene age for the related deposits (table 6.3).

Site	Sample	Primary/Reworked/ Cryptotephra	Volcanic source	Age
Acquedotto	FED-P3	Reworked	Colli Albani - Carapelle tephra	561 ± 2 ka ^a
Gallinaro	GAL-P1	Primary	Colli Albani - Pozzolane Rosse	456 ± 3 ka ^a
Gallinaro	GAL-P2	Primary	Colli Albani - Pozzolane Rosse	456 ± 3 ka ^a
Gallinaro	GAL-P3	Primary	Sabatini - Tufo Rosso a Scorie Nere	449 ± 1 ka ^b
Case alte	CAL-P1	Primary	Sabatini - Tufo Rosso a Scorie Nere	449 ± 1 ka ^b
Case alte	CAL-P2	Primary	Sabatini - Tufo Rosso a Scorie Nere	449 ± 1 ka ^b
Case alte	CAL-P3	Primary	Colli Albani - Pozzolane Rosse	456 ± 3 ka ^a
Antithetic trench	MTA-P1	Reworked	Colli Albani - Carapelle tephra	561 ± 2 ka ^a
250 k	250K-P1	Primary	Sabatini - Tufo di Villa Senni	365 ± 4 ka ^a
Tornante	TFS-P1	Primary	Colli Albani - Pozzolane Rosse	456 ± 3 ka ^a
Parete plastica verde	PPV-P1	Primary	Colli Albani - Carapelle tephra	561 ± 2 ka ^a
Tempera	TEMP-1	Cryptotephra	Colli Albani - Carapelle tephra	561 ± 2 ka ^a
Accircia	ACC	Cryptotephra	Colli Albani - Carapelle tephra	561 ± 2 ka ^a
Fossa Prinesca	SEF-P2	Reworked	Colli Albani - Carapelle tephra	561 ± 2 ka ^a
Fossa Prinesca	SEF-P3	Reworked	Colli Albani - Carapelle tephra	561 ± 2 ka ^a
Poggio Picenze	PPT1	Cryptotephra	Colli Albani - Carapelle tephra	561 ± 2 ka ^a
Poggio Picenze	PPT2	Cryptotephra	Colli Albani - Carapelle tephra	561 ± 2 ka ^a

Table 6.3 – Main results from tephrocronological analyses ^a: Marra et al., 2009; ^b: Karner et al., 2001.

6.3.4 Geological cross sections

In order to obtain a long-term (~ 2 Ma) slip-rate estimate of the PSDFS, a set of 4 geological cross-sections (Appendix C) was drawn across the PSDFS, on the basis of the 1:10.000 scale geological map. The cross-sections aimed at reconstructing the subsurface structure of the PSDFS, focusing on the geometry of the faults and on the stratigraphy of the Quaternary deposits, and allowed us to obtain throw values for the numerous fault splays of the PSDFS by measuring the offset of geological features.

As a first order consideration, we can note that moving southward along the PSDFS (from cross-section 1 to cross-section 4, Appendix C), the number of Quaternary tectonic structures accommodating the net offset increases, in agreement with the results obtained by means of geomorphological mapping.

By a practical point of view, we measured from each geological cross-section the throw associated with the faults dissecting the Quaternary sedimentary units previously identified by means of geologic mapping.

Figure 6.27 shows an example of an offset geologic feature: we can note that the base of the oldest Quaternary deposit outcropping in the area, the “San Nicandro” unit (yellow unit in figure 6.26), appears in this geological cross-section to be downthrown of ~ 420 meters to the SW, due to the activity of the numerous fault splays recognized in this sector of the PSDFS.

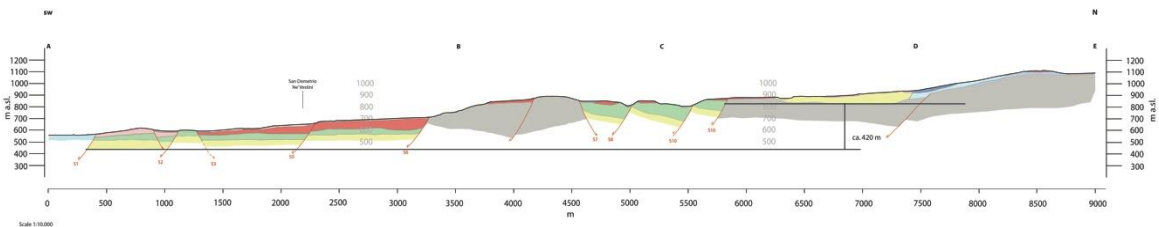


Figure 6.27 - example of the throw measurements on an offset geologic feature. In yellow the “San Nicandro” unit.

By repeating this type of measurements for the other Quaternary units, we were able to define the throw values for the Quaternary deposits deformed by normal faulting along the PSDFS.

Taking into account the age of the deposits involved in the deformation, it was then possible to estimate a vertical slip-rate for the PSDFS covering different time intervals, starting from the Early Pleistocene to the late Middle Pleistocene (table 6.4).

In the example shown in figure 6.27, the Early Pleistocene (1.8 Ma – 781 ka) throw of lacustrine deposits of ~ 420 m results in a minimum vertical slip-rate of 0.23 – 0.54 mm/yr, depending on the considered time interval.

Code	Cross section	Fault	Time interval	Throw (m)	Age max (years)	Age min (years)	Vertical slip-rate min	Vertical slip-rate max
B1	1 - Paganica	P3	Vall'Orsa unit - Early Pleistocene (1.8 Ma - 781 ka)	60	1800000	781000	0.03	0.08
A1	2 - Pescomaggiore	P3 P2 P1 P0	San Nicandro unit - Early Pleistocene (1.8 Ma - 781 ka)	290	1800000	781000	0.16	0.37
B2	2 - Pescomaggiore	P4 P3 P2 P1 P0	Vall'Orsa unit - Early Pleistocene (1.8 Ma - 781 ka)	300	1800000	781000	0.17	0.38
C1	2 - Pescomaggiore	P3 P2	Valle Inferno unit - Middle Pleistocene (781 - 561 ka)	120	781000	559000	0.15	0.21
A2	3 - San Valentino	P1	San Nicandro unit - Early Pleistocene (1.8 Ma - 781 ka)	180	1800000	781000	0.10	0.23
B3	3 - San Valentino	P4 P2 P1	Vall'Orsa unit - Early Pleistocene (1.8 Ma - 781 ka)	450	1800000	781000	0.25	0.58
B3a	3 - San Valentino	P1	Vall'Orsa unit - Early Pleistocene (1.8 Ma - 781 ka)	200	1800000	781000	0.11	0.26
B3b	3 - San Valentino	P4 P2	Vall'Orsa unit - Early Pleistocene (1.8 Ma - 781 ka)	250	1800000	781000	0.14	0.32
C2	3 - San Valentino	P4 P2 P1	Valle Inferno unit - Middle Pleistocene (781 - 561 ka)	210	781000	559000	0.27	0.38
C2a	3 - San Valentino	P1	Valle Inferno unit - Middle Pleistocene (781 - 561 ka)	80	781000	559000	0.10	0.14
D1	3 - San Valentino	P1	San Mauro unit - Middle Pleistocene (561 - 172±12 ka)	50	563000	159600	0.09	0.31
A3	4 - Valle dell'Inferno	S10 - S2	San Nicandro unit - Early Pleistocene (1.8 Ma - 781 ka)	420	1800000	781000	0.23	0.54
A3a	4 - Valle dell'Inferno	S6	San Nicandro unit - Early Pleistocene (1.8 Ma - 781 ka)	230	1800000	781000	0.13	0.29
A3b	4 - Valle dell'Inferno	S10	San Nicandro unit - Early Pleistocene (1.8 Ma - 781 ka)	140	1800000	781000	0.08	0.18
B4	4 - Valle dell'Inferno	S10 - S2	Vall'Orsa unit - Early Pleistocene (1.8 Ma - 781 ka)	260	1800000	781000	0.14	0.33
B4a	4 - Valle dell'Inferno	S6	Vall'Orsa unit - Early Pleistocene (1.8 Ma - 781 ka)	210	1800000	781000	0.12	0.27
C3	4 - Valle dell'Inferno	S10 - S5	Valle Inferno unit - Middle Pleistocene (781 - 561 ka)	300	781000	559000	0.38	0.54
C3a	4 - Valle dell'Inferno	S6	Valle Inferno unit - Middle Pleistocene (781 - 561 ka)	230	781000	559000	0.29	0.41

C3b	4 – Valle dell’Inferno	S10	Valle Inferno unit - Middle Pleistocene (781 - 561 ka)	40	781000	559000	0.05	0.07
D2	4 – Valle dell’Inferno	S5 - S1	San Mauro unit – Middle Pleistocene (561 - 172±12 ka)	65±10	563000	159600	0.34	0.47
D2a	4 – Valle dell’Inferno	S1	San Mauro unit (FLUVIAL) – Middle Pleistocene (561 - 172±12 ka)	40±10	563000	159600	0.19	0.31
D2b	4 – Valle dell’Inferno	S5	San Mauro unit (ALL. FAN)– Middle Pleistocene (561 - 172±12 ka)	25	563000	159600	0.13	0.19

Table 6.4 - vertical slip-rate estimates for the PSDFS covering different time intervals, starting from the Early Pleistocene to the late Middle Pleistocene.

7 Geophysical approach

7.1 Introduction

A multidisciplinary and scale-based geophysical investigation approach was carried out at different sites in the Middle Aterno basin across the Paganica – San Demetrio fault system (PSDFS).

To obtain high-resolution stratigraphic correlations able to highlight possible tectonic offsets, we experimentally applied an innovative methodology that employs core sampling and laboratory and *in situ* measurements of physical properties. We also performed 2D electrical resistivity tomography (ERT) and contributed to a high-resolution seismic tomography campaign.

The main objectives of this approach are: 1) confirm and/or obtain detailed information from sites previously investigated by paleoseismological trenches; 2) include subsurface data in the estimation of cumulative throws; 3) define the precise positions and geometry of blind faults; 4) obtain complementary images of the basin with respect to the information gathered by means of geomorphological and geological investigations.

7.2 High-resolution petrophysical correlations

7.2.1 Introduction

During the whole PhD period, we tested an innovative methodology that uses physical properties measurements of continental deposits as an alternative paleoseismological tool. In order to relate measured physical properties to sediment characteristics and to investigate deformation in recent unconsolidated continental deposits, we experimentally used an automated, non-destructive, high-resolution, multi-sensor tool commonly applied to marine and lacustrine sediments.

Determining physical properties of rocks and deposits plays a significant role in a wide range of geological and environmental studies as well as in the oil and gas exploration and mining industries. Physical properties data are generally considered as good indicators of sediment's composition, depositional and environmental conditions, furnishing proxies for sediment mineralogy as well as for depositional and erosional processes, oceanographic and climatic changes and post-depositional processes such as consolidation and early diagenesis (among many others, Kim et al, 2001; Casas et al., 2006).

A previous work performed in Southern Italy (Improta et al., 2010) highlighted that laboratory physical logging of cored sediments can also be an effective tool in obtaining high-resolution stratigraphic correlations among continental cores. This method is able to provide a viable alternative to detect possible tectonic offsets

across faults when sediment characteristics prevent conventional stratigraphic correlations and/or trenching is impractical.

Taking into account what we learned in that pioneering experiment, we decided to continue testing this methodology and performed physical properties measurements both at a previously investigated trench site (Mo'Tretteca site, see Chapter 5) and directly on an artificial wall close to Fossa village where a secondary fault splay crops out.

7.2.2 Mo'Tretteca site

The main goal at Mo'Tretteca site was to experimentally use the physical properties of continental sediments in order to obtain complementary information from the previously investigated paleoseismological trench. More precisely, the test was focused on the development of an alternative tool able to reproduce the stratigraphy and the deformation of correlative deposits obtained by means of trench logging. Finally, the results of this test are used to estimate the slip-rates associated with that specific fault splay. As already discussed in Chapter 5, the Mo'Tretteca trench was located in the Paganica village at the base of the main fault escarpment and crossed a secondary splay of the 2009 coseismic surface rupture. The SE wall of the trench was studied by means of trench-wall stratigraphic logging, showing that the vertical offset of the deposits across the fault zone increases with depth.

After Mo'Tretteca site trench was interpreted from a paleoseismological point of view (see Chapter 5), four cores were drilled from the top surface, close to the SE wall of the trench down to maximum depth of ~3.2 m. Figure 7.1 shows the location of the cores: two were extracted from the fault footwall (TR-S9 and TR-S8) and the other two from the fault hangingwall (TR-S5 and TR-S4).

We used a vibracoring (gasoline power percussion hammer – see Chapter 5) and sampled the cores with PVC tubes in order to have almost undisturbed sediments to be measured in the laboratory.

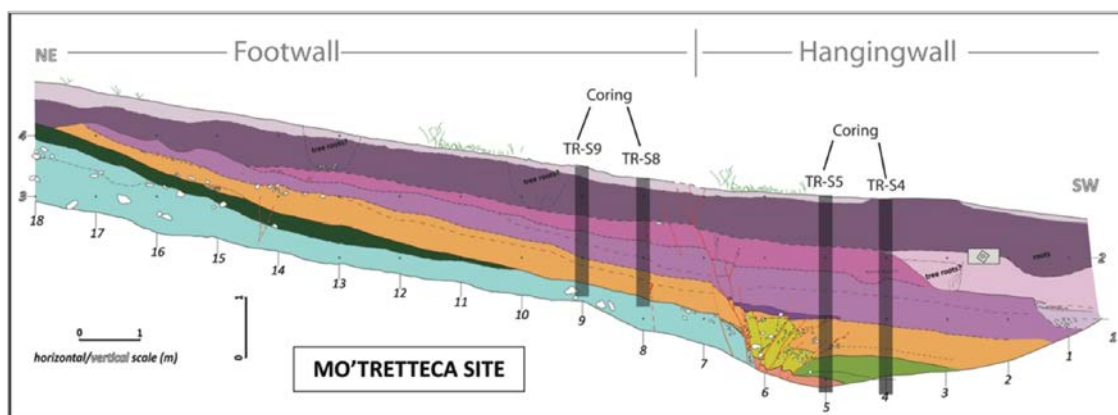


Figure 7.1 – Simplified log of the SE wall of Mo'Tretteca site showing the location of the drilled cores (modified after Cinti et al., 2011).

The sampled cores were then accurately sealed to prevent moisture loss and taken in the laboratory to perform a conventional stratigraphic description and to measure their physical properties using a non-pervasive logging system.

We used a fully automated GEOTEK Multi Sensor Core Logger standard (MSCL-S) available at the IAMC-CNR Petrophysical Laboratory (Naples, Italy). The MSCL-S is a versatile system that can be moved and used in shipboard (as for Integrated Ocean Drilling Program – IODP expeditions) or shore-based laboratories and is able to perform non-destructive, high-resolution (centimetric scale) and multi-sensor physical properties measurements both on whole and split cores.

The MSCL-S configuration used in this work is floor mounted on legs and includes a Bartington MS2E Point sensor and a Bartington MS2C loop sensor for measuring the low-field magnetic susceptibility, a Gamma Ray Attenuation Porosity Evaluator (GRAPE) sensor to determine the bulk density (GRP), a Minolta Spectrophotometer CM 2002 to measure the reflectance parameter L% (the percentage of reflected energy in 10 nm wavelength steps), and two Acoustic Rolling Contact (ARC) transducers, for evaluating the P-wave velocity (figure 7.2).

Generally, individual core sections between 50 and 150 mm in diameter and up to 1.55 m long can be logged by this system at spatial intervals as small as a few millimeters.

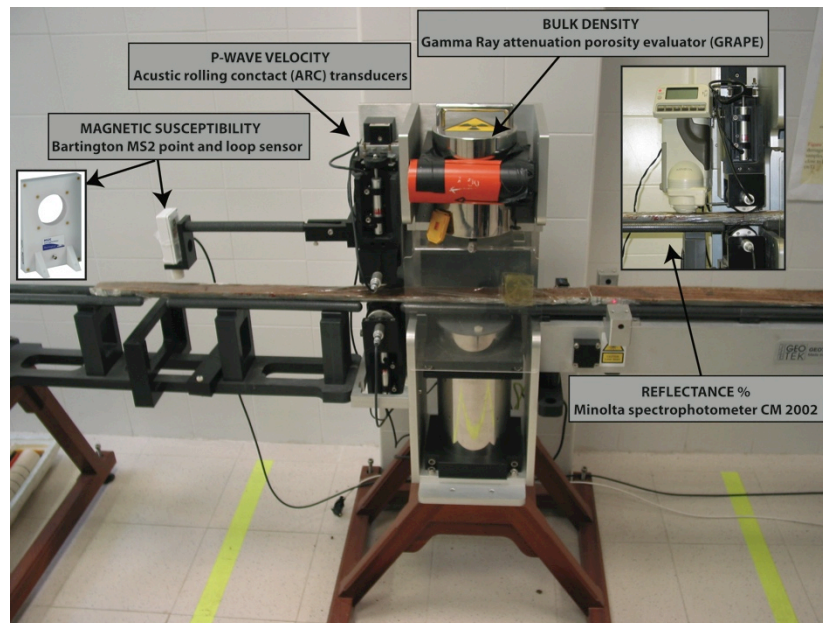


Figure 7.2 – Geotek Multi Sensor Core Logger standard (MSCL-S) available at the IAMC-CNR Petrophysical Laboratory (Naples, Italy).

In our experiment sequential core sections were loaded onto the rails while a pusher system automatically measured the length of each core section and pushed it through the stationary sensor array. In this way a complete core was logged in a continuous process while both the raw and processed data were graphically displayed in real time on a PC screen.

Our laboratory measurements of cored sediments started collecting magnetic susceptibility data for TR-S9, TR-S8, TR-S5 and TR-S4 cores using the Bartington loop sensor (MS2C) on whole cores. Logging was done at a centimetric scale (2 cm interval between each measurement) on all four cores.

At first, we checked the magnetic susceptibility signals measured from the cores in order to detect possible technical problems.

The data were of good quality and thus suitable for the correlation procedure. In figure 7.3 the magnetic susceptibility logs of boreholes TR-S9, TR-S8, TR-S5 and TR-S4 are shown.

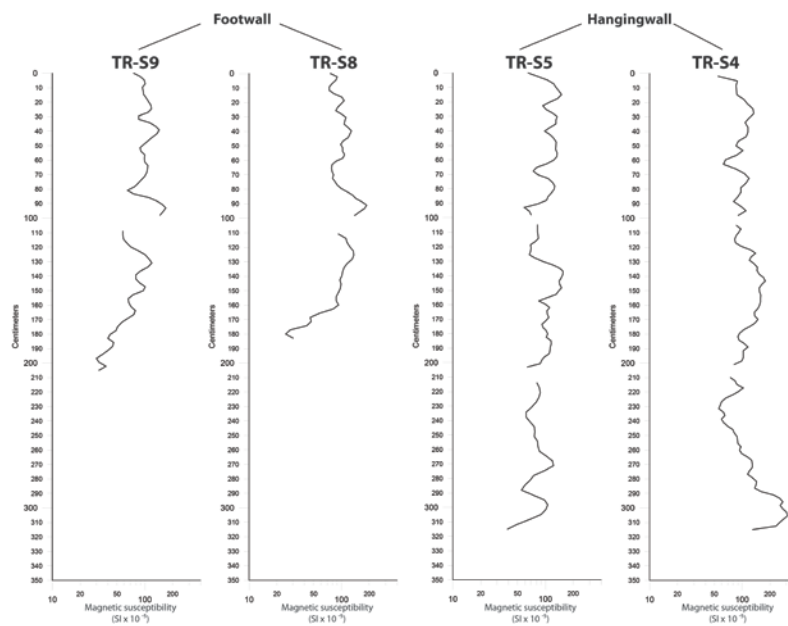


Figure 7.3 - Magnetic susceptibility logs for cores TR-S9 - TR-S8 (footwall sector) and TR-S5 - TR-S4 (hangingwall sector).

We then opened the four cores in order to perform a conventional stratigraphic description and to analyze the cored deposits with the other sensors mounted on the MSCL-S. Unfortunately, the sediments characteristics (the lack of a sufficient amount of matrix and the presence of pebbles up to cm 5 in diameter and coarse deposits, see figure 7.4 prevented to perform a conventional stratigraphic correlation to be done and the other petrophysical properties to be acquired along the entire length of the cores.



Figure 7.4 – Split sections of cores TR-S9 and TR-S4 showing the presence of coarse sediments and pebbles.

In the previous experiment performed in Southern Italy (Improta et al., 2010) we learned that in continental environments the magnetic susceptibility measurements can be highly informative when a significant amount of volcanic material is included in the deposits. Thus, taking into account the abundance of tephra layers embedded in some of the Quaternary deposits found in our study area, we used the magnetic susceptibility signals with the aim to reproduce the stratigraphy of the trench and the deformation observed at Mo'Tretteca site by means of paleoseismological investigations.

We thus carefully inspected the four magnetic susceptibility logs obtained with the loop sensor in order to identify characteristic patterns of the signal, as well as single prominent peaks and troughs that could be correlated between cores.

Overall, we can note that the logs present comparable trends among each pair of “twin” cores drilled in the footwall (TR-S9 and TR-S8) and in the hangingwall (TR-S5 and TR-S4), respectively.

As a first step we identified the main trends that dominate the magnetic susceptibility signals, (red bold lines in figure 7.5) and then, refining our observations, we identified 13 homologous points between cores TR-S9 and TR-S8 and 15 homologous points between cores TR-S5 and TR-S4.

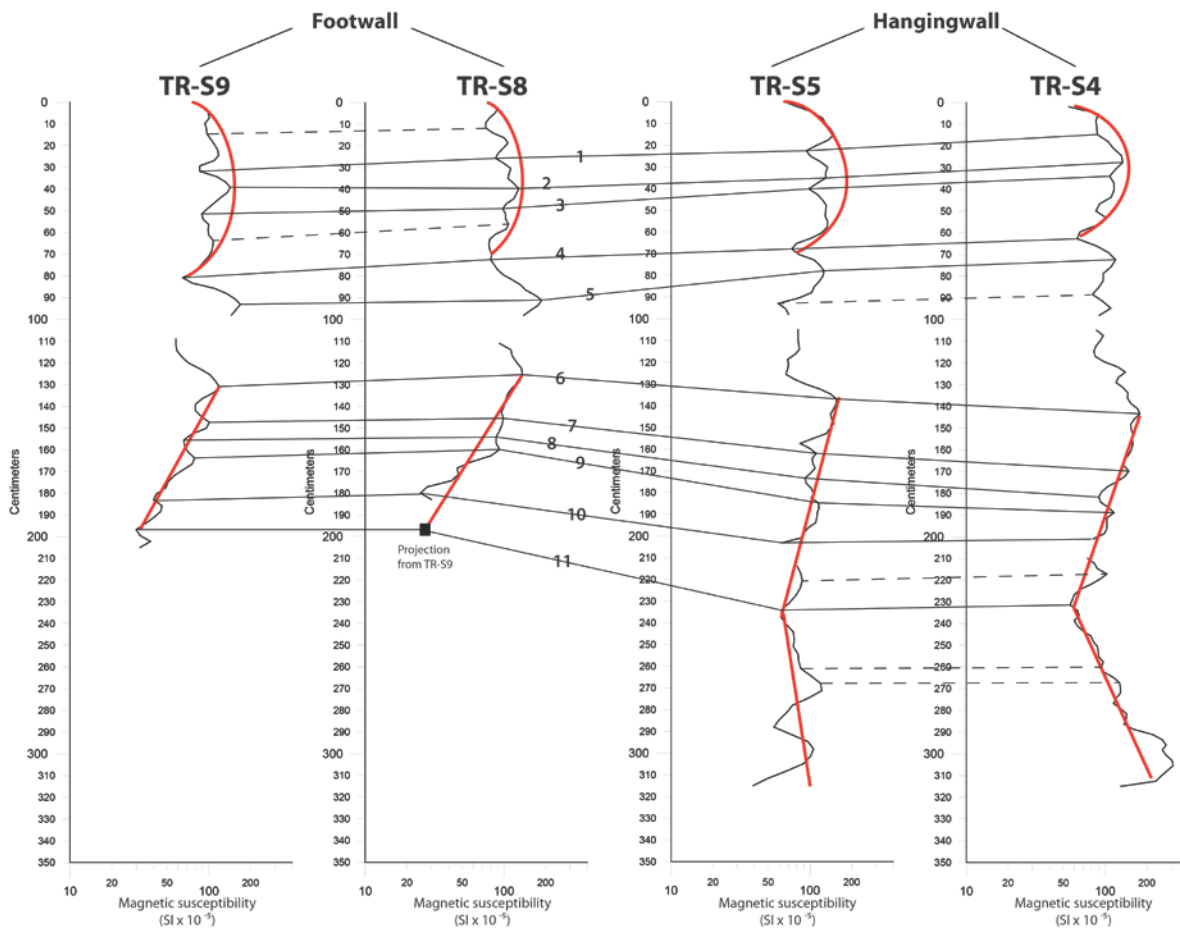


Figure 7.5 – Magnetic susceptibility logs for cores TR-S9, TR-S8, TR-S5 and TR-S4 with main trends of the signals (red solid lines). Correlated piercing points are represented by black solid lines (correlations recognizable between each pair of “twin” cores and between the footwall and hangingwall sector) and by black dotted lines (correlations recognizable only between each pair of “twin” cores).

The overall similarity between cores TR-S9 – TR-S8 and TR-S5 – TR-S4, respectively, is evident from the generally horizontal correlation lines between each pair of piercing points of the two “twin” cores (figure 7.5).

We then measured the vertical offset between each pair of piercing points of the two “twin” cores and plotted these values versus depth (figure 7.6). As we can expect, the vertical offset values are quite aligned along a straight line, suggesting no internal deformation in the footwall and hangingwall areas.

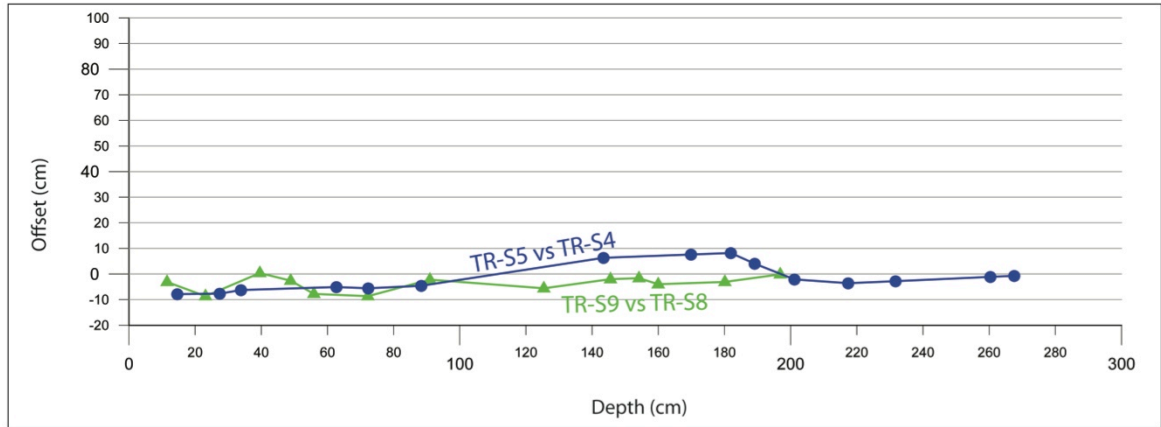


Figure 7.6 – Vertical offset versus depth plot for footwall (TR-S9 and TR-S8) and hangingwall cores (TR-S5 and TR-S4).

After that, we started a careful inspection and comparison of the cores across the fault zone, trying to identify as many as possible homologous points to better constrain the correlation across the fault zone. As a result, we recognized 11 possible homologous points between TR-S9 and TR-S8 cores in the footwall and TR-S5 and TR-S4 cores in the hangingwall, respectively (figure 7.5).

Due to technical problems during drilling, the signal of core TR-S8 does not reach the same depth of the “twin” TR-S9 core, and it was thus not possible to precisely identify the last homologous point between cores TR-S9 and TR-S8. Taking into account the general similarity between the two signals, we extrapolated the position of the last piercing point in core TR-S8, projecting it from core TR-S9.

Remarkably, if we look at the pattern of the resulting high-resolution correlations between the footwall and hangingwall sector, we note a clear change in the angle of the correlation lines.

This pattern reflects a downward increment of the difference in depth of the homologous points between core TR-S5 with respect to core TR-S8 across the fault. This implies an increment of the deformation with depth (figure 7.5).

In order to better define the trend of the deformation at depth, we measured the vertical offset shown by all the pairs of homologous points and plotted the resulting values versus TR-S5 depth (figure 7.7).

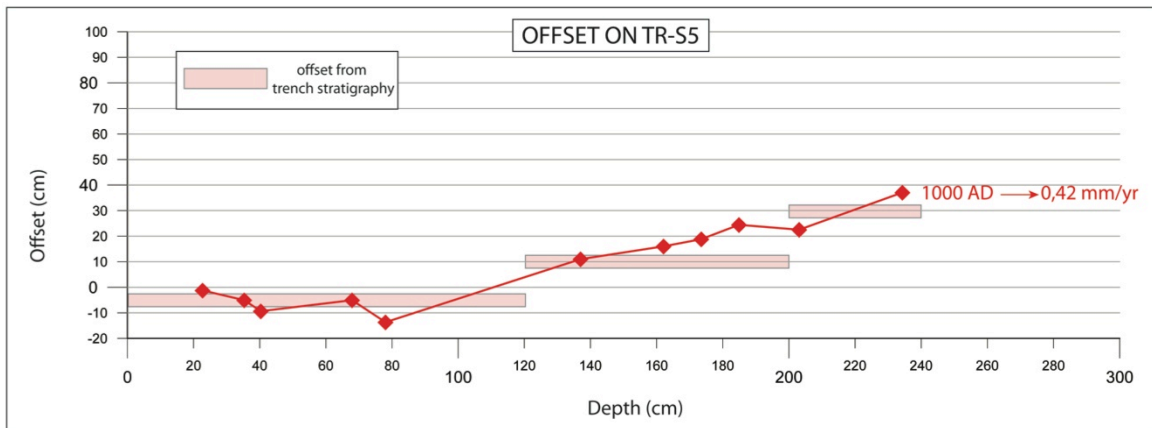


Figure 7.7 - Vertical offset versus depth for TR-S5 core

Figure 7.7 shows the distribution of the vertical offset for TR-S5 core measured by petrophysical logging (red solid line) compared with conventional trench stratigraphic analysis at the same investigation depth (pink boxes).

As a first order consideration, we confirm an increasing vertical offset with depth for both the trench stratigraphy and the petrophysical correlations plots. We can interpret this vertical offset distribution as due to the accumulation of the deformation through time along the fault splay. From figure 7.7 the sediments of the hangingwall at a depth of 2.4 m show a cumulative displacement of 0.42 m that is in good agreement with the trench observations.

In particular, the offset versus depth pattern derived from trench analysis shows a staircase pattern, outlining three different groups of deposits characterized by a well-defined offset (pink boxes in figure 7.7). This vertical offset distribution is due to individual events of displacements able to produce repeated vertical separations at the surface of ~0.15-0.2 m.

Looking at the vertical offset distribution resulting from petrophysical correlations (red solid line in figure 7.7) the increasing offset with depth is clear, however, in this case, is not possible to recognize individual events of deformation. This limitation is likely due to the limited resolution of the petrophysical correlations with such small displacement increments.

Taking into account the total amount of vertical offset measured (0.42 m) by means of high-resolution petrophysical correlations and divide it by the average age of the deposits obtained by means of ^{14}C dating (~1000 years - see Chapter 5 - Mo'Tretteca site), we can estimate a vertical slip-rate of 0.42 mm/yr.

7.2.3 Fossa site

We performed another test of the high-resolution petrophysical correlation method at the Fossa site, located on the western side of the Middle Aterno basin, along the north-east dipping Monticchio-Fossa fault (figure 7.8).

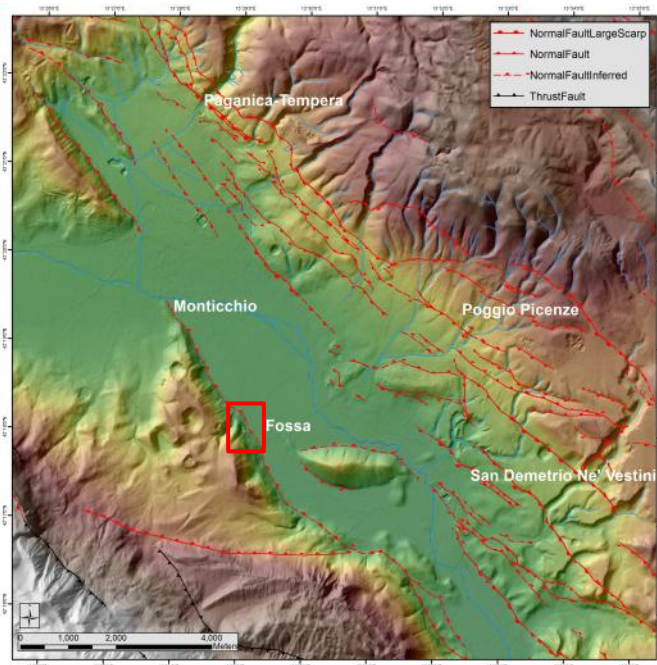


Figure 7.8 – Large-scale view of the Middle Aterno basin showing the location of the Fossa site (red box).

At this site an artificial excavation across the scarp exposed part of the fault zone in unconsolidated colluvial and slope wash deposits. Here, just after the 2009 L'Aquila mainshock, newly formed open cracks without appreciable vertical displacement were observed along pre-existing fault planes. Conventional stratigraphic logging revealed evidence of a constant stratigraphic dip-slip paleo-offset of ~ 0.22 m, with NE-side down and along the main fault plane (figure 7.9). To obtain a reference age for the offset sediments, we dated two samples at this site by means of ^{14}C : Sample 4A yielded an age of 30490-30070BP whereas Sample 9A 5660-5520BC.

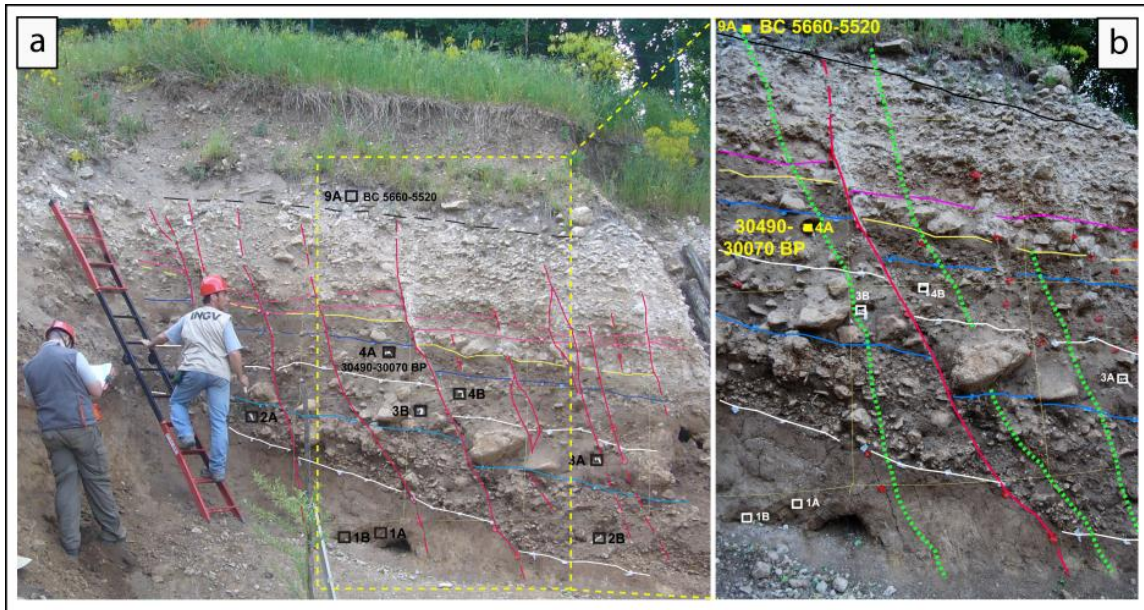


Figure 7.9 – Stratigraphic log of the Fossa site wall (a) and (b) traces of the magnetic susceptibility measurements performed directly on wall (green dotted lines).

As coring was impractical at this site due to the characteristics of the deposits (presence of cobbles and boulders within coarse to fine matrix), we decided to test the high-resolution petrophysical correlation approach by performing the magnetic susceptibility measurements directly on wall, using a hand-held Bartington MS2E point sensor.

Magnetic susceptibility measurements on the wall were collected on both sides of the main fault at a centimetric scale (2 cm interval between each measurement) positioning the sensor directly on the silty-sandy matrix (figure 7.10). We carefully choose our measurements paths on the footwall and hangingwall sector (green dotted line in figure 7.9) in order to avoid the coarser deposits to be measured. We performed two overlapping measurements on the hangingwall, due to the presence of a boulder impeding the sensor to work properly.



Figure 7.10 - Bartington MS2E point sensor performing magnetic susceptibility measurements directly on wall.

The resulting measurements are reported in the magnetic susceptibility logs of figure 7.11 (we merged the hangingwall sector signals obtaining a synthetic log). We used the same procedure of Mo'Tretteca site and recognized 20 piercing points between the footwall and the hangingwall signal.

The pattern of the obtained high-resolution correlations between the footwall and hangingwall sector does not shows a significant variation in the angle of the correlation lines. This behavior suggests the presence of a constant offset produced by a single deformational event affecting the whole exposed stratigraphy.

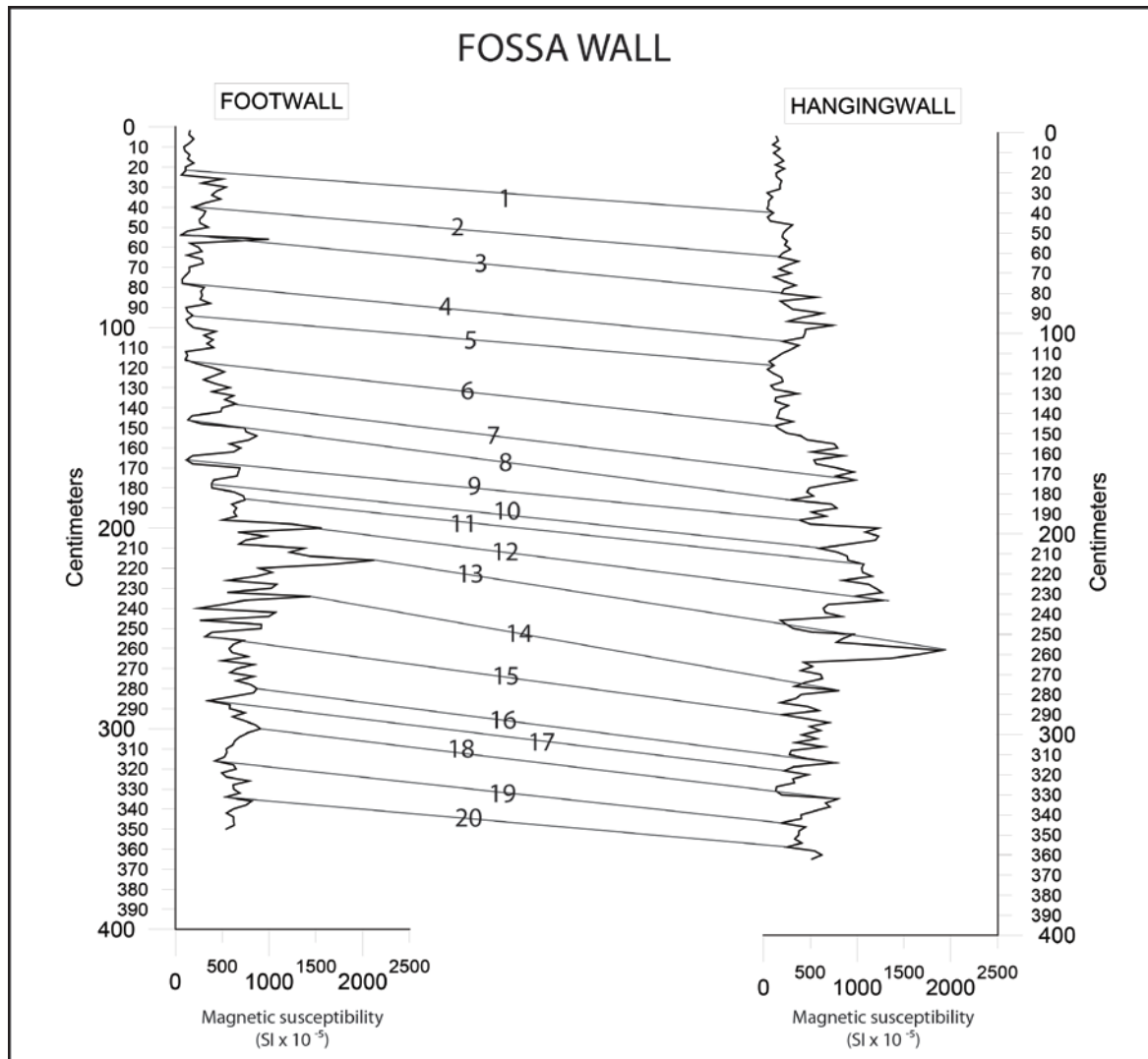


Figure 7.11 - Magnetic susceptibility logs for the footwall and hangingwall sectors at Fossa site. Correlated piercing points are represented by black solid lines.

We then measured the vertical offset of all the pairs of homologous points and corrected these values taking into account the dip of the strata, which showed a different inclination between the top and the bottom section of the exposed wall.

The plot of the vertical offset values obtained by high-resolution petrophysical correlations versus depth is shown in figure 7.12 (red solid line).

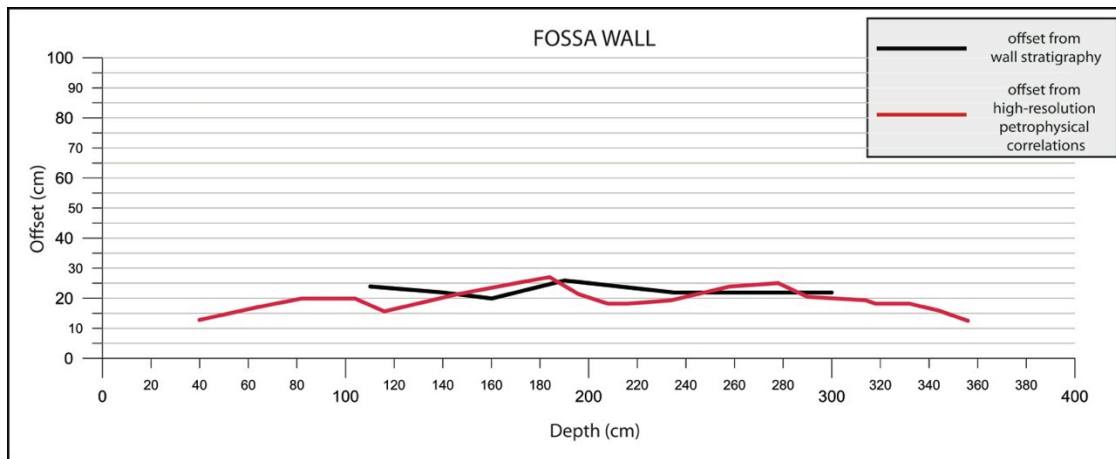


Figure 7.12 – Comparison of the vertical offset versus depth plots obtained by means of stratigraphic analysis (black line) and high-resolution petrophysical correlations (red line).

Figure 7.12 also reports the plot of the offset values obtained by means of conventional stratigraphic logging on the wall (black solid line). A comparison between the two lines highlights that the high-resolution measured offset (average 20 cm) is consistent with the stratigraphic offset (average 22 cm). The magnetic susceptibility measurements were thus effective in reproducing the stratigraphy exposed at this site, with a minimum variability (± 5 cm from ~ 110 cm to ~ 300 cm depth) with respect to the offsets measured with a conventional stratigraphic approach.

7.3 Electrical resistivity tomography

During our field investigations, we also selected six sites suitable for a high-resolution electrical resistivity tomography (ERT) campaign. The ERT surveys were performed along the PSDFS in order to complement the information acquired by means of geomorphological and geological investigations, focusing our efforts on confirming the tectonic nature of previously recognized morphological scarps, calculating the associated fault throws by including also subsurface data, and select new sites for paleoseismological trenching/coring.

7.3.1 Method

ERT is a relatively low cost, noninvasive and widely applied geophysical technique for obtaining 2D high-resolution images of the resistivity subsurface distribution from electrical measurements made on the ground surface.

This near surface imaging technique is effective in detecting active faults and estimating the vertical displacement in Quaternary deposits (e.g. Storz et al., 2000; Suzuki et al., 2000; Demanet et al., 2001; Caputo et al., 2003; Nguyen et al., 2003; Wise et al., 2003; Nguyen et al., 2005).

It consists in transmitting an alternating electrical current into the subsurface via two potential electrodes and in measuring the resulting potential difference ΔV

between two other electrodes. The fundamental physical law used in resistivity surveys is Ohm's Law that governs the flow of current in the ground. The equation for Ohm's Law in vector form for current flow in a continuous medium is given by:

$$J = \sigma E$$

where σ is the conductivity of the medium, J is the current density and E is the electric field intensity.

The apparent resistivity is given by the following relationship:

$$\rho = K \frac{\Delta V}{I}$$

with K being a geometrical factor which only depends on electrode position. The apparent resistivity ρ is the ratio of potential obtained in situ with a specific array and a specific injected current by the potential which will be obtained with the same array and current for a homogeneous and isotropic medium of 1 Ωm resistivity.

The apparent resistivity measurements give information about resistivity for a medium whose volume is proportional to the electrode spacing. It follows that the larger the electrode spacing is, the higher the investigated volume. Several parameters influence electrical resistivity: water content, temperature, particle size, ionic content, and porosity, among many others.

From a technical point of view, we carried out ERT investigations using a Syscal R2 resistivity meter (Iris instruments), coupled with a multielectrode acquisition system (64 electrodes). We performed eight ERT profiles at six sites, setting different array configurations (Wenner and Dipole-Dipole) and electrode spacing, depending on the desired maximum depth of investigation and considering the sensitivity of the array to the vertical and horizontal changes in the subsurface resistivity, the horizontal data coverage and the noise level (figure 7.13 and table 7.1).

In general, the Wenner array configuration is sensitive in resolving vertical changes in the subsurface resistivity but relatively poor in detecting horizontal changes.

Conversely, the dipole-dipole array is most sensitive to horizontal changes in resistivity, but relatively insensitive to vertical changes in the resistivity.

Moreover, when compared to the Wenner array, the dipole-dipole configuration has a shallower depth of investigation.

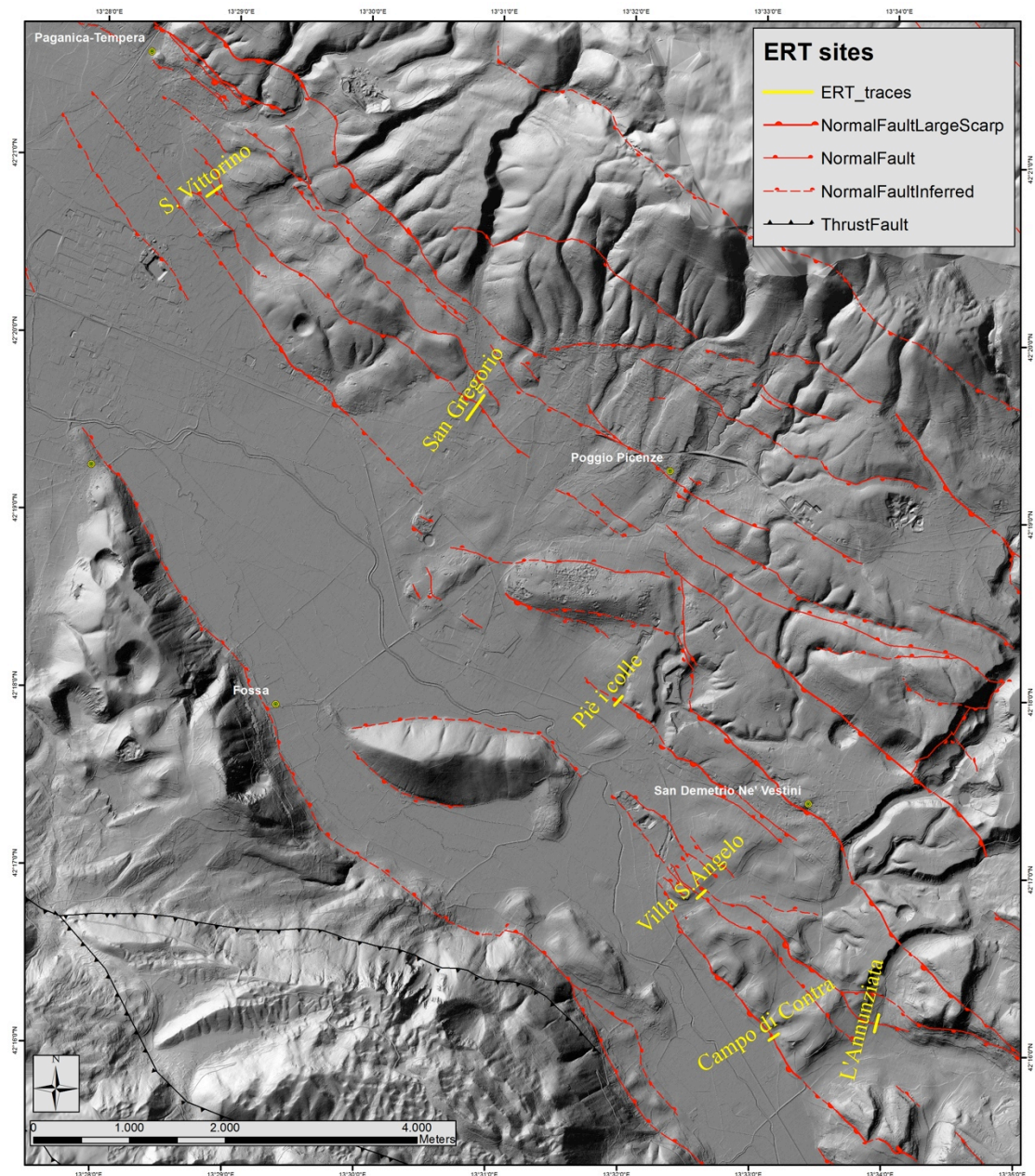


Figure 7.13 – Location of the Electrical Resistivity Tomography (ERT) surveys performed along the PSDFS.

Site	Array configuration	Electrode spacing (m)	Length (m)
San Gregorio	Wenner	5	320
L'Annunziata	Wenner Dipole-dipole	3 2	192 128
San Vittorino	Wenner Dipole-dipole	3 2	192 128
Pie' i colle	Wenner	2	128
Villa Sant'Angelo	Wenner	2	128
Campo di Contra	Dipole-dipole	2	128

Table 7.1 – Electrical Resistivity Tomography (ERT) configurations.

The system automatically performed the pre-defined sets of measurements and provided direct reading of injected current, potential difference and electrode location. In order to obtain a resistivity image from apparent resistivity data it was necessary to carry out an inversion that produced a model (a spatially varying distribution of resistivity) that gave an “acceptable” fit to the data and satisfied any other prescribed constraints. The Wenner and Dipole-Dipole ERT data were inverted using the RES2DINV software, a completely automatic program that uses the smoothness-constrained least-squares inversion technique (Loke et al. 2003) to produce a 2D model of the subsurface from the apparent resistivity data.

7.3.2 Results

In the following section each ERT profile will be briefly described, highlighting its relative contribution to the interpretation of the nature of the geomorphological features observed at the surface and/or to the estimation of fault throw. Even if we were aware of the fact that resistivity values can be extremely variable, it was possible to tentatively associate resistivity values with main lithostratigraphic units thanks to the data gathered through field geological investigations and exploratory boreholes. High resistivity values were in general associated with the presence of limestone bedrock or calcium-carbonate conglomerates and gravels, while low-resistivity values should correspond to fine-grained, silty-sandy eluvial, colluvial and alluvial deposits.

7.3.3 San Vittorino site

Geomorphological analysis at San Vittorino revealed the presence of a subtle NW-SE trending, SW facing morphological scarp (figure 7.14) within a graben-like structure. Moreover, the small morphological scarp, being in line with a clearly identifiable fault-trace to the SE, displays a high potential for a tectonic origin.

In order to verify the nature of the morphological scarp (fault scarp vs. erosional scarp) and to derive a possible throw associated with the activity of the tectonic lineament, we performed two ERT surveys with different configurations.



Figure 7.14 - overview of the San Vittorino site with the subtle morphological scarp (at the transition between the green and brown fields (red arrows). View is toward the WSW).

As a first step, we performed an ERT profile with a Wenner-type array configuration, targeting a maximum investigation depth of ~30 m and crossing the abovementioned morphological scarp approximately between 60 and 90 m distance (figure 7.15 a).

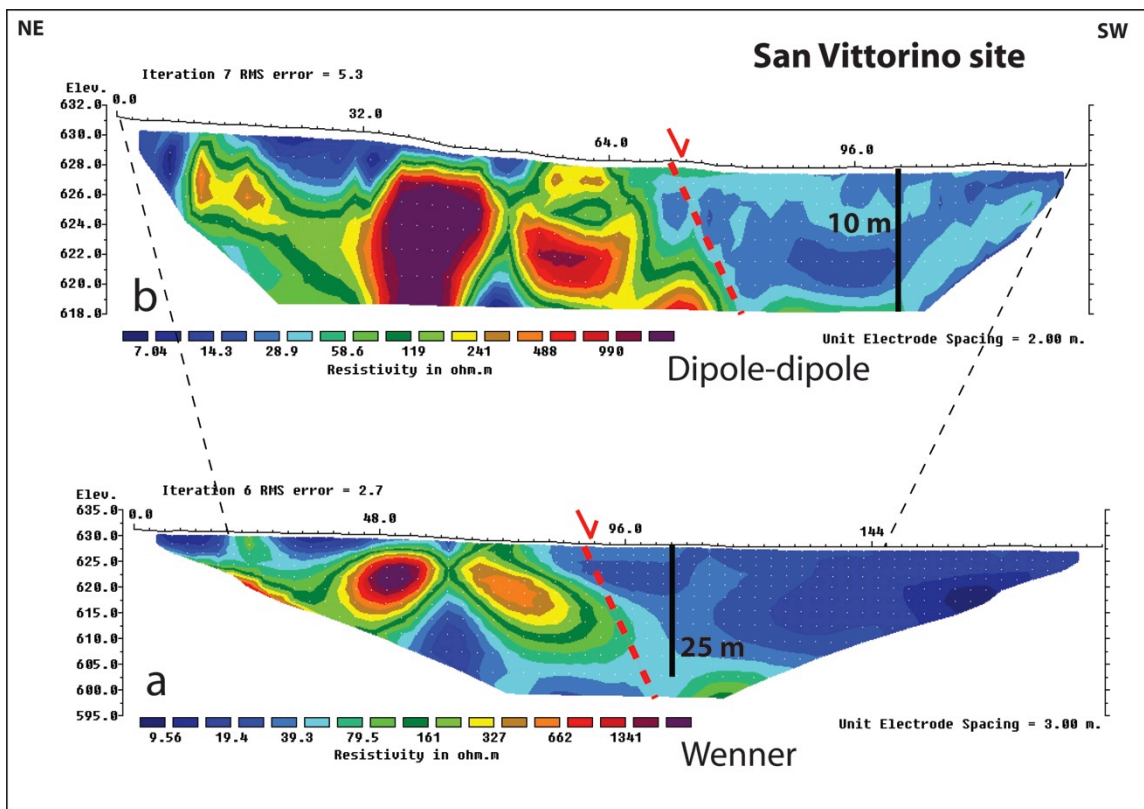


Figure 7.15 – ERT profiles performed at San Vittorino site.

This Wenner survey was effective in highlighting a resistivity pattern characterized by a lateral resistivity contrast (red dotted line in figure 7.15a) and in locating a high-resolution ERT performed using a dipole-dipole array aimed at investigating the same feature with a smaller investigation depth (~ 10 m) but an improved spatial resolution.

The major feature displayed by the high-resolution D-D ERT (figure 7.15b) is a sharp lateral variation of the resistivity, with higher values found in the presumed fault footwall and a decrement in the resistivity values observed in the presumed fault hangingwall.

Taking into account the results of the ERTs at this site, we can confirm the presence of a tectonic lineament (red dotted line in figure 7.15a-b) juxtaposing a high-resistivity body (gravels and conglomerates) in the footwall with low-resistivity deposits in the hangingwall (eluvial-colluvial deposits). Moreover, the ERT profiles gathered information about the displacement associated with this fault. Because the high-resistivity values found in the footwall are not visible at the deeper part of the hangingwall, and considering the normal faulting style of the structure, the correlative high-resistivity deposits are expected to be at a greater depth. Therefore, a minimum throw value for this fault splay of ~ 25 m can be estimated (black bar in figure 7.15a-b).

7.3.4 Villa S. Angelo site

We performed an ERT survey at Villa Sant'Angelo site in order to confirm the tectonic nature of a NE-facing scarp (antithetic to the main faults) identified by means of geomorphological investigations.

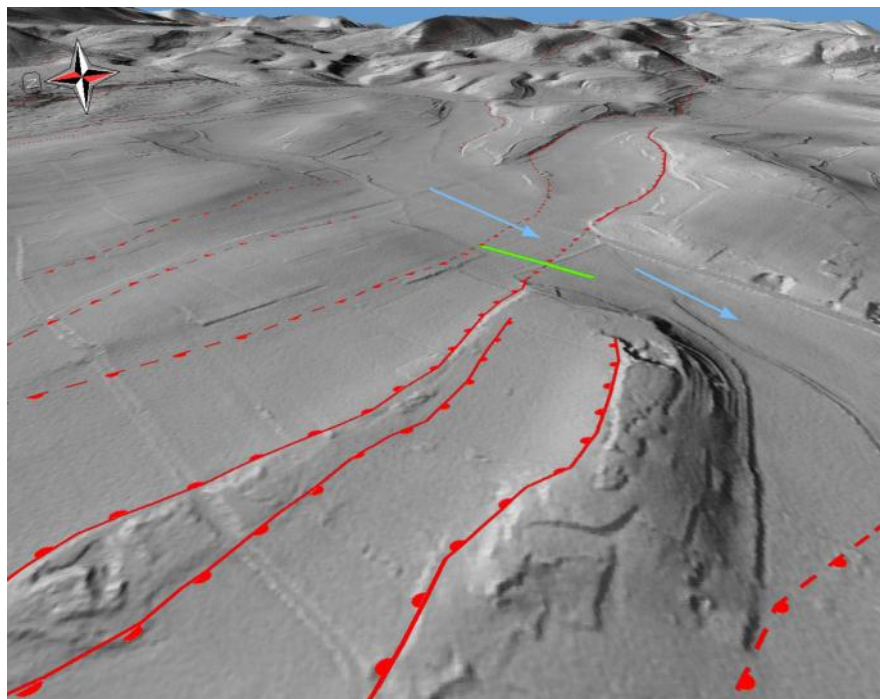


Figure 7.16 – overview of the Villa Sant’ Angelo site. The green bar represents the ERT profile (128 m-long); sky-blue arrows indicate main drainage direction.

This morphological scarp could represent the surficial expression of an antithetic splay of the PSDFS, possibly acting like a damming structure for sediments coming from upslope (figure 7.16).

From figure 7.17 we can note that the ERT Wenner profile performed at this site was effective in detecting a fault splay and in highlighting the presence of a thin layer of low-resistivity deposits at the top of the fault hangingwall, likely associated with the presence of alluvial and colluvial fine deposits.

Moreover, the ERT profile of figure 7.17 provides information about the displacement associated with this fault: the high-resistivity values found in the footwall can be correlated with those in the hangingwall whose top is at ~5 m depth. Therefore a ~5 m throw value for this fault splay (black bar in figure 7.17) can be estimated thus representing a minimum because some footwall erosion may have occurred.

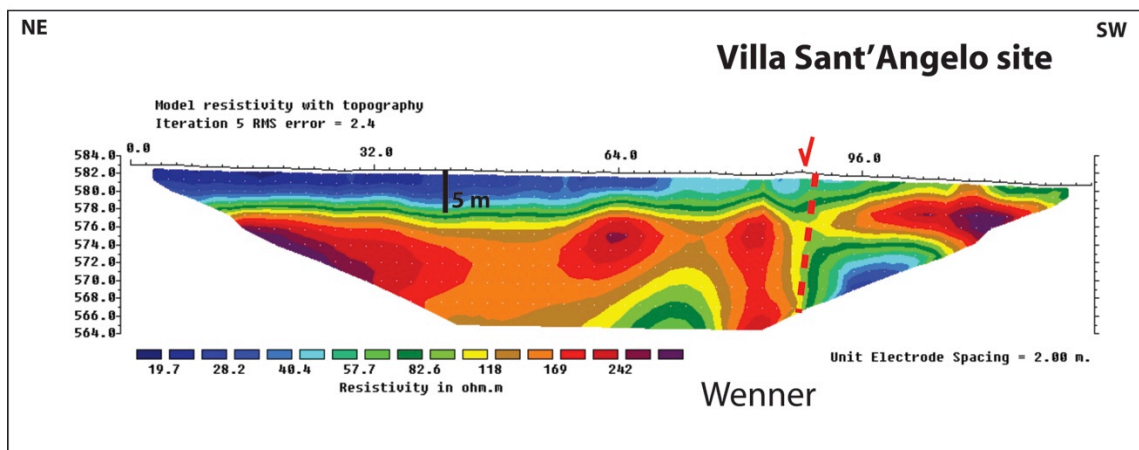


Figure 7.17 – ERT profile performed at Villa Sant’ Angelo site.

7.3.5 L’Annunziata site

At this site the main morphological features suggesting the occurrence of a fault splay are represented by the presence of a clear, partially anthropogenically modified scarp on fine alluvial and colluvial deposits, separating two well-defined morphological surfaces (figure 7.18). Interestingly, at this site a strong linear incision only localized at the footwall of the presumed fault also hints at the presence of a tectonic lineament.

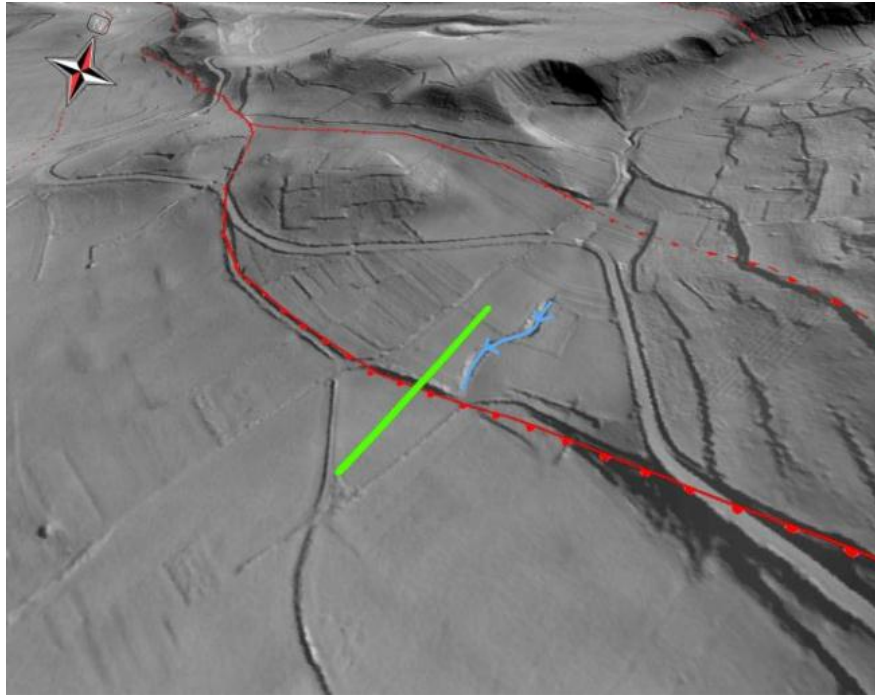


Figure 7.18 – overview of the L'Annunziata site. The green bar represents the ERT profile trace (192 m-long); sky-blue line highlights the strong drainage incision.

We performed two ERT profiles with different resolutions and investigation depth, obtaining the images showed in figure 7.19. Looking at the Dipole-Dipole ERT profile (figure 7.19b) we can note that the morphological scarp lies in correspondence of the variation of resistivity values at depth, confirming the presence of a tectonic lineament affecting the investigated deposits. However, from the Dipole-Dipole ERT profile of figure 7.19b we could not gather information about the displacement associated with this fault, mainly due to low horizontal resistivity contrast of the deposits.

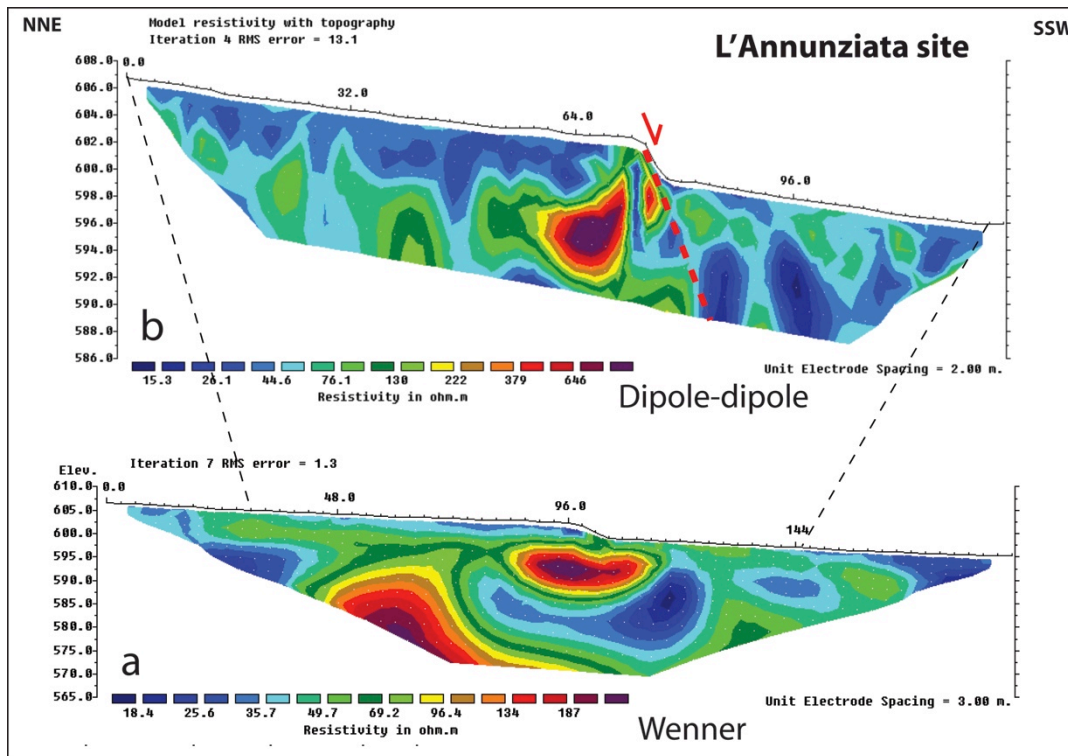


Figure 7.19 - ERT profiles performed at L'Annunziata site.

7.3.6 San Gregorio site

The overall geomorphology of this site is characterized by the presence of a NW-SE oriented limestone ridge bounded by normal faults and defining a horst-like structure. Evidence for surficial faulting at this site is mainly related to the presence of a small SW-facing scarp affecting the alluvial fan deposits dissecting the ridge and to the presence of a strong drainage incision confined between the fault traces (figure 7.20).

The ERT profile done at this site aimed principally at defining the vertical component associated with the activity of the SW-facing fault splay. We realized a more than 300m-long ERT Wenner profile, targeting a maximum depth of ~50 m. The profile started on top of the small bedrock ridge, and then run on alluvial fan deposits.

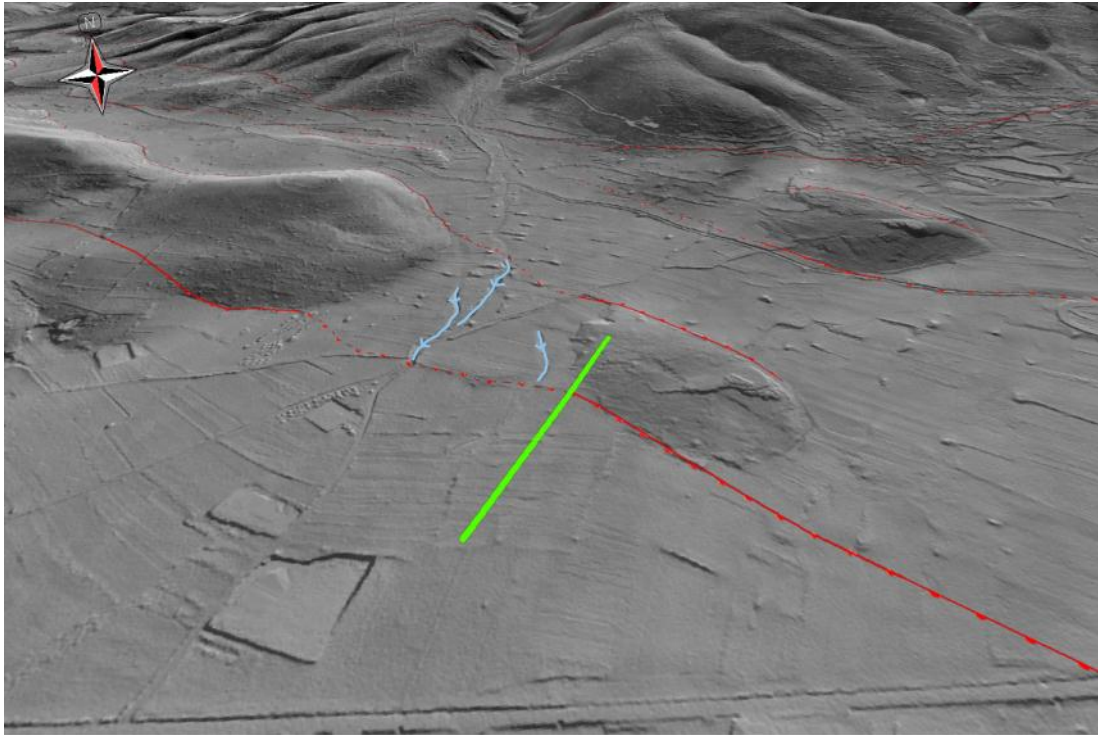


Figure 7.20 - overview of the San Gregorio site. The green bar represents the ERT profile trace (320 m-long); sky-blue line highlights the strong drainage incisions.

The main results of this investigation are presented in figure 7.21 and allowed us to confirm the tectonic nature of the surficial scarp (red dotted line). The high-resistivity body, characterized by values of more than 3500 Ωm , corresponds to the same limestone bedrock exposed at surface, while the low resistivity values are likely associated with the alluvial fan deposits.

Moreover, ERT allowed us to calculate a minimum vertical offset at this site of ~ 50 m, due to the lack of the high-resistivity body at the fault hangingwall. Taking into account a minimum throw value of ~ 10 m resulting from topographic profile number 16 (Chapter 6 and appendix D), we obtain a total minimum throw of the bedrock at this point of ~ 60 m.

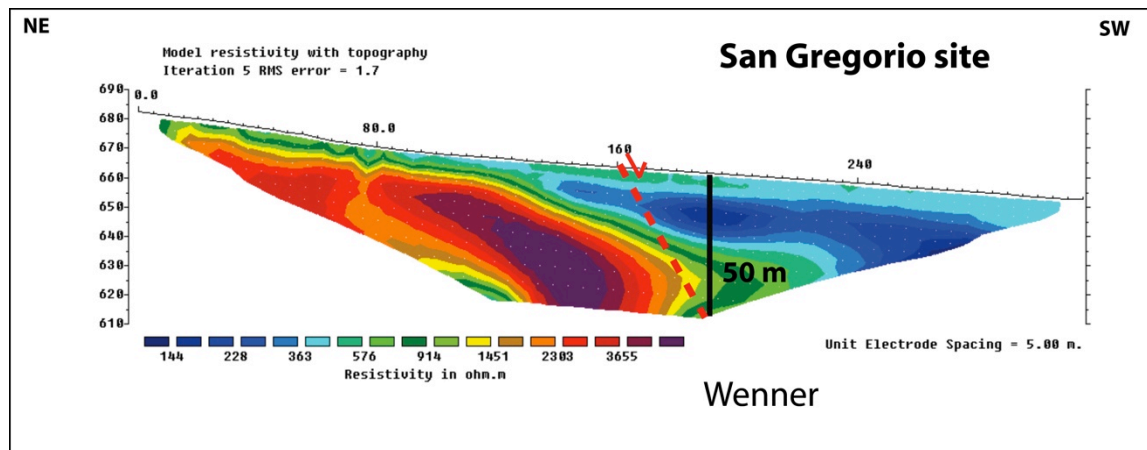


Figure 7.21 - ERT profile performed at San Gregorio site.

7.3.7 Pie' i colle site

From geomorphological and geological investigations the Pie' i colle site is characterized by the presence of a small morphological scarp (figure 7.22) lying along the lateral continuation of a well expressed fault scarp (~30 m height) affecting Middle Pleistocene alluvial deposits.



Figure.7.22 - overview of the Pie' i colle site. The red dotted line lies at the base of the small morphological scarp possibly related to a tectonic lineament. The yellow line is the ERT profile trace (128 m-long). View is toward the NE.

We performed a Wenner ERT profile aimed at verifying a possible continuation of the tectonic lineament and at calculating relative fault throw.

The results of Pie' i colle ERT are shown in figure 7.23, here a high-resistivity body at the very bottom of the NE portion of the profile is overlaid by a ~15 m thick sequence of low-resistivity deposits .

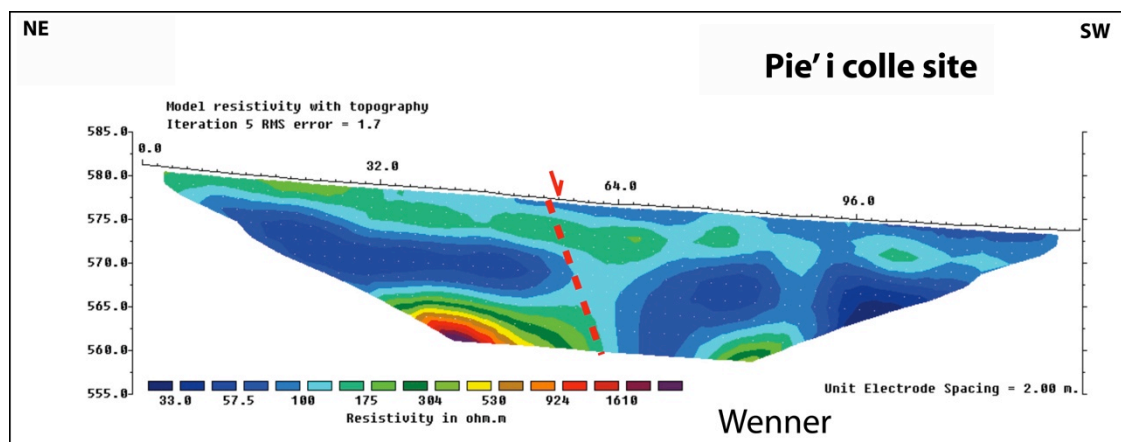


Figure 7.23 - ERT profile performed at Pie' i colle site.

The ERT survey performed at this site did not provide a clear evidence for a very shallow fault splay. We can speculate about the presence of a fault splay at larger depth if we interpret the morphological scarp observable at this site as related to the mimicking at the surface of a deeper fault with respect to the depth investigated. Due to low horizontal resistivity contrast of the deposits overlaying the high-resistivity body it is however difficult to discriminate the deformation produced by the tectonic lineament.

Another possibility is that the footwall has been eroded away by a strongly incising river, but this interpretation may be difficult to sustain due to the lack of an important drainage at this site.

7.3.8 Campo di Contra site

At Campo di Contra site we were mainly interested at verifying the presence at depth of a tectonic structure, suggested by a small morphological scarp lying at the base of the main fault escarpment at the surface (figure 7.24).

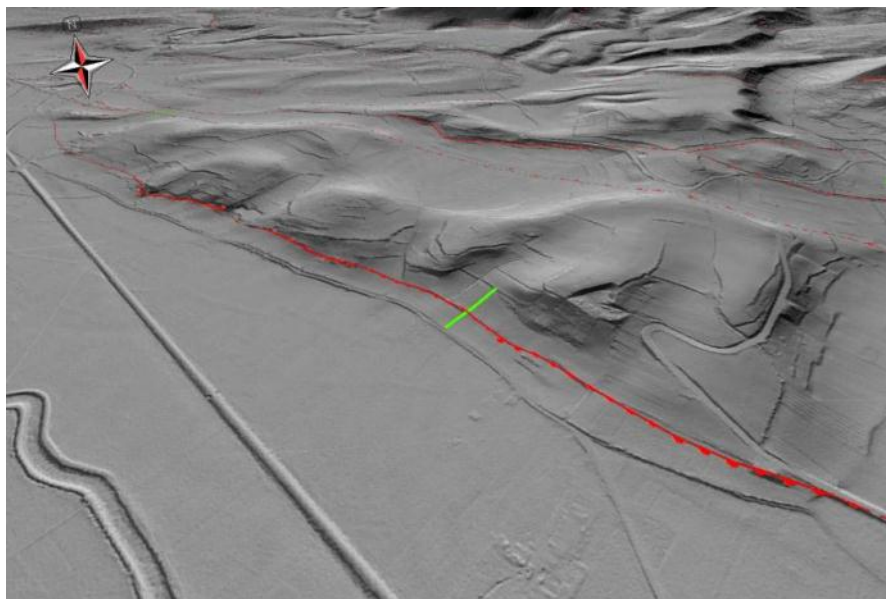


Figure 7.24 - overview of the San Gregorio site. The green bar represents the ERT profile trace (128 m-long);

We performed here an ERT profile using a Dipole-Dipole array configuration, with a target investigation depth of ~ 10 m. The ERT investigations revealed the presence of sedimentary bodies characterized by relatively small resistivity contrast and affected by three faults.

Figure 7.25 shows that the main resistivity contrasts are visible in the NE portion of the ERT profile, outlining a fault zone characterized by a graben-like structure at the base of the main fault escarpment. The resistivity pattern also suggests the presence of a synthetic fault splay in correspondence of the small morphological scarp visible at the surface.

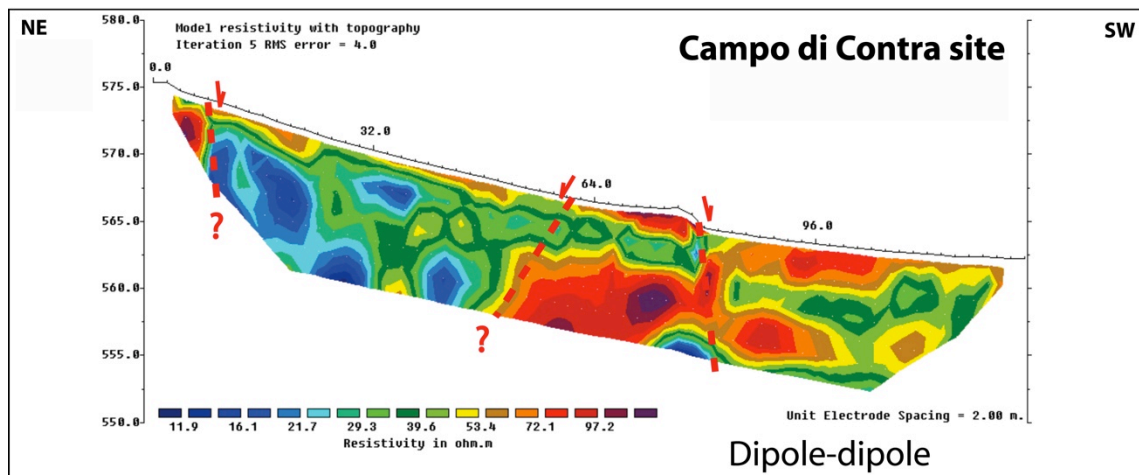


Figure 7.25 - ERT profile performed at Campo di Contra site.

This ERT profile was thus effective in providing new subsurface data about the structure of the fault zone along this fault splay. Due to low horizontal resistivity contrast of the deposits overlaying the high-resistivity body it is however difficult to define the amount of the deformation produced by the tectonic lineament at this site.

7.4 High-resolution seismic tomography

During my PhD program I had the opportunity to join a team of researchers of the Istituto Nazionale di Geofisica e Vulcanologia (INGV, Italy) during a ten-day-long experiment aimed at acquiring high-resolution shallow seismic profiles across the Middle Aterno Valley.

7.4.1 Method

High-resolution shallow seismic profiling is an effective tool in imaging near-surface fault systems and providing valuable information about shallow basin geometry (Morey and Schuster, 1999; Improta et al, 2003; Improta et al., 2010).

No commercial seismic exploration data were acquired in the epicentral area, so no reliable subsurface constraints about the basin structure were available. The seismic survey was carried out in order to image both the subsurface geometry and internal architecture of the Middle Aterno basin, as well as to estimate possible fault throws across the PSDFS.

The seismic experiment was realized through the acquisition of 5 NE-SW profiles for a total length of ~7 km, targeting the northwestern portion of the Middle Aterno basin in the Paganica – Bazzano sector (figure 7.26).

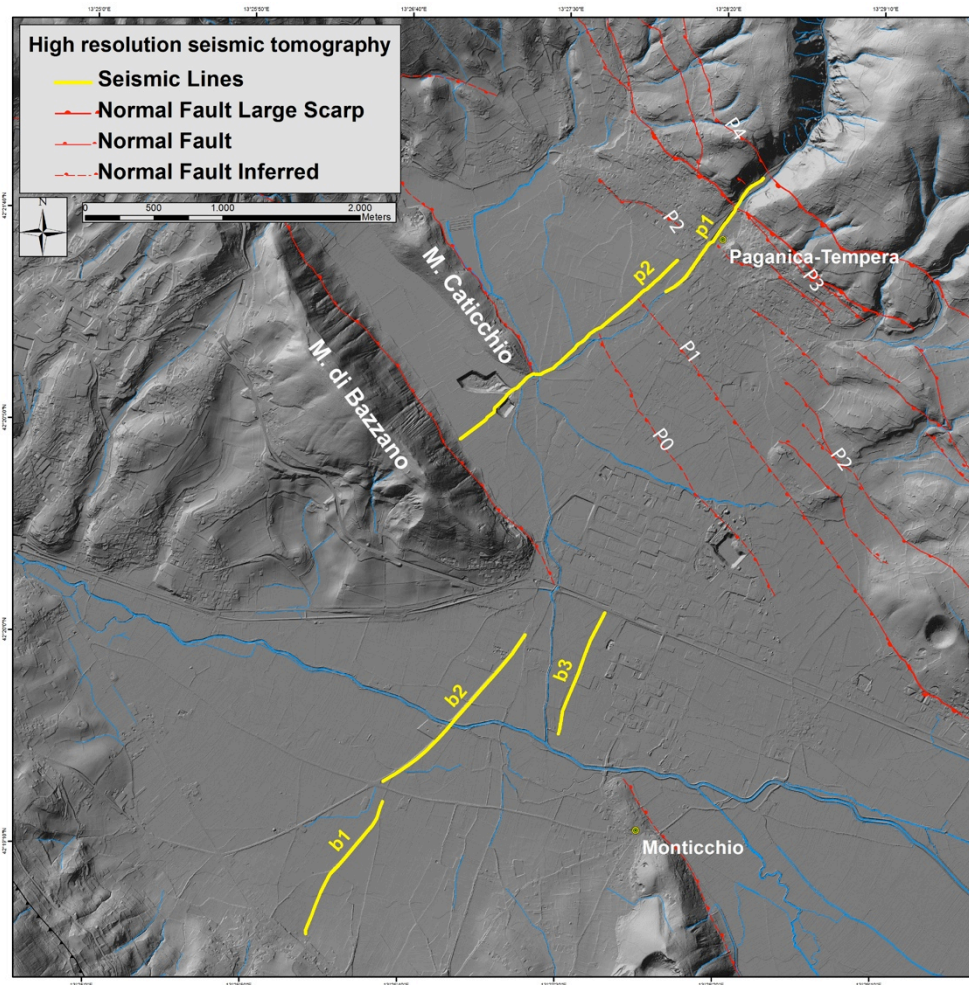


Figure 7.26 - Shaded relief topography of the Middle Aterno basin with location of the five seismic lines and main fault splays.

The survey geometry was designed based on preliminary analysis of aerial photos and geological investigations and represented the best compromise between specific geologic targets and logistic/environmental difficulties.

Specific target sites of the investigations were:

- the sector of the basin where the clearest coseismic surface ruptures were observed (profile p1);
- the hanging-wall of the PSDFS and NE-dipping antithetic splays (profile p2);
- the extensional faults bounding the Bazzano-Monticchio ridge (profile b3);
- the sector of the basin that experienced the maximum coseismic subsidence (profiles b1 and b2) (see Chapter 3).

Seismic data were collected according to the innovative dense wide aperture acquisition geometry (Operto et al., 2004), combining both seismic reflection imaging and seismic tomography techniques.

7.4.2 Results

Being a very complex work involving several researchers, picking and interpretation of the data is still ongoing, however some preliminary results are available. Figure 7.27 shows the long-wavelength Vp model for the profile Paganica 2, representative of the large-scale basin structure in the western portion of the hangingwall of the PSDFS. This profile runs for a length of ~2080 meters and ends to the SW against the eastern slope of the Bazzano ridge.

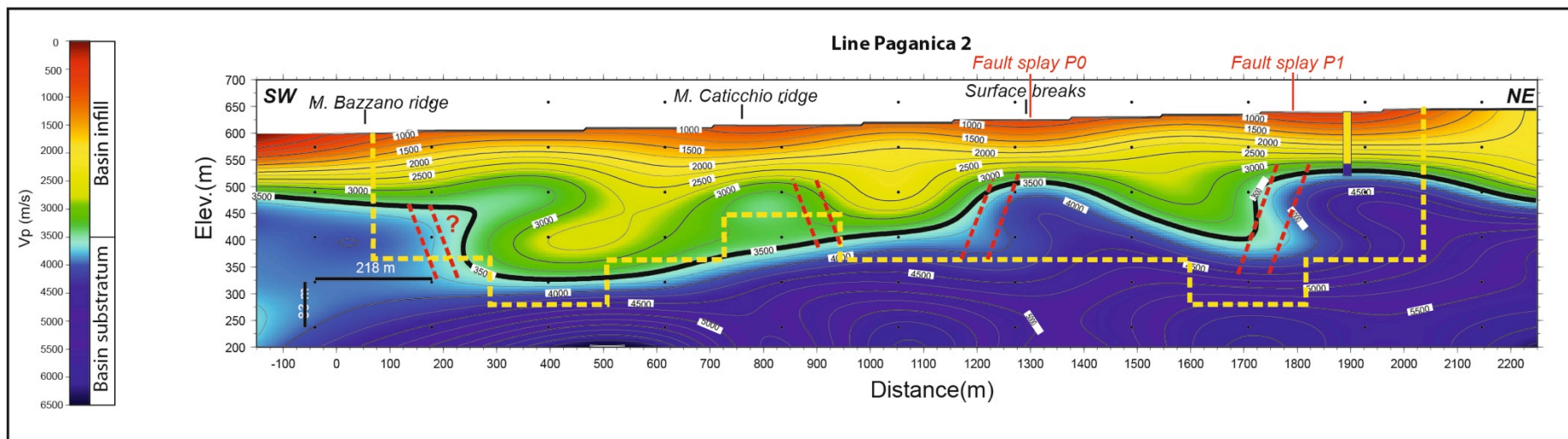


Figure 7.27 – Long wavelength Vp model of line p2. The figure also shows the location of the borehole reaching the bedrock at -78 m depth and the location of some of the discontinuous surface breaks reported in Chapter 3.

At a basin-wide scale, we note that the tomographic image (figure 7.27) shows a velocity field characterized by strong lateral V_p variations, with high-velocity ($V_p > 3250$ m/s) bumps located at ~ 800 , ~ 1300 and ~ 1900 m distance along the line.

On the basis of the analysis of ray paths of critical refractions and of the projection of the bedrock drilled at 78 m depth (id 156626 - <http://sgi1.isprambiente.it/GeoMapView/index.html>), the ~ 3500 m/s contour line (black bold line in figure 7.27) may tentatively be considered as the top of the Meso-Cenozoic basin substratum, suggesting that the basin reaches ~ 250 m depth in the PSDFS hangingwall.

The bodies characterized by $V_p < 3500$ m/s are interpreted as the Quaternary continental deposits forming the basin infill.

Moreover, the top of the basin substratum seems to be characterized by an articulated geometry: the rise of the ~ 3500 m/s contour line approximating the top of the bedrock at the SW end of the line is in agreement with the presence of the Bazzano limestone ridge at the surface, bounded by an antithetic fault. To the NW, strong lateral heterogeneities and steps (high V_p bumps located at ~ 1100 - 1300 m and ~ 1700 - 1900 m distance) may be evidence of buried SW-dipping fault splays (red dotted line in figure 7.27) of the PSDFS that juxtapose bedrock limestone against basin infill deposits. Seismic tomography provides also hints for estimating displacements along these fault splays, with throw values of ~ 100 m and ~ 150 m, respectively.

Interestingly, the surface projection of the step at ~ 1100 - 1300 m distance coincides with the occurrence of some aligned discontinuous surface ruptures (figure 7.27 – see also Chapter 3).

The subsurface geometry in this sector of the PSDFS hangingwall appears therefore to be more complicated than suspected from surface geomorphological and geological investigations likely because high sedimentation rates compared to tectonic rates. However, this complexity appears still coherent with the overall PSDFS structural setting.

Profile p1 is currently under elaboration and will not be presented in this chapter. The other profiles of the high-resolution seismic tomography investigations as well as the technical details of seismic experiment are presented in the attached article which I co-authored: “High-resolution controlled-source seismic tomography across the Middle Aterno basin in the epicentral area of the 2009, Mw 6.3, L’Aquila earthquake (central Apennines, Italy), in press on the Italian Journal of Geoscience (Appendix I).

8 Discussion

The multidisciplinary approach proposed in this thesis was designed to better define the tectonic style, geometry, kinematics and texture of the whole Paganica – San Demetrio fault system (PSDFS hereinafter), as well as to define its behavior over time and space. These results are translated into seismic fault behavior parameters and discussed in the light of the seismic hazard of this area.

8.1 Tectonic style of the PSDFS

The detailed geomorphological and geological analysis of the PSDFS, also integrated with subsurface geophysical investigations, was used to define the fault system tectonic style, arrangement, kinematics, extent, geometry and boundaries.

At a basin-wide scale, the multidisciplinary investigations highlighted the existence of a complex structural setting of the PSDFS at the surface. This is characterized by the presence of several normal parallel fault splays (i.e. overlapping strands with similar trends) frequently arranged in a quasi-fractal sequence of horsts and grabens of variable size.

Looking at the surface pattern, we can distinguish two main sectors of the PSDFS characterized by different structural arrangements (figure 8.1 and Chapter 6) and by diverse extent and age of outcropping deposits.

In the Paganica sector (northern portion of the PSDFS), the deformation is accommodated by a narrow fault zone, forming a less than 1 km-wide deformational band and controlling the basin evolution with a persistent depocenter location since Early Quaternary (~2 Ma).

In the San Demetrio sector (southern portion of the PSDFS), the structural arrangement of the fault system becomes more complex and the deformation appears to be accommodated by several tectonic structures, affecting a wider fault system with respect to the northern area. In fact, here the PSDFS opens into a set of parallel, km-spaced fault traces that exhume and dissect the Quaternary basin and produce a staircase landform with deposits progressively younger and less elevated toward the present Aterno River bed. This setting is suggestive of a progressive migration in time of the basin depocenter toward the present-day valley bottom.

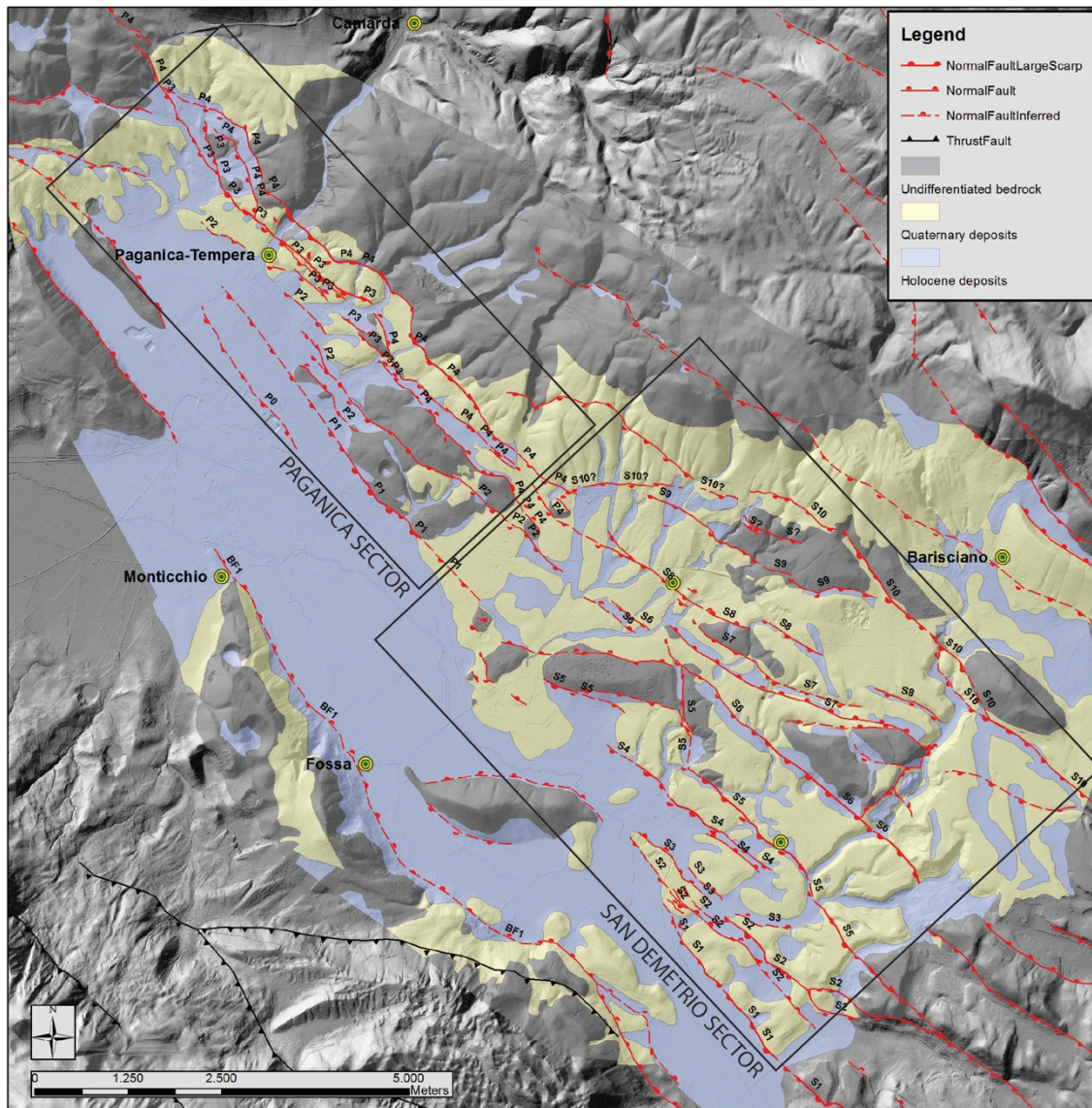


Figure 8.1 - Map of the PSDFS showing the structural arrangement of the fault system and the extent and age of outcropping Quaternary and Holocene deposits. Boxes enclose the Paganica and San Demetrio sectors.

8.2 PSDFS length

Tectonic geomorphological analysis allowed also us to define the extent of the fault system at the surface as well as a first-order hierarchy, in terms of relative contribution to the net deformation, among the numerous fault splays that characterize the morphological expression of the PSDFS.

The complexity of the fault system setting makes it difficult to define its actual extent and boundaries on the basis of classical geomorphological and structural approaches (e.g. Schwartz and Coppersmith, 1984; Burbank and Anderson, 2001). To overcome this difficulty we built up an along-strike plot of all the morphological throw values measured across the PSDFS (Chapter 6). This was done following the concept that, in individual normal faults, the deformation tends to distribute along

strike following a typical symmetric bow-shaped curve (see Chapter 2). By summing up the along-strike contribution of all the single fault splays of the PSDFS, we obtained the morphological throw graph of figure 8.2 (yellow solid line) that actually approximates a symmetric bell-shaped curve. On this basis the tips of the curve represent the fault boundaries that can be considered stationary at least for the last morphogenic phase of landform shaping (possibly up to ~2 Ma). The northern boundary is placed near the village of Collebrincioni, where a series of WNW trending, right, en echelon splays occur and may act as a structural boundary. The southern boundary is set about 3 km south of the latitude of San Demetrio n  Vestini village, and coincides with the southern edge of the Quaternary basin and with a subtle deviation of the trend of the tectonic structures with respect to the average PSDFS strike, as shown by fault splays to the south of the Ripa valley.

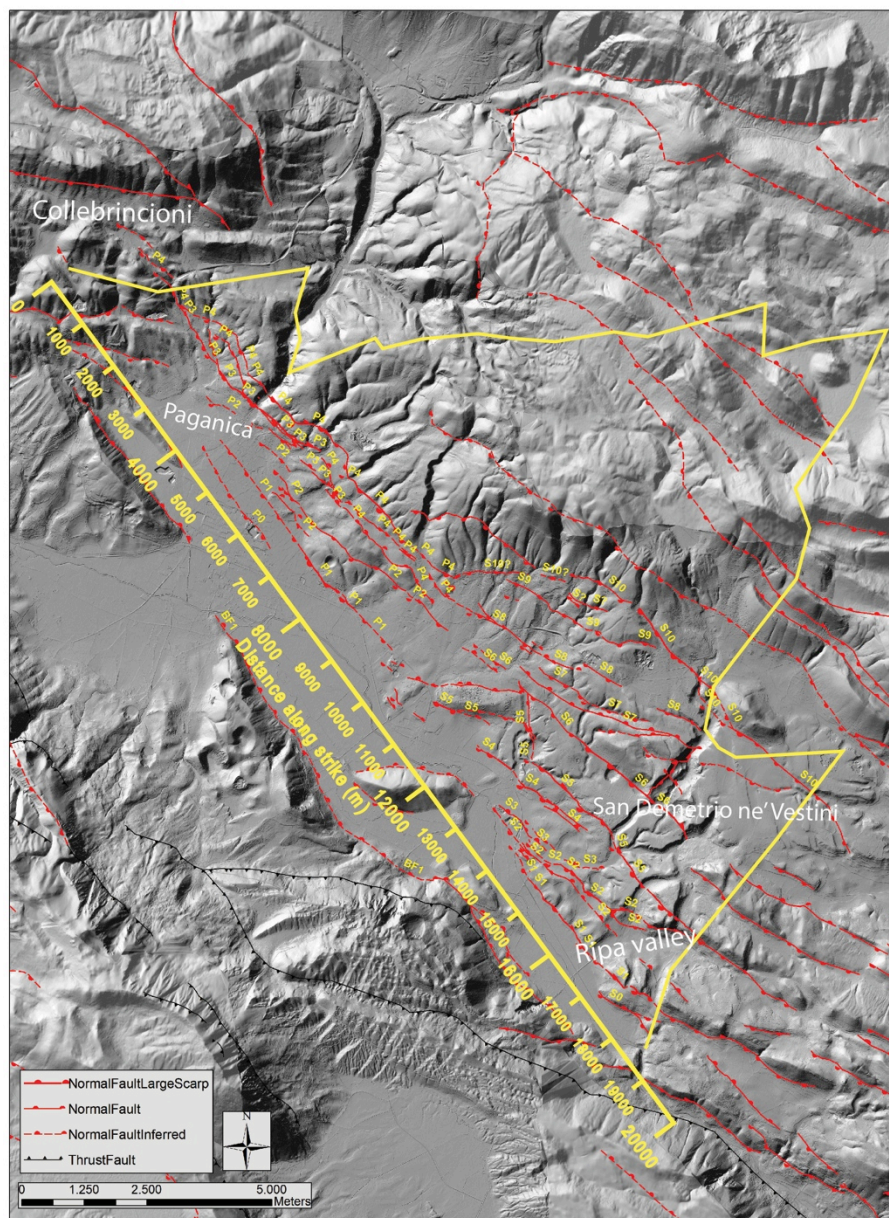


Figure 8.2 – overall length of the PSDFS as defined by the plot of the morphological throws.

Under this interpretation, the resulting overall length of the PSDFS approximates 19 km. This is in good agreement with the length of the seismogenic fault that ruptured at depth during the April 6 earthquake, as defined by coseismic seismologic and geodetic observations (from 15 to 18 km, see Chapter 3).

Primary coseismic surface ruptures observed in 2009 occurred only along a 3 km-long part of the Paganica sector and in few sparse locations along the central and northern part of the fault system. Therefore, the 19 km-long geomorphic expression of the fault cannot have been built up by repeated 2009-type earthquakes, but in the past, the system should have ruptured the surface for all its length.

Thus, larger magnitude earthquakes or earthquakes with a different and more superficial slip distribution with respect to the 2009 event, are expected on the PSDFS.

8.3 Partitioning of deformation along the PSDFS

The overall symmetric bell-shaped curve of figure 8.3 suggests a persistence of the deformation through time and for the whole length of the fault system, although partitioned across a narrow zone (Paganica sector) and a wider zone (San Demetrio sector).

The plot of figure 8.3 shows the different contribution of individual fault splays to the overall deformation across the PSDFS.

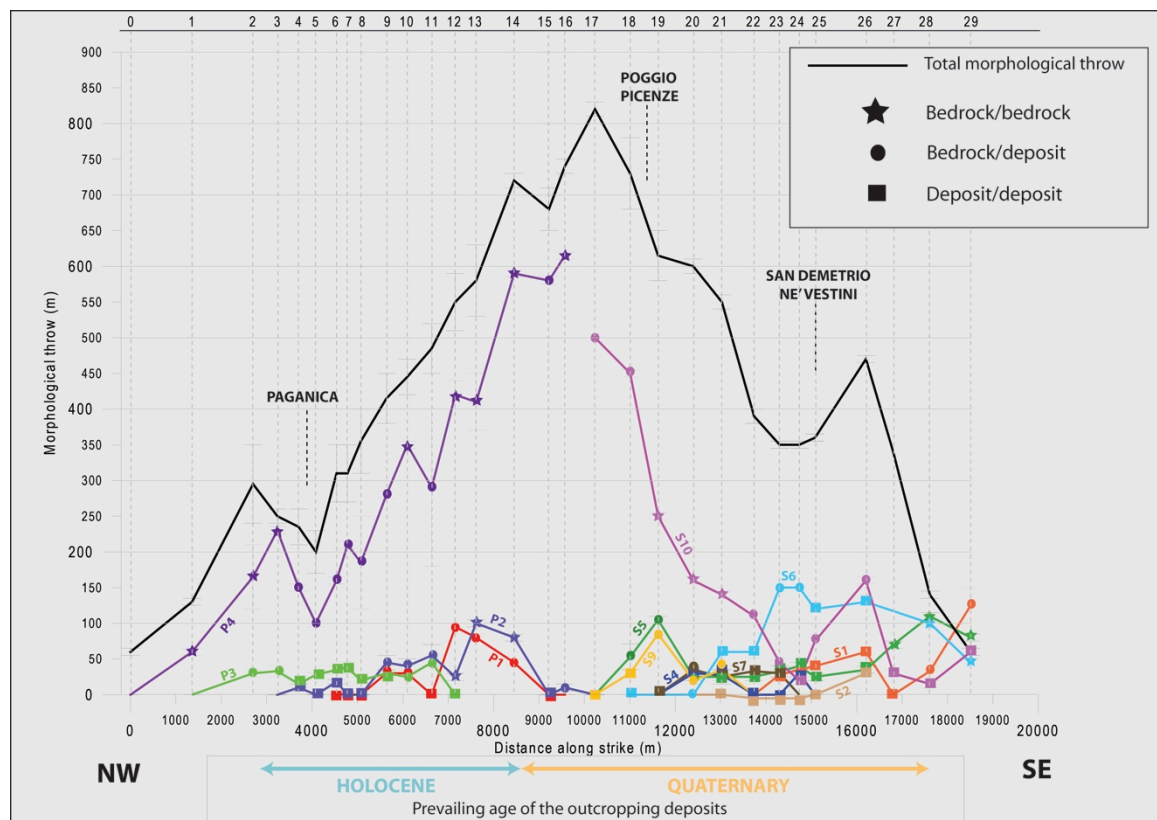


Figure 8.3 - Along-strike plot of the morphological throws measured from the topographic profiles across the PSDFS (see also Chapter 6).

Most of the deformation in the area is accommodated by the two easternmost basin-bounding fault splays (P4 and S10) that, because affect mainly the geomorphic markers carved in bedrock, cannot be dated and confidently used to define the present fault system behavior. Conversely, among the fault splays affecting mainly the Quaternary deposits (last ~2Ma), an important contribution to the overall deformation is accommodated by fault splays P3 and S6. Interestingly, these two fault splays are quite aligned in map view and share a similar prominent geomorphic expression. The lack of clear surface evidence of fault-related deformation between the two splays in the central portion of the PSDFS can be justified by the intersection with an alluvial fan that had a Late Pleistocene (ca. 27 ka – Chapter 7) strong activity that buried/eroded the missing fault scarp (see also Chapter 7 – ERT profiling at San Gregorio site).

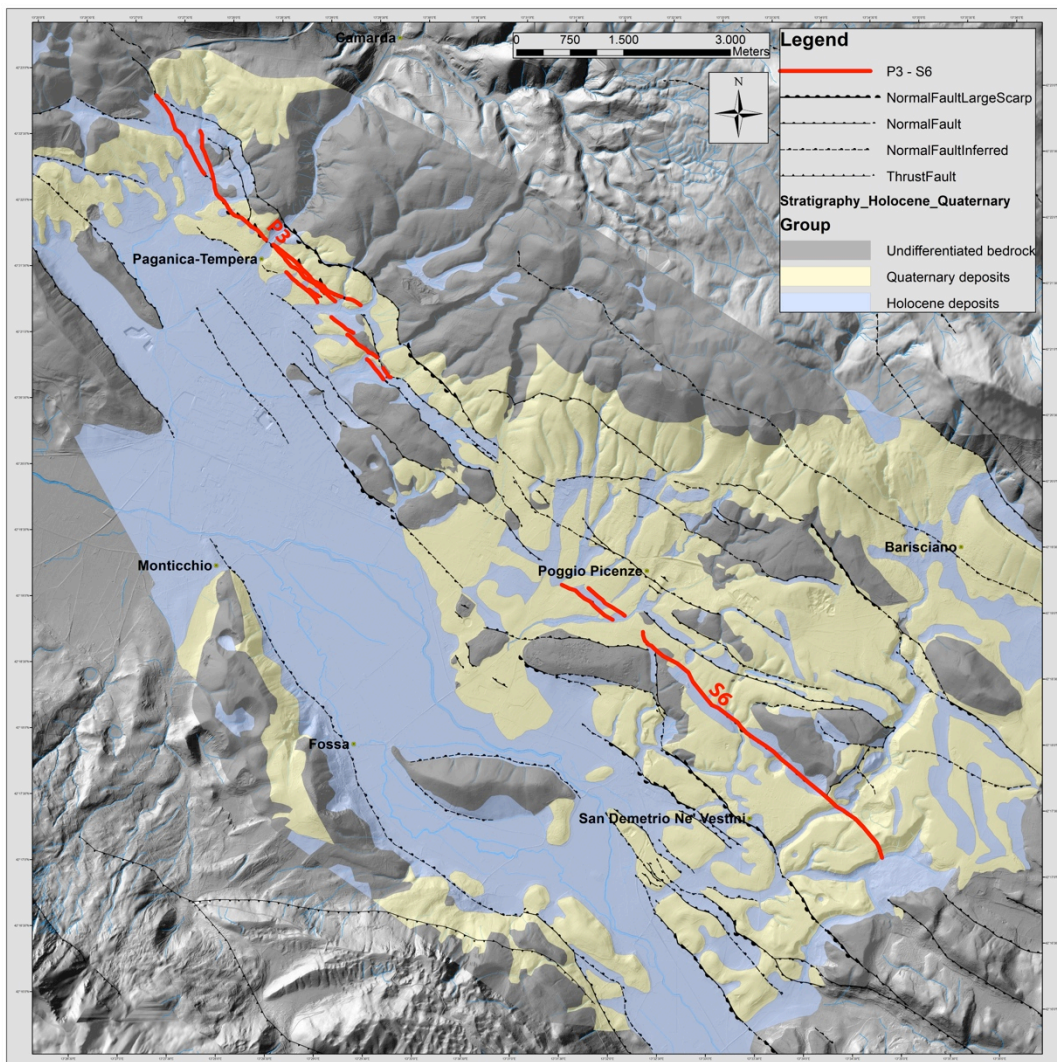


Figure 8.4 - Map of the PSDFS showing the possible linkage of fault splays P3 (to the northwest) and S6 (to the southeast).

The linkage of these two fault splays may represent the most active surface trace of the PSFDS during the Quaternary.

This hypothesis is also supported by the fact that the 3 km-long 2009 coseismic rupture occurred along fault splay P3.

However, in the Paganica sector, the high-resolution shallow seismic profiling (Chapter 7) shows the presence of two buried SW-dipping fault splays (red dotted lines in figure 8.5 and P0 and P1 in the map of figure 8.1) in the Paganica sector that involve bedrock and basin infill deposits with throw values of ~100 m and ~150 m.

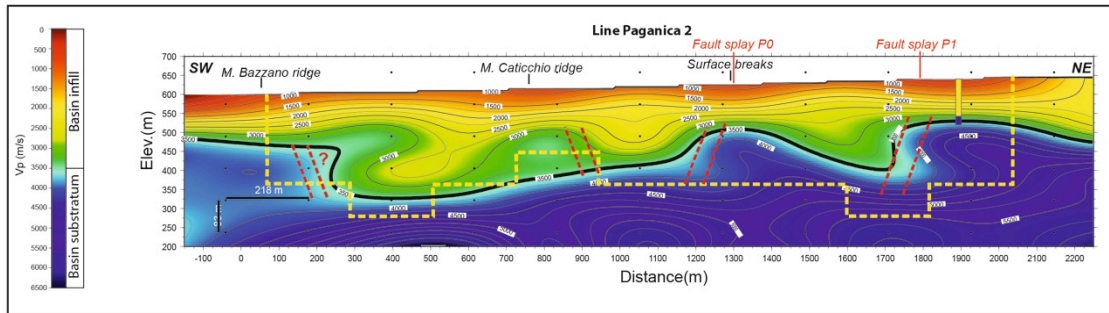


Figure 8.5 - Long wavelength V_p model of line p2. The figure also shows the location of the borehole reaching the bedrock at -78 m depth and the location of some of the discontinuous surface breaks reported in Chapter 3.

Interestingly, the surface projection of fault splay P0 coincides with the occurrence of some aligned but highly discontinuous 2009 coseismic surface ruptures (figure 8.6 – see also Chapter 3).

In this light, fault splay P3 may not be the only presently active trace within the narrow deformation zone of the Paganica sector, but we should also take into account the deformation accommodated by the 2 SW-dipping buried fault splays (P0 and P1). The latter splays do not show a clear morphological expression likely because of their location in the active hangingwall of the fault system and the high sedimentation rates.

The subsurface geometry in this sector of the PSDFS hangingwall appears therefore to be more complicated than expected from surface geomorphological and geological investigations.

8.4 Slip-rate of the PSDFS

Vertical slip-rates were defined for different time intervals in the Quaternary on the basis of the integration of all the data resulting from paleoseismological, geomorphological, geophysical and geological investigation. Table 8.1 summarizes the results from each approach.

Paleoseismological investigations show evidence for the occurrence of repeated Late Pleistocene-Holocene surface faulting events and allowed for vertical slip-rate estimates at a very short time scale with respect to the whole ~2 Ma long time interval investigated. These data are available only for the Paganica sector of the

PSDFS where we dug exploratory trenches after the April 6, 2009 shock. A Late Holocene (last 5 ka) vertical slip-rate was estimated by using the age and throws of individual paleoearthquakes recognized on the studied trench walls and resulted in an average value of 0.26-0.51 mm/yr.

Furthermore, a Late Holocene vertical slip-rate at Mo'Tretteca site of ~ 0.4 mm/yr was obtained for the past ~ 1000 years by means of high-resolution petrophysical correlations and the age of the deposits, thus in good agreement with those obtained from the classical paleoseismological approach.

Furthermore, data from the trenches allowed us also to calculate a vertical slip-rate for the Late Pleistocene of 0.21-0.25 mm/yr for the Paganica sector of the PSDFS.

Geomorphological, geophysical and geological investigations were integrated to estimate long-term slip-rates for the PSDFS at different time intervals:

Period A) 1.8 Ma – 781 ka: Bottom of the Early Pleistocene;

Period B) 1.8 Ma – 781 ka: Top of the Early Pleistocene;

Period C) 781 - 561 ± 2 ka: Bottom of the Middle Pleistocene;

Period D) 561 ± 2 - 172 ± 12 ka: Top of the Middle Pleistocene.

For each time interval we estimated vertical slip-rates across transects crossing most of the fault splays affecting the deposits belonging to that specific time-interval, being aware of the fact that we may have missed some deformation (lack of information, erosion, etc.). Transects are schematically represented in figure 8.6 as light shaded areas.

The slip-rates estimated across these transects can be considered as representative of the actual strain across the PSDFS. This is both because a common decrease of the slip from depth to surface, but also because, in this case, at the surface the strain tends to be distributed among parallel fault splays, whereas at depth it concentrates on a narrow zone (according to the modeling of the 2009 earthquake causative fault). Therefore, the strain accommodated by the PSDFS, should be derived by the sum of the relative contribution of each fault splay (i.e. transects) and represent a minimum.

Vertical slip-rates fall in the following ranges and are reported in bold in table 8.1:

- Period A: 0.1 - 0.54 mm/yr;
- Period B: 0.14 - 0.58 mm/yr;
- Period C: 0.15 - 0.54 mm/yr;
- Period D: 0.09 - 0.47 mm/yr;

When well-constrained throws and ages were available also for individual fault splays, we estimated vertical slip-rates associated with individual faults (see table 8.1 – regular fonts and figure 8. 6).

Although slip-rates shown in table 8.1 were estimated by means of methods operating at very different temporal resolutions and across different time intervals (i.e. paleoseismology vs. Quaternary geology), the obtained values are well comparable.

Given the consistency both in time and space among the vertical slip-rates across the system, to obtain an overall average Quaternary vertical slip-rate of 0.22 – 0.39

mm/yr for the PSDFS, we averaged the minimum and maximum values estimated from the transects that included most of the splays (bold values in table 8.1).

All the vertical slip-rates were converted into slip-rates on the fault plane and into extension-rates. This is done under the assumption that we are dealing with a simple regular structure and we know its dip angle. As for this latter parameter, taking into account all the information coming from subsurface geophysical imaging (chapter 7) and geological investigations (chapter 6) as well as from the modeling of the 2009 earthquake causative fault (Chapter 3), we can assume an average 55° dipping fault plane as typical for the PSDFS. All the converted values are reported in table 8.1.

Following this procedure, the overall average Quaternary vertical slip-rate is converted into overall Quaternary slip-rate and extension-rate of 0.27 - 0.48 mm/yr and of 0.15 - 0.27 mm/yr, respectively.

Code	Site	Fault	Time interval	Vertical slip-rate min (mm/yr)	Vertical slip-rate max (mm/yr)	Slip-rate min (mm/yr)	Slip-rate max (mm/yr)	Extension min (mm/yr)	Extension max (mm/yr)
F	Paganica trenches	P3	Late Holocene (last 5 ka)	0.26	0.51	0.32	0.62	0.18	0.36
E	Paganica trenches	P3	Late Pleistocene (30 ka)	0.21	0.25	0.26	0.30	0.15	0.17
B1	1 - Paganica	P3	Vall'Orsa unit - Early Pleistocene (1.8 Ma - 781 ka)	0.03	0.08	0.04	0.09	0.02	0.05
A1	2 - Pescomaggiore	P3 P2 P1 P0	San Nicandro unit - Early Pleistocene (1.8 Ma - 781 ka)	0.16	0.37	0.20	0.45	0.11	0.26
B2	2 - Pescomaggiore	P4 P3 P2 P1 P0	Vall'Orsa unit - Early Pleistocene (1.8 Ma - 781 ka)	0.17	0.38	0.20	0.47	0.12	0.27
C1	2 - Pescomaggiore	P3 P2	Valle Inferno unit - Middle Pleistocene (781 - 561 ka)	0.15	0.21	0.19	0.26	0.11	0.15
A2	3 - San Valentino	P1	San Nicandro unit - Early Pleistocene (1.8 Ma - 781 ka)	0.10	0.23	0.12	0.28	0.07	0.16
B3	3 - San Valentino	P4 P2 P1	Vall'Orsa unit - Early Pleistocene (1.8 Ma - 781 ka)	0.25	0.58	0.30	0.70	0.17	0.40
B3a	3 - San Valentino	P1	Vall'Orsa unit - Early Pleistocene (1.8 Ma - 781 ka)	0.11	0.26	0.14	0.31	0.08	0.18
B3b	3 - San Valentino	P4 P2	Vall'Orsa unit - Early Pleistocene (1.8 Ma - 781 ka)	0.14	0.32	0.17	0.39	0.10	0.22
C2	3 - San Valentino	P4 P2 P1	Valle Inferno unit - Middle Pleistocene (781 - 561 ka)	0.27	0.38	0.33	0.46	0.19	0.26
C2a	3 - San Valentino	P1	Valle Inferno unit - Middle Pleistocene (781 - 561 ka)	0.10	0.14	0.12	0.17	0.07	0.10
D1	3 - San Valentino	P1	San Mauro unit - Middle Pleistocene (561 - 172±12 ka)	0.09	0.31	0.11	0.38	0.06	0.22
A3	4 - Valle dell'Inferno	S10 - S2	San Nicandro unit - Early Pleistocene (1.8 Ma - 781 ka)	0.23	0.54	0.28	0.66	0.16	0.38
A3a	4 - Valle dell'Inferno	S6	San Nicandro unit - Early Pleistocene (1.8 Ma - 781 ka)	0.13	0.29	0.16	0.36	0.09	0.21
A3b	4 - Valle dell'Inferno	S10	San Nicandro unit - Early Pleistocene (1.8 Ma - 781 ka)	0.08	0.18	0.09	0.22	0.05	0.13

B4	4	–	Valle dell'Inferno	S10 - S2	Vall'Orsa unit - Early Pleistocene (1.8 Ma - 781 ka)	0.14	0.33	0.18	0.41	0.10	0.23
B4a	4	–	Valle dell'Inferno	S6	Vall'Orsa unit - Early Pleistocene (1.8 Ma - 781 ka)	0.12	0.27	0.14	0.33	0.08	0.19
C3	4	–	Valle dell'Inferno	S10 - S5	Valle Inferno unit - Middle Pleistocene (781 - 561 ka)	0.38	0.54	0.47	0.65	0.27	0.38
C3a	4	–	Valle dell'Inferno	S6	Valle Inferno unit - Middle Pleistocene (781 - 561 ka)	0.29	0.41	0.36	0.50	0.21	0.29
C3b	4	–	Valle dell'Inferno	S10	Valle Inferno unit - Middle Pleistocene (781 - 561 ka)	0.05	0.07	0.06	0.09	0.04	0.05
D2	4	–	Valle dell'Inferno	S5 - S1	San Mauro unit – Middle Pleistocene (561 - 172±12 ka)	0.34	0.47	0.42	0.57	0.24	0.33
D2a	4	–	Valle dell'Inferno	S1	San Mauro unit (FLUVIAL) – Middle Pleistocene (561 - 172±12 ka)	0.19	0.31	0.23	0.38	0.13	0.22
D2b	4	–	Valle dell'Inferno	S5	San Mauro unit (ALL. FAN)– Middle Pleistocene (561 - 172±12 ka)	0.13	0.19	0.15	0.23	0.09	0.13

Table 8.1 - Slip-rate values for the whole Paganica-San Demetrio fault system.

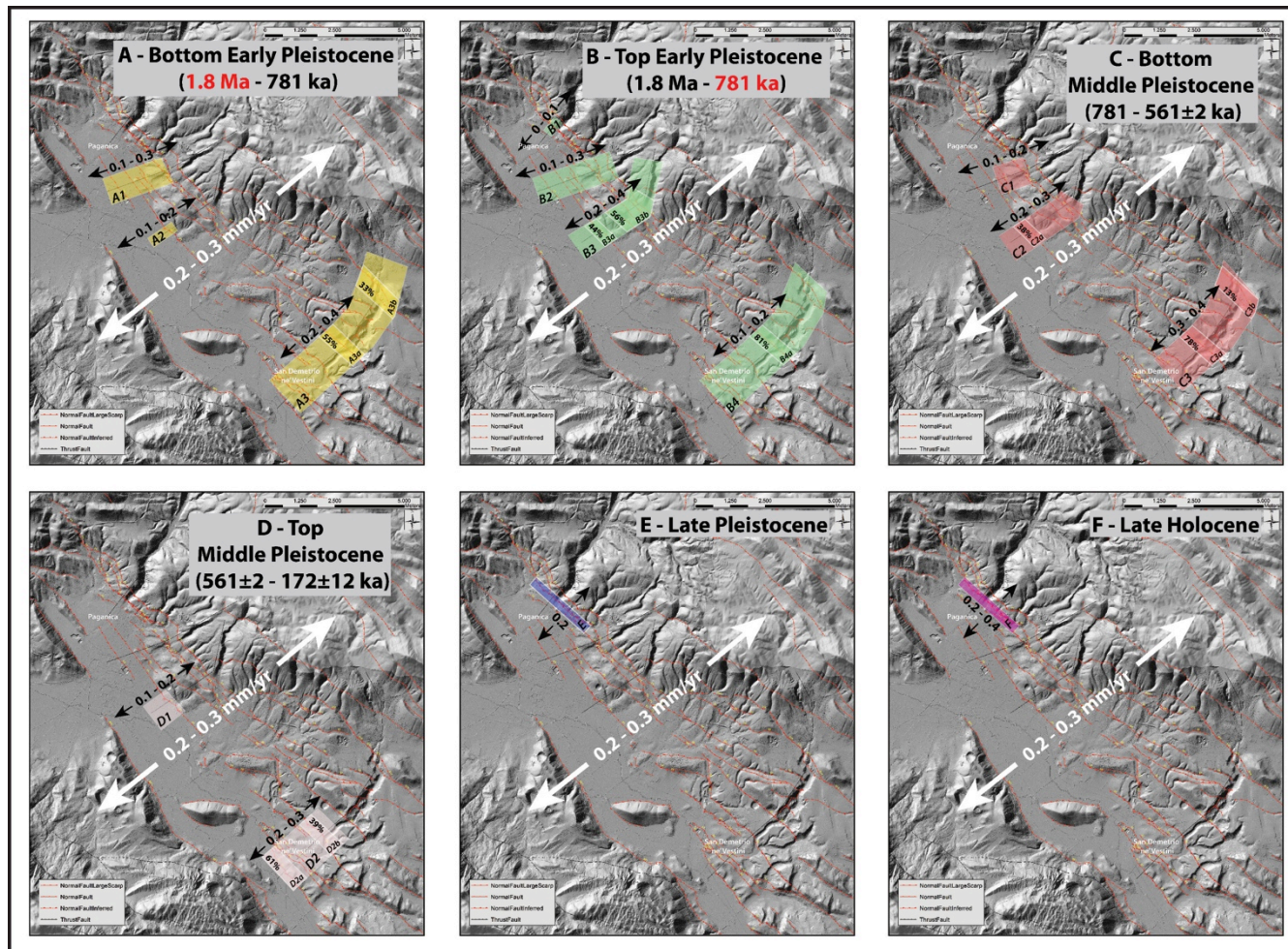


Figure 8.6 – Evolution in time and space of the extension-rates of the PSDFS. The overall average Quaternary extension-rate of the PSDFS is reported inside the white arrows and is used as a reference to analyze the relative contribution to the deformation of different sectors and splays. Light-shaded areas are the transects across which the extension-rates were estimated for each specific time-interval (keyed with a capital letter and a number that are the same in text and table 8.1). When available, individual contribution of single fault splays is reported as percentage of the extension-rate estimated in each transect (keyed with letters and a number that are the same in text and table 8.1)

see also Appendix F.

8.5 Slip-rates through time and space

Slip-rates were analyzed in different time windows, so they are averaged from the oldest age of the displaced deposits to present. Following this approach, we identified six time intervals (table 8.1 and figure 8.6 – see also Appendix F).

In the following discussion we refer to figure 8.6 and use extension-rates as representative of the component of deformation of normal faults in map view.

Taking into account all the uncertainties in the calculation of the extension-rates (intrinsic in both vertical slip-rate values and average fault dip angle), in the following text and in figure 8.6 we rounded these values to the first decimal number. For example, the abovementioned overall average Quaternary extension-rate of 0.15 - 0.27 mm/yr for the whole PSDFS is reported as 0.2 - 0.3 mm/yr.

As already mentioned, because this latter value is considered as representative of the extension across the whole PSDFS (see previous section), we use it as a reference to analyze the relative contribution to the deformation of different sectors and splays. Figure 8.6 shows the specific transects where the data were collected and is subdivided in 6 boxes, each one representing a different period.

Period A – Bottom of the Early Pleistocene (figure 8.6A) - In the Paganica sector the extension rates derived across transects A1 and A2 (both not including all the fault splays, e.g. P4) are slightly lower than the overall average Quaternary extension-rate. This suggests that also the splays not included in the transect were active in this period of time and thus that all the parallel splays (P0 to P4) were likely active.

In the San Demetrio sector, we note a general agreement between the overall average Quaternary extension-rate and the value estimated in transect A3 (including all the splays but S1). Moreover, taking into account the relative contribution of individual fault splays to the extension in the specific transect, we note that S6 (box A3a) and S10 (box A3b) account for 55% and 33%, respectively, that is for most of the deformation along this transect.

Period B - Top of the Early Pleistocene (figure 8.6B) - In the Paganica sector the extension-rate estimated across transects B3 and B2 is comparable to the overall average Quaternary value, suggesting that during this time interval the deformation continued to be accommodated by all the fault splays. Transect B1, crossing only a few splays, accounts only for part of the overall extension-rate, implicitly confirming the need for a contemporaneous activity of the all the fault splays. Moreover, transect B3 shows that most of the deformation is accommodated by the fault splays falling in box B3b (P2 and P4) and in box B3a (P1) accounting for 56% and 44%, respectively.

In the San Demetrio sector transect B4 (including all the splays but S1) can explain most of the overall deformation, although part of it may have already been taken by S1. Interestingly splay S6 (box B4a) contributes for the 81% of it, with a net increment with respect to the previous time interval.

Period C- Bottom of the Middle Pleistocene (figure 8.6C) - In the Paganica sector the extension-rate obtained from transect C2 (fault splays P1 – P2 and P4) is consistent

with the overall average Quaternary extension-rate whereas transect C1 (containing only P2 and P3) do not fully explain the overall extension, suggesting that all the fault splays in this sector have to be active. This is even more clear when we look at transect C2 where the individual contribution of fault splay P1 (box C2a) is 38% of the total.

In the San Demetrio sector, we note that transect A3 (including fault splays S5 to S10) satisfies the whole overall average Quaternary extension-rate. Moreover, the deformation appears to persist on fault splay S6 (box C3a) that accommodate a 78% whereas, fault splay S10 (box C3b) adjust only the 13%, reducing its importance within the system.

Period D - Bottom of the Middle Pleistocene (figure 8.6D) – In the Paganica sector there is only one extension-rate available (transect D1 containing only fault splay P1) that accounts only for part of the overall average Quaternary extension-rate, suggesting that some of the faults to the northeast continued to contribute to the extension in this period.

In the San Demetrio sector, transect D2 explains the whole overall average Quaternary extension-rate, highlighting that if the fault splays to the northeast are still active they contribute for a negligible part of the deformation. The relative contribution of individual fault splay S1 (box D2a) and S5 (box D2b) accommodated 61% and 39% of the extension, respectively, together accounting for all the deformation observed along this transect.

Period E - Late Pleistocene (figure 8.6E) – for this time interval only a rate from paleoseismology is available and only for fault splay P3 along the Paganica sector (box E). This falls in the lower part of the overall average Quaternary extension-rate, suggesting that other fault splays contributed to the extension.

Period F - Late Holocene (figure 8.6F) - similarly to time interval E, only a fault splay (P3) allows us estimating extension-rate. This latter is consistent with the overall average Quaternary extension-rate, suggesting that most of the extension is taken by P3. Consequently, fault splay P4 may be negligibly active; limited data do not allow to estimate the relative contribution of the southwestern splays (P0 and P1).

8.6 Strain migration

On the basis of the results of this work, starting from the understanding of the tectonic style and of the strain distribution on the PSDFS, we discuss the possible PSDFS evolution in time and space at the surface and discuss the possible meaning for the understanding of the fault at depth.

The distribution of the extension-rates in space and over the different time intervals shown in figure 8.6 highlight different strain distributions along the two sectors of the PSDFS during the Quaternary and suggests the occurrence of strain migration across the San Demetrio sector.

- In the Paganica sector the strain has been concentrated since Early Quaternary (~2 Ma) along the same fault zone, 1 to 2 km-wide, controlling

the basin evolution as well as the persistence of the depocenter location until present. Only during Late Holocene P4 activity may become negligible and P3, that is also the splay that ruptured in 2009, takes most of the extension.

- In the San Demetrio sector the strain at the surface has not been homogeneously distributed among all fault splays during the whole Quaternary. The presence of a wider Quaternary basin (~5 km) suggests that the inset of the deformation in Early Pleistocene occurred along the easternmost basin-bounding fault splay (S10), where the oldest tectonically displaced Quaternary deposits are found.

With time, most of the extension migrated toward the southwestern splays. Since ~550 ka (Middle Pleistocene – figure 8.6D), most of the extension is taken by fault splays S1 to S5 and the activity of the former basin-bounding splay (S10) becomes negligible.

The fact that the Paganica sector appears mostly stationary through time and space and vice versa San Demetrio sector shows migration, finds support also by the along-strike plot of the morphological throws (figure 8.7).

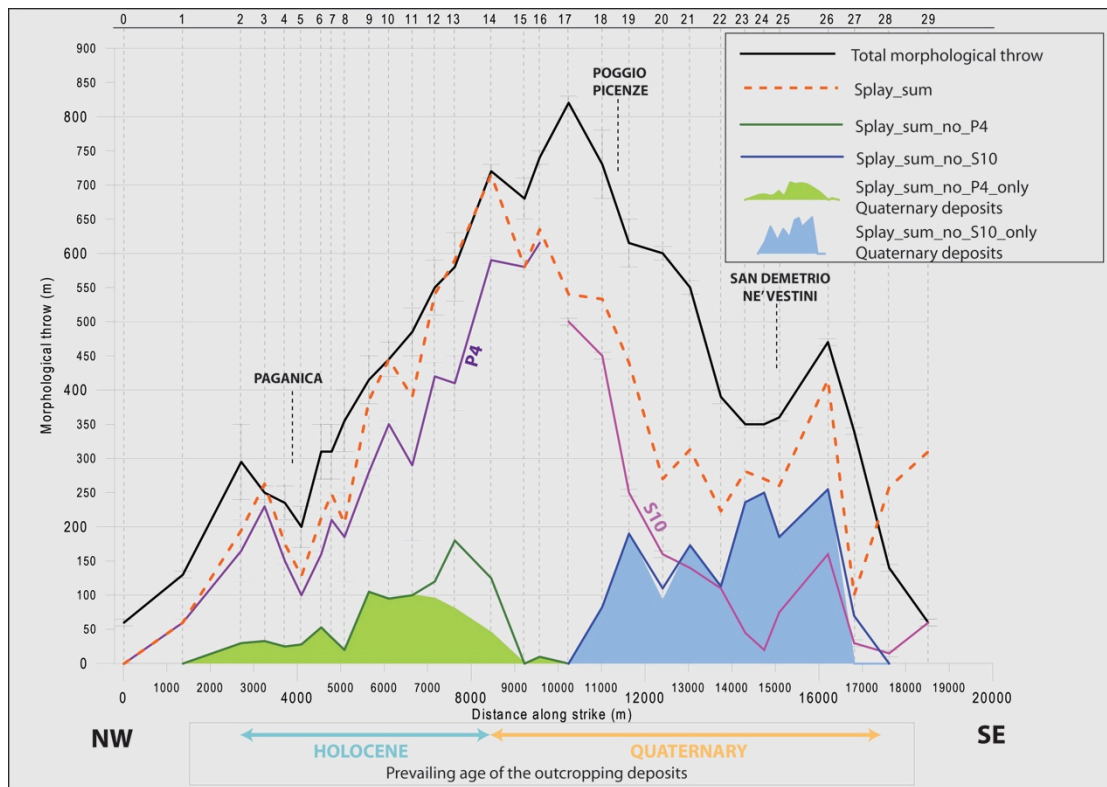


Figure 8.7 - Along-strike plot of all the morphological throw values measured from the topographic profiles. The orange dotted curve represents the sum of the relative contribution of each fault, while the green and the blue solid lines represent the sum of all the fault splays with exception of P4 and S10, respectively. Green and blue areas show the relative contribution of the splays displacing Quaternary sediments in the Paganica and San Demetrio sector, respectively.

In fact, the relative contribution to the total strain of the fault splays affecting only Quaternary deposits (green and blue areas in figure 8.7) is substantially smaller for

the Paganica sector with respect to the San Demetrio sector. This is because in the Paganica sector the deformation persisted on a narrow band, creating a relatively small Quaternary basin, affected by few fault splays; differently, in the San Demetrio sector, the strain migration through time allowed an important deformation to be recorded by the Quaternary deposits.

8.7 Contribution to seismic hazard

As we wrote at the beginning of this thesis, the slip-rate of a fault represents a critical information for seismic hazard assessment of an area, because it describes the fault activity and its relevance with respect to nearby faults.

We estimated an overall Quaternary average slip-rate of the PSDFS of 0.27 - 0.48 mm/yr. This compares with the lower range of slip-rates observed in the area on nearby faults that is from 0.4 to 1.2 mm/yr, with intermediate values preferred, i.e. 0.6-0.8 mm/yr (Galadini and Galli, 2000; Galli et al., 2008 and references therein). This agreement suggests a similarity in behavior of the faults active in this area, possibly related to a characteristic strength of the crust and of a homogeneous distribution of the extension in the area.

We can also attempt an interesting comparison between geologically and geodetically determined extension-rates.

GPS analyses of D'Agostino et al., 2011 show a contemporary deformation field over central Apennines characterized by a NE-SW oriented extension-rate of 2.7 ± 0.2 mm/yr, focused in coincidence of the belt axis.

We have seen that the overall Quaternary average slip-rate of the PSDFS (0.27 - 0.48 mm/yr) is in general agreement with the slip-rates observed in the area on nearby faults, and that this value can be translated into an extension-rate of 0.2 - 0.3 mm/yr. Geological studies accomplished so far across central Apennines have shown the presence of 2, maximum 6 almost parallel active faults, with average Late Quaternary fault slip-rates estimates typically < 0.5 mm/yr (Boncio et al., 2004; Roberts and Michetti, 2004; Galli et al., 2008). Only in some cases, they are slightly larger than 1 mm/yr (Pantosti et al., 1996; Galli et al., 2008).

Assuming GPS-derived extension-rates are representative and comparable over Quaternary time, and if the crustal extension is accommodated only by elastic strain distributed on several tectonic structures, to reconcile with geodetically determined rates each fault would have to accommodate 0.5–1.5 mm/yr of extension.

Thus, the extension-rate obtained by summing Late Quaternary fault displacements is generally not sufficient to accommodate the geodetic estimates.

This discrepancy may be related to different factors:

- A significant amount of elasto-plastic strain release;
- Strain produced by faults at depth that do not break at the surface (blind structures) or that produce small surface ruptures (commonly related to events with $M < 6.5$), characterized by a poor geomorphic signature (hidden

structures), and thus difficult to recognize by means of geomorphological and paleoseismological investigations;

- A significant amount of strain accommodated by unknown/blind or estimated to be inactive major faults, even if such active structures usually have a clear geomorphic expression in central Italy;
- GPS data (years to decades long) may be unrepresentative of the long-term geological deformation rate.

Another key information for seismic hazard assessment is represented by the maximum expected magnitude on the fault. To obtain such information, we need to recognize and measure maximum slip per event and rupture lengths of seismogenetic faults. The overall long-term geomorphic expression of the PSDFS defines a ~19 km-long fault. The total length of the presently most active traces at surface (linking P3 and S6) reaches ~15 km (figure 8.4). Moreover, Wells and Coppersmith (1994), indicated that surface rupture length typically is equal to 75% of the subsurface rupture length. This translates in a total fault length at depth of at least 20 km.

The fault length defined by 2009 coseismic seismologic and geodetic observations ranges from 15 to 18 km.

In summary, taking into consideration the data presented above, a ~20 km-long fault may well represent the maximum rupture length of the PSDFS.

Given this interpretation, and according to the empirical relationships among magnitude and surface rupture length (Wells and Coppersmith, 1994) we can hypothesize that the PSDFS may generate the contemporaneous rupture of the northwestern and southeastern fault splays, potentially producing a $M_w \geq 6.3$ earthquake.

It is worth noting that from our paleoseismological investigations we observe that the amount and the style of deformation in past events (vertical displacement of 0.4 - 0.8 m, well-preserved colluvial wedges, large graben structures, intensive sheared zone, backtilting) suggest the occurrence of old earthquakes larger than the 2009 event (Cinti et al, 2011). The observed vertical displacements of 0.4 - 0.8 m can be converted to a slip per event on the fault plane of 0.5 - 1 m assuming an average 55° dipping fault plane as typical of the whole PSDFS. Assuming these values as representative of the average fault displacement they would account for moment magnitude earthquakes ranging between 6.5 and 6.8 (Wells and Coppersmith, 1994).

Thus, the different lengths of the PSDFS and the slip per event resulting from our paleoseismological investigations converge toward the possibility for the occurrence of past surface faulting earthquakes characterized by a moment magnitude between 6.3 and 6.8, notably larger than the 2009 event, and compatible with the M range observed in historical earthquakes in the area. The 2009 earthquake would be the smallest expected, opening the possibility that the same fault generates also more energetic events. This changes substantially the hazard of the area.

The understanding of the evolution of the PSDFS through time and space was critical to assess the seismic potential of the PSDFS. The overall picture deciphered so far highlighted the existence of a complex structural setting of the PSDFS at the surface, characterized by the presence of several parallel normal fault splays.

Looking at the geometry of the PSDFS, the identified segment boundaries and the step over separating Paganica from San Demetrio sectors, are likely related to inherited structures/discontinuities related to earlier tectonic phases.

In fact these may represent both geometrical and structural barriers to fault and slip propagation, thus influencing the development of the fault system.

Moreover, we have also shown that in the San Demetrio sector the strain has not been homogeneously distributed over time and space across the fault system and that, with time, most of the extension migrated toward the southwestern fault splays.

The abovementioned considerations are critical in terms of assessment of the seismic hazard of the area. The occurrence of strain migration, in particular, has a significant implication in terms of surface faulting hazard in the area. This topic is important because often it determines a substantial risk where urban areas and/or important infrastructures and facilities are developed or planned. This was actually the case of the 2009 L'Aquila earthquake, where buildings and lifelines located in coincidence (on top/near) of the observed coseismic surface ruptures suffered significant damages (e.g. the Tempera aqueduct pipe broke because crossed by surface faulting).

9 Conclusions

The L'Aquila Mw 6.3 April 6, 2009 earthquake causative fault was used as a test site to apply a multidisciplinary and multiscale-based strategy aimed at improving the normal faults seismogenic characterization, focusing mainly on slip-rate estimate as a measure of the fault activity.

This thesis integrated the application, testing, and refinement of traditional or innovative approaches aimed at providing a detailed knowledge in terms of location, geometry, and characterization of the 2009 L'Aquila earthquake source fault, and at developing a reference approach useful for extending these investigations to other seismogenic normal faults.

In particular we performed a three steps approach:

1. paleoseismological, including a trenching and coring campaign with the excavation of 4 trenches and the realization of 2 boreholes;
2. geomorphological and geological, integrating field survey and dating of Quaternary layers by means of Optically Stimulated Luminescence (OSL), radiocarbon dating and tephrochronology together with LiDAR-derived high resolution DEM and air-photo analysis;
3. geophysical, including high resolution petrophysical correlations, electrical resistivity tomography (ERT) and shallow seismic profiling.

By a methodological point of view, the multidisciplinary and multiscale-based investigation strategy emphasizes the advantages of the joint application of different approaches and methodologies for active faults identification and characterization.

Our work suggests that each approach alone may provide sufficient information but only the application of a multidisciplinary strategy is effective in providing a proper framework of active faults and robust results. For the case of the PSDFS, the results obtained from this multidisciplinary approach are certainly unique for this portion of the Apennines.

The detailed multidisciplinary and scale-based investigations were crucial to provide a precise knowledge in terms of location, geometry and characterization of the 2009 L'Aquila earthquake source fault, that is the PSDFS.

The integration of geomorphology, geology as well as shallow geophysics, was essential to produce a geomorphological and geological map of the PSDFS and to define its tectonic style, arrangement, kinematics, extent, geometry and boundaries. A detailed geomorphological and geological map of the fault is reported in Chapter 6 and in appendix A and appendix B.

At a basin-wide scale, the fault system is characterized by a complex structural setting at the surface, with several normal parallel fault splays frequently arranged in a quasi-fractal sequence of horsts and grabens of variable size. Moreover, our

investigations highlighted that the PSDFS is arranged in two main sectors: the Paganica sector to the NW and the San Demetrio sector to SE. The Paganica sector is characterized by a narrow deformation zone, with a relatively small (but deep) Quaternary basin affected by few fault splays. The San Demetrio sector is characterized by a strain distribution at the surface that is accommodated by several tectonic structures, with the system opening into a set of parallel, km-spaced fault traces that exhume and dissect the Quaternary basin.

Among the numerous tectonic structures that characterize the morphological expression of the PSDFS we were able to define a first-order hierarchy, identifying the different contribution of individual fault splays to the overall deformation across the fault system (Chapters 6 and 8). Most of the deformation of the PSDFS is accommodated by the two easternmost basin-bounding fault splays (P4 and S10) affecting mainly the bedrock. Among the fault splays affecting mainly the Quaternary deposits (last ~2Ma), an important contribution to the overall deformation is accommodated by fault splays P3 and S6.

On the basis of the long-term morphological expression of the fault system at surface and by analyzing the cumulative displacement distribution along strike, we set the fault boundaries and defined the actual extent of the PSDFS at the surface (chapter 8). This was one of the main questions raised by the occurrence of the 2009 earthquake. The resulting overall length of the PSDFS, from our multidisciplinary approach, approximates 19 km, and is in good agreement with the 15 to 18 km-long 2009 earthquake causative fault, as defined by coseismic seismologic and geodetic observations.

The integration of all the fault displacement data and age constraints resulting from paleoseismological, geomorphological, geophysical and geological investigation played a primary role in our estimate of the slip-rate of the active PSDFS. Although estimated by means of methods operating at very different temporal resolutions and across different time intervals (i.e. high-resolution petrophysical correlations vs. paleoseismology vs. Quaternary geology), the obtained slip-rates are quite comparable and thus represent a reliable dataset.

Slip-rates were estimated for different time intervals in the Quaternary, ranging from Early Pleistocene (1.8 Ma) to Late Holocene (last 5 ka) and resulted in an average Quaternary slip-rate for the PSDFS of 0.27 - 0.48 mm/yr.

This compares with the lower part of the range of slip-rates observed in the area on nearby faults that range from 0.4 to 1.2 mm/yr. This agreement suggests a similarity in behavior of the faults active in this area possibly related to a characteristic strength of the crust and of a homogeneous distribution of the extension in the area.

A part from slip-rate estimates, a further contribution of this work to the understanding of the PSDFS seismic behavior and thus of the local seismic hazard derives from estimate of the max expected magnitude for this fault on the basis of its

length and slip per event, and from the understanding of the evolution of the PSDFS through time and space for highlighting the presently active fault splays.

The length of the PSDFS as defined by its long-term geomorphological expression, as well as the slip per event resulting from our paleoseismological investigations converge toward the possibility for the occurrence on the PSDFS of past surface faulting earthquakes characterized by a moment magnitude between 6.3 and 6.8, notably larger than the 2009 event and compatible with the M range observed in historical earthquakes in the area. The 2009 earthquake would be the smallest expected, opening the possibility that the same fault generates also more energetic events. This changes substantially the hazard of the area.

On the basis of the slip-rate distribution over time and space and starting from the understanding of the tectonic style and of the strain partitioning on the PSDFS, we highlighted different strain distributions along the two sectors of the PSDFS during the Quaternary. Our results indicate that in the Paganica sector the strain has been concentrated since Early Quaternary (~2 Ma) along the same narrow fault zone, 1 to 2 km-wide, controlling the basin evolution as well as the persistence of the depocenter location until present; differently, in the San Demetrio sector, the strain at the surface has not been continuously distributed among all fault splays during the whole Quaternary. The presence of a wider Quaternary basin (~5 km) suggests the occurrence of strain migration through time, starting from the Early Pleistocene inset of the deformation along the easternmost basin-bounding fault splay and followed by a migration of the strain, with time, toward the southwestern splays. Since ~550 ka (Middle Pleistocene), most of the extension is taken by the fault splays located at the present Aterno river valley bottom and the activity of the former basin-bounding splays becomes negligible.

The understanding of the evolution of the PSDFS through time and space was critical to assess the seismic potential of the PSDFS. The occurrence of strain migration, in particular, has a significant implication in terms of surface faulting hazard in the area, because it can contribute defining the fault splays that have a higher potential to slip during future earthquakes along the PSDFS.

This topic is particularly important because often it determines a substantial risk where urban areas and/or important infrastructures and facilities are developed or planned. This was actually the case of the 2009 L'Aquila earthquake, where buildings and lifelines located in coincidence (on top/near) of the observed coseismic surface ruptures suffered significant damages (e.g. the Tempera aqueduct pipe broke because crossed by surface faulting).

In summary, the integration of traditional or innovative approaches, such as paleoseismology, geomorphology and geology, shallow geophysical investigations and high-resolution petrophysical correlations, gave compelling constraints to improve our knowledge in terms of location, geometry, and characterization of the

2009 L'Aquila earthquake source fault, and developed a reference approach useful for extending the investigation to other seismogenetic normal faults.

By a methodological point of view, this thesis was also thought to apply, test, and improve innovative methodologies and evaluate their strength or limitations. The most innovative methodology we applied, as an alternative paleoseismological tool, was based on core sampling (done at one trench site by collecting 4 cores just across the 2009 surface rupture) and laboratory analyses or also *in situ* measurements of physical properties. Applying the high-resolution petrophysical correlations method, we obtained a Late Holocene vertical slip-rate at Mo'Tretteca site of ~ 0.4 mm/yr. This slip-rate estimate is in good agreement with the slip-rates obtained for the same time interval from the classical paleoseismological approach. Moreover, the results from another test site (Fossa village) indicate that high-resolution petrophysical correlations were effective in reproducing the offset visible on the exposed stratigraphy, with a minimum variability with respect to the measurements performed with a conventional stratigraphic approach.

This approach seems to have a good potential for future investigations and can be an effective tool to investigate recent faulting in unconsolidated continental sediments and to estimate fault slip-rates, providing a viable alternative when sediment characteristics prevent reliable stratigraphic correlations and/or classical paleoseismological trenching is impractical and a less invasive approach is needed.

Electrical resistivity tomography (ERT) and shallow seismic profiling complemented the geomorphological and geological investigations and were effective in imaging the position and geometry of the faults splays and, in some cases, in estimating the fault throw.

Classical geomorphological and geological investigations took advantages of the availability of high-resolution (1 m) topographic data derived from the elaboration and analysis of an airborne LiDAR survey of the area. This substantially increased our confidence to identify and map the numerous faults splays of the PSDFS through an enhanced visualization of the morphological features related to faulting activity.

Moreover, the integration of Optically Stimulated Luminescence (OSL) dating with ^{14}C and tephrochronology, as well as with archeological evaluation of pottery shards, allowed us to develop a chronological framework and to obtain new and essential age constraints for the observed displacements/offsets.

References

- Adams, K. D. and S. G. Wesnousky (1999), Surficial characteristics, soil development and regional Shoreline correlation, *Geomorphology* 30: 357-392.
- Akinci, A., F. Galadini, D. Pantosti, M. Petersen, L. Malagnini and D. Perkins (2009), Effect of time dependence on probabilistic seismic-hazard maps and deaggregation for the central Apennines, Italy, *Bull. Seismol. Soc. Am.*, 99, 585–610. doi:10.1785/0120080053.
- Akinci, A., L. Malagnini and F. Sabetta, F. (2010), Characteristics of the strong ground motions from the 6 April 2009 L' Aquila earthquake, Italy, *Soil Dynamics and Earthquake Engineering* 30, 320- 335.
- Anderson, E.M., The dynamics of faulting, *Trans. Edinburgh Geol. Soc.*, 8 (3), 387-402, 1905.
- Anderson, E.M., The Dynamics of Faulting and Dyke Formation With Application to Britain, 2nd ed., 206 pp., Oliver and Boyd, Edinburgh, 1951.
- Angelier, J. (1994) Fault slip analysis and palaeostress reconstruction. In Hancock, P.L. (ed.) *Continental Deformation*, pp. 53– 100. Pergamon Press, Tarrytown, NY.
- Anzidei, M., E. Boschi, V. Cannelli, R. Devoti, A. Esposito, A. Galvani, D. Melini, G. Pietrantonio, F. Riguzzi, V. Sepe and E. Serpelloni (2009), Coseismic deformation of the destructive April 6, 2009 L'Aquila earthquake (central Italy) from GPS data, *Geophys. Res. Lett.*, 36, L17307. doi:10.1029/2009GL039145.
- Amos, C. B., K. I. Kelson, D. H. Rood, D. T. Simpson and R. S. Rose (2010), Late Quaternary slip rate on the Kern Canyon Fault at Soda Spring, Tulare County, California, *Lithosphere*, 2(6):411-417.
- APAT - Agenzia per la Protezione dell'Ambiente ed i servizi Tecnici, Servizio Geologico d'Italia (2006), foglio 359 L'Aquila. Carta Geologica d'Italia alla scala 1:50000. S.EL.CA., Firenze, Italy.
- Arrowsmith, J. R., O. Zielke (2009). Tectonic geomorphology of the San Andreas Fault zone from high resolution topography: An example from the Cholame segment, *Geomorphology*, doi:10.1016/j.geomorph.2009.01.002.
- Atzori, S., I. Hunstad, M. Chini, S. Salvi, C. Tolomei, C. Bignami, S. Stramondo, E. Trasatti, and A. Antonioli (2009), Finite fault inversion of DInSAR coseismic displacement of the 2009 L'Aquila earthquake (central Italy), *Geophys. Res. Lett.*, 36, L15305. doi:10.1029/2009GL039293.
- Avallone A, Selvaggi G., D'Anastasio E., D'Agostino N., Pietrantonio G., Riguzzi F., Serpelloni E., Anzidei, M., Casula G., Cecere G., D'Ambrosio C., De Martino P., Devoti R., Falco L., Mattia M., Rossi M., Tammaro, U., Zarrilli L. (2010), The RING network: improvement of a GPS velocity field in Central Mediterranean. *Annals of Geophysics*, 2/53.
- Bagh, S., L. Chiaraluce, P. De Gori, M. Moretti, A. Govoni, C. Chiarabba, P. Di Bartolomeo, and M. Romanelli (2007), Background seismicity in the central Apennines of Italy: The Abruzzo region case study, *Tectonophysics*, 444, 80 – 92, doi:10.1016/j.tecto.2007.08.009.
- Bagnaia, R., A. D'Epifanio, and S. Sylos Labini (1992), Aquila and sub-aequan basins: an example of Quaternary evolution in central Apennines, Italy, *Quat. Nova*, II, 187–209.

- Begg, J. G. and V. Mouslopoulou (2010), Analysis of late Holocene faulting within an active rift using lidar, Taupo Rift, New Zealand. *Journal of Volcanology and Geothermal Research*, 190, 152–167, doi:10.1016/j.jvolgeores.2009.06.001.
- Ben-Avraham Z., Boccaletti M., Cello G., Grasso M., Lentini F., Torelli L. and Tortorici L. (1990), Principali domini strutturali originatisi dalla collisione continentale neogenico-quaternaria nel Mediterraneo centrale. *Mem. Soc. Geol. It.*, 45: 453-462.
- Bertini T. and Bosi C. (1993), La tettonica quaternaria della conca di Fossa (L'Aquila). *Il Quaternario (Italian Journal of Quaternary Science)* 6, 293- 314.
- Boncio, P., G. Lavecchia and B. Pace (2004), Defining a model of 3D seismogenic sources for Seismic Hazard Assessment applications: the case of central Apennines (Italy), *J. Seismol.*, 8(3), 407–425.
- Boncio, P., A. Pizzi, F. Brozzetti, G. Pomposo, G. Lavecchia, D. Di Naccio and F. Ferrarini (2010), Coseismic ground deformation of the 6 April 2009 L'Aquila earthquake (central Italy, Mw6.3), *Geophys. Res. Lett.*, 37, L06308, doi:10.1029/2010GL042807.
- Boschi, E., D. Giardini, D. Pantosti, G. Valensise, R. Arrowsmith, P. Basham, R. Bürgmann, A.J. Crone, A. Hull, R.K. McGuire, D. Schwartz, K. Sieh, S.N. Ward and R.S. Yeats (1996). New trends in active faulting studies for seismic hazard assessment. *Annali di Geofisica*, XXXIX, 1301-1307.
- Bosi C. and Bertini T. (1970), La geologia della media valle dell'Aterno. *Mem. Soc. Geol. It.* 9, 719-777.
- Bosi C., Galadini F., Giaccio B., Messina P. and Sposato A. (2003), Plio-Quaternary continental deposits in the Latium-Abruzzi Apennines: the correlation of geological events across different intermontane basins. *Il Quaternario (Italian Journal of Quaternary Sciences)* 16, 55-76.
- Bronk Ramsey, C. (2008). Deposition models for chronological records. *Quaternary Science Reviews*, 27(1-2), 42-60.
- Brunori, C.A., Civico, R., Cinti, F.R., Ventura, G., (2011), Characterization of active fault scarps from LiDAR data: a case study from Central Apennines (Italy), submitted to *International Journal of Geographical Information Science*
- Burbank, D. W., & Anderson, R. S. (2001). *Tectonic Geomorphology*. Oxford: Blackwell Science, 274 p.
- Calamita F. and Pizzi A. (1994), Recent and active extensional tectonics in the southern Umbro-Marche Apennines (Central Italy). *Mem. Soc. Geol. It.* 48, 541-548.
- Caputo, R., S. Piscitelli, A. Oliveto, E. Rizzo and V. Lapenna (2003), The use of electrical resistivity tomographies in active tectonics: Examples from the Tyrnavos Basin, Greece, *J. Geodyn.*, 36, 19–35, doi:10.1016/S0264-3707(03)00036-X.
- Cartwright, J.A., Trudgill, B.D., Mansfield, C.S., 1995. Fault growth by segment linkage: an explanation for scatter in maximum displacement and trace length data from the Canyonlands grabens of SE Utah. *Journal of Structural Geology* 17, 1319±1326.
- Casas, D., Ercilla, G., Lykousis, V., Chryssanthi, I. and Perissoratis, C., (2006), Physical properties and their relationship to sedimentary processes and texture in sediments from mud volcanoes in the Anaximander Mountains (Eastern Mediterranean), *Scientia Marina* 70(4), 643-659.
- Caskey, S. J., S. G. Wesnousky, P. Zhang and D. B. Slemmons (1996), Surface faulting of the 1954 Fairview Peak (MS 7.2) and Dixie Valley (MS 6.8) earthquakes, central Nevada, *Bulletin of the Seismological Society of America*, Jun 1996; 86: 761 – 787.
- Casnedi, R., U. Crescenti, C. D'amato, F. Mostardini, and U. Rossi (1981), Il Plio-Pleistocene del sottosuolo molisano, *Geol. Romana*, 20, 1 – 42.

- Castello, B., Olivieri, M. & Selvaggi, G., (2007), Local and duration magnitude determination for the Italian earthquake catalogue (1981–2002), *Bull. Seism. Soc. Am.*, 97(1B), 128–139.
- Cavinato G.P., Cosentino D., De Rita D., Funicciello R. and Parotto M. (1994), Tectonic-sedimentary evolution of intrapenninic basins and correlation with the volcano-tectonic activity in central Italy. *Memorie Descrittive della Carta Geologica d'Italia* 49, 63-76.
- Cavinato G.P. and De Celles P.G. (1999), Extensional basins in the tectonically bimodal central Apennines fold-thrust belt, Italy: response to corner flow above a subducting slab in retrograde motion. *Geology* 27(10), 955-958.
- Centamore E. and Nisio S. (2003), The effects of uplift and tilting in the Central Apennine. *Quaternary International* 101-102 (2003), 93-101.
- Cheloni, D., N. D'Agostino, E. D'Anastasio, A. Avallone, S. Mantenuto, R. Giuliani, M. Mattone, S. Calcaterra, P. Gambino, D. Dominici, F. Radicioni and G. Fastellini (2010), Coseismic and initial post-seismic slip of the 2009 Mw6.3 L'Aquila earthquake, Italy, from GPS measurements, *Geophys. J. Int.*, 181, 1539-1546, doi:10.1111/j.1365-246x.2010.04584.x.
- Chiarabba, C., L. Jovane and R. Di Stefano (2005), A new view of Italian seismicity using 20 years of instrumental recordings, *Tectonophysics*, 395, 251–268, doi:10.1016/j.tecto.2004.09.013.
- Chiarabba, C., A. Amato, M. Anselmi, P. Baccheschi, I. Bianchi, M. Cattaneo, G. Cecere, L. Chiaraluce, M. G. Ciaccio, P. De Gori, G. De Luca, M. Di Bona, R. Di Stefano, L. Faenza, A. Govoni, L. Improta, F. P. Lucente, A. Marchetti, L. Margheriti, F. Mele, A. Michelini, G. Monachesi, M. Moretti, M. Pastori, N. Piana Agostinetti, D. Piccinini, P. Roselli, D. Seccia and L. Valoroso (2009), The 2009 L'Aquila (central Italy) Mw6.3 earthquake: main shock and aftershocks, *Geophys. Res. Lett.*, 36, L18308, doi:10.1029/2009GL039627.
- Chiaraluce L., Valoroso L., Anselmi M., Bagh S. and Chiarabba C.; 2009: A decade of passive seismic monitoring experiments with local networks in four Italian regions. *Tectonophysics*, 476, 85-98.
- Ciaccio M.G., Palombo B. and Bernardi F. (2009), The main seismic sequences occurred between 1981-2008 in the L'Aquila region. In: *Proceedings FIST, Rimini* 9-11 September 2009.
- Ciarapica G. and Passeri L. (2002), The paleogeographic duplicity of the Apennines. *Boll. Soc. Geol. It., Vol. spec. 1*, 67-75.
- Cinque, A., Patacca, E., Scandone, P., Tozzi, M., 1993. Quaternary kinematic evolution of the Southern Apennines. Relationships between surface geological features and deep lithospheric structures. *Annali di Geofisica* 36, 249–260.
- Cinti, F. R., L. Faenza, W. Marzocchi and P. Montone (2004), Probability map of the next large earthquakes in Italy, *G Cubed*, 5, 1. doi:10.1029/2004GC000724.
- Cinti, F.R., Pantosti, D., De Martini, P.M. Pucci, S., Civico, R., Pierdominici, S., Cucci, L., Brunori, C.A., Pinzi, S. and Patera, A., (2011), Evidence for surface faulting events along the Paganica fault prior to The 6 April 2009 L'Aquila Earthquake Central Italy. *J. Geophys. Res.*, 116, B07308, doi:10.1029/2010jb007988.
- Cirella, A., A. Piatanesi, M. Cocco, E. Tinti, L. Scognamiglio, A. Michelini, A. Lomax and E. Boschi (2009), Rupture history of the 2009 L'Aquila (Italy) earthquake from non-linear joint inversion of strong motion and GPS data, *Geophys. Res. Lett.*, 36, L19304. doi:10.1029/2009GL039795.

- Cohen, K.M., and Gibbard, P., (2010), Global chronostratigraphical correlation table for the last 2.7 million years, v. 2010, documentation at: <http://www.quaternary.stratigraphy.org.uk/charts>
- Collettini C., Sibson R.H. (2001), Normal faults, normal friction?: *Geology*, v. 29, p. 927–930, doi: 10.1130/0091-7613(2001)029<0927:NFNF>2.0.CO;2.
- Consiglio Nazionale delle Ricerche (1992), Structural model of Italy and gravity map, scale 1:500,000, Progetto Finalizzato Geodin, vol. 3, Quad. Ric. Sci., 114.
Cosentino D. and Parotto M. (1986), Assetto strutturale dei Monti Lucretili settentrionali (Sabina): nuovi dati e schema tettonico preliminare. *Geol. Romana* 25, 73-90.
- CPTI Working Group (2004), Catalogo Parametrico dei Terremoti Italiani, versione 2004 (CPTI04), INGV, Bologna. Available at: <http://emidius.mi.ingv.it/CPTI04/>.
- Cunningham, D., S. Grebby, K. Tansey, A. Gosar and V. Kastelic (2006) Application of airborne LiDAR to mapping seismogenic faults in forested mountainous terrain, southeastern Alps, Slovenia, *Geophys. Res. Lett.*, 33, L20308, doi:10.1029/2006GL027014.
- D'Addezio, G., E. Masana, D. Pantosti (2001), The Holocene paleoseismicity of the Aremogna-Cinque Miglia Fault (central Italy), *J. Seismol.*, 5, 181-205.
- D'Agostino, N., F. Speranza, and R. Funicello (1997), Le Breccie Mortadella dell'Appennino Centrale: primi risultati di stratigrafia magnetica, *Il Quaternario*, 10 (2), 385-388.
- D'Agostino N., Jackson JA., Dramis F., Funicello R. (2001), Interactions between mantle upwelling, drainage evolution and active normal faulting: an example from the central Apennines (Italy). *Geophys. J. Int.* 147, 475- 479.
- D'Agostino, N., Mantenuto, S., D'Anastasio, E., Giuliani, R., Mattone, M., Calcaterra, S., Gambino, P., and L. Bonci (2011), Evidence for localized active extension in the central Apennines (Italy) from global positioning system observations, *Geology*, April 2011, v. 39, p. 291-294, doi:10.1130/G31796.1.
- Davis, G.H., and Reynolds, S.J., 1996, *Structural Geology of Rocks and Regions* (2nd Edition): New York, John Wiley and Sons, Inc., 776 p.
- Dewey, J. F., Pitman, W. C., Ryan, W. B. F., and Bonnin, J. (1973), Plate Tectonics and the Evolution of the Alpine System, *Bull. Geol. Soc. Am.* 84, 3137–3180.
- DeLong, S. B., G. E. Hilley, M. J. Rymer and C. Prentice (2010). Fault zone structure from topography: Signatures of an echelon fault slip at Mustang Ridge on the San Andreas Fault, Monterey County, California, *Tectonics*, 29, TC5003, doi:10.1029/2010TC002673.
- De Luca G., Scarpa R., Filippi L., Gorini A., Marcucci S., Marsan P., Milana G. and Zambonelli E. (2000), A detailed analysis of two seismic sequences in Abruzzo, central Apennines, Italy. *Jour. Seismol.*, 4, 1-21.
- Demanet, D., Renardy, F., Vanneste, K., Jongmans, D., Camelbeeck, T., and Meghraoui, M., (2001), The use of geophysical prospecting for imaging active faults in the Roer Graben, Belgium: *Geophysics*, Vol. 66, No.1, P. 78-89.
- Dietrich W. E., D. Bellugi and R. R. Asua (2001), Validation of the Shallow Landslide Model, SHALSTAB, for Forest Management. In *Land Use and Watershed: Human Influence on Hydrology and Geomorphology in Urban Forest Areas*. Water Science Application. AGU Vol., 2, 195-227.
- Dorsey, R. J., B. A. Housen, S. U. Janecke, C.M. Fanning and A. L.F. Spears (2011), Stratigraphic record of basin development within the San Andreas fault system: Late

- Cenozoic Fish Creek–Vallecito basin, southern California, *Geological Society of America Bulletin*, May 2011, v. 123, no. 5-6, p. 771-793, doi:10.1130/B30168.1
- Doser, D. I. (1986), Earthquake processes in the Rainbow Mountain-Fairview Peak-Dixie Valley, Nevada region 1954-1959, *J. Geophys. Res.*, 91, 12,572-12,586.
 - Dramis, F. (1983), Morfogenesi di versante nel Pleistocene superiore in Italia: i depositi detritici stratificati, *Geografia Fisica e Dinamica Quaternaria*, 6, 180-182.
 - Dramis, F., A. M. Blumetti (2005), Some considerations concerning seismic geomorphology and paleoseismology, *Tectonophysics*, 408, 1-4, 177-191, doi:10.1016/j.tecto.2005.05.032.
 - Duller, G. A. T. (2004), Luminescence dating of Quaternary sediments: Recent advances. *Journal of Quaternary Science* 19, 183–192.
 - Emergeo Working Group (2010), Evidence for surface rupture associated with the Mw 6.3 L'Aquila earthquake sequence of April 2009 (central Italy), *Terra Nova*, 22, 1, 43-51, doi: 10.1111/j.1365-3121.2009.00915.x.
 - Falcucci, E., S. Gori, E. Peronace, G. Fubelli, M. Moro, M. Saroli, B. Giaccio, P. Messina, G. Naso, G. Scardia, A. Sposato, M. Voltaggio, P. Galli and F. Galadini (2009), The Paganica Fault and surface coseismic ruptures caused by the 6 April 2009 earthquake (L'Aquila, central Italy), *Seism. Res. Lett.*, 80, 6, 940-950.
 - Frankel, K. L., J. F. Dolan, R. C. Finkel, L. A. Owen and J. S. Hoefft (2007). Spatial variations in slip rate along the Death Valley-Fish Lake Valley fault system determined from LiDAR topographic data and cosmogenic ¹⁰Be geochronology, *Geophys. Res. Lett.*, 34, L18303, doi:10.1029/2007GL030549.
 - Friedrich, A. M., B. P. Wernicke, N. A. Niemi, R. A. Bennett, and J. L. Davis, (2003), Comparison of geodetic and geologic data from the Wasatch region, Utah, and implications for the spectral character of Earth deformation at periods of 10 to 10 million years, *J. Geophys. Res.*, 108(B4), 2199, doi:10.1029/2001JB000682.
 - Gabriel, A. K., R. M. Goldstein, and H. A. Zebker (1989), Mapping small elevation changes over large areas: Differential interferometry, *J. Geophys. Res.*, 94, 9183–9191, doi:10.1029/JB094iB07p09183.
 - Galadini, F. and P. Galli (1999), The Holocene paleoearthquakes on the 1915 Avezzano earthquake faults (central Italy): implications for active tectonics in the central Apennines, *Tectonophysics*, 308, 1-2, 143-170, doi:10.1016/S0040-1951(99)00091-8.
 - Galadini F., Galli P. (2000). Active tectonics in the central Apennines (Italy) Input data for seismic hazard assessment. *Nat Hazards* 22, 225-270.
 - Galadini, F. and P. Galli (2003), Paleoseismology of silent faults in the Central Apennines (Italy): the Mt. Vettore and Laga Mts. Faults, *Ann. Geophys.*, 46, n. 5, 815-836.
 - Galadini, F., P. Galli and M. Moro (2003a), Paleoseismology of silent faults in the Central Apennines (Italy): the Campo Imperatore Fault (Gran Sasso Range Fault System), *Ann. Geophys.*, 46, 793–813.
 - Galadini F., Messina P., Giaccio B., Sposato A. (2003b). Early uplift history of the Abruzzi Apennines (central Italy): available geomorphological constraints. *Quat. Int.* 101-102, 125-135.
 - Galadini F., Messina P. (2004). Early-Middle Pleistocene eastward migration of the Abruzzi Apennine (central Italy) extensional domain. *J. Geodyn.* 37, 57-81.
 - Galadini, F., D. Pantosti, P. Boncio, P. Galli, P. Messina, P. Montone, A. Pizzi and S. Salvi (2009), Il terremoto del 6 aprile e le conoscenze sulle faglie attive dell'Appennino centrale. *Progettazione Sismica*, 3, 1, 37-48.

- Galli, P., F. Galadini, M. Moro and C. Giraudi (2002), New paleoseismological data from the Gran Sasso d'Italia area (central Apennines), *Geophys. Res. Lett.*, 29, 38.1–38.4. doi:10.1029/2001GL013292.
- Galli P., Galadini F., Pantosti D. (2008). Twenty years of paleoseismology in Italy. *Earth-Science Rev.* 88, 89-117.
- Galli, P. and R. Camassi, eds. (2009), Report on the effects of the Aquilano earthquake of 6 April 2009; Dipartimento della Protezione Civile Istituto Nazionale di Geofisica e Vulcanologia QUEST Team, http://www.mi.ingv.it/eq/090406/quest_eng.html.
- Galli, P., B. Giaccio, P. Messina (2010), The 2009 central Italy earthquake seen through 0.5 Myr-long tectonic history of the L'Aquila faults system, *Quaternary Science Reviews*, 29, 3768-3789, doi:10.1016/j.quascirev.2010.08.018.
- Gasperini, P., G. Vannucci, D. Tripone and E. Boschi (2010), The location and sizing of historical earthquakes using the attenuation of macroseismic intensity with distance, *Bull. Seism. Soc. Am.*, 100, 5A, 2035-2066, doi:10.1785/0120090330.
- Glenn, N. F., D. R. Streutker, D. J. Chadwick, G. D. Thackray, S. J. Dorsch (2006), Analysis of LiDAR-derived topographic information for characterizing and differentiating landslide morphology and activity, *Geomorphology*, Volume 73, Issues 1-2, Pages 131-148, ISSN 0169-555X, 10.1016/j.geomorph.2005.07.006.
- Gruppo di Lavoro M.P.S. (2004), Redazione della mappa di pericolosità sismica prevista dall'Ordinanza PCM del 20 marzo 2003, Rapporto Conclusivo per il Dipartimento della Protezione Civile, INGV, Aprile 2004, 65pp. + 5 appendici. Available at: <http://zonesismiche.mi.ingv.it/>.
- Haugerud, R. A., D. J. Harding, S. Y. Johnson, J. Harless, C. S. Weaver and B. L. Sherrod, (2003), High-resolution lidar topography of the Puget Lowland, Washington - A bonanza for earth science: *GSA Today*, v. 13, no. 6, p. 4–10.
- Hasegawa, H., H. P. Sato and J. Iwahashi (2007), Continuous Caldera Changes in Miyakejima Volcano after 2001. *Bulletin of the GSI*, 54, 60-64.
- Hilley, G. E., S. DeLong, C. Prentice, K. Blisniuk and J. R. Arrowsmith (2010), Morphologic dating of fault scarps using airborne laser swath mapping (ALSM) data, *Geophys. Res. Lett.*, 37, L04301, doi:10.1029/2009GL042044.
- Hunstad, I., Selvaggi, G., D'Agostino, N., England, P., Clarke, P., Pierozzi, M., 2003. Geodetic strain in peninsular Italy between 1875 and 2001. *Geophys. Res. Lett.* 30 (4), 1181. doi:10.1029/2002GL016447.
- IAEA (2010), Seismic hazards in site evaluation for nuclear installations, Safety Standards Series No. SSG-9, p. 60, <http://www-ns.iaea.org/standards/>.
- Improta, L., A. Zollo, P. P. Bruno, A. Herrero, and F. Villani (2003), High resolution seismic tomography across the 1980(Ms 6.9) Southern Italy earthquake fault scarp, *Geophys. Res. Lett.*, 30(10), 1494, doi:10.1029/2003GL017077.
- Improta, L., L. Ferranti, P. M. De Martini, S. Piscitelli, P. P. Bruno, P. Burrato, R. Civico, A. Giocoli, M. Iorio, G. D'addezio and L. Maschio (2010), Detecting young, slow-slipping active faults by geologic and multidisciplinary high-resolution geophysical investigations: A case study from the Apennine seismic belt, Italy. *J. Geophys. Res.*, 115, B11307, doi:10.1029/2010JB000871.
- Jackson J.A., White N.J. 1989, Normal faulting in the upper continental crust: Observations from regions of active extension: *Journal of Structural Geology*, v.11, p. 15–36, doi: 10.1016/0191-8141(89)90033-3.
- Jackson, J. and Blenkinsop, T. (1993). The Malawî earthquake of March 10, 1989: Deep faulting within the east African rift system. *Tectonics* 12(5): doi: 10.1029/93TC01064. issn: 0278-7407.

- Jackson, J., and T. Blenkinsop (1997), The Bilila-Mtakataka fault in Malaŵi: An active, 100-km long, normal fault segment in thick seismogenic crust, *Tectonics*, 16(1), 137–150, doi:10.1029/96TC02494.
- Karner, D.B., Marra, F. and Renne, P., (2001), The History of the Monti Sabatini and Alban Hills volcanoes: groundwork for assessing volcanic–tectonic hazards for Rome. *Journal of Volcanology and Geothermal Research* 107, 185–219.
- Kastens, K., et al. (1988), ODP Leg 107 in the Tyrrhenian Sea: Insights into passive margin and back-arc basin evolution, *Geol. Soc. Am. Bull.*, 100, 1140 – 1156.
- Keller, E.A., and Pinter, N., (2002), *Active Tectonics – Earthquakes, Uplift, and Landscape* (2nd edition): Prentice Hall, London, 362 p.
- Kim, D.C., Sung, J.Y., Park, S.C., Lee, G.H., Choi, J.H., Kim, G.Y., Seo, Y.K. and Kim, J.C., (2001), Physical and acoustic properties of shelf sediments, the South Sea of Korea, *Marine Geology* **179**, 39-50.
- Kondo, H., S. Toda, K. Okumura, K. Takada and T. Chiba (2008), A fault scarp in an urban area identified by LiDAR survey: A Case study on the Itoigawa–Shizuoka Tectonic Line, central Japan, *Geomorphology*, Volume 101, Issue 4, 1, Pages 731-739, ISSN 0169-555X, 10.1016/j.geomorph.2008.02.012.
- Lavecchia G. (1988), The Tyrrhenian-Apennines system: structural setting and seismotectogenesis. *Tectonophysics*, 147, 263-296.
- Lavecchia G., Barchi M., Brozzetti F. and Menichetti M. (1994). Sismicità e tettonica nell'area umbro-marchigiana. *Boll. Soc. Geol. It.* 113, 483-500.
- Lentini, F., S. Carbone, A. Di Stefano, and P. Guarnieri (2002), Stratigraphical and structural constraints in the Lucanian Apennines (southern Italy): Tools for reconstructing the geological evolution, *J. Geodyn.*, 34, 141–158, doi:10.1016/S0264-3707(02)00031-5.
- Loke, M.H., I. Acworth and T. Dahlin (2003), A comparison of smooth and blocky inversion methods in 2D electrical imaging surveys. *Exploration Geophysics*, 34, 182-187.
- Nederbragt, A.J., Thurow, J.W., Russell B. M., in Lyle, M., Koizumi, I., Richter, C., and Moore, T.C., Jr. (Eds.), 2000, *Proceedings of the Ocean Drilling Program, Scientific Results*, Vol. 167.
- Mazzoli, S., & Helman, M. (1994), Neogene Patterns of Relative Plate Motions for Africa-Europe: Some Implications for Recent Central Mediterranean Tectonics, *Geol. Rundsch.* 83, 464–468.
- Mariucci M.T., Montone P., Pierdominici S., 2010. Present-day stress in the surroundings of 2009 L'Aquila seismic sequence (Italy). *Geophys. J. Int.*, 182 (2), 1096-1102. doi: 10.1111/j.1365-246X.2010.04679.x
- Marra, F., D. B. Karner, C. Freda, M. Gaeta, and P. Renne (2009), Large mafic eruptions at Alban Hills volcanic district (central Italy): Chronostratigraphy, petrography and eruptive behaviour. *Journal of Volcanology and Geothermal Research* 179, 217–232.
- Marzocchi, W., J. Selva, F. R. Cinti, P. Montone, S. Pierdominici, R. Schivardi and E. Boschi (2009), On the recurrence of large earthquakes: new insights from a model based on interacting faults embedded in a realistic tectonic setting, *J. Geophys. Res.*, Vol. 114, B01307, doi:10.1029/2008JB005822.
- Mattson, A., R. L. Bruhn and G. T. Schuster (2003), Beneath the trench: High-resolution seismic tomograms and sediment cores applied to paleoseismology, Mercur, Utah, paper presented at Annual Meeting, Geol. Soc. of Am., Seattle, Wash., 2 –5 Nov.

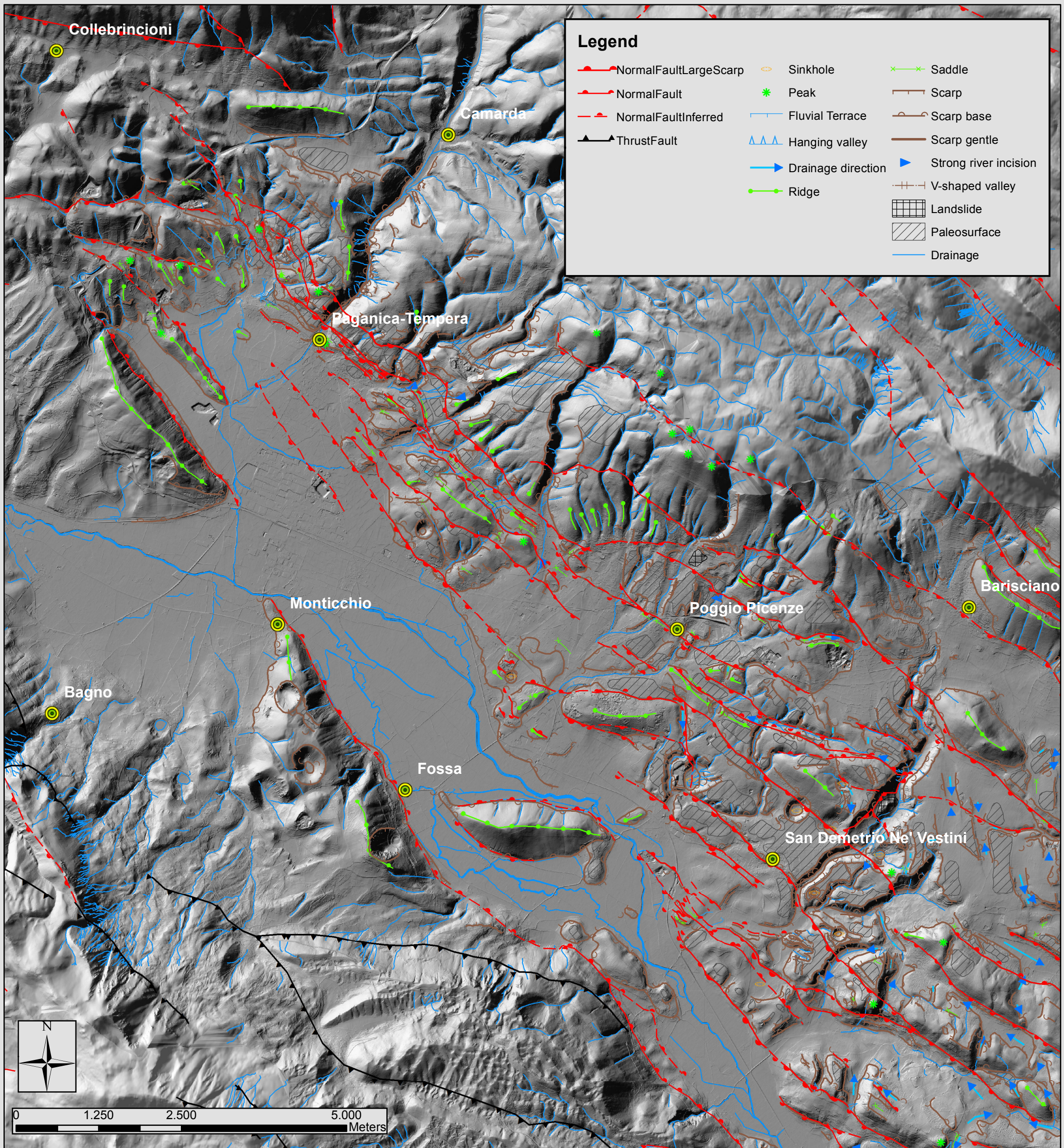
- Messina, P., P. Galli, B. Giaccio and E. Peronace (2009), Quaternary tectonic evolution of the area affected by the Paganica fault (2009 L'Aquila earthquake), 29th GNGTS Conference, Extended abstract Volume, pp. 47-50, Trieste (Italy), November 2009.
- Michetti, A. M., F. Brunamonte, L. Serva and E. Vittori (1996), Trench investigations of the 1915 Fucino earthquake fault scarps (Abruzzo, central Italy): Geological evidence of large historical events, *J. Geophys. Res.*, 101(B3), 5921–5936, doi:10.1029/95JB02852.
- Montone, P., Amato, A. & Pondrelli, S., 1999. Active stress map of Italy, *Journal of Geophysical Research.*, 104, 25 595–25 610.
- Montone, P., Mariucci, M. T., Pondrelli, S. and Amato, A. (2004), An improved stress map for Italy and surrounding regions (central Mediterranean), *J. Geophys. Res.*, 109, B10410.
- Morey, D., and G. T. Schuster (1999), Paleoseismicity of the Oquirrh fault, Utah, from shallow seismic tomography, *Geophys. J. Int.*, 138, 25–35, doi:10.1046/j.1365-246x.1999.00814.x.
- Moro, M., V. Bosi, F. Galadini, P. Galli, B. Giaccio, P. Messina and A. Sposato (2002), Analisi paleosismologiche lungo la faglia del M. Marine (alta valle dell'Aterno): Risultati preliminari, *Il Quaternario*, 15, 267–278.
- Murray, A.S. and Olley, J.M. (2002), Precision and accuracy in the optically stimulated luminescence dating of sedimentary quartz: a status review. *Geochronometria* 21, 1-15.
- Nguyen, F., Garambois, S., Chardon, D., Jongmans, D., Bellier, O., and Hermitte, D. (2003), Slow active fault detection and imaging using multiple geophysical methods: the Trevaresse thrust (Provence, France), *Geophys. Res. Abstracts*, 5, 10878, ISSN Print:1029-7006, ISSN Electronic: 1607–7962.
- Nguyen, F., S. Garambois, D. Jongmans, E. Pirard and M. H. Loke (2005), Image processing of 2D resistivity data for imaging faults, *J. Appl. Geophys.*, 57, 260–277, doi:10.1016/j.jappgeo.2005.02.001.
- Operto, S., C. Ravaut, L. Improta, J. Virieux, A. Herrero and P. Dell'aversana (2004), Quantitative imaging of complex structures from dense wide-aperture seismic data by multiscale travelttime and waveform inversions: a case study. *Geophys. Prospect.*, 52, 625– 651, doi:10.1111/j.13652478.2004.00452.x.
- Pace B., Boncio P. and Lavecchia G. (2002), The 1984 Abruzzo earthquake (Italy): an example of seismogenic process controlled by interaction between differently oriented synkinematic faults. *Tectonophysics*, 350, 237-254.
- Pace, B., L. Peruzza, G. Lavecchia and P. Boncio (2006), Layered seismogenic source model and probabilistic seismic hazard analyses in central Italy, *Bull. Seismol. Soc. Am.*, 96, 107–132.
- Pantosti, D., G. D'Addezio and F. R. Cinti (1996), Paleoseismicity of the Ovindoli-Pezza fault, central Apennines, Italy: a history including a large, previously unrecorded earthquake in the Middle Ages (860–1300 A.D.), *J. Geophys. Res.*, 101 (B3) 5937–5959.
- Papanikolaou, I. D., M. Fomelis, I. Parcharidis, E. L. Lekkas, and I. G. Fountoulis (2010), Deformation pattern of the 6 and 7 April 2009, MW=6.3 and MW=5.6 earthquakes in L'Aquila (Central Italy) revealed by ground and space based observations, *Nat. Hazards Earth Syst. Sci.*, 10, 73-87, doi:10.5194/nhess-10-73-2010.
- Patacca E., Sartori R. and Scandone P. (1990), Tyrrhenian basin and apenninic arcs: kinematic relations since late Tortonian times. *Mem. Soc. Geol. It.* 45, 425-451.

- Patacca, E., Sartori, R., Scandone, P., 1992. Tyrrhenian Basin and Apenninic Arcs: kinematics relations since Late Tortonian time. *Memorie della Società Geologica Italiana* 45, 425–451.
- Patacca E. and Scandone P. (2001), Late thrust propagation and sedimentary response in the thrust-belt-foredeep system of the southern Apennines (Pliocene- Pleistocene). In: Vai GB, Martini IP (ed), *Anatomy of an Orogen: the Apennines and Adjacent Mediterranean Basins*. Kluwer Academic Publishers, Dordrecht 401-440.
- Patacca, E., and P. Scandone (2007), *Geology of the southern Apennines*, *Boll. Soc. Geol. Ital.*, 7, 75–119.
- Pino, N. A. and F. Di Luccio (2009), Source complexity of the 6 April 2009 L'Aquila (central Italy) earthquake and its strongest aftershock revealed by elementary seismological analysis, *Geophys. Res. Lett.*, 36, L23305, doi:10.1029/2009GL041331.
- Pizzi A. (2003), Plio-Quaternary uplift rates in the outer zone of the central Apennine fold-and-thrust belt, Italy. *Quat. Int.*, 101-102, 229-237.
- Pondrelli, S., Salimbeni, S., Ekström, G., Morelli, A., Gasperini, P. & Vannucci, G., (2006), The Italian CMT dataset from 1977 to the present, *Phys. Earth planet. Int.*, 159, 286–303.
- Pondrelli, S., S. Salimbeni, A. Morelli, G. Ekström, M. Olivieri and E. Boschi (2010), Seismic moment tensors of the April 2009, L'Aquila (Central Italy), earthquake sequence, *Geophys. J. Int.* doi:10.1111/j.1365-246X.2009.04418.x.
- Reid, H.F. (1910), On mass-movements in tectonic earthquakes. The California earthquake of April 18, 1906. Report of the state earthquake investigation commission: Carnegie Institute of Washington, D.C.
- Reimer, P. J., M. G. Baillie, E. Bard, A. Bayliss, J. W. Beck, C. J. H. Bertrand, P.G. Blackwell, C. E. Buck, G. S. Burr, K. B. Cutler, P. E. Damon, R. L. Edwards, R. G. Fairbanks, M. Friedrich, T. P. Guilderson, A. G. Hogg, K. A. Hughen, B. Kromer, F. G. McCormac, S. W. Manning, C. B. Ramsey, R. W. Reimer, S. Remmele, J. R. Southon, M. Stuiver, S. Talamo, F. W. Taylor, J. van der Plicht and C. E. Weyhenmeyer, (2004), IntCal04 Terrestrial radiocarbon age calibration, 26 - 0 ka BP, *Radiocarbon* 46, 1029-1058.
- Roberts, G. and Michetti, A.M., (2004), Spatial and temporal variations in growth rate along active normal fault systems: an example from The Lazio Abruzzo Apennines, central Italy, *J. Struct. Geol.*, 26, 339–376, doi:10.1016/S0191-8141(03)00103-2.
- Roberts, G.P., P. Cowie, I. Papanikolaou and A. M. Michetti (2004), Fault scaling relationships, deformation rates and seismic hazards: an example from the Lazio–Abruzzo Apennines, central Italy, *J. Struct. Geol.*, 26, 377–398.
- Sallenger, A.H., W. Krabill, J. Brock, R. Swift, M. Jansen, S. Manizade, B. Richmond, M. Hampton and D. Eslinger (1999), Airborne laser study quantifies El Niño-induced coastal change: *Eos (Transactions American Geophysical Union)*, v. 80, p. 89, 92–93.
- Salustri Galli C., Torrini A., Doglioni C. and Scrocca D. (2002), Divide and highest mountains vs subduction in the Apennines. *Studi Geologici Camerti*, 1, 143-153.
- Salvi, S., F. R. Cinti, L. Colini, G. D'Addezio, F. Doumaz and E. Pettinelli (2003), Investigation of the active Celano–L'Aquila fault system, Abruzzi, *Geophys. J. Int.*, 155, 805–818.
- Scholz, C.H., *The Mechanics of Earthquakes and Faulting*, 439 pp., Cambridge Univ. Press, New York, 1990.
- Schwartz, D. P. and K. J. Coppersmith (1984), Fault Behavior and Characteristic Earthquakes: Examples From the Wasatch and San Andreas Fault Zones, *J. Geophys. Res.*, 89(B7), 5681–5698, doi:10.1029/JB089iB07p05681.

- Sherrod, B.L., T. M. Brocher, C. S. Weaver, R. C. Bucknam, R. J. Blakely, H. M. Kelsey, A. R. Nelson, R. Haugerud (2004), Holocene fault scarps near Tacoma, Washington, USA, *Geology* 32: 9-12.
- Shimazaki, K. and T. Nakata (1980), Time-predictable recurrence model for large earthquakes, *Geophys. Res. Lett.*, 7, 279–282.
- Silberling, N.J., and Wallace, R.E., 1967, Geologic map of the Imlay quadrangle, Pershing County, Nevada: U.S. Geological Survey Geologic quadrangle Map GQ-666, scale 1:62,500
- Slemmons, D.B., 1957, Geological effects of the Dixie Valley-Fairview Peak, Nevada, earthquakes of December 16, 1954: *Seismol. Soc. America Bull.*, v. 47, no. 4, p. 353-375.
- Slemmons, D.B., and De Polo C.M., 1986: Evaluation of active faulting and associated hazards, in: *Geophysics Study Committee: Active Tectonics*; National Academy Press, Washington D.C.
- State of California. (2007), “Alquist-Priolo Earthquake Fault Zones.” [Online] July, 11, 2008. <http://www.conservation.ca.gov/cgs/rghm/ap/Pages/affected.aspx>.
- Stewart, I.S. and P. L. Hancock (1990), What is a fault scarp? *Episodes* 13, pp. 256–263.
- Storz, H., Storz, W., and Jacobs, F. (2000), Electrical resistivity tomography to investigate geological structures of the earth’s upper crust, *Geophys. Prospect.*, 48, 455–471.
- Stuiver, M., Reimer, P. J., and Reimer, R. W. (2005). CALIB 6.0:<http://calib.qub.ac.uk/calib/>
- Suzuki, K., S. Toda, K. Kusunoki, Y. Fujimitsu, T. Mogi and A. Jomori (2000), Case studies of electrical and electromagnetic methods applied to mapping active faults beneath the thick quaternary, *Eng. Geol. Amsterdam*, 56, 29–45, doi:10.1016/S0013-7952(99)00132-5.
- Tertulliani, A., A. Rossi, L. Cucci and M. Vecchi (2009), L’Aquila (Central Italy) earthquakes: the predecessors of the April 6, 2009 event, *Seism. Res. Lett.*, 80, 6, 1008-1013.
- Thorarinsson S. (1974), The terms tephra and tephrochronology, in Westgate, J.A. and Gold, C.M., eds., *World bibliography and index of Quaternary tephrochronology*: University of Alberta, p. xix – xxi.
- Trasatti, E., C. Kyriakopoulos and M. Chini (2011), Finite element inversion of DInSAR data from the Mw 6.3 L’Aquila earthquake, 2009 (Italy), *Geophys. Res. Lett.*, 38, L08306, doi:10.1029/2011GL046714.
- Vezzani, L. and F. Ghisetti (1998), *Carta Geologica dell’Abruzzo*, Scala 1:100,000. S.EL.CA., Firenze.
- Wallace, R.E., Tatlock, D.B., Silberling, N.J., and Irwin, W.P., 1969, Geologic map of the Unionville quadrangle, Pershing County, Nevada: U.S. Geological Survey Geologic quadrangle Map GQ-820, scale 1:62,500.
- Wallace, R. E. (1977), Profiles and ages of young fault scarps, north-central Nevada. *Geological Society of America Bulletin* 88, 1267-1281.
- Wallace, R. E. (1987), Grouping and migration of surface faulting and variation in slip rates on faults in the Great Basin province, *Bull. Seismol. Soc. Am.*, 77, 868– 877.
- Wallace, R. E. (1989), Fault plane segmentation in brittle crust and anisotropy in loading system. In: *Fault Segmentation and Controls of Rupture Initiation and Termination* (edited by Schwartz, D. P. & Sibson, R. H.). U.S. geol. Surv. Open-file Rep. 89-315,400-408.

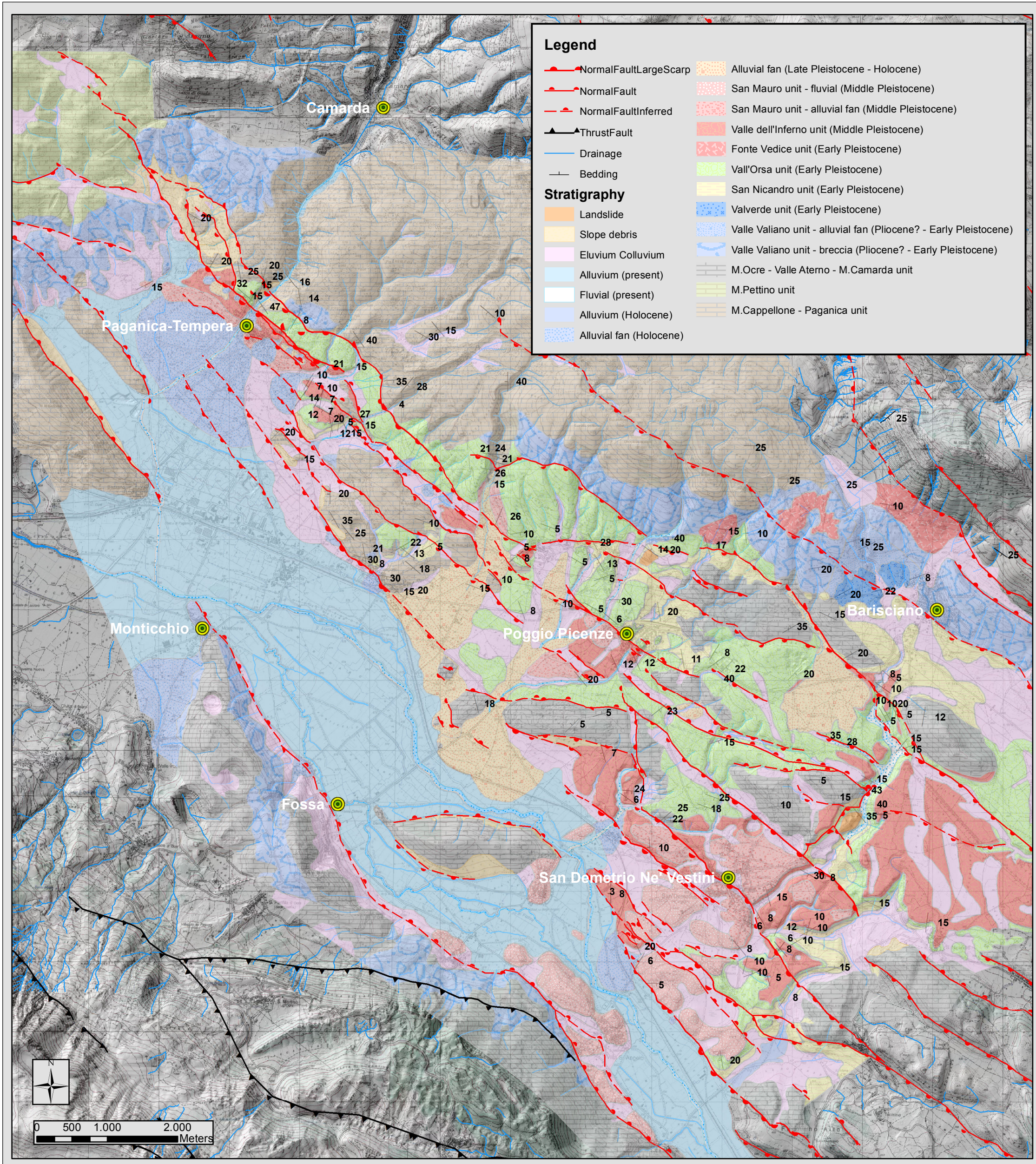
- Walters, R. J., J. R. Elliott, N. D'Agostino, P. C. England, I. Hunstad, J. A. Jackson, B. Parsons, R. J. Phillips and G. Roberts (2009), The 2009 L'Aquila earthquake (central Italy): A source mechanism and implications for seismic hazard, *Geophys. Res. Lett.*, 36, L17312, doi:10.1029/2009GL039337.
- Wells, D.L. and K.J. Coppersmith (1994), New empirical relationships among Magnitude, rupture length, rupture width, rupture area, and surface displacement, *Bull. Seismol. Soc. Am.*, 84, 974-1002.
- Wesnousky, S. G. (2005), Active faulting in the Walker Lane, *Tectonics*, 24, TC3009, doi:10.1029/2004TC001645.
- Wintle, A. G. 2008 (November): Luminescence dating: where it has been and where it is going. *Boreas*, Vol. 37, pp. 471-482. 10.1111/j.1502-3885.2008.00059.x. ISSN 0300-9483.
- Wise, D. J., J. Cassidy and C. A. Locke (2003), Geophysical imaging of the Quaternary Wairoa North Fault, New Zealand: A case study, *J. Appl. Geophys.*, 53, 1-16, doi:10.1016/S0926-9851(03)00013-2.
- Vittori, E., Di Manna, P., Blumetti, A.M., Commerci, V., Guerrieri, L., Esposito, E., Michetti, A.M., Porfido, S., Piccardi, L., Roberts, G.P., Berlusconi, A., Livio, F., Sileo, G., Wilkinson, M., McCaffrey, K.J.W., Phillips, R.J., and P.A. Cowie (2011), Surface faulting of the 6 April 2009 Mw 6.3 L'Aquila earthquake in central Italy, *Bulletin of the Seismological Society of America*, 101(4):1507-1530.
- WSSPC (Western States Seismic Policy Council) (2011), Definitions of Fault Activity for the Basin and Range Province. WSSPC Policy Recommendation 11-2 White Paper, April 4, 2011, Boise, Idaho, p.6.
- Yokoyama, Y., Lambeck, K., De Deckker, P., Johnston, P., Fifield, L.K., (2000), Timing of the Last Glacial Maximum from observed sea-level minima. *Nature* 406, 713-716.

APPENDIX A - GEOMORPHOLOGICAL MAP OF THE PAGANICA - SAN DEMETRIO FAULT SYSTEM



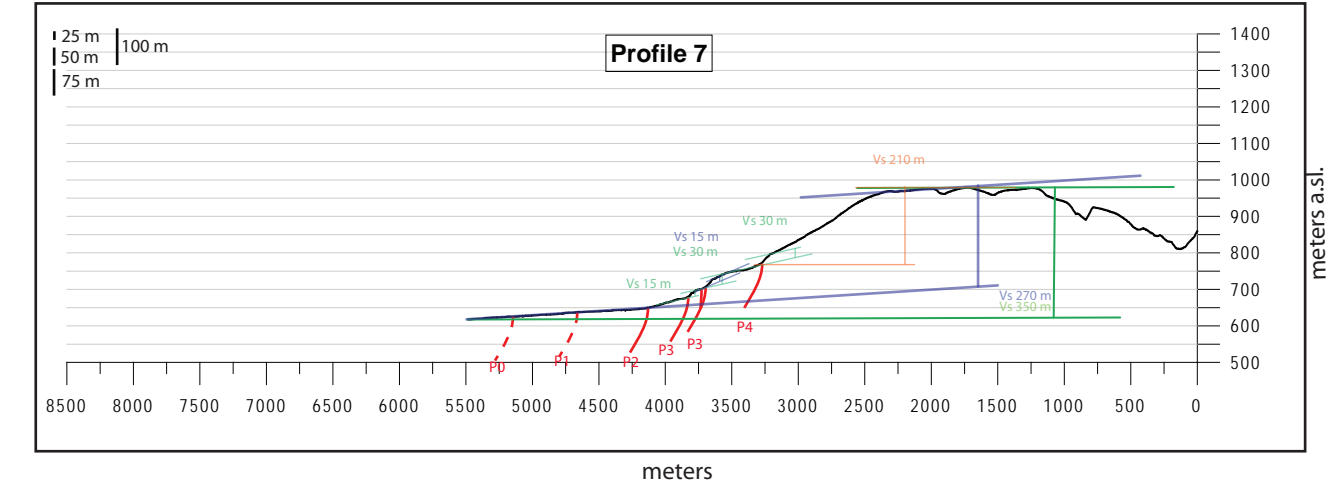
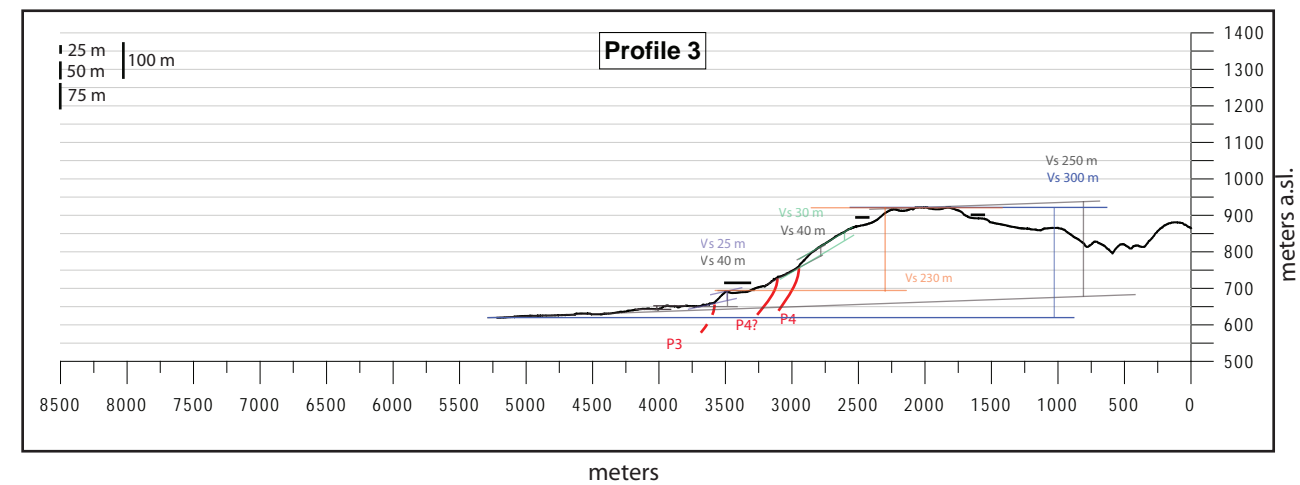
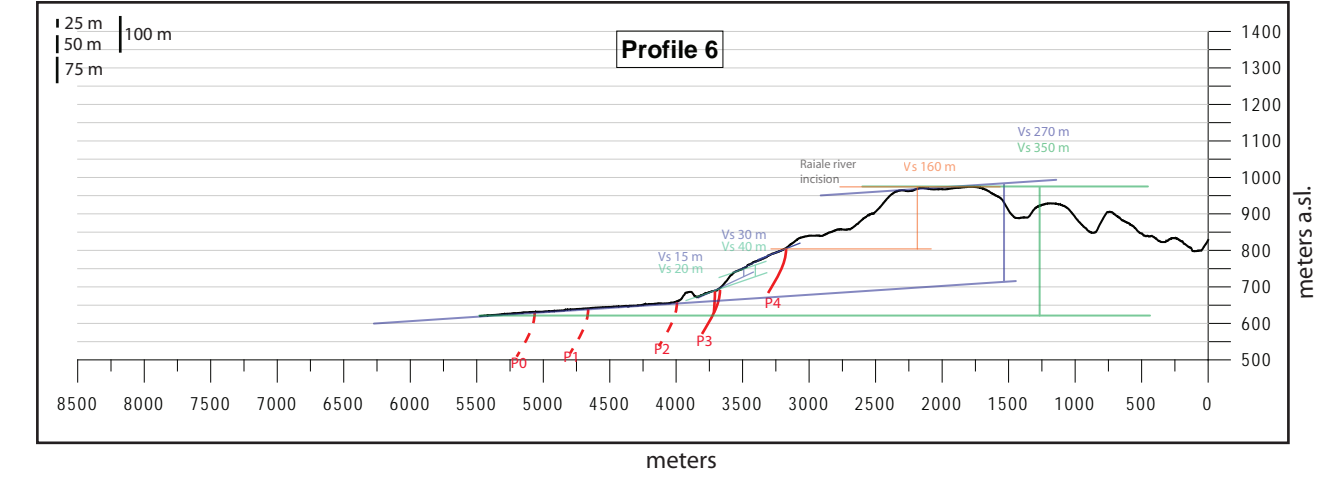
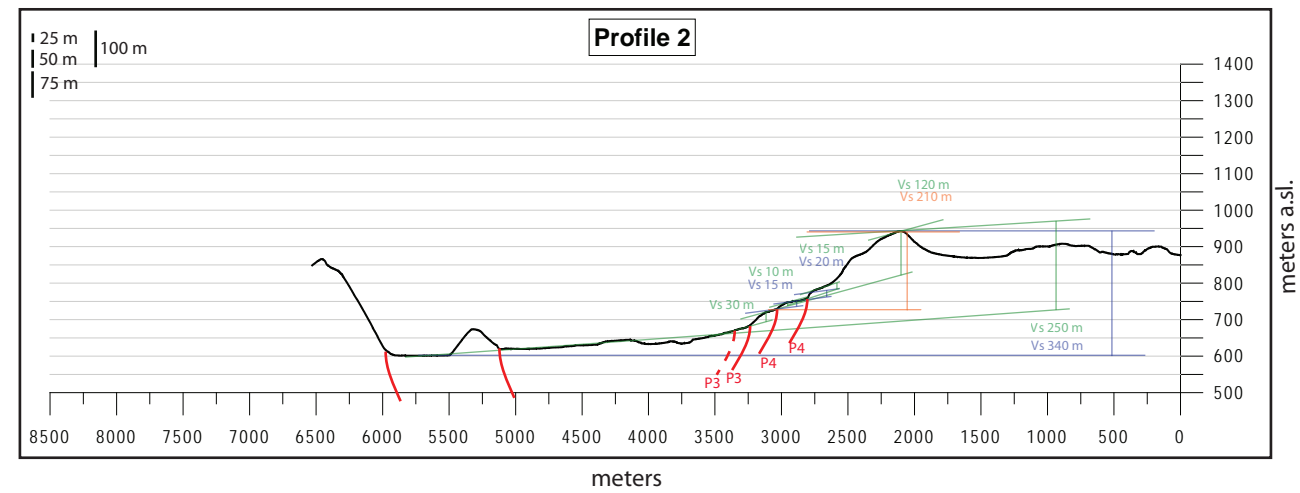
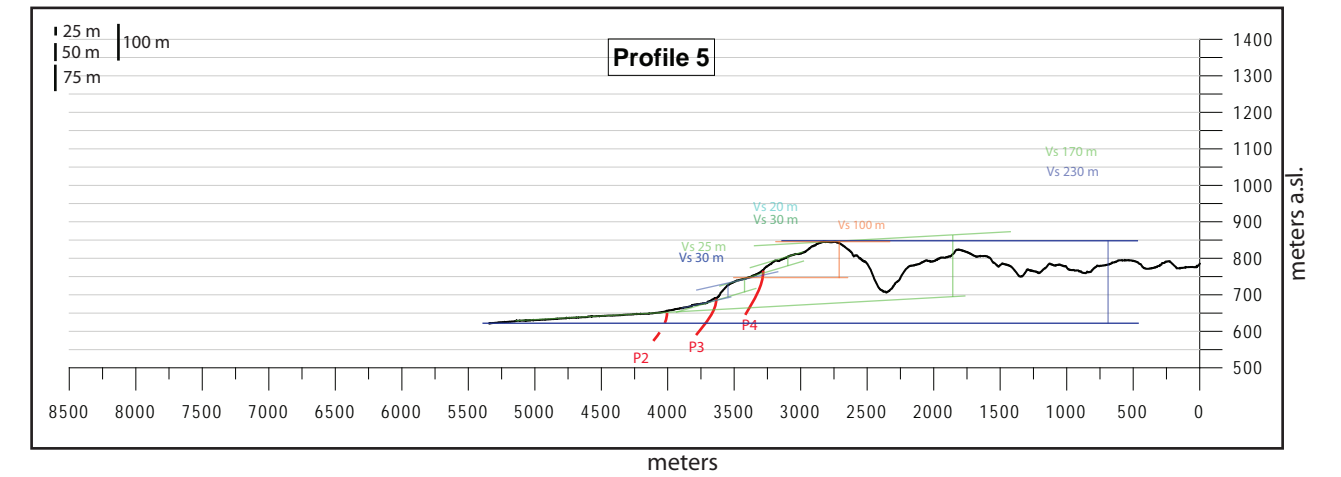
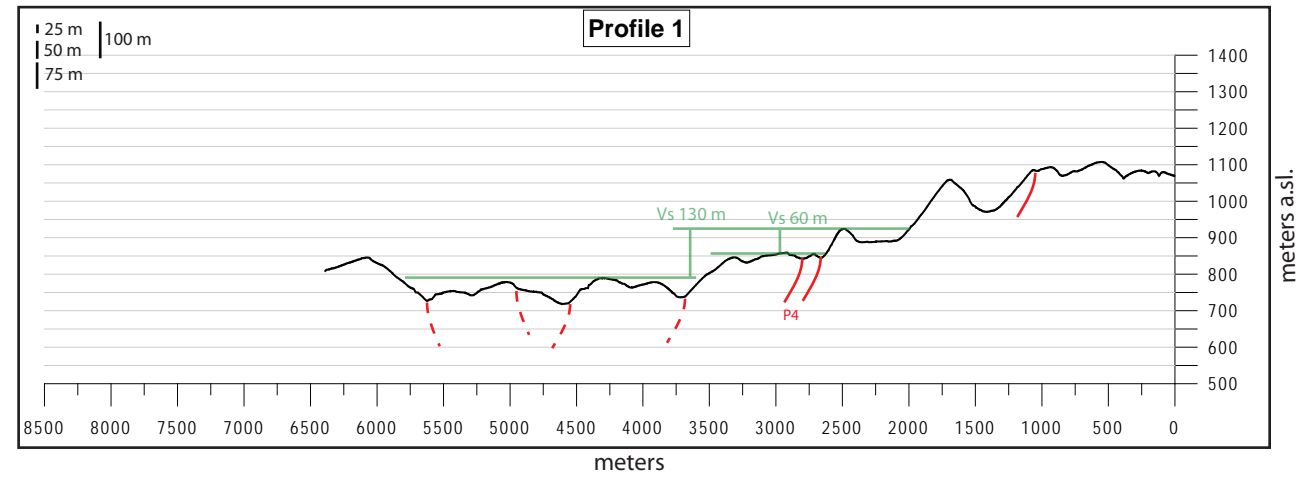
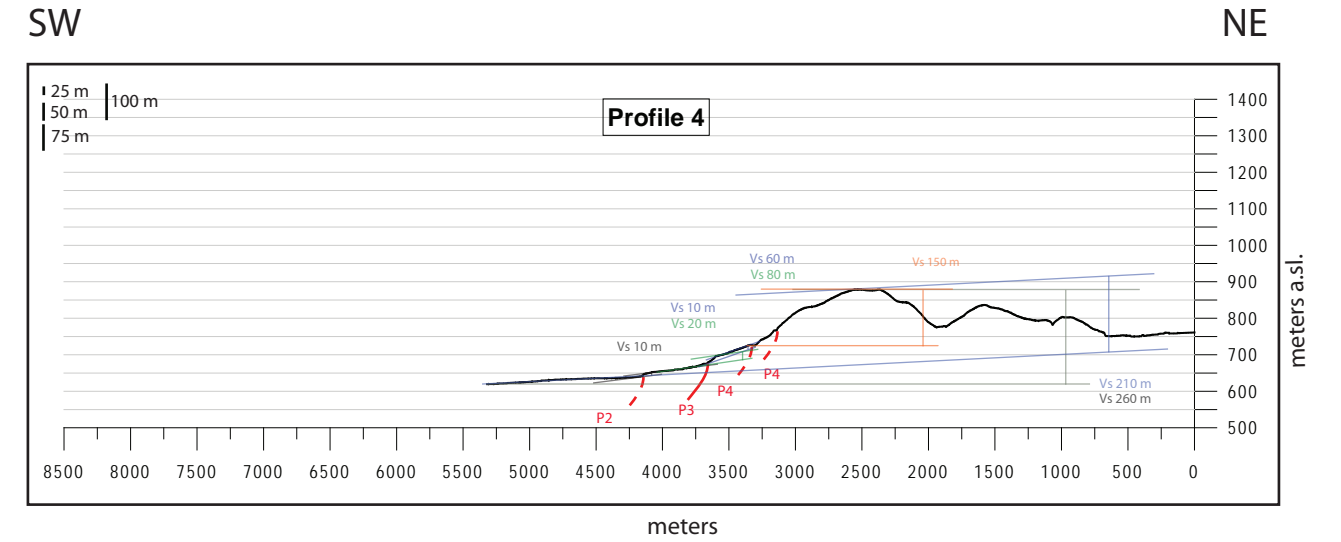
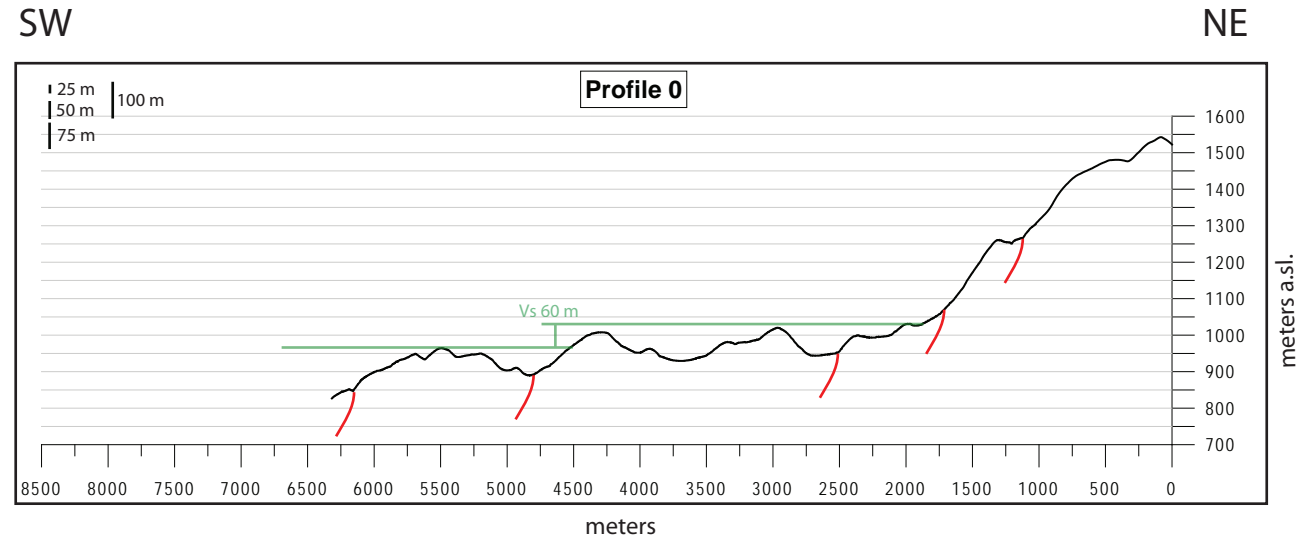
Riccardo Civico (2012) - Integrating new and traditional approaches for the estimate of slip-rates of active faults: examples from the Mw 6.3, 2009 L'Aquila earthquake area, Central Italy. PhD thesis.

APPENDIX B - GEOLOGICAL MAP OF THE PAGANICA - SAN DEMETRIO FAULT SYSTEM

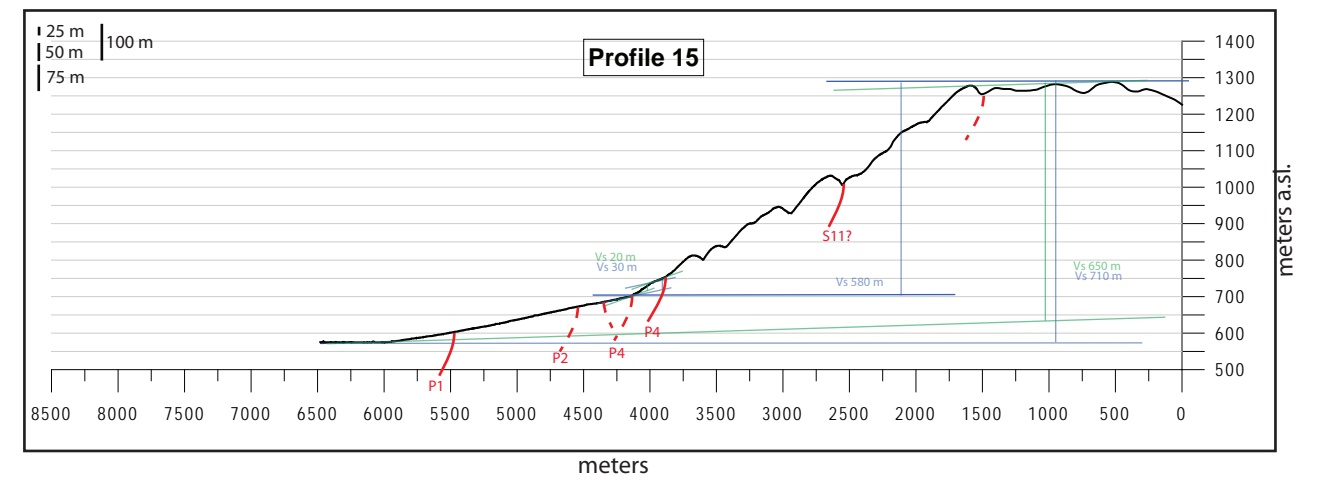
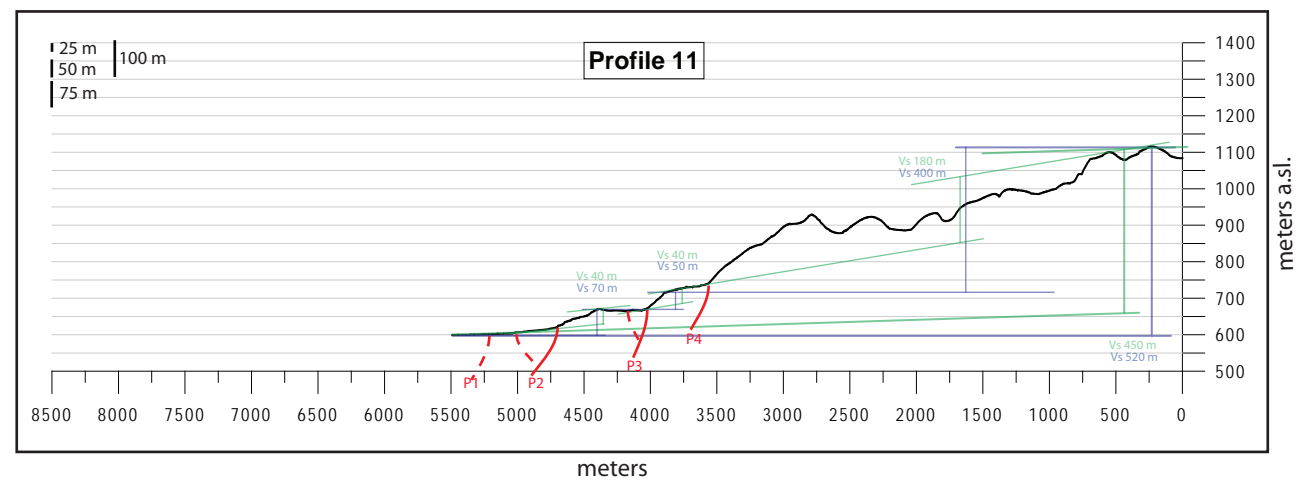
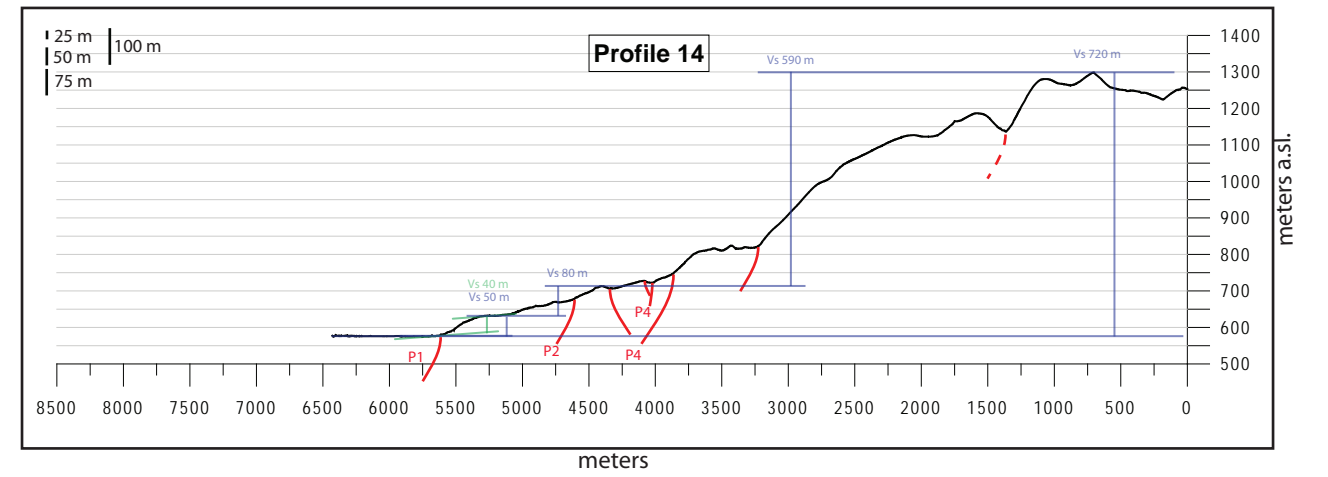
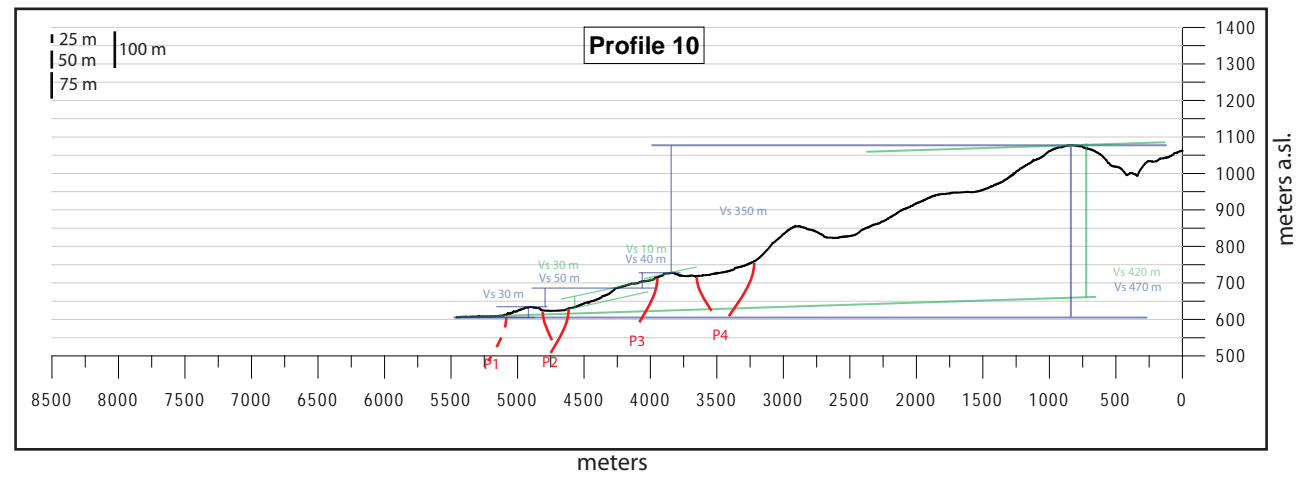
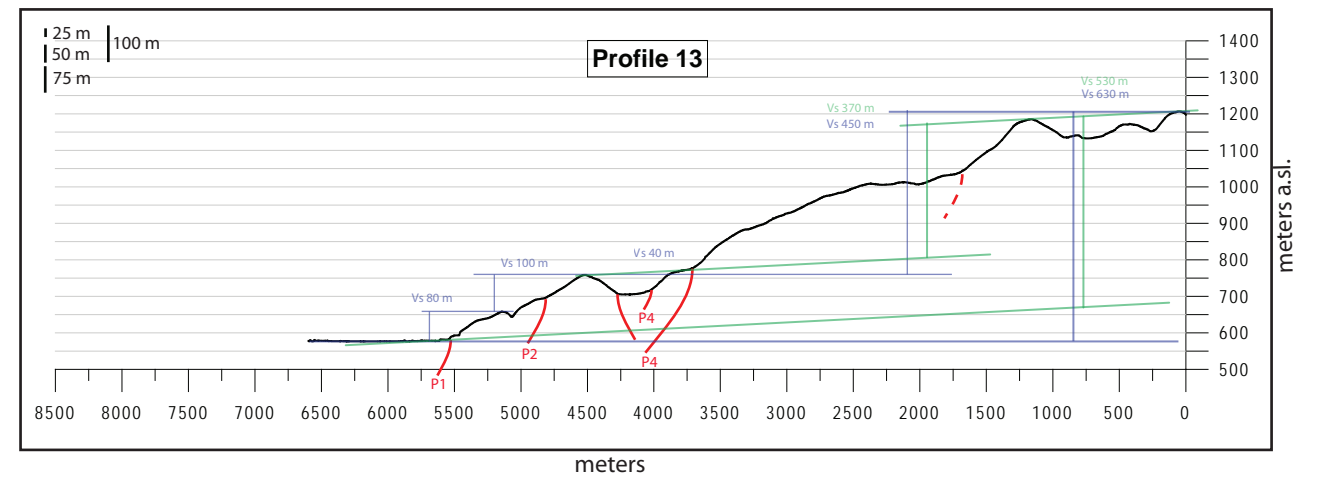
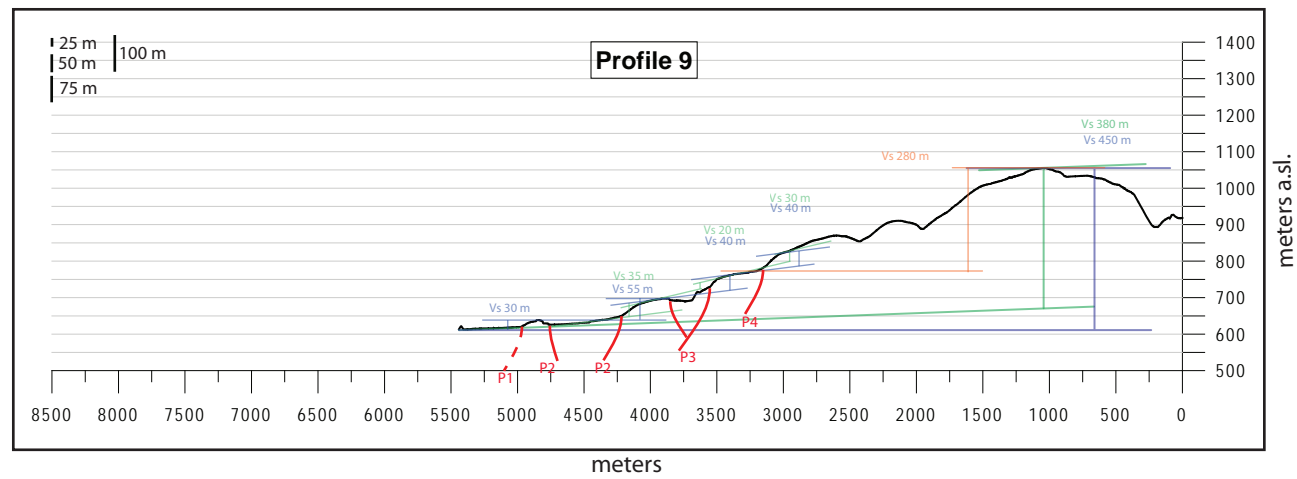
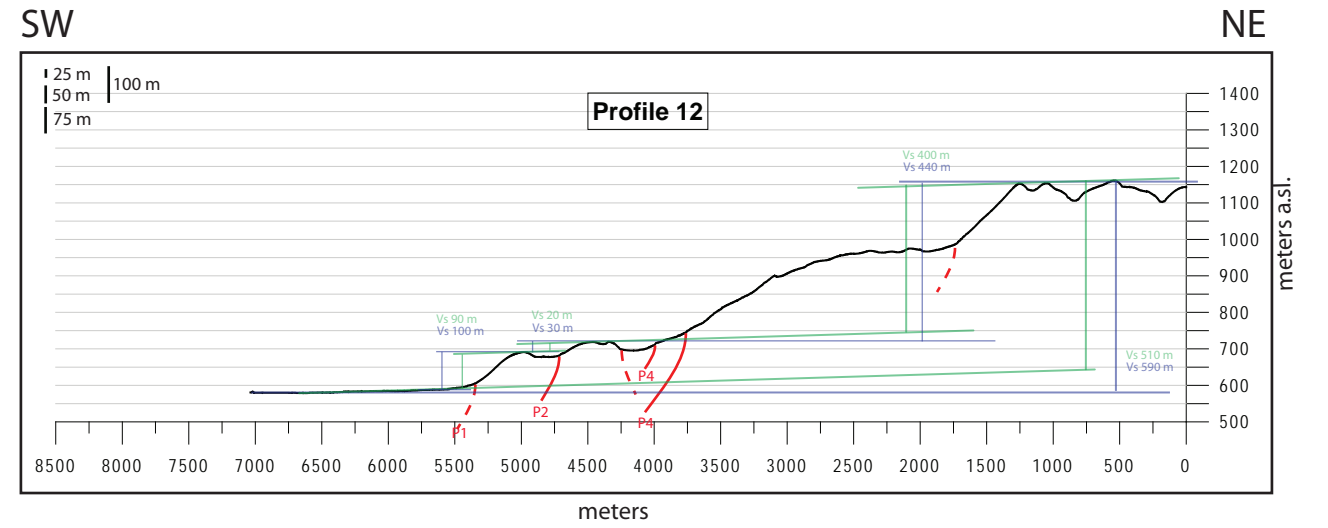
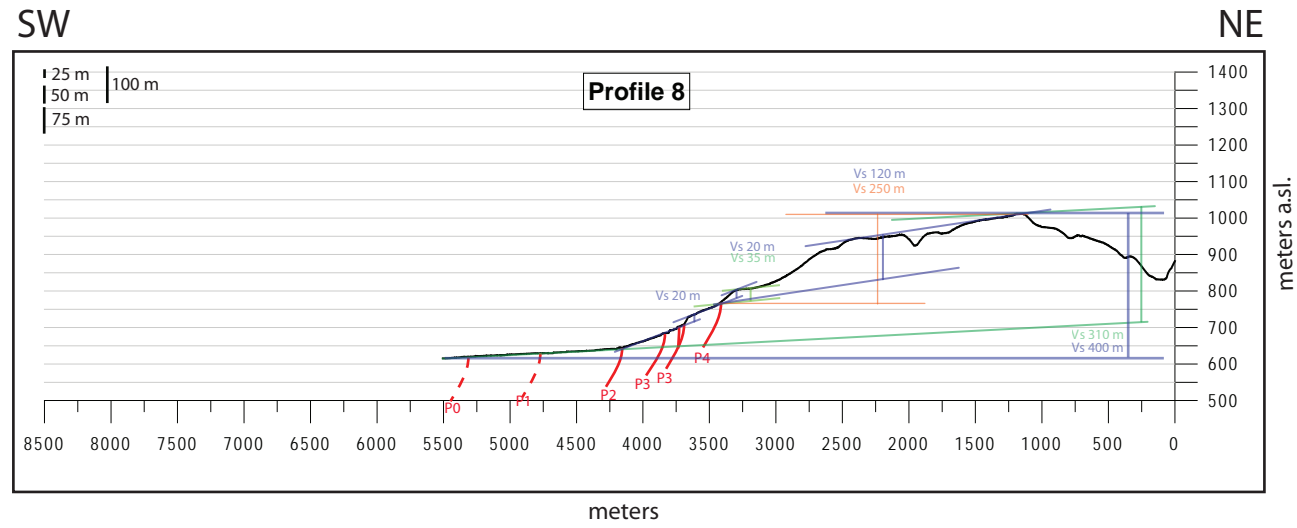


Riccardo Civico (2012) - Integrating new and traditional approaches for the estimate of slip-rates of active faults: examples from the Mw 6.3, 2009 L'Aquila earthquake area, Central Italy. PhD thesis.

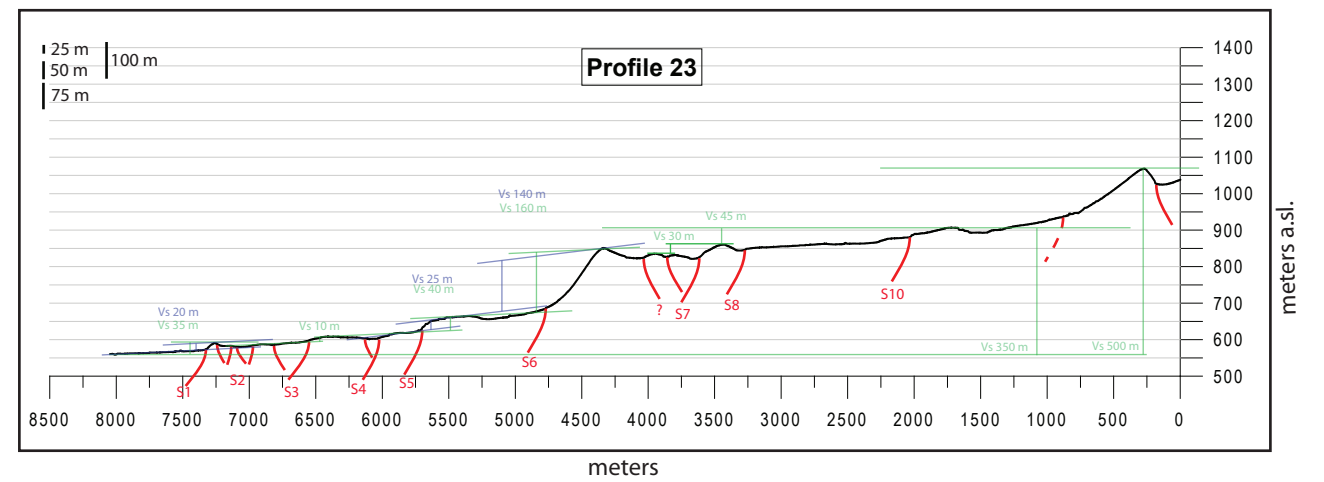
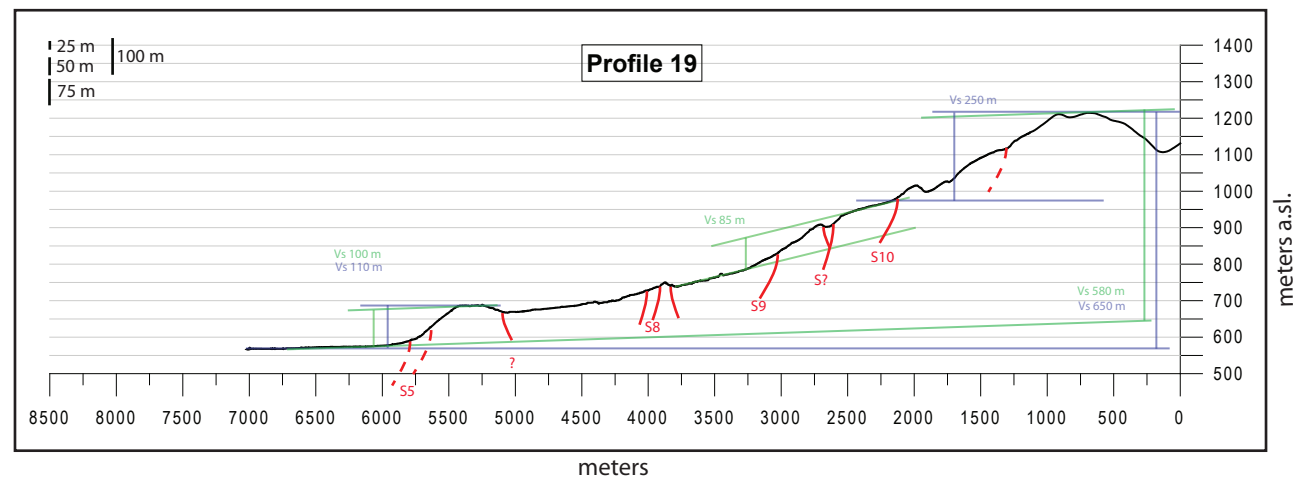
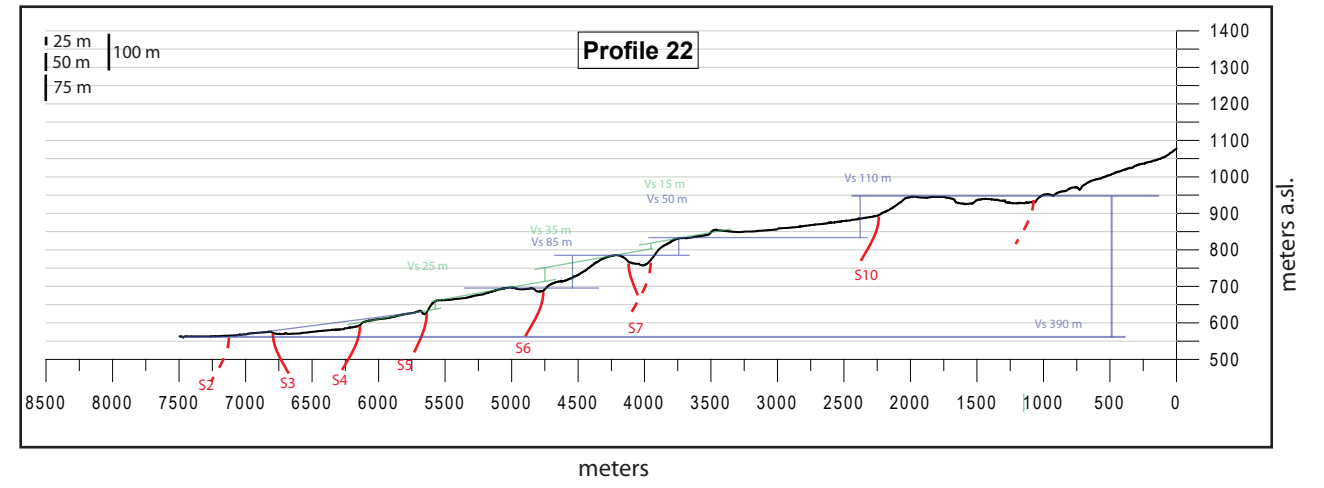
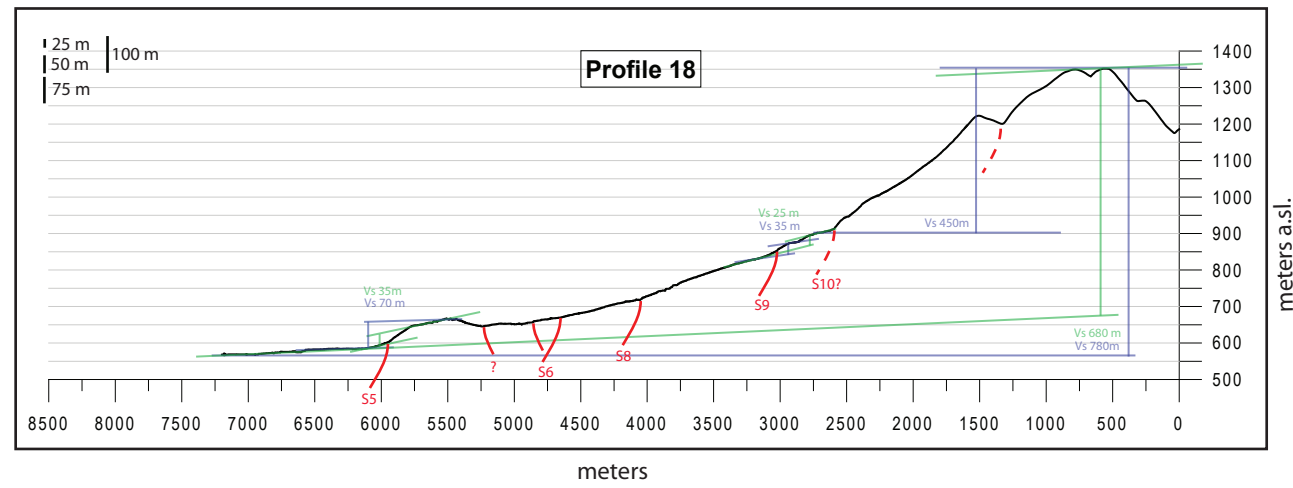
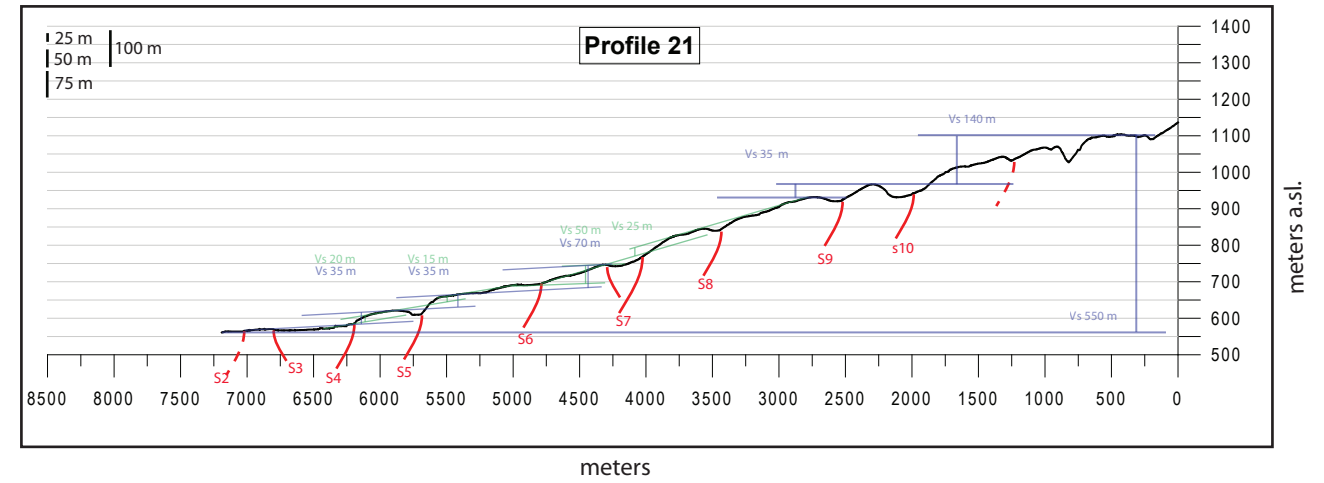
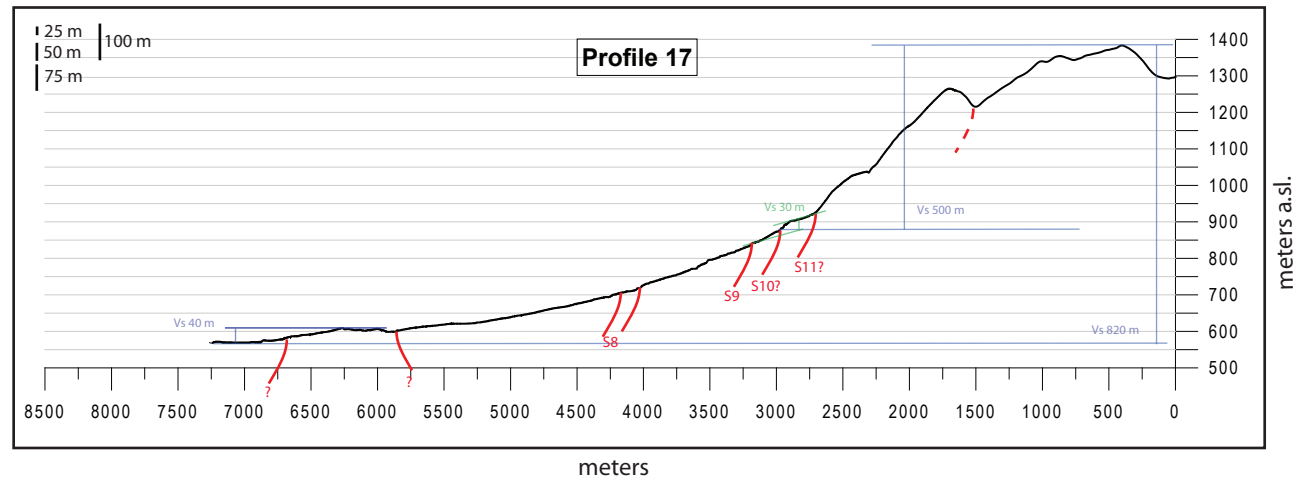
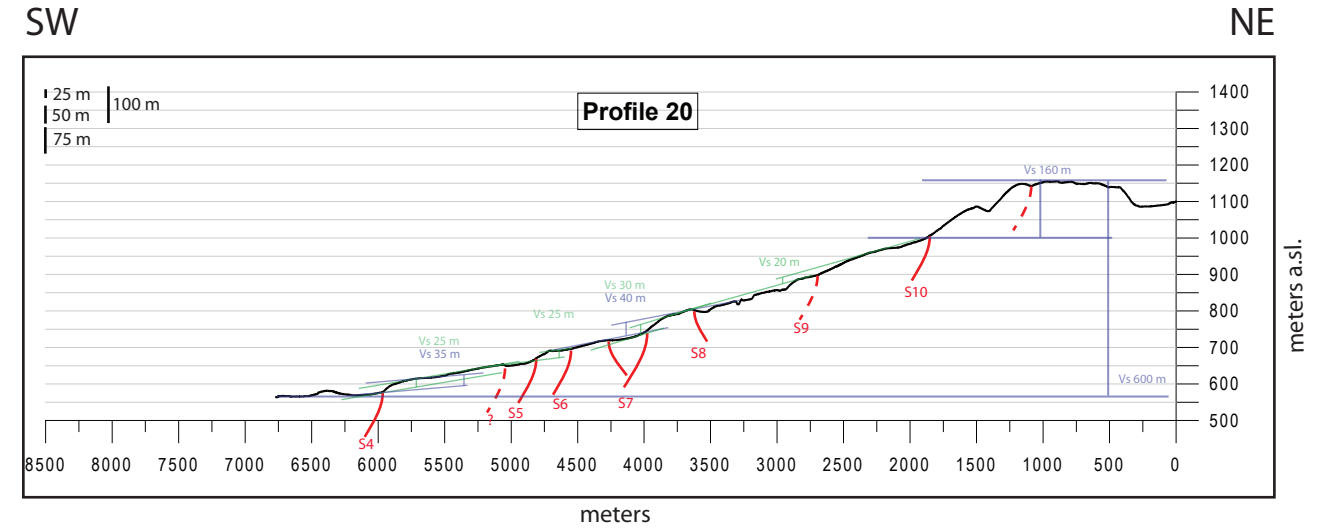
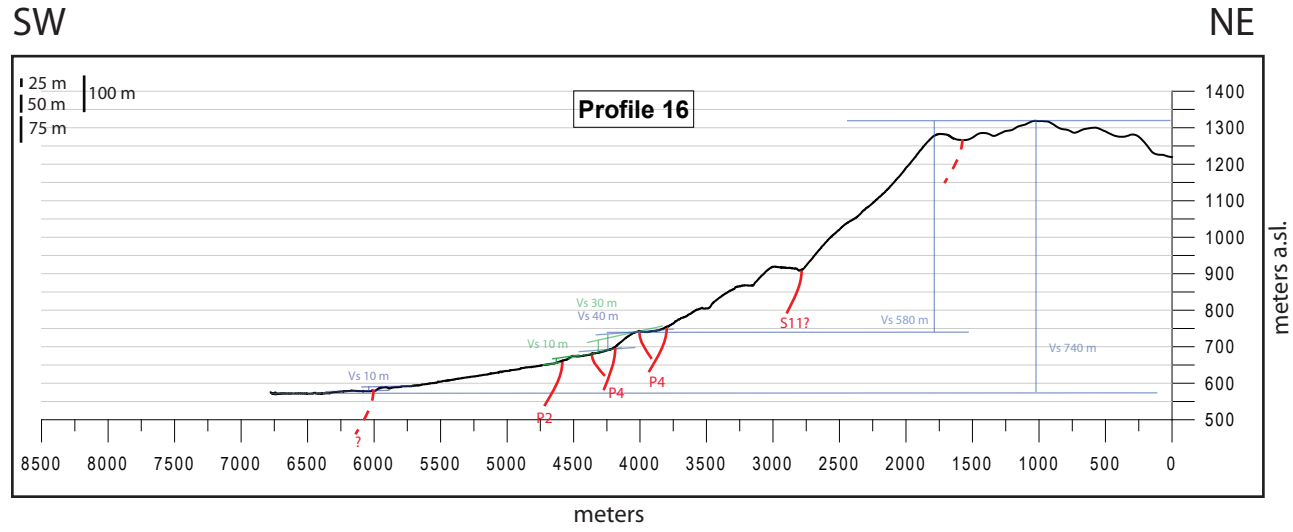
APPENDIX D1 - TOPOGRAPHIC PROFILES 0 - 7



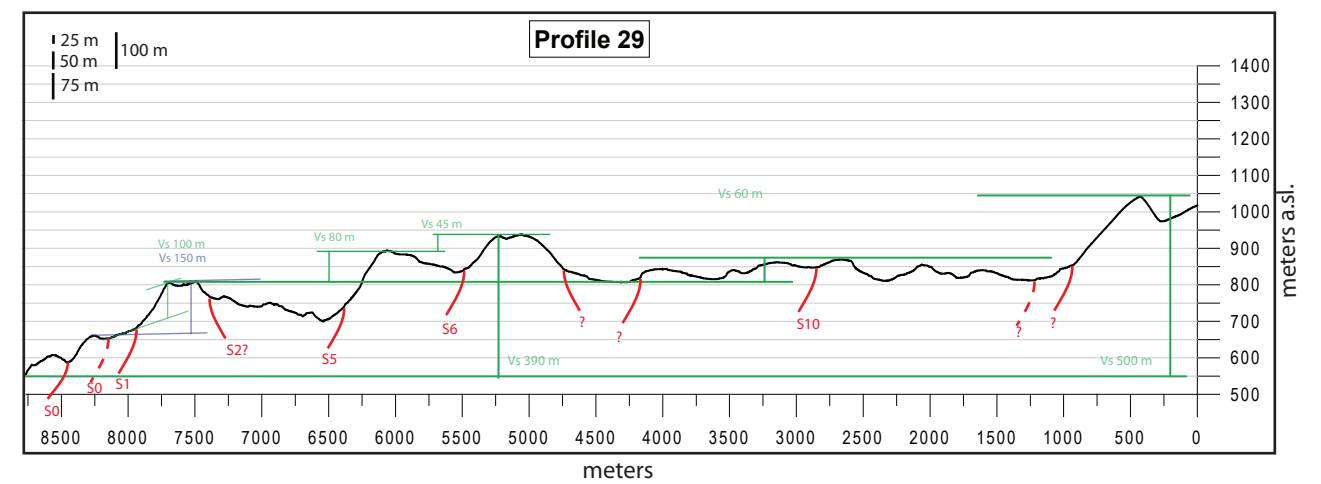
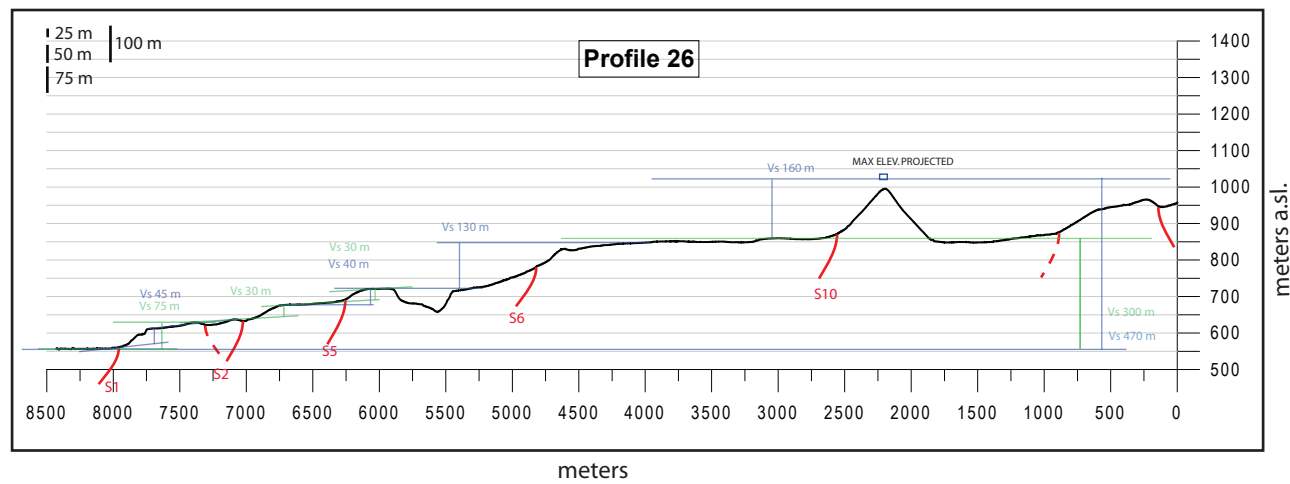
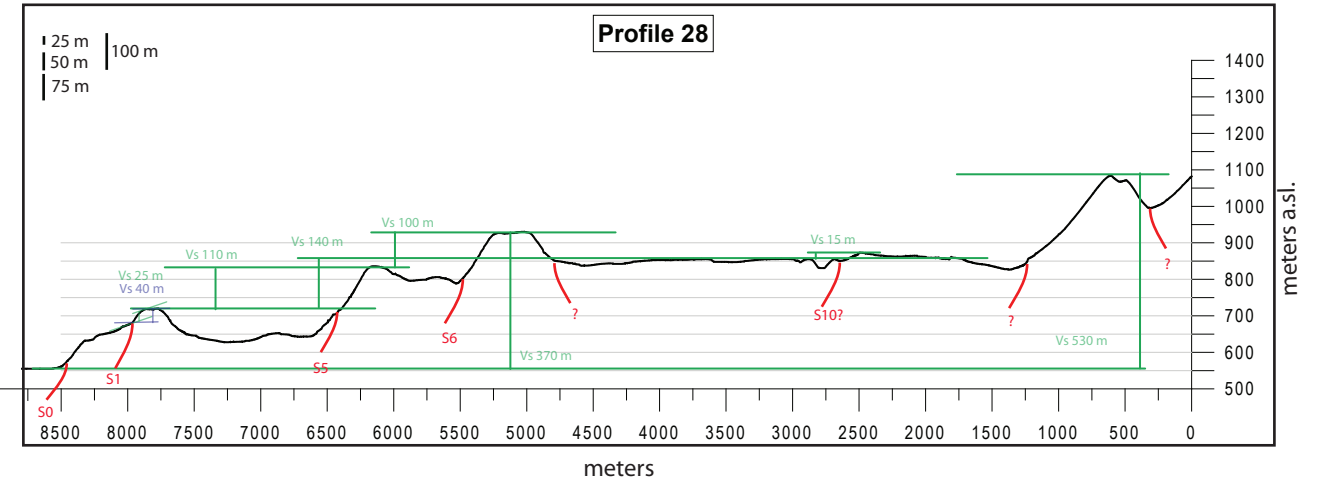
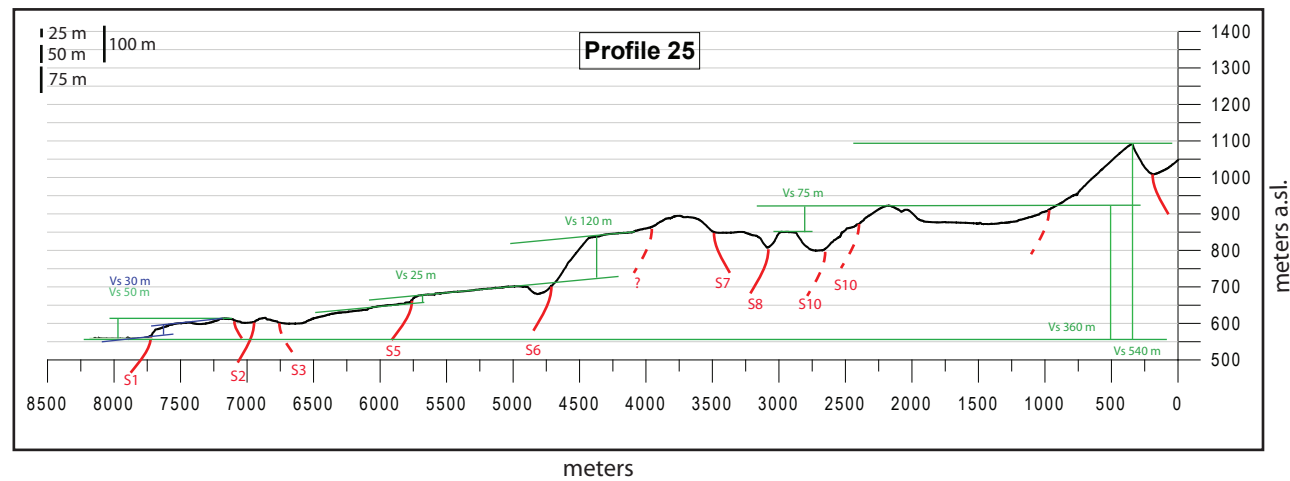
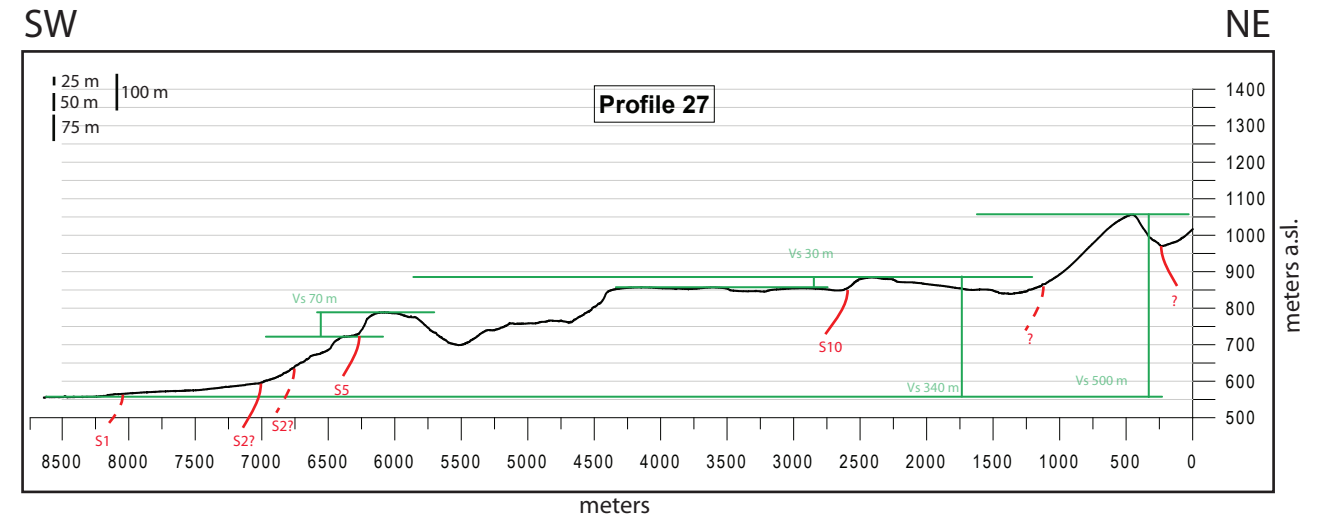
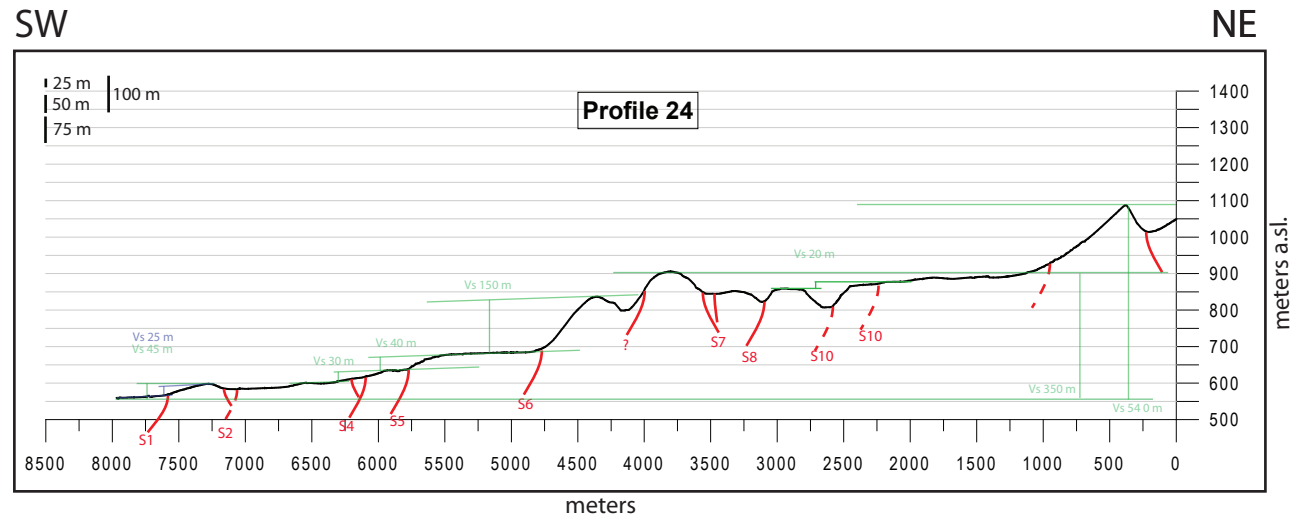
APPENDIX D2 - TOPOGRAPHIC PROFILES 8 - 15

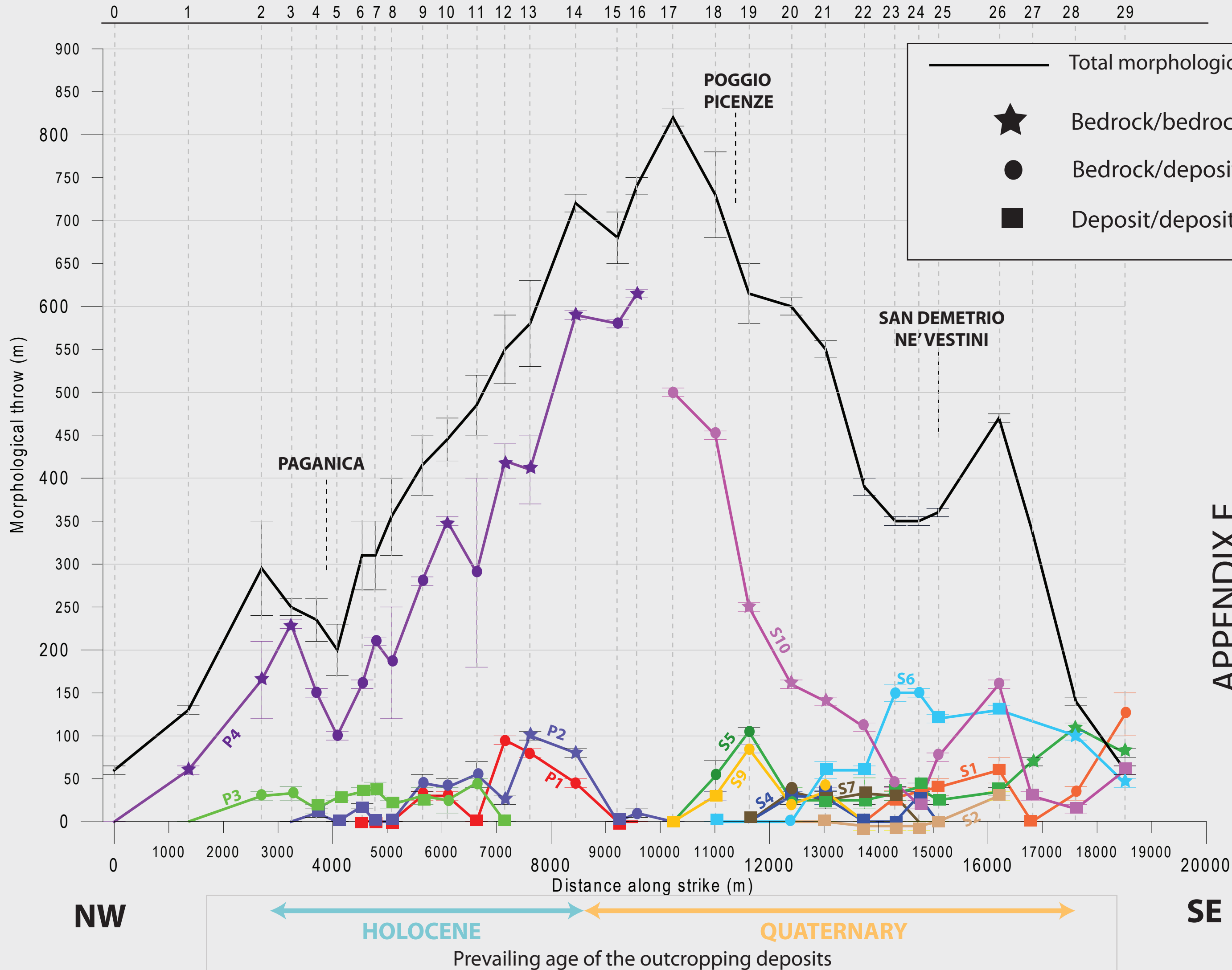


APPENDIX D3 - TOPOGRAPHIC PROFILES 16 - 23



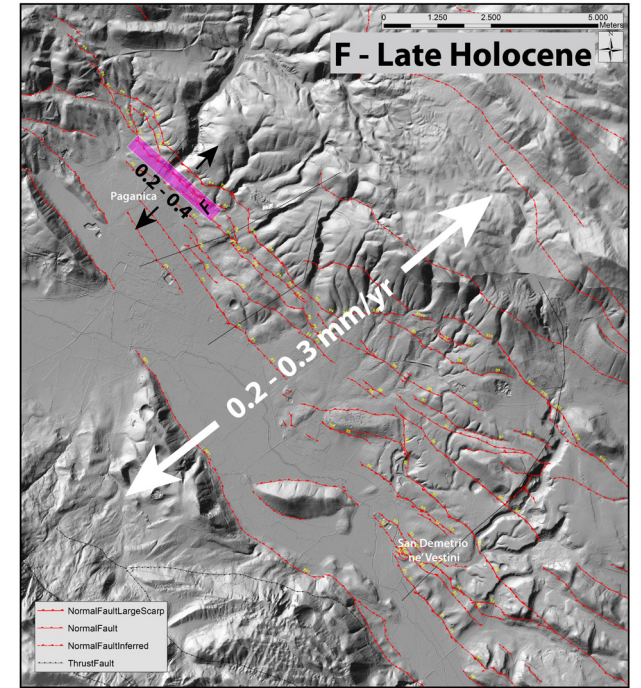
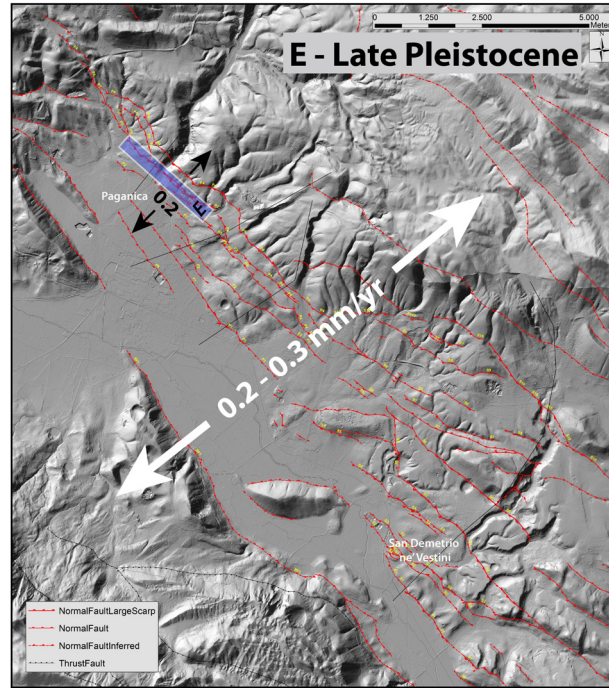
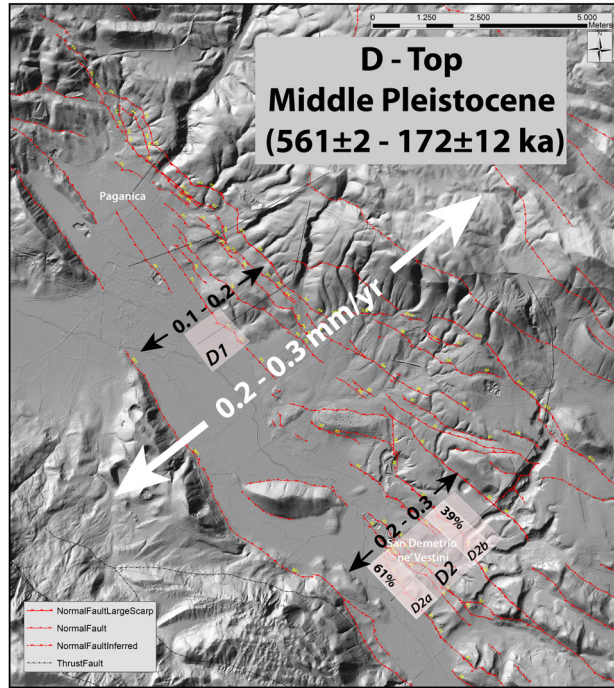
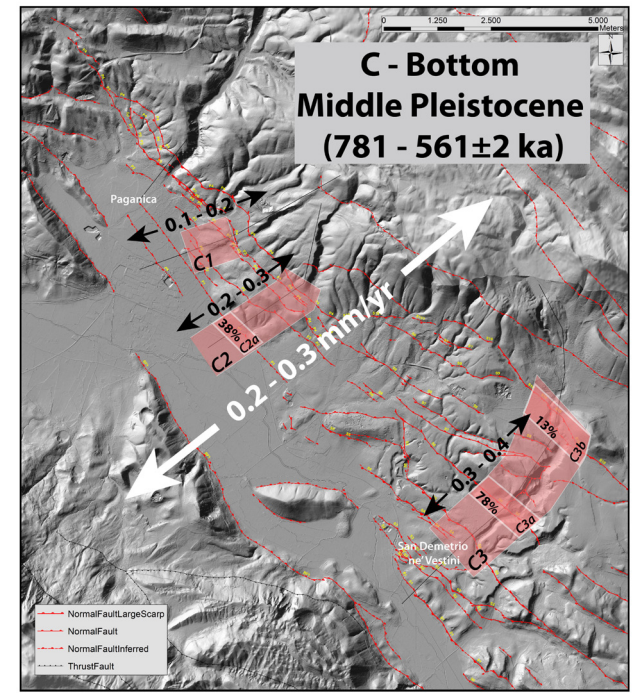
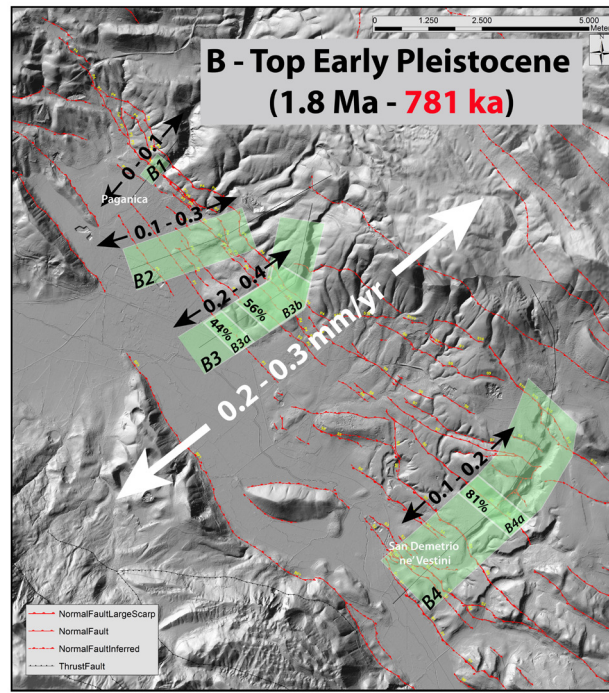
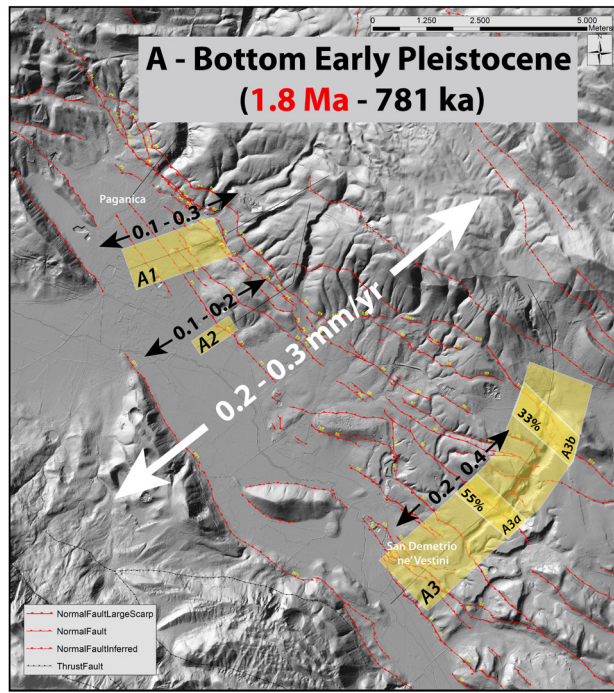
APPENDIX D4 - TOPOGRAPHIC PROFILES 24 - 29





APPENDIX E

Along -strike plot of the morphological throws measured from the topographic profiles across the PSDFS. Morphological throws for each fault sply are presented in different colors and with different symbols to distinguish between throw values calculated from offset reference surfaces (i.e. piercing points) carved in bedrock (star) or in unconsolidated deposits (square) or a combination of the abovementioned (point).



The overall average Quaternary extension-rate of the PSDFS is reported inside the white arrows and is used as a reference to analyze the relative contribution to the deformation of different sectors and plays. Light-shaded areas: transects across which the extension-rates were estimated for each specific time-interval (keyed with a capital letter and a number that are the same in text and table 8.1). When available, individual contribution of single fault splays is reported as percentage of the extension-rate estimated in each transect (keyed with letters and a number that are the same in text and table 8.1).